Doctoral Dissertation

February 11, 2021

Measurement of Higgs boson properties using the decay channel to b-quarks following associated production with a vector boson in pp collisions at $\sqrt{s} = 13$ TeV

Department of Physics, Graduate School of Science, Kyoto University

Yohei Noguchi

Abstract

The Higgs boson was discovered by the ATLAS and CMS experiments using the Large Hadron Collider at CERN. After the discovery, it became important to measure the properties of the Higgs boson to validate the Higgs mechanism in the Standard Model (SM) by measuring all the production and decay modes. In addition, the properties of the Higgs boson such as the coupling and the differential production cross-sections are sensitive to physics beyond the Standard Model (BSM) desired from both theoretical viewpoints and cosmological observations. The measurement of these properties of the Higgs boson is also an indirect search for BSM.

The cross-section of the Higgs boson production associated with either a W or Z boson (WH and ZH) times the branching fraction of the $H \to b\bar{b}$ decay is measured using data of pp collisions at the center-of-mass energy of 13 TeV with an integrated luminosity of 139 fb^{-1}. The measurement includes the $WH \to \ell\nu b\bar{b}$, $ZH \to \nu\bar{\nu}b\bar{b}$, and $ZH \to \ell^+\ell^- b\bar{b}$ channels. Two main improvements are introduced in the $ZH \to \ell^+\ell^- b\bar{b}$ channel compared with the previous measurement with fewer data statistics. One is an improvement in the performance of a multivariate method achieved by exploiting the difference in the polarization of the Z boson between the signal and the background processes. The other is a development of a new methodology to model top-quark production backgrounds and to eliminate approximately 10% systematic uncertainties of these background processes. This new modeling approach makes the results more reliable.

The signals are observed (expected) with the significance of 4.0 (4.1) and 5.3 (5.1) standard deviations for WH and ZH with respect to the background-only hypothesis, respectively. These results are the first evidence of the WH production and the first observation of the ZH production, respectively. The analysis yields signal strengths, the ratios of the observed production cross-sections times the branching ratio to the prediction of the Standard Model, for the WH and ZH productions as $\mu^{bb}_{WH} = 0.95^{+0.27}_{-0.25}$ and $\mu^{bb}_{ZH} = 1.08^{+0.25}_{-0.23}$, respectively. Measurement of a differential production cross-section times the branching fraction as a function of the transverse momentum of the vector boson (p^V_{T}) is also performed, and the results are: 19.0 ± 12.1 fb ($150 \le p^W_{\mathrm{T}} < 250$ GeV), 7.2 ± 2.2 fb ($p^W_{\mathrm{T}} \ge 250$ GeV) for WH and 42.5 ± 35.9 fb ($75 \le p^Z_{\mathrm{T}} < 150$ GeV), 20.5 ± 6.2 fb ($150 \le p^Z_{\mathrm{T}} < 250$ GeV), 5.4 ± 1.7 fb ($p^Z_{\mathrm{T}} \ge 250$ GeV) for ZH. The measured differential cross-sections are all consistent with the prediction of the Standard Model within the uncertainties ranging from 85% to 30% depending on the p^V_{T} regions.

The analysis sets constraints on BSM scenarios that affect the differential cross-section of the VH production. In order to provide the experimental constraints in a model-independent way, the results are interpreted in the Standard Model Effective Field Theory framework, and the Wilson coefficients of dimension-6 interactions, $c^{(3)}_{Hq}$, c_{Hu}, c_{HW} and c_{HWB}, are constrained.

The 125 GeV Higgs boson may be a CP-mixed state in a BSM model such as the 2 Higgs Doublet Model, which contains the CP-odd interaction of the 125 GeV scaler particle and the vector bosons (VVH vertex). The measurement of the p^V_{T} spectrum is a test of general BSM scenario and can constrain those CP-odd interactions. However, the measurement can not tell whether the BSM interaction violates the CP symmetry because the spectrum can also be affected by CP-even BSM interactions. The decay angle of $Z \to \ell^+\ell^-$ in the ZH channel depends on the tensor structure of the VVH vertex. An analysis that exploits the decay

angle to probe the CP-odd tensor structure of this vertex is proposed. This angular analysis provides weaker constraints on the tensor structure than the analysis using the p_{T}^{V} differential measurement. The same effect on the VVH vertex can also be accessed via the decay modes of the Higgs boson: $H \to ZZ^{*} \to 4\ell$ and $H \to WW^{*} \to e\nu\mu\nu$. The constraint on the corresponding Wilson coefficient derived from the VH production using the p_{T}^{V} spectrum is roughly 30-40 times more stringent than the constraints by the decay channels using the pp collision at 7 and 8 TeV (LHC ATLAS Run 1). The analysis using the decay angle in the $ZH \to \ell^{+}\ell^{-}b\bar{b}$ channel yields roughly 5-10 times more stringent constraint on the same Wilson coefficient than the analysis of the Higgs decay channels in the Run1.

The inclusive measurement of VH, $H \to b\bar{b}$ is included in the combined measurement of the Higgs couplings with all the available production and decay modes in ATLAS. The experimental observable is the branching ratio, the partial decay width divided by the total width of the Higgs boson. The $H \to b\bar{b}$ decay has the largest branching ratio of 58% among the decay modes in the Standard Model, and the measurement of the $H \to b\bar{b}$ decay constrains the total width. Consequently, the measurement significantly contributes to the constraints of the other Higgs couplings as well as the $H \to b\bar{b}$ coupling. Approximately 3 times more stringent constraints on the Higgs coupling to Z, W, and b-quark and 15-40% more stringent constraints on the coupling to t-quark, τ-lepton, and muon are observed compared to the measurement without including the VH, $H \to b\bar{b}$ analysis.

Acknowlegements

I deeply appreciate Dr. Toshi Sumida for supporting all my activities during the master and doctor course, for a lot of suggestions on almost all of my compositions and presentations both in English and Japanese, and for many discussions in the weekly ATLAS meetings.

I express my deepest gratitude to Dr. Tatsuya Masubuchi for all his advice on the analysis, the presentations, how to contribute to the group, and all the other things. I also appreciate him for working as the coordinator of the analysis team. I really enjoyed the discussions on physics and have been helped by his knowledge and passion.

I appreciate Prof. Kunihiro Nagano for reading and examining this thesis, and providing useful suggestions. I also thank him for leading the ATLAS-Trigger group to provide the high-quality data and make my studies possible.

I express my gratitude to Prof. Tsuyoshi Nakaya for giving me the opportunity to work in the field of experimental particle physics. I also express my gratitude to Prof. Masaya Ishino for inviting me to the ATLAS experiment and supporting my first step as a researcher, and for his hard work as the ATLAS Run Coordinator, providing the good data, and making my studies possible.

I appreciate Dr. Yuji Enari and Prof. Yasuyuki Okumura for many discussions in the weekly ATLAS-J Higgs meetings and a lot of advice.

I am grateful to Dr. Junya Nakamura for pointing the role of the polarization in the analysis, which is one of the essential components of the studies.

I would like to thank Dr. Elisabeth Schopf and Dr. Thomas Calvet for all their works to organize the VHbb team and for showing a role model of how young leaders act in the team. I appreciate Dr. Chikuma Kato, Dr. Stephen Jiggins, and Dr. Yanhui Ma for all your works to realize our great results. I appreciate Dr. Luca Ambroz, Dr. Konie Al Khoury, Dr. Simona Gargiulo for working for the 0- and 1-lepton channels, and realizing our results. The activities of these same-age teammates were stimulating. I express my special thanks to Prof. Paolo Francavilla and Mr. Philipp Windischhofer for guiding me to the EFT studies. I was greatly stimulated by Philipp's works and talent. I greatly appreciate Dr. Nicolas Morange for a lot of interesting discussions and sharing deep insight into the statistical analysis, which were stimulating. I appreciate Dr. Hannah Arnold, Dr. Andrew Chisholm, and Dr. Valerio Dao for the coordination of the ATLAS Hbb group.

I would express my great appreciation to Dr. Marcus M. Morgenstern, Dr. Mark Owen, Dr. Savanna M. Shaw, and Prof. Yu H. Nakahama for working together for the ATLAS Muon Trigger Signature Group and supporting my tasks. I also thank Dr. Yohei Yamaguchi and Prof. Yuji Yamazaki for helping my activities and organizing the ATLAS-J Muon HLT group.

I greatly thank Dr. Kenta Uno and Dr. Shunichi Akatsuka for sharing time of research, eating, drinking, refreshing, and all the other things, which were the relaxing part of my life at CERN. I appreciate

Mr. Ryunosuke Iguchi for leading the ATLAS-J Higgs meetings as a chairperson. I thank Mr. Kenta Uchida, Mr. Atsushi Mizukami, and Mr. Naoki Yamaguchi for helping and sharing my life in Ferney.

I greatly appreciate Mr. Alberto Pace for hosting my life in Ferney and at CERN.

I appreciate Dr. Takuya Tashiro and Dr. Takuto Kunigo for their supports at CERN and in Kyoto especially in the first two years in ATLAS. I thank Mr. Yuta Okazaki and Mr. Yuya Mino for the discussion and for sharing time for eating and drinking. I also thank Mr. Koichiro Kuniyoshi, Mr. Masayuki Hatano, Mr. Ren Kobayashi, Mr. Yoshiaki Tsujikawa, Mr. Takane Sano, and Mr. Nobuyuki Yoshimura for interesting presentations on the muon trigger at the meetings.

I am grateful to the members of the Kyoto University HEP group, especially Dr. Shunichi Akatsuka, Dr. Yosuke Ashida, Dr. Ayami Hiramoto, Ms. Yoshie Kageyama (Nakanishi), and Mr. Shunsuke Tanaka for sharing fun and stimulating as colleagues for years. I appreciate Prof. Roger A. Wendell for the nice title of this thesis. I also thank Prof. Atsuko Ichikawa, Prof. Osamu Tajima, Dr. Junya Suzuki, and Dr. Tatsuya Kikawa for interesting stories, and Prof. Osamu Tajima for examining this thesis and useful suggestions.

I thank all the other members for their supports, a nice time over suppers and coffee. I greatly appreciate Ms. Eriko Hayashi, Ms. Harumi Sekiguchi, Ms. Mana Sasaki, and other secretaries at Kyoto University for all the support.

Finally, I deeply appreciate warm support from my family, Toshihiro, Kaoru, Kensuke, and Tatsuhiko.

Contents

List of Figures

List of Tables

1 Introduction

The smallest units of the matter are called *elementary particles*. The Standard Model of particle physics (SM) describes all known elementary particles and interactions among those particles. Wide variety of experimental phenomena are explained by the SM. However, the SM still has theoretical and cosmological problems. One of the theoretical issues is that the SM does not provide a natural explanation of the light mass of the Higgs boson [1–6], which is subjected to a large quantum correction. This problem is referred to as *hierarchy problem*. One of the cosmological/phenomenological issues is that the SM is not able to generate the observed baryon asymmetry of the universe (BAU). All these remaining issues imply the need for physics beyond the Standard Model (BSM).

The Higgs boson was discovered in the $H \to \gamma\gamma$, $H \to ZZ^* \to 4\ell$ and $H \to WW^* \to e\nu\mu\nu$ decay channels [7, 8] by the ATLAS [9] and CMS experiments [10] using proton-proton (pp) collisions at $\sqrt{s} = 7$ and 8 TeV (LHC Run 1). The Higgs decay to a pair of τ leptons is observed[1] using the same Run 1 dataset [11–13]. Using collision data of 79.8 fb^{-1} with the center-of-mass energy increased to $\sqrt{s} = 13$ TeV (LHC Run 2), there was the observation of the Higgs production in association with a pair of top-quarks [14, 15] using collision data of 79.8 fb^{-1}, which directly confirms the Higgs coupling to the top-quarks. Finally, the observations of the Higgs production in association with a vector boson (VH production) and the Higgs decay to a pair of b-quarks were achieved [16, 17] using the 79.8 fb^{-1} data at $\sqrt{s} = 13$ TeV in addition to the data at $\sqrt{s} = 7$ and 8 TeV.

Given the confirmation of the Higgs coupling to the gauge bosons and the third generation fermions, the attention of the Higgs physics is focused on precision measurements of this particle aiming at precision tests of the Higgs mechanism and searches for hidden effect from BSM. The VH production and the $H \to b\bar{b}$ decay are focused in this thesis using the 139 fb^{-1} pp collision data at $\sqrt{s} = 13$ TeV collected with the ATLAS detector.

The $H \to b\bar{b}$ decay is caused by the Yukawa coupling to the b-quarks, and its branching ratio of 58% [18] is largest compared to the other decay modes in the SM. The precision measurements of the bottom Yukawa coupling provides tests of BSM models such as *2 Higgs Doublet Model (2HDM)* [19], which can be relevant to the BAU [20, 21].

The VH production mode allows us to study the $H \to b\bar{b}$ decay by requiring the leptonic decay channel of the vector boson to reduce backgrounds significantly. Measurements of the differential cross-section as a function of the transverse momentum of the vector boson (p_{T}^V) can also be tests of BSM models because BSM models generally affect the cross-section of the VH production in the final state with high p_{T}^V. Since the VH production is caused by the same VVH vertex as the $H \to ZZ^* \to 4\ell$ and $H \to WW^* \to e\nu\mu\nu$ decay modes [22], a BSM affects both the VH production and the decays. However, the effects are more significant in phenomena at a large energy scale (large virtuality of the vector boson). The energy scales in the decays are bounded by the mass of the Higgs boson whereas there is no such boundary for kinematics

[1] In the field of the experimental elementary particle physics, the confirmation of a phenomenon with greater statistical significance than 5 standard deviations is referred to as *observation*.

in the VH production. Therefore, the VH production mode is more sensitive to effects from BSM than the Higgs decay channels. One example for such BSM models is the *Heavy Vector Triplet (HVT) model* [23]. This model appears as a low energy description of many models. The Minimal Composite Higgs Model [24], which provides a solution to the hierarchy problem, is an example that reproduces the HVT model at low energy.

The scope of this thesis is as follows. Two major improvements to the analysis channel targeting the $Z \to \ell^+\ell^-$ decay following the ZH production are achieved. One is an improvement in the performance of multivariate analysis incorporating the information on the polarization of the Z boson. This improves the final sensitivity. The other is a new modeling method for top-quark production backgrounds to eliminate systematic uncertainties of that background. With these improvements, the differential cross-sections of the WH and ZH productions as functions of the transverse momentum of the vector boson are measured. Interpretation of the measurements of the cross-section is performed using the Standard Model Effective Field Theory [25, 26] to provide constraints for general BSM. A new analysis using the decay angle of $Z \to \ell^+\ell^-$ in the ZH channel is developed to probe the CP-odd modification of the VVH vertex, which may follow the CP-mixed 125 GeV scalar particle in the 2HDM [27, 28]. In addition, the Higgs couplings are measured including this analysis of VH and $H \to b\bar{b}$ [29]. The contribution of the analysis to the coupling measurement is also discussed.

This thesis is organized as the following. In Chapter 2, theoretical backgrounds are described including a short description of the Standard Model and the Higgs boson physics. In Chapter 3, the experimental apparatus, the Large Hadron Collider and the ATLAS detector, is described. In Chapter 4, the data and simulations used in the analysis are described. In Chapter 6, the strategy of the analysis is discussed. In Chapter 7, methods for the background estimation are described. In Chapter 8, systematic uncertainties considered in the analysis are explained. In Chapter 9, methods for statistical analysis are described. In Chapter 10, the results of the cross-section measurements are presented. In Chapter 11, interpretations of the measurements and the contribution to the Higgs coupling measurement are discussed. Finally, in Chapter 12, conclusions are stated.

The author's contributions to the results are as follows: the improvement of the multivariate analysis is discussed in Section 6.6.4. The new modeling method of the top-quark backgrounds is discussed in Sections 7.2.2 and 9.2.2. The analysis using the $Z \to \ell^+\ell^-$ decay angle for probing the CP structure of the VVH vertex is discussed in Section 11.2.

2 Theoretical backgrounds

The theoretical backgrounds which this thesis is based on are introduced in this chapter. The Standard Model of particle physics is summarized in Section 2.1. Theoretical aspects of the Higgs boson and its properties are reviewed in Section 2.2. Remained issues in particle physics after the foundation of the Standard Model are raised in Section 2.3, and the approaches of this thesis to these issues are explained in Sections 2.4 and 2.5.

2.1 The Standard Model of particle physics

The *Standard Model of particle physics (SM)* is a field theory that includes fields corresponding to the observed particles. "Particles" appear by quantizing the motion of these fields. The SM has the following three ingredients. (i) *Fermions*, which constitute matters. This type of particles consists of *quarks* and *leptons*. (ii) *Gauge symmetry*, from which the interactions of the fermions are derived. Fields of another type called *gauge bosons* are required. (iii) *The origin of the mass* is explained by introducing *Higgs field*.

The elementary particles are summarized in Tables 2.1 and 2.2. Known interactions of these particles are *electromagnetic interaction*, *weak interaction*, *strong interaction* and *gravity*. The electromagnetic and weak interactions are unified into *electroweak interactions*. Three interactions excluding the gravity are derived from *gauge symmetry* and mediated by corresponding *gauge bosons*.

The basic description of the SM is presented in the next sections following arguments given in Refs. [30, 31].

Gauge symmetry

Lagrangian of the elementary fields is required to be invariant (symmetric) under certain *gauge transformations* which are explained in the next paragraph. The set of gauge transformations forms a group called

Table 2.1: Fermions in the Standard Model.

Type	Generation			Spin	Charge	Strong interaction
	1	2	3			
Leptons	ν_e	ν_μ	ν_τ	1/2	0	-
	e	μ	τ	1/2	-1	-
Quarks	u	c	t	1/2	2/3	✓
	d	s	b	1/2	-1/3	✓

Table 2.2: Bosons in the Standard Model.

Type	Symbol	Field	Spin	Charge	Role
Gauge bosons	$W^{\pm}$	$W^{\pm}_{\mu}$	1	1	Weak interaction
	Z	Z_{μ}	1	0	Weak interaction
	g	G_{μ}	1	0	Strong interaction
	γ	A_{μ}	1	0	Electromagnetic interaction
Scaler boson	φ	φ	0	0	Origin of the masses

gauge group. An example is the *Yang-Mills* Lagrangian:

$$\mathcal{L} = -\frac{1}{4}F^{a}_{\mu\nu}F^{a\mu\nu} + \bar{\psi}(i\not{D})\psi - m\bar{\psi}\psi. \tag{2.1}$$

The anti-symmetric tensor $F^{a}_{\mu\nu}$ is defined as:

$$F^{a}_{\mu\nu} = \partial_{\mu}A^{a}_{\nu} - \partial_{\nu}A^{a}_{\mu} + g f^{abc}A^{b}_{\mu}A^{c}_{\nu}, \tag{2.2}$$

where A^{a}_{μ} are vector fields and f^{abc} is the *structure constants* of the gauge group. ψ is a set of fermion fields. The *covariant derivative* D_{μ} is defined as

$$D_{\mu} = \partial_{\mu} - igA^{a}_{\mu}t^{a}, \tag{2.3}$$

where g is the *gauge coupling constant* and t^{a} is the generators of the gauge group[1].

The Yang-Mills Lagrangian in Eq. 2.1 is invariant under the following gauge transformation. The fermion fields are transformed as:

$$\psi \rightarrow \exp\left(i\alpha^{a}t^{a}\right)\psi, \tag{2.4}$$

where $\alpha^{a} = \alpha^{a}(x)$ are functions of the spacetime. For an infinitesimal transformation, this is rewritten as

$$\psi \rightarrow (1 + i\alpha^{a}t^{a})\psi. \tag{2.5}$$

The transformation of the vector fields are

$$A^{a}_{\mu} \rightarrow A^{a}_{\mu} + \frac{1}{g}\partial_{\mu}\alpha^{a} + f^{abc}A^{b}_{\mu}\alpha^{c}. \tag{2.6}$$

Under these transformations, the components in the Lagrangian are transformed as:

$$(\partial_{\mu} - igA^{a}_{\mu}t^{a})\psi \rightarrow (1 + i\alpha^{b}t^{b})(\partial_{\mu} - igA^{a}_{\mu}t^{a})\psi + O(\alpha^{2}), \tag{2.7}$$

$$F^{a}_{\mu\nu} \rightarrow F^{a}_{\mu\nu} + g f^{abc}F^{b}_{\mu\nu}\alpha^{c} + O(\alpha^{2}). \tag{2.8}$$

In the second line, the *Jacobi identity*[2] is used. Using these rules, the terms in the Yang-Mills Lagrangian are invariant under these gauge transformations.

The electroweak and strong interactions are described as Yang-Mills theories based on the gauge groups $SU(2)_{L} \times U(1)_{Y}$ and $SU(3)_{C}$, respectively. The implication of these theories are explained in the following sections.

[1] Generators which belong to different simple Lie sub-algebras of the gauge group can have different coupling constants.
[2] $f^{ade}f^{bcd} + f^{cde}f^{abd} + f^{bde}f^{cad} = 0$.

Electroweak interaction

The SM unifies the electromagnetic and weak interactions as *electroweak interaction*. The behavior of the electroweak interaction is understood as an individual interaction of right-handed and left-handed fermions. The right and left-handed fermions are defined by the eigen states of 1 and -1 of the γ^5 matrix, where γ^5 is $i\gamma^0\gamma^1\gamma^2\gamma^3$ and γ^μ ($\mu = 0, \cdots, 3$) are the *Dirac matrices*. The left-handed fermions form *isospin doublets* combining *neutrino* and *electron*, *up quark* and *down quark*. The electroweak interaction is identified as a gauge interaction based on $SU(2)_L \times U(1)_Y$. The interaction between these isospin doublets and gauge bosons W^a_μ ($a = 1, 2, 3$) and B_μ are described as:

$$-i\bar{L}\gamma^\mu \left(g\tau^a W^a_\mu + g' \frac{Y_L}{2} B_\mu \right) L, \tag{2.9}$$

$$-i\bar{Q}\gamma^\mu \left(g\tau^a W^a_\mu + g' \frac{Y_Q}{2} B_\mu \right) Q, \tag{2.10}$$

where $L = (\nu_{eL}, e_L)$, $Q = (u_L, d'_L)$ and τ^a ($a = 1, 2, 3$) are the half of the Pauli matrices: $\tau^a = \sigma^a/2$. There are three copies of L and Q referred to as *generation*, and they are described by the same Lagrangian. d'_L is an eigen state of the weak interaction and related to a mass eigen state d_L through the Cabbibo-Kobayashi-Maskawa matrix V_{CKM} as:

$$\begin{pmatrix} d'_L \\ s'_L \\ b'_L \end{pmatrix} = V_{\mathrm{CKM}} \begin{pmatrix} d_L \\ s_L \\ b_L \end{pmatrix}. \tag{2.11}$$

Y_L and Y_Q are called *hyper charge* and the values are summarized in Table 2.3.

Table 2.3: Charge of the electroweak interaction. The values for ν_R are written for the case that they exist. T^3 has a value of $\tau^3/2$ for the left-handed fields, and 0 for the right-handed fields. Q_{em} is the electric charge and $T^3 + Y/2 = Q_{\mathrm{em}}$ is satisfied.

Types		T_3	Y	Q_{em}
Leptons	$L = \begin{pmatrix} \nu_L \\ e_L \end{pmatrix}$	$\frac{1}{2}$ $-\frac{1}{2}$	-1	0 -1
	ν_R	0	0	0
	e_R	0	-2	-1
Quarks	$Q = \begin{pmatrix} u_L \\ d'_L \end{pmatrix}$	$\frac{1}{2}$ $-\frac{1}{2}$	$\frac{1}{3}$	$\frac{2}{3}$ $-\frac{1}{3}$
	u_R	0	$\frac{4}{3}$	$\frac{2}{3}$
	d_R	0	$-\frac{2}{3}$	$-\frac{1}{3}$
Higgs	$\varphi = \begin{pmatrix} \varphi_1 \\ \varphi_2 \end{pmatrix}$	$\frac{1}{2}$ $-\frac{1}{2}$	1	1 0

The gauge fields W_μ^i and B_μ in Eqs. 2.9 and 2.10 are related to the gauge bosons in Table 2.2 by:

$$W_\mu^\pm = \frac{W_\mu^1 \mp i W_\mu^2}{\sqrt{2}} \tag{2.12}$$

$$\begin{pmatrix} Z_\mu \\ A_\mu \end{pmatrix} = \begin{pmatrix} \cos\theta_W & -\sin\theta_W \\ \sin\theta_W & \cos\theta_W \end{pmatrix} \begin{pmatrix} W_\mu^3 \\ B_\mu \end{pmatrix}, \tag{2.13}$$

where θ_W is the Weinberg angle, which is related to the gauge couplings through:

$$\cos\theta_W = \frac{g}{\sqrt{g^2 + g'^2}}, \ \sin\theta_W = \frac{g'}{\sqrt{g^2 + g'^2}}. \tag{2.14}$$

On the other hand, the right-handed fermions do not form isospin doublets but are isospin singlets. In this case, these right-handed fermions do not interact with the W boson. The interaction of the right-handed and the gauge boson are described as:

$$-ig'\frac{Y_e}{2}\bar{e_R}\gamma^\mu B_\mu e_R, \tag{2.15}$$

$$-ig'\frac{Y_u}{2}\bar{u_R}\gamma^\mu B_\mu u_R, \tag{2.16}$$

$$-ig'\frac{Y_d}{2}\bar{d_R}\gamma^\mu B_\mu d_R. \tag{2.17}$$

By rewriting Eq. 2.9 in terms of the observed field A_μ, Z_μ and $W_\mu^\pm$, the equation becomes

$$-i\frac{g}{\sqrt{2}}\bar{L}\gamma^\mu\left(\tau^+ W_\mu^+ + \tau^- W_\mu^-\right)L + -i\sqrt{g^2+g'^2}\bar{L}\gamma^\mu\left(\tau_3\cos^2\theta_W - \frac{Y_L}{2}\sin^2\theta_W\right)LZ_\mu - ie\bar{L}\gamma^\mu\left(\tau^3 + \frac{Y_L}{2}\right)LA_\mu \tag{2.18}$$

$$\begin{aligned} &= -i\frac{g}{\sqrt{2}}\left(\bar{\nu}_L\gamma^\mu e_L W_\mu^+ + \bar{e}_L\gamma^\mu\nu_L W_\mu^-\right) \\ &\quad -i\sqrt{g^2+g'^2}\left[\bar{\nu}_L\gamma^\mu\nu_L - \left(\frac{1}{2} - \sin^2\theta_W\right)\bar{e}_L\gamma^\mu e_L\right]Z_\mu - ie\bar{e}_L\gamma^\mu e_L A_\mu, \end{aligned} \tag{2.19}$$

where $\tau^\pm = (\tau^1 \mp i\tau^2)$, and e is the electric charge of the electron:

$$e = \frac{gg'}{\sqrt{g^2+g'^2}}. \tag{2.20}$$

Note that in Eq. 2.19 the values of hypercharges in Table 2.3 are substituted. Similarly, Eq. 2.15 becomes

$$-ig'\frac{Y_e}{2}\bar{e}_R\gamma^\mu\left(\cos\theta_W A_\mu - \sin\theta_W Z_\mu\right)e_R \tag{2.21}$$

$$= ig'\sin\theta_W\bar{e}_R\gamma^\mu e_R Z_\mu - ie\bar{e}_R\gamma^\mu e_R A_\mu. \tag{2.22}$$

The values of hypercharges in Table 2.3 are substituted.

A scalar field in isospin doublet called *Higgs field* is introduced, and the motion of this field is described as:

$$\left|\left(\partial_\mu - ig\tau^a W_\mu^a - i\frac{g'}{2}B_\mu\right)\varphi\right|^2 + V(\varphi), \tag{2.23}$$

$$V(\varphi) = \mu^2\varphi^\dagger\varphi - \lambda\left(\varphi^\dagger\varphi\right)^2. \tag{2.24}$$

The minimum of $V(\varphi)$ is given when $(\varphi^\dagger\varphi) = \mu^2/2\lambda$. The vacuum goes to one of the minima

$$\varphi = \begin{pmatrix} 0 \\ \frac{\mu}{\sqrt{2\lambda}} \end{pmatrix} = \frac{1}{\sqrt{2}} \begin{pmatrix} 0 \\ v \end{pmatrix}, \tag{2.25}$$

where v is a constant called *vacuum expectation value (VEV)*. This is referred to as *electroweak symmetry breaking (EWSB)*. After the EWSB, Eq. 2.24 becomes

$$\left(\frac{vg}{2}\right)^2 W_\mu^+ W^{-\mu} + \frac{1}{8}v^2(gW_\mu^3 + g'B_\mu)^2 \tag{2.26}$$

$$= \left(\frac{vg}{2}\right)^2 W_\mu^+ W^{-\mu} + \frac{1}{8}v^2(g^2 + g'^2)Z_\mu Z^\mu. \tag{2.27}$$

The masses of $W_\mu^\pm$ and Z_μ are identified as:

$$m_W = \frac{1}{2}vg,\ m_Z = \frac{1}{2}v\sqrt{g^2 + g'^2}. \tag{2.28}$$

The mass of A_μ is $M_A = 0$.

It is possible to add terms:

$$\lambda_e \left(\bar{L}\varphi e_R + \bar{e}_R\varphi^* L\right), \tag{2.29}$$

$$\lambda_d \left(\bar{Q}\varphi d_R + \bar{d}_R\varphi^* Q\right), \tag{2.30}$$

$$\lambda_u \left(\bar{Q}\varphi_c u_R + \bar{u}_R\varphi_c^* Q\right) \qquad (\varphi_c = -i\tau_2\varphi^*), \tag{2.31}$$

thanks to the Higgs field that absorbs the difference in the representation of the left- and right-handed fermions. The λ_f $(f = e, d, u)$ are called *Yukawa coupling constants*. After the EWSB $(\langle\varphi\rangle = (0, v)/\sqrt{2})$, these terms become

$$\frac{\lambda_e v}{\sqrt{2}}(\bar{e}_L e_R + \bar{e}_R e_L), \tag{2.32}$$

$$\frac{\lambda_d v}{\sqrt{2}}\left(\bar{d}_L d_R + \bar{d}_R d_L\right), \tag{2.33}$$

$$\frac{\lambda_u v}{\sqrt{2}}(\bar{u}_L u_R + \bar{u}_R u_L). \tag{2.34}$$

The fermions acquire their masses:

$$m_f = \frac{\lambda_f v}{\sqrt{2}}\ (f = e, u, d, \cdots). \tag{2.35}$$

For completeness, the kinetic terms of the gauge bosons are given by

$$-\frac{1}{4}W_{\mu\nu}^a W^{a\mu\nu} - \frac{1}{4}B_{\mu\nu}B^{\mu\nu}. \tag{2.36}$$

The antisymmetric tensors $W_{\mu\nu}^a$ and $B_{\mu\nu}$ are defined as:

$$W_{\mu\nu}^a = \partial_\mu W_\nu^a - \partial_\nu W_\mu^a + g\epsilon^{abc}W_\mu^b W_\nu^c, \tag{2.37}$$

$$B_{\mu\nu} = \partial_\mu B_\nu - \partial_\nu B_\mu. \tag{2.38}$$

Strong interaction

The quarks have a degree of freedom called *color*. By imposing the $SU(3)_C$ gauge symmetry on a color triplets of Dirac fields $\boldsymbol{\psi}$, the triplet interacts with new gauge fields, gluon G^a_μ ($a = 1, \cdots, 8$) as:

$$-ig_s\bar{\boldsymbol{\psi}}\gamma^\mu t^a \boldsymbol{\psi} G^a_\mu, \tag{2.39}$$

where t^a are the representation matrices of $SU(3)$. The kinetic term of the gluon is written as:

$$-\frac{1}{4}G^a_{\mu\nu}G^{a\mu\nu}, \tag{2.40}$$

where

$$G^a_{\mu\nu} = \partial_\mu G^a_\nu - \partial_\nu G^a_\mu + g_s f^{abc} G^b_\mu G^c_\nu. \tag{2.41}$$

f^{abc} is the structure constant of $SU(3)$. This gauge theory based on the $SU(3)_C$ symmetry is referred to as *Quantum Chromodynamics (QCD)*.

The leptons are color singlet unlike the quarks. Hence, the leptons do not interact with the gluon.

2.2 Higgs boson

The Higgs boson and its interaction

When the Higgs doublet has the VEV as Eq. 2.25, the Higgs field is parametrized using real fields h, ϕ^1, ϕ^2 and ϕ^3 as:

$$\varphi = \frac{1}{\sqrt{2}}\begin{pmatrix} -i(\phi^1 - i\phi^2) \\ v + h + i\phi^3 \end{pmatrix}. \tag{2.42}$$

h corresponds to a physical scalar particle called *Higgs boson*. ϕ^i are *Nambu-Goldstone bosons*, and they are absorbed into the gauge bosons W^i as their longitudinal degrees of freedom. Dropping terms of the Nambu-Goldstone bosons, Lagrangian in terms of the Higgs boson is transformed as

$$(\partial_\mu\varphi)^2 + \mu^2\varphi^\dagger\varphi - \lambda(\varphi^\dagger\varphi)^2 \tag{2.43}$$

$$= \frac{1}{2}(\partial_\mu h)^2 - \frac{m_h^2}{2}h^2 - \sqrt{\frac{\lambda}{2}}m_h h^3 - \frac{\lambda}{4}h^4, \tag{2.44}$$

where $m_h = \sqrt{2}\mu = \sqrt{2\lambda}v$, which is identified as the mass of the Higgs boson.

Higgs couplings to the gauge bosons is expressed by terms of Lagrangian:

$$\left[m_W^2 W^+_\mu W^{-\mu} + \frac{m_Z^2}{2}Z_\mu Z^\mu\right]\left(1 + \frac{h}{v}\right)^2, \tag{2.45}$$

where m_W and m_Z are defined as Eq. 2.28. Higgs couplings to the fermions are described as

$$\mathcal{L} = -m_f\bar{\psi}_f\psi_f\left(1 + \frac{h}{v}\right), \tag{2.46}$$

where m_f is the fermion mass defined in Eq. 2.35.

Production mechanisms of the Higgs boson

The Higgs boson is produced in proton-proton collisions by four processes: gluon-gluon fusion (ggF) [18, 32], vector boson fusion (VBF) [18, 32], associated production with a top-quark pair (ttH) [33–38], associated production with a vector boson (VH)[39]. The cross-sections as functions of the Higgs boson mass m_h are shown in Figure 2.1. The mechanisms and the production cross-sections at the $m_h = 125.09$ GeV, measured in the $H \to \gamma\gamma$ and $H \to ZZ^* \to 4\ell$ decay channels [40], of four processes are explained below.

The ggF process is expressed by the Feynman diagram shown in Figure 2.2. The cross-section of ggF are calculated at N3LO (QCD) and NLO (EW) acuracy [33, 41, 43]. The value of the cross-section is

$$\sigma_{\mathrm{ggF}} = 48.52(\,\mathrm{pb})^{+4.56\%}_{-6.72\%}(\mathrm{theory}) \pm 1.86\%(\mathrm{PDF})^{+2.61\%}_{-2.59\%}(\alpha_s). \tag{2.47}$$

The PDF and α_S uncertainties are derived following the recommendation of the PDF4LHC working group [44]. The "theory" is remaining theory uncertainties including scale variations, PDF uncertainties, uncertainties on electroweak correction, effects from missing mass of quarks, and other uncertainties [33]. For the scale variations, a short comment is given in Appendix A.

The VBF production is expressed by the Feynman diagram shown in Figure 2.3. The cross-section of VBF is calculated at NNLO (QCD) and NLO (EW) accuracy [33, 41]. The result of the cross-section is

$$\sigma_{\mathrm{VBF}} = 3.779\,\mathrm{pb}^{+0.4\%}_{-0.3\%}(\mathrm{scale}) \pm 2.1\%(\mathrm{PDF}) \pm 0.5\%(\alpha_s) \tag{2.48}$$

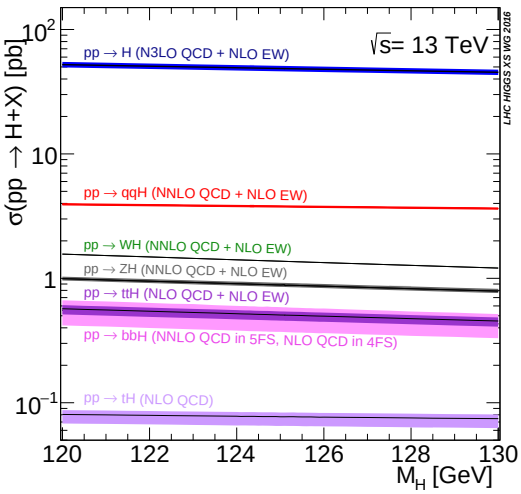

Figure 2.1: Theoretical calculation of the production cross-sections of the Higgs boson as functions of M_h at $\sqrt{s} = 13$ TeV [33, 41, 42].

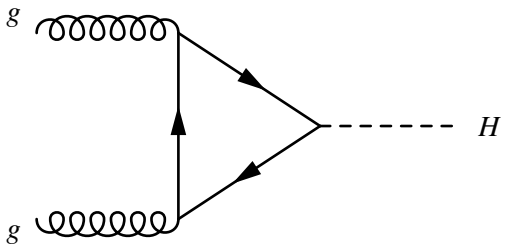

Figure 2.2: Feynman diagram of the gluon-gluon fusion.

The ttH production is expressed by the Feynman diagram in Figure 2.4. The cross-section of the ttH production is calculated at NLO (QCD) and NLO (EW) accuracy [33, 41]. The result is

$$\sigma_{ttH} = 0.5065\,\text{pb}^{+5.8\%}_{-9.2\%}(\text{scale}) \pm 3.0\%(\text{PDF}) \pm 2.0\%(\alpha_s). \tag{2.49}$$

The VH productions are processes shown in Figure 2.5. The cross-section of the WH production and the $qq \to ZH$ contribution in the ZH production are calculated at NNLO (QCD) and NLO (EW) accuracy [33, 41]. The resulting values are

$$\sigma_{WH} = 1.369\,\text{pb}^{+0.5\%}_{-0.7\%}(\text{scale}) \pm 1.7\%(\text{PDF}) \pm 0.9\%(\alpha_s), \tag{2.50}$$

$$\sigma_{qq\to ZH} = 0.7612\,\text{pb}^{+0.5\%}_{-0.6\%}(\text{scale}) \pm 1.7\%(\text{PDF}) \pm 0.9\%(\alpha_s). \tag{2.51}$$

The ZH production is contributed by a loop-induced process $gg \to ZH$ expressed by the right Feynman diagram in Figure 2.5. The cross-section of $gg \to ZH$ is calculated at NLO+NLL (QCD) accuracy. The value is

$$\sigma_{gg\to ZH} = 0.1227\,\text{pb}^{+25.1\%}_{-18.9\%}(\text{scale}) \pm 1.8\%(\text{PDF}) \pm 1.6\%(\alpha_s). \tag{2.52}$$

The total ZH cross-section is

$$\sigma_{ZH} = \sigma_{qq\to ZH} + \sigma_{gg\to ZH} = 0.8839\,\text{pb}^{+3.8\%}_{-3.1\%}(\text{scale}) \pm 1.3\%(\text{PDF}) \pm 0.9\%(\alpha_s). \tag{2.53}$$

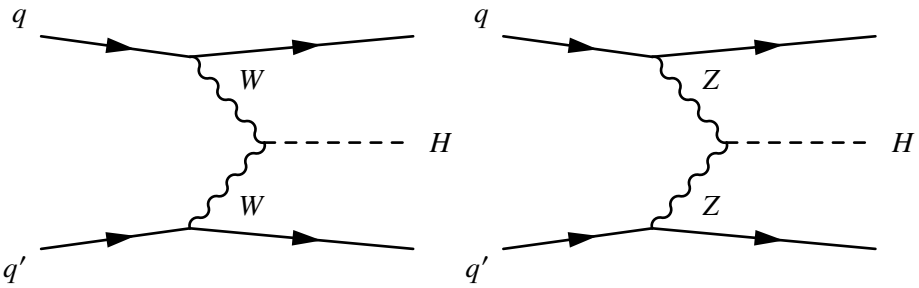

Figure 2.3: Feynman diagrams for the VBF production

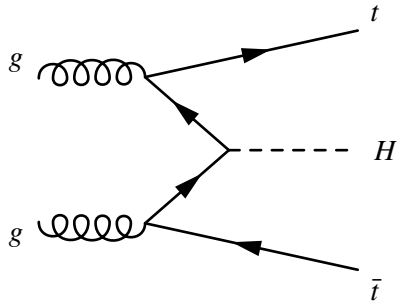

Figure 2.4: Feynman diagrams for the associated production with $t\bar{t}$ (ttH).

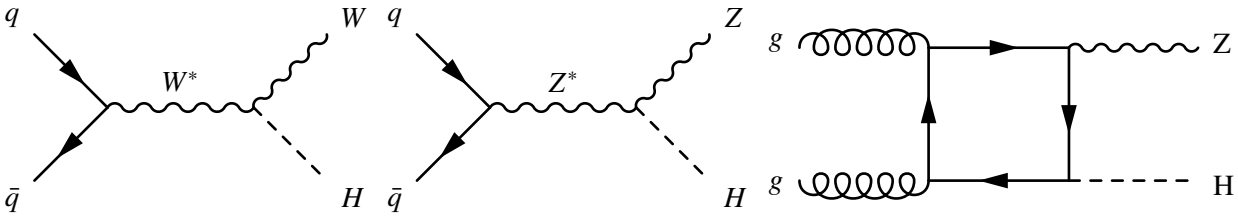

Figure 2.5: Feynman diagrams for the associated production with a vector boson (VH).

Decay channels of the Higgs boson

The mechanisms of Higgs decays are categorized into three groups. The first group includes decays to a pair of fermions. These decays occur via Yukawa couplings, and the corresponding Lagrangian term is Eq. 2.46. The Feynman diagrams are shown in Figure 2.6. The second group includes decays to four fermions with a WW^* and ZZ^* pair in the intermediate state. These decays occur via the Higgs boson couplings to the gauge boson in Eq. 2.45, and the Feynman diagrams are shown in Figure 2.7. The third group contains decays to massless gauge bosons such as $\gamma\gamma$ and gg. These decays are induced by a loop of fermions as shown in Figure 2.8.

Observables relevant to the decays are the branching ratios. Methods for the calculation of the Higgs branching ratios are presented in Ref. [18] in detail. The calculated branching ratios [45] are shown in Figure 2.9 and Table 2.4.

2.3 Remaining issues in the particle physics

There are several issues remaining after the establishment of the Standard Model. Issues relevant to this thesis are described in this section.

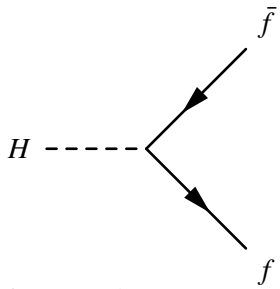

Figure 2.6: Higgs decay to a pair of fermions

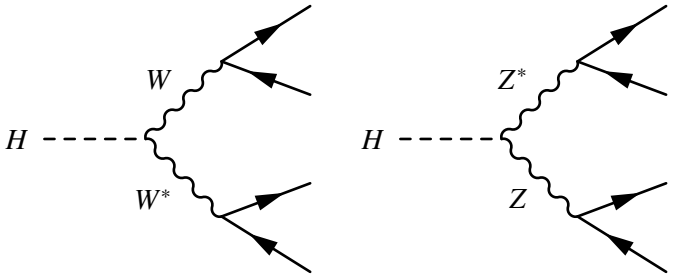

Figure 2.7: Higgs decays to a pair of vector bosons

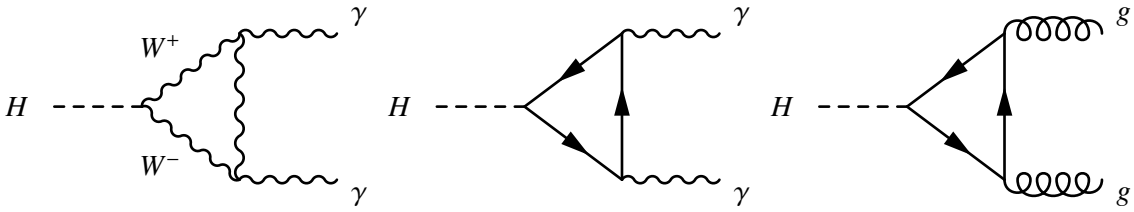

Figure 2.8: Loop induced Higgs decay.

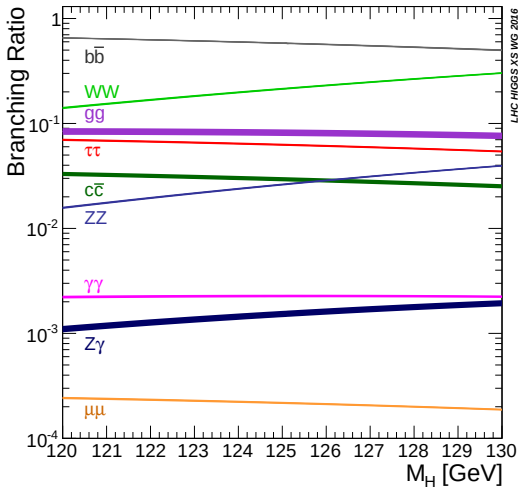

Figure 2.9: Theoretical calculation of the branching ratios of the Higgs boson as functions of the Higgs mass M_h [18].

Table 2.4: Theoretical calculation of the branching ratios of the Higgs boson [18]. These branching ratios are calculated with the Higgs mass $M_h = 125.09$ GeV [40]. The uncertainties indicated as "theory" are uncertainties due to the missing higher-order corrections. The uncertainties indicated as "m_q" and "α_S" are due to the experimental uncertainties of these input parameters.

Decay	Branching ratio
$h \to b\bar{b}$	$5.809 \times 10^{-1}\ ^{+0.65\%}_{-0.65\%}(\text{theory})^{+0.72\%}_{-0.74\%}(m_q)^{+0.77\%}_{-0.79\%}(\alpha_S)$
$h \to WW^*$	$2.152 \times 10^{-1}\ ^{+0.99\%}_{-0.99\%}(\text{theory})^{+0.98\%}_{-0.98\%}(m_q)^{+0.64\%}_{-0.62\%}(\alpha_S)$
$h \to ZZ^*$	$2.64 \times 10^{-2}\ ^{+0.99\%}_{-0.99\%}(\text{theory})^{+0.98\%}_{-0.98\%}(m_q)^{+0.64\%}_{-0.62\%}(\alpha_S)$
$h \to \tau\tau$	$6.256 \times 10^{-2}\ ^{+1.17\%}_{-1.16\%}(\text{theory})^{+0.98\%}_{-0.98\%}(m_q)^{+0.62\%}_{-0.62\%}(\alpha_S)$
$h \to c\bar{c}$	$2.884 \times 10^{-2}\ ^{+1.20\%}_{-1.20\%}(\text{theory})^{+5.27\%}_{-0.94\%}(m_q)^{+1.26\%}_{-1.25\%}(\alpha_S)$
$h \to gg$	$8.180 \times 10^{-2}\ ^{+3.40\%}_{-3.41\%}(\text{theory})^{+1.12\%}_{-1.14\%}(m_q)^{+3.70\%}_{-3.59\%}(\alpha_S)$
$h \to \gamma\gamma$	$2.270 \times 10^{-3}\ ^{+1.73\%}_{-1.72\%}(\text{theory})^{+0.97\%}_{-0.94\%}(m_q)^{+0.66\%}_{-0.61\%}(\alpha_S)$
$h \to \mu\mu$	$2.171 \times 10^{-4}\ ^{+1.23\%}_{-1.23\%}(\text{theory})^{+0.97\%}_{-0.99\%}(m_q)^{+0.60\%}_{-0.64\%}(\alpha_S)$
$h \to Z\gamma$	$1.541 \times 10^{-3}\ ^{+5.71\%}_{-5.71\%}(\text{theory})^{+0.91\%}_{-1.00\%}(m_q)^{+0.58\%}_{-0.64\%}(\alpha_S)$
Total width [GeV]	
$4.100 \times 10^{-3}\ ^{+0.73\%}_{-0.73\%}(\text{theory})^{+0.99\%}_{-0.97\%}(m_q)^{+0.60\%}_{-0.61\%}(\alpha_S)$	

2.3.1 Baryon asymmetry of the universe (BAU)

The baryon number of the universe is inferred from the Cosmic Microwave Background Radiation. Since there was no net baryon numbers at the beginning of the universe, the baryon asymmetry is somehow generated.

Sakharov pointed out conditions that a theory should satisfy to generate BAU [46]:

(1) Violation of both the C and CP symmetry,

(2) Process that changes the baryon number,

(3) Departure from the thermal equilibrium.

It is understood that the CP violation in the Standard Model with the CKM matrix does not provide sufficient baryons [47]. Therefore, an additional sources of the CP violation must exist.

2.3.2 Hierarchy problem of the Higgs boson

The Higgs boson of the Standard Model receives the radiative correction from the Feynman diagram in Figure 2.10 to its mass. The correction is quadratic in the cutoff Λ as[3]:

$$\Delta m_h = -\frac{3}{8\pi} y_t \Lambda^2. \tag{2.54}$$

Λ is usually thought as a very large quantity such as the energy scale of the Grand Unification of the gauge interactions. In order to keep the physical mass of the Higgs boson at 125 GeV, an extremely fine tuning of the bare mass of the Higgs boson is required[4]. Physicists normally think that such a fine-tuning is *unnatural*, and this is referred to as a *hierarchy problem of the Higgs boson*.

Theories with *supersymmetry* [48–50] provide a solution of this issue by introducing extra particles that can cancel out the large radiative correction. To cancel the diagram with a top-quark, its super-partner (*scalar-top*) must have the mass below 1 TeV . However, it is not found in the LHC data.

Issues with the Standard Model imply necessities for *physics beyond the Standard Model (BSM)*, in particular, existence of new fields and interactions with the SM fields.

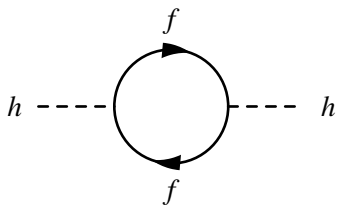

Figure 2.10: 1-loop correction to the propagator of the Higgs boson.

[3] "3" is the color factor for the top-quark

[4] In the renormalization group picture, the mass of the Higgs boson should finely be tuned in physics at the cutoff scale.

2.4 Measurements of the properties of the Higgs boson assuming CP even scenarios

2.4.1 Effective Field Theories and model-independent measurement

Production cross-sections and decay widths of particles are affected by extra interactions added to the Standard Model. Since the nature of BSM is not known, it is useful to express the experimental results in a model-independent way. Standard Model Effective Field Theory (SMEFT) [51] can describe phenomena caused by a large variety of additional heavy fields, below the energy scale of the new physics.

Formalism of the Standard Model Effective Field Theory

The first part of the SMEFT consists of the renormalizable terms of the Standard Model Lagrangian constructed by the field operators with mass dimensions less than five. The SMEFT adds operators of the SM fields with mass dimensions higher than four. In the renormalization group picture, contributions of these higher dimensional operators get smaller in low energy phenomena. Thus, these operators are referred to as *irrelevant operators*. The Lagrangian density of the SMEFT is written as:

$$\mathcal{L} = \mathcal{L}_{\mathrm{SM}} + \frac{1}{\Lambda}\sum C_i^{(5)} Q_i^{(5)} + \frac{1}{\Lambda^2}\sum C_i^{(6)} Q_i^{(6)} + O\left(\frac{1}{\Lambda^3}\right), \tag{2.55}$$

where $Q_i^{(d)}$ are field operators with mass dimension d and Λ is the energy scale of new physics, which is typically larger than the electroweak scale. $C_i^{(d)}$ are dimensionless parameters associated to the dimension-d operators, $Q_i^{(d)}$, which are referred to as *Wilson coefficients*. Contributions from BSM appear in the irrelevant operators. The Wilson coefficients specify phenomena at low energy. Λ can not be determined from the measurement of processes below the energy scale of new physics. In other words, only $C^{(5)}/\Lambda$ and $C^{(6)}/\Lambda^2$ can be measured.

Since a model is specified by setting the Wilson coefficients, cross-sections and branching ratios are also expressed as functions of the coefficients. There are six operators which affect both $qq \to WH$ and $qq \to ZH$, and 7 operators which affect only $qq \to ZH$. The scattering amplitude of $qq \to VH$ process shown in Figure 2.5 is dimensionless regardless of the Feynman diagram. An amplitude that includes a dimension-6 interaction linearly depends on $C^{(6)}/\Lambda^2$ with the mass-dimension of -2 while the diagram by the Standard Model (SM) includes the electroweak gauge couplings (g, g') and m_V^2/v. By dimensional analysis, the amplitude by the dimension-6 term roughly depends on the momentum scale as $O(p^2)$ compared to the SM amplitude whose dependence is roughly $O(p^{-1})$. There is one subtlety in the argument above: the longitudinal component of a vector boson have the size of E_V/m_V in the relativistic regime while the size of the transverse components remain $O(1)$. Thus, the dependence of the scattering amplitudes on the momentum is different in different operators due to polarization of the vector boson. Nevertheless, the cross-section of the VH processes in the high p_{T}^V phase space can show significant effects from these dimension-6 terms in the Lagrangian. Thus, the goal of this thesis is to derive limits on the Wilson coefficients, especially for dimension-6 operators, by interpreting the measurements of the differential cross-section of the VH production.

Choice of how to expand dimension-6 interactions in the effective Lagrangian (*basis*) is not unique. Basis used in this thesis are called *Warsaw basis* [26], which respects the gauge symmetry of the Standard Model

$(SU(3)_C \times SU(2)_L \times U(1)_Y)$. However, another basis, *Strongly Interacting Light Higgs boson (SILH) basis* [25], is often found in literature. The SILH formalism expands in terms of the fields that diagonalize the mass matrix.

2.4.2 Heavy Vector Triplet and its UV completed theories

To explain that the limits on the Wilson coefficients serve as limits on an actual model, explicit models are described below.

An example of BSM models that can be described in the SMEFT framework is the *Heavy Vector Triplet (HVT) model* [23], which introduces real vector fields V_μ^a $(a = 1, 2, 3)$ in the adjoint representation of $SU(2)_L$. The Lagrangian of HVT is written as:

$$\begin{aligned}\mathcal{L} = &-\frac{1}{4} D_{[\mu} V^a_{\nu]} D^{[\mu} V^{\nu]a} + \frac{m_V^2}{2} V^a_\mu V^{\mu a} \\ &+ i g_V c_H V^a_\mu H^\dagger \tau^a \overleftrightarrow{D}^\mu H + \frac{g^2}{g_V} c_F V^a_\mu \sum_f \bar{f}_L \gamma^\mu \tau^a f_L \\ &+ \frac{g_V}{2} c_{VVV} \epsilon_{abs} V^a_\mu V^{\mu a} D^{[\mu} V^{\nu]c} + g_V^2 c_{VVHH} V^a_\mu V^{\mu a} H^\dagger H - \frac{g}{2} c_{VVW} \epsilon_{abc} W^{\mu\nu a} V^b_\mu V^c_\nu, \end{aligned} \tag{2.56}$$

where the bracket means the anti-commutation with respect to the Lorentz indices:

$$D_{[\mu} V^a_{\nu]} \equiv D_\mu V^a_\nu - D_\nu V^a_\mu, \qquad D_\mu V^a_\nu \equiv \partial_\mu V^a_\nu + g \epsilon^{abc} W^b_\mu V^c_\nu, \tag{2.57}$$

τ^a are the half of the Pauli matrices: $\tau^a = \sigma^a/2$. The arrow assigned to the covariant derivative represents Hermitian derivative as:

$$i H^\dagger \tau^a \overleftrightarrow{D}^\mu H \equiv i H^\dagger \tau^a (D^\mu H) - i (D^\mu H)^\dagger \tau^a H. \tag{2.58}$$

The heavy vector resonances V_μ^a are mixed with the SM vector bosons, $W^\pm$ and Z, through the term associated the c_H in Eq. 2.56. However, this mixing is small when the mass hierarchy, $m_W/m_V < 10^{-1}$, is imposed [23][5]. Therefore, the mixing is ignored in this analysis.

The HVT model introduces additional contribution to the VH production through the diagrams in Figure 2.11 that affect Wilson coefficients. In order to evaluate the contribution to the VH production,

$$\begin{aligned} i g_V c_H V^a_\mu (H^\dagger \tau^a \overleftrightarrow{D}^\mu H) = i g_V c_H V^a_\mu \Big[&(\tau^a H)^\dagger \partial_\mu H - (\partial_\mu H)^\dagger \tau^a H \\ &- i \frac{g}{2} W^a_\mu H^\dagger H - i g' B_\mu H^\dagger \tau^a H \Big]. \end{aligned} \tag{2.59}$$

In the second line, $\{\tau^a, \tau^b\} = \frac{1}{2}\delta^{ab}$ is used. The second line is further transformed as:

$$\begin{aligned} i g_V c_H V^a_\mu \left[-i \frac{g}{2} W^a_\mu H^\dagger H - i g' B_\mu H^\dagger \tau^a H \right] &= g_V c_H \frac{(v+h)^2}{2} \left[\frac{g}{2} V^a_\mu W^{a\mu} + \frac{g'}{2} V^3_\mu B^\mu \right] \\ &= g_V c_H \frac{(v+h)^2}{2} \left[\frac{g}{2} V^+_\mu W^{-\mu} + \frac{g}{2} V^-_\mu W^{+\mu} + \frac{\sqrt{g^2+g'^2}}{2} V^3_\mu Z^\mu \right], \end{aligned} \tag{2.60}$$

[5] This is presented for g_V and c_H of $O(1)$ in Ref. [23]. This picture may be altered for the stronger couplings.

where $V^{\pm} = (V^1 \mp iV^2)/\sqrt{2}$. In the first line, the terms including the Goldstone bosons are dropped. For the interaction between the quarks and the heavy vector fields,

$$\begin{aligned}\frac{g^2}{g_V} c_F \bar{q}_L \gamma^\mu \tau^a q_L V_\mu^a &= \frac{g^2}{g_V} c_F \bar{q}_L \gamma^\mu \left(\sqrt{2}\tau^+ V_\mu^+ + \sqrt{2}\tau^- V_\mu^- + \tau^3 V_\mu^3 \right) q_L \\ &= \frac{g^2}{g_V} c_F \left[\frac{1}{\sqrt{2}} \bar{d}_L \gamma^\mu u_L V_\mu^- + \frac{1}{\sqrt{2}} \bar{u}_L \gamma^\mu d_L V_\mu^+ + \frac{1}{2} \left(\bar{u}_L \gamma^\mu u_L - \bar{d}_L \gamma^\mu d_L \right) V_\mu^3 \right]. \end{aligned} \tag{2.61}$$

By combining Eqs. 2.60 and 2.61, Feynman diagrams on the left of Figure 2.11 are obtained. The scattering amplitudes represented by these Feynman diagrams are approximated by the amplitudes indicated by the Feynman diagrams on the right of the figure when the momentum p is much lower than the mass of the heavy resonance.

In the Warsaw basis, interactions which include two quarks, the gauge boson, and the Higgs boson are parametrized as:

$$\begin{aligned}\mathcal{L} = &\frac{c_{Hq}^{(3)}}{\Lambda^2} (H^\dagger i\tau^a \overleftrightarrow{D}_\mu H)(\bar{q}_L \tau^a \gamma^\mu q_L) + \frac{c_{Hq}^{(1)}}{\Lambda^2} (H^\dagger i \overleftrightarrow{D}_\mu H)(\bar{q}_L \gamma^\mu q_L) \\ &+ \frac{c_{Hu}}{\Lambda^2} (H^\dagger i \overleftrightarrow{D}_\mu H)(\bar{u}_R \gamma^\mu u_R) + \frac{c_{Hd}}{\Lambda^2} (H^\dagger i \overleftrightarrow{D}_\mu H)(\bar{d}_R \gamma^\mu d_R) + \cdots . \end{aligned} \tag{2.62}$$

To match the HVT model to the EFT description, the following must be satisfied:

$$\frac{c_{Hq}^{(3)}}{\Lambda^2} = -\frac{g^2 c_H c_F}{m_V^2} = -\frac{4 g_H g_q}{m_V^2}, \tag{2.63}$$

$$c_{Hq}^{(1)} = c_{Hu} = c_{Hd} = 0. \tag{2.64}$$

Here, $g_H \equiv g_V c_H/2$ and $g_q \equiv g^2 c_F/2g_V$. This can also be written as:

$$\begin{aligned}\mathcal{L} = -\frac{g_H g_q}{2m_V^2} \Big\{ &2\sqrt{2} v h g \left[\bar{d}_L i\gamma^\mu u_L W_\mu^- + \bar{u}_L i\gamma^\mu d_L W_\mu^+ \right] \\ &+ 2v h \sqrt{g^2 + g'^2} \left[\bar{u}_L i\gamma^\mu u_L - \bar{d}_L i\gamma^\mu d_L \right] Z_\mu \Big\}. \end{aligned} \tag{2.65}$$

This agrees with the result in Ref. [33].

The following combinations of the parameters reduce to the same SMEFT and show the same phenomena at low energy as in the next paragraph.

- Strongly coupled: $m_V = 7$ TeV, $g_H = -g_q = 1.75$
- Moderately coupled: $m_V = 2$ TeV, $g_H = -g_q = 0.5$
- Weakly coupled: $m_V = 1$ TeV, $g_H = -g_q = 0.25$

Thus, a measurement of anomalous interactions has sensitivities to various ranges of parameters and is interpreted as an *indirect search* for BSM.

These additional terms affect the production of the Higgs boson with a vector boson (VH) in the phase space with the high transverse momentum of V (p_{T}^V). This is shown in Figure 2.12. Thus, Wilson coefficients

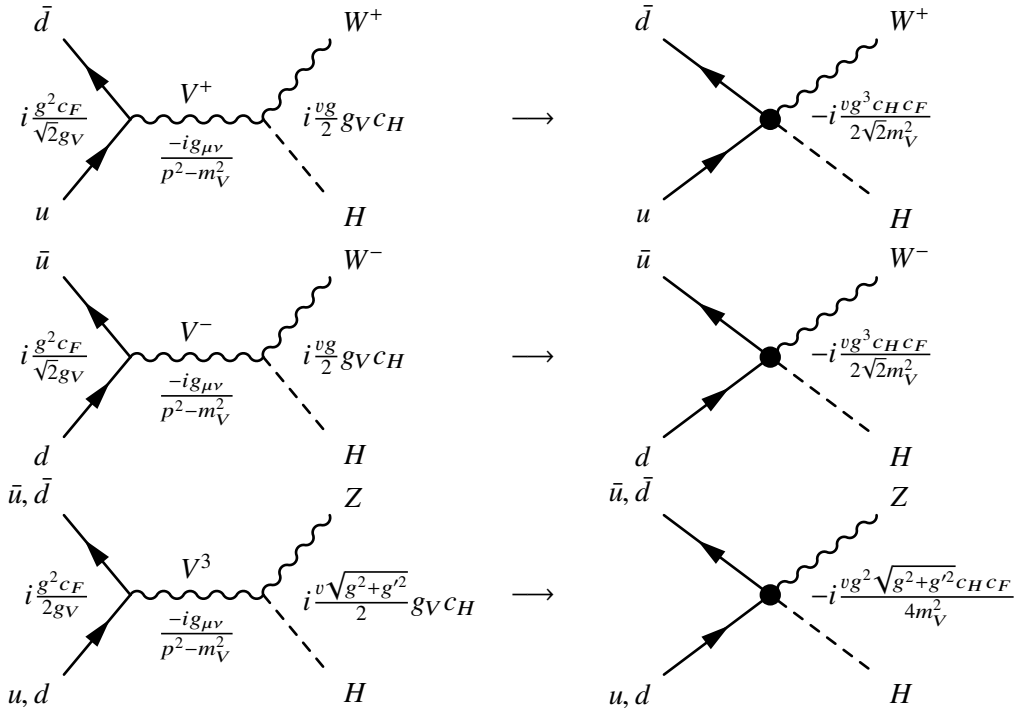

Figure 2.11: Contribution from the HVT model to the WH and ZH production. While W and Z represent the gauge bosons of the Standard Model, V represents the heavy vector field. The amplitudes are approximated by the ones obtained from the Feynman diagram on the right when $p \ll m_V$.

corresponding to these models are studied through the measurement of the differential cross-section of the VH production as functions of p_{T}^V.

Direct searches for the heavy resonance V have been performed in final states with two SM weak bosons using the 139 fb^{-1} data of ATLAS, and have excluded these resonances below 3-5 TeV [52, 53]. From the discussions above, the higher mass region can be searched if the coupling is sufficiently strong by the indirect search through the differential cross-section measurement of the VH production.

Composite Higgs model

The HVT model can also be an effective description of another theory.

An example is the *Minimum Composite Higgs Model (MCHM)*, which is shortly described below. The MCHM has a $SO(5)$ global symmetry that is broken to the $SO(4)$ subgroup by a strongly interacting sector [24]. The lightest vector resonances in the MCHM are described by the HVT model [23]. The four pseudo Nambu-Goldstone bosons (PNGB) corresponding to the preserving $SO(4)$ symmetry form a complex doublet of $SU(2)_L$. A loop correction involving the top quark generates a potential for the PNGBs giving a VEV to these bosons. Then, the EWSB takes place as $SO(4) \to SO(3)$, and one remaining PNGB is identified as the Higgs boson. The mass of the Higgs boson is protected by the approximate $SO(5)$ symmetry from large radiative corrections [54]. Hence, the hierarchy problem of the Higgs boson is solved.

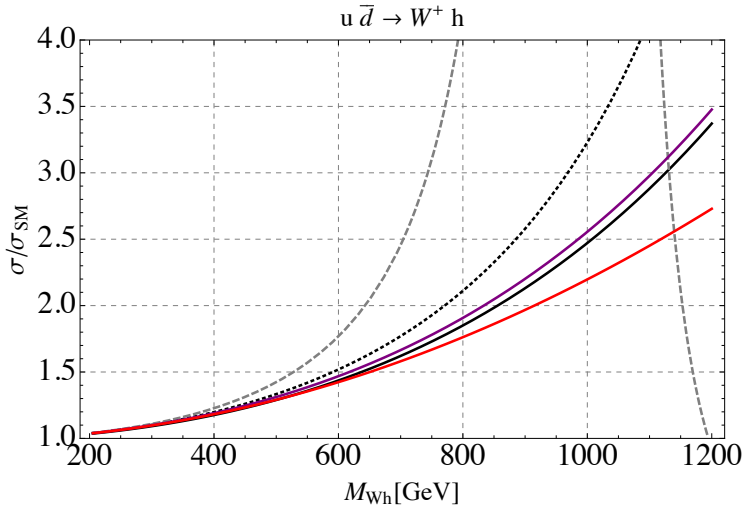

Figure 2.12: Differential partonic cross-sections of the WH production as a function of the center-of-mass energy of the initial partons predicted by HVT models and corresponding effective field theories. The black curves are the predictions from the HVT model with $m_V = 1$ TeV, $g_H = -g_q = 0.25$ (dashed), $m_V = 2$ TeV, $g_H = -g_q = 0.5$ (dotted) and $m_V = 7$ TeV, $g_H = -g_q = 1.75$ (solid). The red curve represents the EFT prediction when considering only the terms of the cross-section linear in Wilson coefficients. The purple curve represents the same effective theory but considering the quadratic and linear terms. The plot is taken from [33].

Extended gauge symmetry

The gauge coupling of the HVT Lagrangian can also be weak. Although it may be less attractive than the composite Higgs model, it is still a possible BSM scenario. This effective model arises when a symmetry breaking pattern, $SU(2)_1 \times SU(2)_2 \times U(1) \rightarrow SU(2)_L \times U(1)_Y$, realizes [23, 55].

Validity of the Effective Field Theory

In order to think about the validity of the effective description truncated at the dimension-6, dimension-8 contribution is discussed below following the argument in Ref. [33]. Here, the dimension-8 contribution from the following expansion of the propagator of the heavy resonance is taken as an example:

$$\frac{-ig^{\mu\nu}}{p^2 - m_V^2} = \frac{ig^{\mu\nu}}{m_V^2} - \frac{ig^{\mu\nu}}{m_V^2}\frac{p^2}{m_V^2} + O\left(\left(\frac{p}{m_V}\right)^4\right). \tag{2.66}$$

In the HVT model, the coefficient of the second terms is $g_H g_q$ similar to the dimension-6 term. The amplitude of the SM contribution scales as g_{SM} (=g or g') whereas the amplitude by the dimension-6 operator scales as $g_H g_q \times p^2/\Lambda^2$. When $g_H g_q$ is large compared to g_{SM}^2, equivalently Λ is large, there is an energy range that the VH process is dominated by the dimension-6 operator while the EFT description is still valid:

$$g_H g_q p^2/\Lambda^2 > g_{SM}^2 \Longleftrightarrow \Lambda \times g_{SM}^2/g_H g_q < p^2 < \Lambda. \tag{2.67}$$

In this kinematic region, the dimension-6 term in the cross-section, $|\mathcal{M}_{\text{dim-6}}|^2$, is relevant even though this term includes the factor Λ^{-4}. On the other hand, the dimension-8 contribution to the cross-section with

Λ^{-4} comes from the interference between the SM and dimension-8 operators, $2\mathrm{Re}\left[\mathcal{M}_{\mathrm{SM}}\mathcal{M}^{*}_{\text{dim-8}}\right]$. For the example above, this term scales as $g^2_{\mathrm{SM}}g_H g_q \times p^4/\Lambda^4$ and is suppressed by a factor $g^2_{\mathrm{SM}}/g_H g_q$ compared to $|\mathcal{M}_{\text{dim-6}}|^2$. Therefore, the approximation becomes good when the energy scale of the BSM is high even if the dim-6 term is the same.

2.5 Measurements of the properties of the Higgs boson relevant to CP violation

2.5.1 Electroweak of baryogenesis via the Yukawa couplings to the top and bottom quarks

There can be two or more Higgs fields in theories. A model that contains two Higgs doublets is called *2 Higgs Doublet Model (2HDM)* [19]. For example, theories with supersymmetry must include two Higgs doublets to avoid anomalies and make the theory sensible. The Yukawa interaction in the general *2HDM* is written as:

$$\mathcal{L}_Y = -\bar{f}_L(Y_1\Phi_1 + Y_2\Phi_2)f_R + \text{h.c.}, \tag{2.68}$$

where Φ_1 and Φ_2 are scalar fields of $SU(2)_L$ doublet. These scalars include five physical particles (Higgs bosons): h, H, $H^{\pm}$ (scalars) and A (pseudo-scalars). With these Higgs bosons, Eq. 2.68 is rewritten as:

$$\mathcal{L}_Y = -\bar{f}_L y^f_\phi f_R + \bar{u}\left[V\rho^d P_R - \rho^{u\dagger}VP_L\right]dH^+ + \text{h.c.}, \tag{2.69}$$

where coupling constants y^f_{ij} for flavor $f = u, d, e$ are defined as:

$$y^f_{hij} = \frac{\lambda^f_i}{\sqrt{2}}\delta_{ij}\sin(\beta-\alpha) + \frac{\rho^f_{ij}}{\sqrt{2}}\cos(\beta-\alpha), \tag{2.70}$$

$$y^f_{Hij} = \frac{\lambda^f_i}{\sqrt{2}}\delta_{ij}\cos(\beta-\alpha) + \frac{\rho^f_{ij}}{\sqrt{2}}\sin(\beta-\alpha), \tag{2.71}$$

$$y^f_{Aij} = \mp i\frac{\rho^f_{ij}}{\sqrt{2}}. \tag{2.72}$$

In these formulae, i and j indicate the flavor, and $\tan\beta$ represents the ratio of the two vacuum expectation values (VEVs) of Φ_1 and Φ_2. α is the mixing angle of h which is constructed from the Φ_1 and Φ_2 components.

The phenomenological importance of the 2HDM is that it can include CP violation in the Higgs sector. *It is proposed that the BAU can be generated in general 2HDM framework* [20, 21] avoiding limits from experiments such as flavor physics and the electric dipole moments of the electron, the neutron, and the proton. In this scenario, the baryon number is generated when the electroweak phase transition (EWPT) took place. At the EWPT, a domain with the broken electroweak symmetry expands to the whole universe. For the left-handed fields, more quarks are reflected by interaction with the domain wall of the EWPT than anti-quarks (Sakharov's condition 1). Similarly, for the right-handed fields, more anti-quarks are generated. In the symmetric phase, *sphaleron process* frequently occurs since the sphaleron energy is proportional to the VEV. The sphaleron process acts only left-handed fields, which means the net baryon number is generated (Sakharov's condition 2). If the EWPT is strongly first order, the generated baryon number is conserved in the broken phase (Sakharov's condition 3).

Measurements of the Higgs boson coupling at the LHC, especially the coupling of the Higgs boson to the t and b-quarks, are sensitive to viable regions for the electroweak baryogenesis (EWBG) in a complementary way to other experiments. The viable regions for the EWBG via extra bottom Yukawa coupling in the general 2HDM are shown in Figure 2.13. Thus, measurements of the coupling of the Higgs boson and the b-quark is important in the context of EWBG. This measurement is discussed in Section 11.3.

The coupling of the Higgs boson to the top quark can also be relevant to the EWBG. Ref. [20] suggests a parameter space viable for the EWBG with the $H \to \gamma\gamma$ decay width as shown in Figure 2.14. As seen in this figure, the measurement of the Higgs coupling to the top quark is sensitive to parts of the parameter values that can generate a sufficient baryon number. The most stringent limit on the electron EDM (eEDM) is $|d_e| < 1.1 \times 10^{-29}$ $e$cm [56]. However, the eEDM can be smaller by choosing another parameter ρ_{ee} in this model, and EWBG is still possible [57]. Therefore, a test by the measurement of the Higgs couplings is still motivated.

The measurement of the $H \to b\bar{b}$ coupling also contributes to the precision of other couplings of the Higgs boson because the $H \to b\bar{b}$ coupling has the largest contribution to the total width of the Higgs boson. Experimental observables are branching ratios, which are partial widths divided by the total width. Thus, to constrain partial widths or coupling constants, it is necessary to constrain the total width. This is discussed in Section 11.3.

2.5.2 Measurement of CP property in the VVH vertex

While theoretical works are rarely found for models that generate the BAU via CP violation in the VVH vertex, it is possible that the VVH vertex has a CP-odd structure. For example, these CP-odd BSM interactions can be generated by the CP-mixed 125 GeV Higgs boson in a BSM such as 2HDM [27, 28].

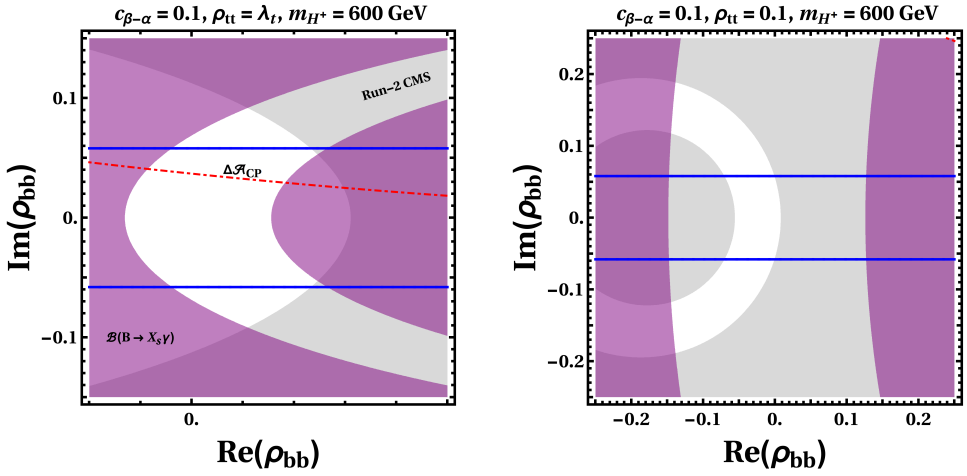

Figure 2.13: Contours of viable regions of the EWBG via the extra Yukawa coupling of the bottom quark in the general 2HDM framework are shown in the blue line [21]. The regions excluded with 2σ are shown as the following. The gray shaded regions represent the Higgs measurements at the LHC. The purple regions correspond to measurements of the branching ratio of B-hadrons: $B \to X_s\gamma$. The red curve shows a measurement of the difference of the CP-asymmetry between charged and neutral $B \to X_s\gamma$ decays. The parameters for the 2HDM is selected as indicated in the plots.

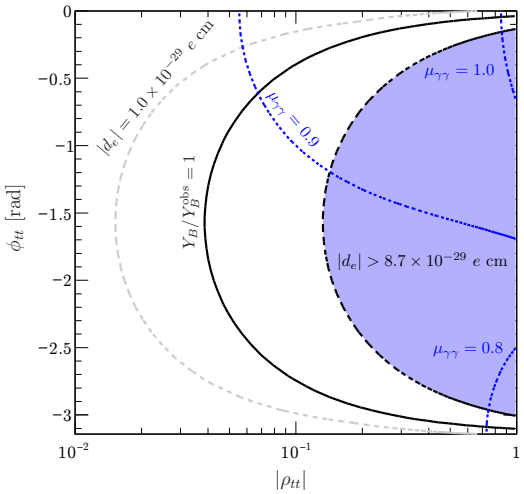

Figure 2.14: Contour of a viable region of the EWBG via the extra Yukawa coupling of the top quark [20]. $Y_B/Y_B^{\rm obs} = 1$ corresponds to the observed asymmetry of the baryon number. The limits from the electron EDM are indicated with d_e. The blue dashed curves show the variation of the $H \to \gamma\gamma$ width that can be tested by the LHC.

The CP structure of the coupling of the Higgs and vector bosons was studied in the Higgs decays. An analysis was performed using datasets from ATLAS Run 1 [22]. In the analysis, the Higgs coupling to the vector bosons is parametrized as:

$$\begin{aligned}\mathcal{L}^V = \Bigg\{ & \kappa_{\rm SM} \cos\alpha \left[\frac{1}{2} g_{HZZ} Z_\mu Z^\mu + g_{HWW} W_\mu^+ W^{-\mu} \right] \\ & - \frac{1}{4}\frac{1}{\Lambda} \left[\kappa_{HZZ} \cos\alpha Z_{\mu\nu} Z^{\mu\nu} + \kappa_{AZZ} \sin\alpha Z_{\mu\nu} \widetilde{Z}^{\mu\nu} \right] \\ & - \frac{1}{2}\frac{1}{\Lambda} \left[\kappa_{HWW} \cos\alpha W_{\mu\nu}^+ W^{-\mu\nu} + \kappa_{AWW} \sin\alpha W_{\mu\nu}^+ \widetilde{W}^{-\mu\nu} \right] \Bigg\} \cdot h. \end{aligned} \tag{2.73}$$

In this parametrization, $Z_{\mu\nu}Z^{\mu\nu}$ and $W_{\mu\nu}^+ W^{-\mu\nu}$ is connected to CP-even BSM contributions while $Z_{\mu\nu}\widetilde{Z}^{\mu\nu}$ and $W_{\mu\nu}^+ \widetilde{W}^{-\mu\nu}$ is connected to CP-odd BSM contributions. When results are presented, the parameters κ_{HVV} and κ_{AVV} are redefined as:

$$\widetilde{\kappa}_{AVV} = \frac{1}{4}\frac{v}{\Lambda}\kappa_{AVV}, \qquad \widetilde{\kappa}_{HVV} = \frac{1}{4}\frac{v}{\Lambda}\kappa_{HVV}. \tag{2.74}$$

Constraints on the parameters $(\widetilde{\kappa}_{AVV}/\kappa_{\rm SM}) \cdot \tan\alpha$ and $\widetilde{\kappa}_{HVV}/\kappa_{\rm SM}$ were derived and summarized in Table 2.5. The profiled likelihood scans for these coupling ratios are also shown in Figure 2.15.

The momentum scale is bounded in the Higgs mass when studying the Higgs decays. Thus, effects from BSM (via irrelevant terms) are suppressed by a factor m_h/Λ^d. By studying the VH production, the momentum scale can be higher than the decay channels since it is bounded by the beam energy. It is suggested that the VH production is sensitive to the CP structure in the VVH vertex [58]. An analysis is performed in Chapter 11.

Table 2.5: Expected and observed fitted values of $\widetilde{\kappa}_{HVV}/\kappa_{\mathrm{SM}}$ and $(\widetilde{\kappa}_{AVV}/\kappa_{\mathrm{SM}}) \cdot \tan\alpha$, and the 95% excluded regions derived from the $H \to ZZ^* \to 4\ell$ and $H \to WW^* \to e\nu\mu\nu$ decays. The signal strengths are considered as independent for decay channels and the beam energy ($\sqrt{s} = 7, 8$ TeV). The table is taken from Ref. [22].

	Best-fit value	95% CL Exclusion Regions	
Coupling ratio	Observed	Expected	Observed
$\tilde{\kappa}_{HVV}/\kappa_{\mathrm{SM}}$	-0.48	$(-\infty, -0.55] \cup [4.80, \infty)$	$(-\infty, -0.73] \cup [0.63, \infty)$
$\tilde{\kappa}_{AVV}/\kappa_{\mathrm{SM}} \cdot \tan\alpha$	-0.68	$(-\infty, -2.33] \cup [2.30, \infty)$	$(-\infty, -2.18] \cup [0.83, \infty)$

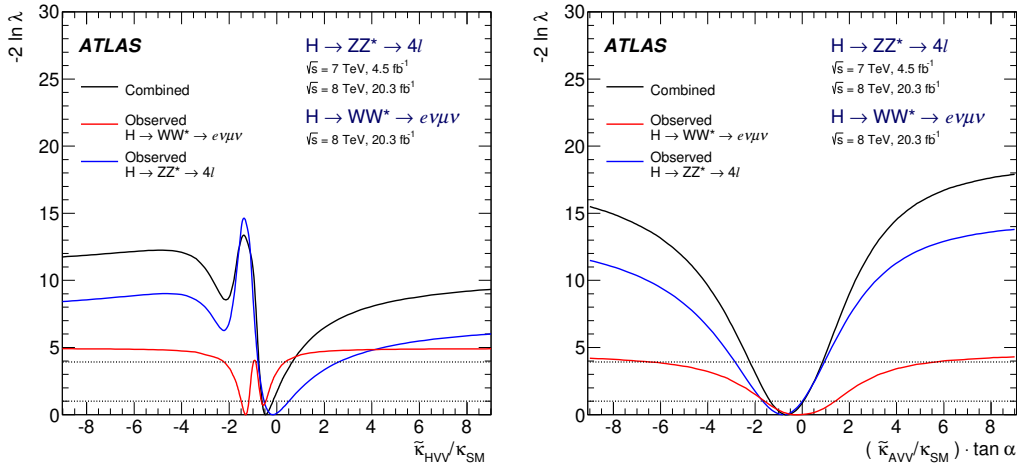

Figure 2.15: Observed scanned values of the log likelihood ratio as functions of $\widetilde{\kappa}_{HVV}/\kappa_{\mathrm{SM}}$ and $(\widetilde{\kappa}_{AVV}/\kappa_{\mathrm{SM}}) \cdot \tan\alpha$ derived from the analysis of the Higgs decays. The red and blue curves represent the $H \to WW^* \to e\nu\mu\nu$ and $H \to ZZ^* \to 4\ell$ decays, respectively. The black curve corresponds to the combination of the two decay channels assuming $\widetilde{\kappa}_{HZZ} = \widetilde{\kappa}_{HWW} = \widetilde{\kappa}_{HVV}$ and $\widetilde{\kappa}_{AZZ} = \widetilde{\kappa}_{AWW} = \widetilde{\kappa}_{AVV}$. The 68% and 95% confidence intervals are indicated by the dotted and dotted-dashed lines indicated in the plots. The plots are taken from Ref. [22].

Interpretation of the differential cross-section as a function of p_{T}^{V}

CP-odd dimension-6 operators also modify the spectrum of p_{T}^{V} in the VH production. Similar to the interpretation with the CP-even SMEFT, limits on the Wilson coefficients of the CP-odd operators can be derived as an interpretation of the differential cross-section as a function of p_{T}^{V}. This analysis is presented in Section 11.2.

Interpretation of the differential cross-section as a function of a lepton angle

Since the differential cross-section as a function of p_{T}^{V} can be modified by both CP-even and CP-odd dimension-6 operators, the p_{T}^{V} spectrum can not tell whether the dimension-6 interaction is CP-even/odd when an anomalous interaction is found. An analysis using an angular distribution of the $Z \to \ell^+\ell^-$ decay is proposed to probe CP-violation in the VH production. Since an effect on the angular distribution is smaller than the effect on the p_{T}^{V} spectrum, the use of the angular information does not provide stronger constraint on the CP-odd operators than the analysis using the p_{T}^{V} spectrum. However, this angular analysis

may be useful to test the CP property when an anomalous VVH coupling is found. This analysis is presented in Section 11.2.

3 LHC and the ATLAS detector

In this chapter, experimental apparatuses are summarized. The Large Hadron Collider and the ATLAS detector are introduced in Sections 3.1 and 3.2, respectively.

3.1 The Large Hadron Collider

Before injecting proton beams into the Large Hadron Collider (LHC) [59], several accelerators are used [60]. Protons from a source are accelerated up to 50 MeV by LINAC2. The second step is the Proton Synchrotron Booster (PSB), which increases the energy to 1.4 GeV. Proton Synchrotron (PS) accelerates the beam to 26 GeV, and a 40 MHz bunch structure is formed. Then, Super Proton Synchrotron (SPS) accelerates it to 450 GeV. Finally, the beam is injected into the LHC. This injector chain is summarized in Figure 3.1.

The LHC is a circular collider with a circumference of 27 km. The LHC consists of two rings for proton beams orbiting in opposite directions. As shown in Figure 3.2, the LHC has eight straight and arc sections. The proton beams are bent and focused in the arc sections whereas they are accelerated with an RF cavity in one of the straight sections Four straight sections provide collisions of two proton beams, and four detector systems are constructed at the points. Two detectors, ATLAS [9] and CMS [10], are general-purpose detectors that allow for studies from tests of the Standard Model to searches for the phenomena beyond the Standard Model. A detector called LHCb [62] was designed to study physics in B-hadron systems. The last detector is ALICE [63] which is optimized to study heavy-ion collisions to explore QCD phenomena such as Quark Gluon Plasma.

The LHC accelerates the proton beams up to 6.5 TeV corresponding to the center-of-mass energy ($\sqrt{s}$) of 13 TeV in the proton-proton collisions. The highest recorded instantaneous luminosity in Run 2 (see the next paragraph) is approximately $2.0 \times 10^{34}\,\mathrm{cm}^{-2}\mathrm{s}^{-1}$. As already mentioned, the beam of the LHC has a bunch structure with a frequency of 40 MHz.

The first operation of the LHC was taken place at $\sqrt{s} = 7$ TeV in 2010. The collision energy is increased to $\sqrt{s} = 8$ TeV in 2012. Data of 4.7 fb^{-1} and 20.3 fb^{-1} were collected by the ATLAS detector at $\sqrt{s} = 7$ TeV and 8 TeV, respectively. These operation periods are called LHC Run 1. After shutting down until 2014, the LHC started providing collisions at $\sqrt{s} = 13$ TeV, which is called Run 2 operation. Until the shutdown of the LHC at the end of 2018, ATLAS recorded 139 fb^{-1} data for physics analyses. The 139 fb^{-1} dataset at $\sqrt{s} = 13$ TeV is used in this thesis.

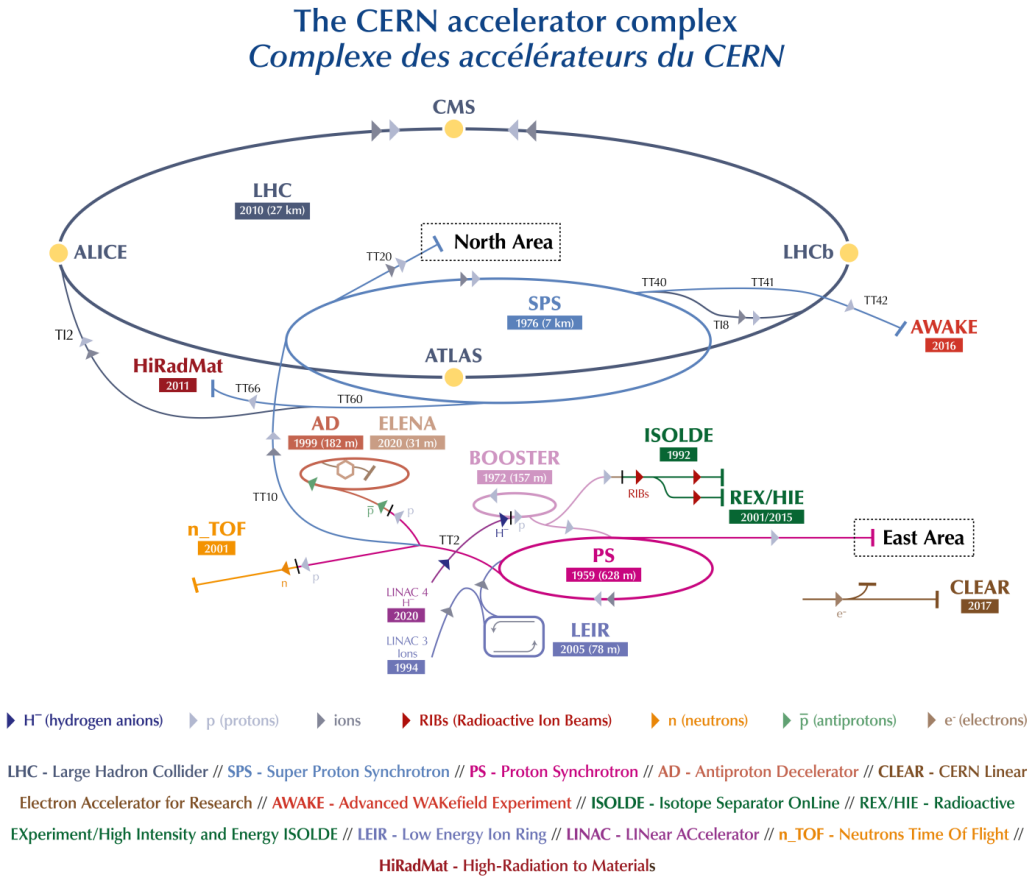

Figure 3.1: Schematic view of the CERN accelerator complex [61]. Before injecting beams in the LHC (large dark blue ring), the smaller linear and circular accelerators are used.

3.2 The ATLAS detector

Overview

The ATLAS detector is a general-purpose detector designed to perform a variety of physics studies in high energy proton-proton collisions. The ATLAS detector is divided into subsystems from inside to outside: Inner Detector, Calorimeter, and Muon Spectrometer as shown in Figure 3.3. The subsystems are discussed in Sections 3.2.1, 3.2.2 and 3.2.3. To perform experiments with hadron collisions, online event selection referred to as *trigger* is crucial. This is explained in Section 3.2.4

To fulfill physics goals, each subsystem is designed to satisfy the requirements summarized in Table 3.1

Coordinate systems

Cartesian coordinate in the ATLAS detector is defined in Figure 3.4 as the right-handed coordinate system with the x-axis pointing to the center of the LHC ring and the y-axis orienting vertically upward. Thus, the

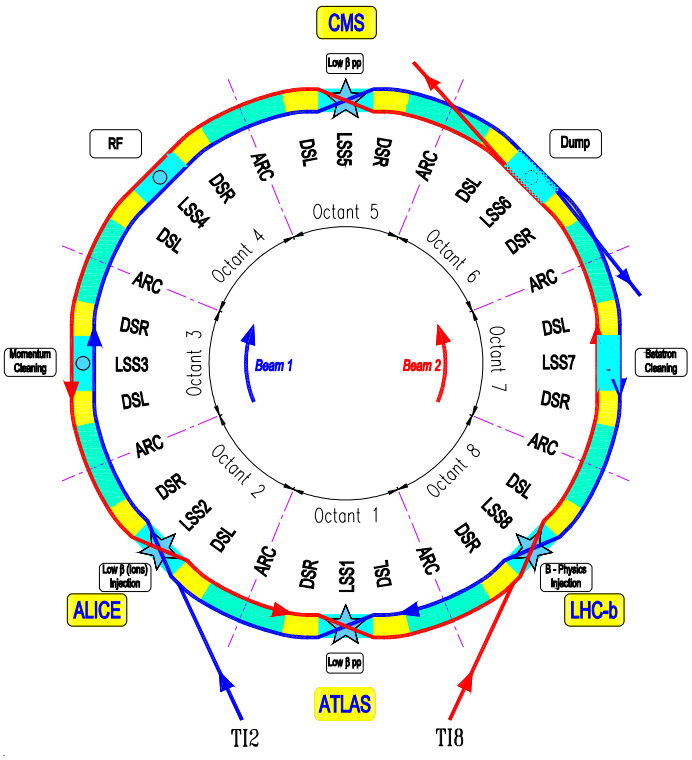

Figure 3.2: Schematic layout of the LHC [59]. Beam 1 (blue) circulates clockwise and Beam 2 circulates counter-clockwise.

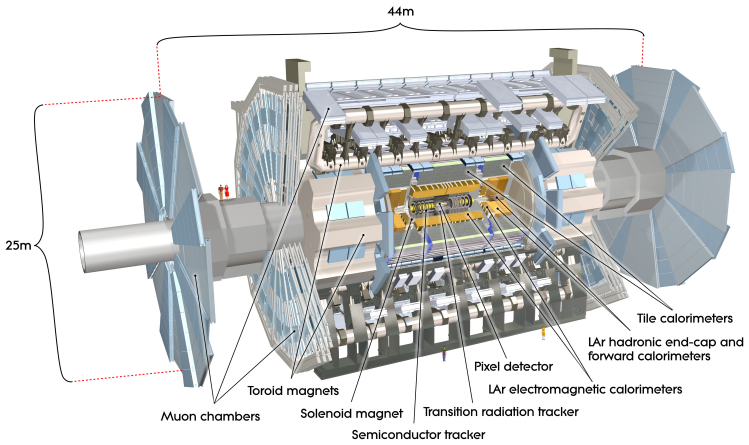

Figure 3.3: Cut-away view of the ATLAS detector [9]. The dimensions of the detector are 25 m in height and 44 m in length. The overall weight of the detector is approximately 7000 tonnes.

Table 3.1: Required performance of the ATLAS detector [9]. The units for E and p_{T} are in GeV. The Inner Detector is not used in the Level-1 Trigger. The coverage of the High Level Trigger is the same as the "measurement". See Section 3.2.4 for the Level-1 and High Level Triggers.

Detector component	**Required resolution**	**η coverage**	
		Measurement	Level-1 trigger
Tracking	$\sigma_{p_{\mathrm{T}}}/p_{\mathrm{T}} = 0.05\% p_{\mathrm{T}} \oplus 1\%$	± 2.5	-
EM calorimeter	$\sigma_E/E = 10\%\sqrt{E} \oplus 0.7\%$	± 3.2	± 2.5
Hadronic calorimeter (jets)			
barrel and end-cap	$\sigma_E/E = 50\%\sqrt{E} \oplus 3\%$	± 3.2	± 3.2
forward	$\sigma_E/E = 100\%\sqrt{E} \oplus 10\%$	$3.1 < \lvert\eta\rvert < 4.9$	$3.1 < \lvert\eta\rvert < 4.9$
Muon Spectrometer	$\sigma_{p_{\mathrm{T}}}/p_{\mathrm{T}} = 10\%$ at $p_{\mathrm{T}} = 10$ TeV	± 2.7	± 2.4

z is defined as the counterclockwise direction of the LHC. Since physics processes and the ATLAS detector has cylindrical symmetry, a cylindrical coordinate system (r, z, ϕ) is useful to specify directions.

Pseudo rapidity η is defined as the high energy limit of the rapidity y:

$$\eta = \lim_{E,|\mathbf{p}|\to\infty} y = \lim_{E,|\mathbf{p}|\to\infty} \frac{1}{2} \ln\left(\frac{E + p_z}{E - pz}\right) = \frac{1}{2} \ln\left(\frac{1 + \cos\theta}{1 - \cos\theta}\right) = \frac{1}{2} \ln \frac{\cos(\theta/2)}{\sin(\theta/2)} = -\frac{1}{2} \ln \tan(\theta/2). \quad (3.1)$$

This is useful since its difference $\eta_1 - \eta_2$ is an invariant of Lorentz boost in the z-direction. The angle ϕ is also an invariant of the same Lorentz boost. Thus, $\Delta R = \sqrt{(\eta_1 - \eta_2)^2 + (\phi_1 - \phi_2)^2}$ is invariant angular separation and used extensively in this thesis.

The cylinder-shaped region with low $|\eta|$ is called *barrel*, and the disk-shaped regions with high $|\eta|$ are called *end-caps*. The region with $|\eta| \gtrsim 2.5$ is sometimes called *forward*. Since the coverage of the Inner Detector (tracker) is limited to $|\eta| \lesssim 2.5$, the forward region usually needs different techniques in analyses.

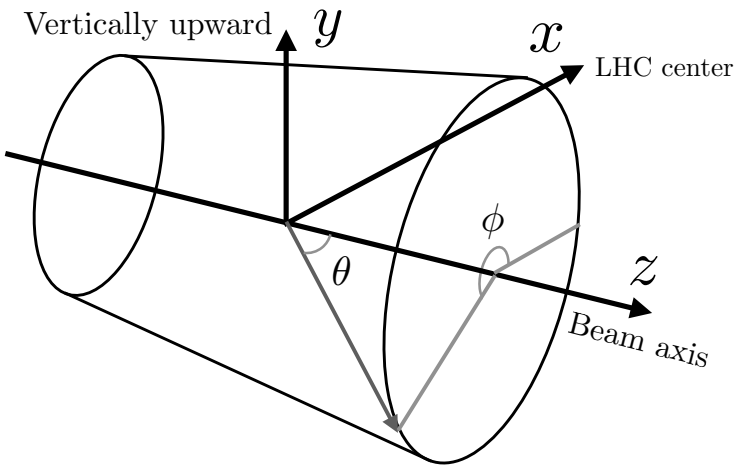

Figure 3.4: Schematic view of the ATLAS coordinate system.

3.2.1 Inner Detector

The Inner Detector (ID) is installed in the innermost layer of the ATLAS detector. The ID consists of Insertable B-Layer (IBL), Pixel, Silicon Microstrip Tracker (SCT), and Transition Radiation Tracker (TRT). Hits in the ID are used to reconstruct the tracks of charged particles. Combining with the track reconstruction and the 2T solenoid magnetic field in the z direction, the momenta of these tracks are measured. The ID is installed in $0 < R < 1150\,\text{mm}$, $0 < |z| < 3512\,\text{mm}$, corresponding to the coverage $|\eta| < 2.4$ as shown in Figure 3.5.

Pixel detector and Insertable B-Layer

The sensor of Pixel adopts an n-type wafer for bulk. A highly positive dose (p^+) region is placed on one side and the reverse voltage is applied. A readout is placed on a highly negative dose (n^+) region on the other side. The n^+ region improves the electron collection efficiency.

The sensors are segmented in pixels with size of $\Delta\phi \times \Delta z(\text{barrel}) = \Delta\phi \times \Delta R(\text{end-cap}) = 50 \times 400\,\mu\text{m}^2$. The size of the pixels for the IBL is $\Delta\phi \times \Delta z = 50 \times 250\,\mu\text{m}^2$. Measurement of the positions of charged particles is performed with these pixels.

For the barrel region, 1 IBL layer and 3 Pixel layers are installed in $33.3(\text{IBL}) < R < 122.5\,\text{mm}$ and $0 < |z| < 400.5\,\text{mm}$. For the end-cap region, 3 Pixel disks are installed in $88.8 < R < 149.6\,\text{mm}$ and $495 < |z| < 650\,\text{mm}$ in each side.

Silicon Microstrip Tracker

The SCT sensor consists of strip-shaped p-type wafers as the cathode implanted in n-type bulk. Reverse voltage is applied to enlarge sensitive volume and make electrons and holes drift to the electrodes. AC-coupled readout strips are placed on the p-type cathodes.

In the barrel region, $80\,\mu\text{m}^2$ pitch strips are equipped on the silicon wafer to measure ϕ coordinates. These strips run in the beam direction and are referred to as *axial strips*. The SCT also has strips with 40 mrad stereo angles (*stereo strips*) to allow for two-dimensional measurement. In the end-cap region, strips run radial direction to measure the ϕ coordinate and strips with 40 mrad stereo angles are also used. The average pitch of the strips is also $80\,\mu\text{m}^2$.

4 layers are installed in $299 < R < 514\,\text{mm}$ and $0 < |z| < 749\,\text{mm}$ for barrel, and 9 disks are installed in $275 < R < 560\,\text{mm}$ and $839 < |z| < 2735\,\text{mm}$ for each end-cap.

Transition Radiation Tracker

The TRT consists of straw tubes made of polyimide. The tubes are embedded in stacks of foils or fibers of polypropylene or polyethylene that produce transition radiation X-rays [64]. Xe-based gas mixture (70% Xe, 27% CO_2, 3% O_2) is filled in the tubes to detect the transition radiation photons.

Many hits (typically 36 per track) are provided by the 4 mm diameter straw tubes with 130 μm accuracy per tube. The tubes run along the beam axis in the barrel whereas in the radial direction in the end-cap, which provide measurements of $R - \phi$ (barrel) and $z - \phi$ (end-cap) positions of tracks. Combining with

the high precision silicon trackers at small radii, the TRT provides robust pattern recognition for track reconstruction. The TRT greatly contributes to momentum measurement due to hits at large radii. The TRT improves the separation of electrons from $\pi^{\pm}$ by detection of the transition radiation from the electron.

73 planes of straw tubes are equipped in $563 < R < 1066$ mm and $0 < |z| < 712$ mm for barrel, whereas 160 planes are equipped in $644 < R < 1004$ mm and $848 < |z| < 2710$ mm for end-cap.

3.2.2 Calorimeters

The ATLAS Calorimeter system consists of electromagnetic (EM) calorimeters and hadronic calorimeters. Forward calorimeter that works as both as EM and hadronic calorimeter is used in $3.1 < |\eta| < 4.9$.

The EM calorimeters measure the energy and the positions of electrons and photons absorbing their energy. The hadronic calorimeter measures the energy and the positions of hadronic objects such as jets.

The calorimeters are installed outside of the Inner Detector as shown in Figure 3.6. The thickness of the calorimeters is designed to fully contain EM and hadronic shows and is 11 interaction length (λ) at $\eta = 0$ including the outer support. The active material has $\sim 9.7\ \lambda$ in the barrel and $\sim 10\ \lambda$ in the end-cap

Electromagnetic Calorimeter

The EM calorimeter uses lead for the absorber and liquid Ar (LAr) for the scintillator. An accordion structure is used for the absorber and the electrode as shown in Figure 3.7. This geometry realizes uniformity in ϕ.

The EM calorimeter is divided into three layers in the depth direction as shown in Figure 3.7. The granularity of the EM calorimeter is specified by the cells with the size of $\Delta\eta \times \Delta\phi \sim 0.003 \times 0.1$ (Layer 1), $\sim 0.025 \times 0.025$ (Layer 3) and $\sim 0.025 \times 0.05$ (Layer 3). A presampler with the granularity $\Delta\eta \times \Delta\phi \sim 0.025 \times 0.1$ and 11 mm (barrel), 5 mm (end-cap) thick is used as "Layer 0" and placed inner

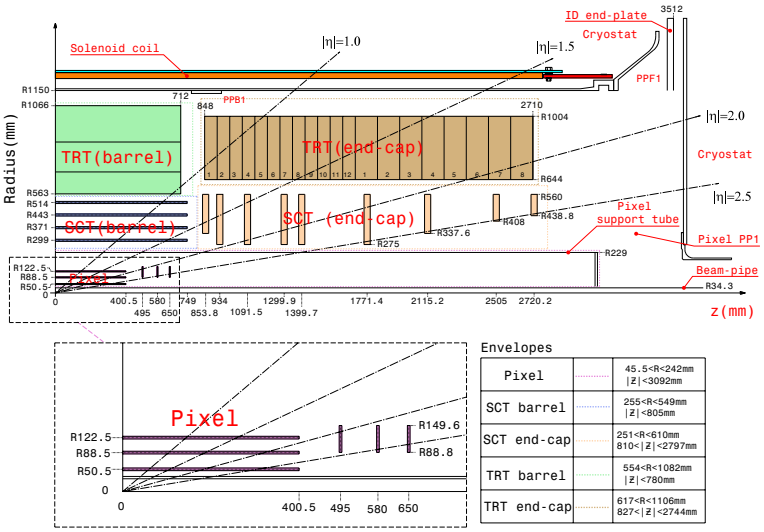

Figure 3.5: Layout of the ATLAS Inner Detector. This shows the quarter-section of the system.

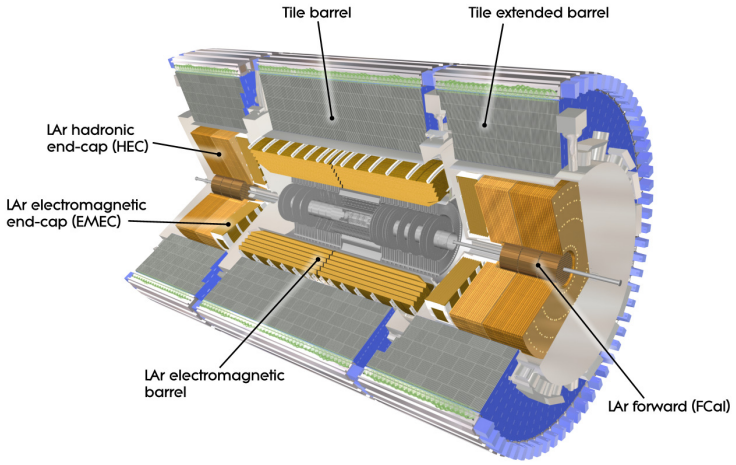

Figure 3.6: Cut-away view of the ATLAS Calorimeter system.

side of the Layer 1. The presampler is used to correct the energy of electrons and photons by detecting showers caused by the interaction between electrons/photons and the Inner Detector.

The barrel part of the calorimeter covers $|\eta| < 1.475$ and the end-cap part covers $1.375 < |\eta| < 3.2$. More than 22 radiation length (X_0) in the barrel and more than 24 X_0 in the end-caps.

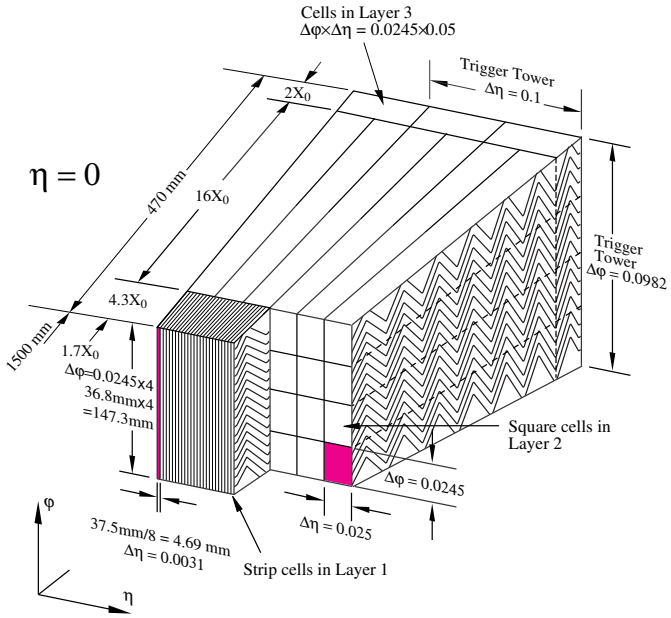

Figure 3.7: Sketch of a barrel module of the EM calorimeter showing three layers. The granularity is defined by "cells". The wavy lines drawn on the side are the accordion structure of the EM calorimeter.

Hadronic Calorimeter

The Tile calorimeter combines steel as the absorber and scintillation tiles as the active material as shown in Figure 3.8.

The Tile calorimeter is segmented into three layers in the depth direction. The thickness of these layers is 1.5, 4.1, and 1.8 λ for the barrel and 1.5, 2.6, and 3.3 λ for the extended barrel. The granularity in $\Delta\eta \times \Delta\phi$ is 0.1×0.1 in the first two layers and 0.2×0.1 in the outermost layer.

The Tile calorimeter is placed outside the EM calorimeter from $r = 2.28\,\mathrm{m}$ to $r = 4.25\,\mathrm{m}$ and covers the barrel region ($|\eta| < 1.0$) and the extended barrel region ($0.8 < |\eta| < 1.75$). The corresponding total thickness of the detector is 9.7 λ at the outer surface of the Tile calorimeter at $|\eta| = 0$.

The Hadronic End-cap Calorimeter (HEC) consists of 25 or 50 mm thick copper plates as the absorber. The 8.5 mm gaps of the copper plates are filled with LAr for the active material.

The HEC is segmented into four layers in the depth direction. The granularity in $\Delta\eta \times \Delta\phi$ is 0.1×0.1 in $|\eta| < 2.5$ and 0.2×0.2 in the higher η region.

The HEC is placed outside the end-cap EM calorimeter. The inner radius is $r = 0.475\,\mathrm{m}$ or $0.372\,\mathrm{m}$, and the outer radius is $r = 2.04\,\mathrm{m}$, corresponding to the coverage of $1.5 < |\eta| < 3.2$. The detailed layout is shown in Figure 3.9.

The Forward Calorimeter (FCal) is composed of three modules. The first module uses copper as the absorber for electromagnetic measurement. The second and third modules use tungsten which is suited for the measurement of hadronic interactions. The absorbers are constructed with rod and tube structure, and the gap is filled with LAr.

The granularity of the FCal is $\Delta x \times \Delta y = O(1\,\mathrm{cm} \times 1\,\mathrm{cm})$ and different in regions [65]

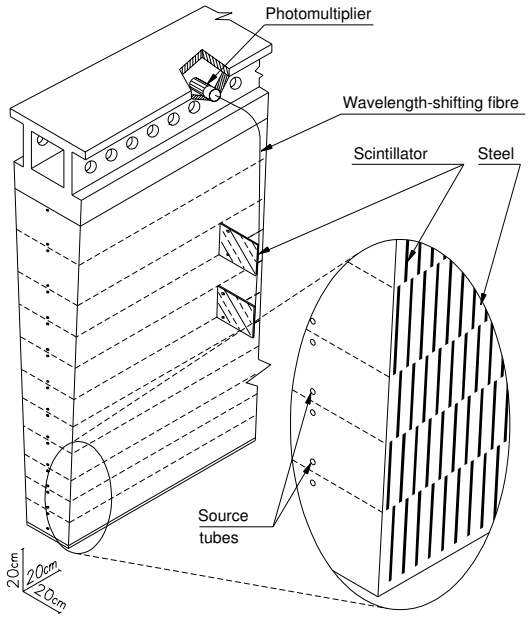

Figure 3.8: Sketch of a Tile calorimeter module.

The FCal is $\sim 10\ \lambda$ thick. The FCal is placed in the region between the beam pipe and the HEC in $4.7 < |z| < 6.1$ mm, and covers $3.1 < |\eta| < 4.9$. The layout is summarized in Figure 3.9.

3.2.3 Muon Spectrometer

The Muon Spectrometer (MS) is placed at the outermost layer of the ATLAS detector. The MS consists of 4 detector technologies: Resistive Plate Chamber (RPC), Thin Gap Chamber (TGC), Monitored Drift Tube (MDT), and Cathode Strip Chamber (CSC).

Combined with the 1T toroidal magnet, the MDT and the CSC provide a precision reconstruction of muons. The RPC and the TGC are used for triggering muons with high transverse momenta.

The chambers of the MS are placed in layers called "stations". For the barrel region, stations are located at $R \sim 5$ m, 7.5 m, 10 m. All three layers are in the magnetic field. For the end-cap region, stations are located at $|z| \sim 7.4$ m, 14 m, 21.5 m. A station called "EE" is installed before Run 2 at $|z| \sim 10.8$ m. The end-cap toroidal magnet is installed between the first and the second layers. Three stations are called *inner, middle* and *outer stations*, respectively. The MS covers $|\eta| < 2.7$. The overall layout of the MS is shown in Figure 3.10.

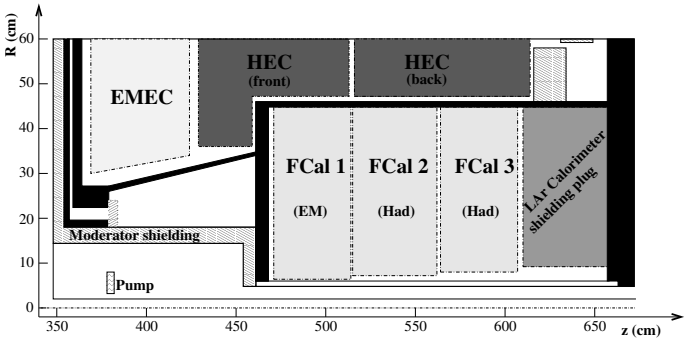

Figure 3.9: Layout of the end-cap calorimeter modules.

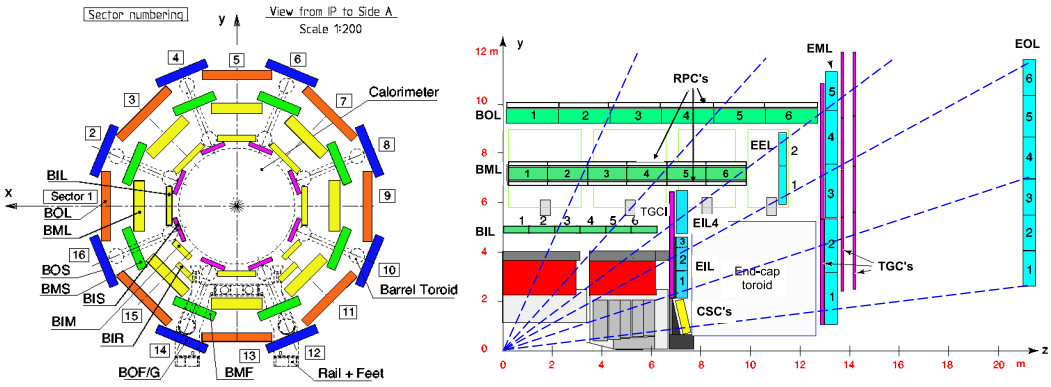

Figure 3.10: Cross-section of the Muon Spectrometer in x-y (left) and y-z (right). For the left figure, the stations are indicated with colors. The toroidal magnets are shown in the dashed lines. For the right figure, the MDT is shown in green (barrel) and light blue (end-cap). The other types of chambers are indicated with different colors.

Resistive Plate Chamber

The RPC consists of 2 mm gas gaps between resistive plates as shown in Figure 3.11. The gas contain 94.7% $C_2H_2F_4$, 5% Iso-C_4H_{10} and 0.3% AF_6 and electric field of 4.9 kV/mm is applied. Readout strips are placed on the other side of the PET foils and capacitively coupled with the electrodes.

The readout strips on one side of the gas gap measure the z coordinate, and the ones on the other side measure the ϕ coordinate. Combining with the toroidal magnetic field, the RPC is used for triggering muons.

The RPC is used only in the barrel region ($|\eta| < 1.05$). The layout of the RPC is shown in Figure 3.11

Thin Gap Chamber

The TGC is a multi-wire chamber as shown in Figure 3.12. A gas mixture with 55% CO_2 and 45% n-pentane is filed in the 2.8 mm gap, and the high voltage of 2900 ± 100 V is applied. The TGC has a fast response time due to the short drift length between the wires (anode) and the strips (cathode).

The wires and the strip provide measurements of r and ϕ coordinates, respectively. The resolution of these measurements are summarized in Table 3.2. The TGC is used for triggering muons in the end-cap region ($|\eta| < 2.4$).

Three layers of the TGC are placed in the middle station. The TGC is also installed in the inner station. A requirement of the coincidence of this layer with the middle station is useful to reduce backgrounds caused by charged particles emerging from the beam pipe.

Monitored Drift Tube

The MDT consists of 29.97 mm diameter drift tubes shown in Figure 3.13. Gas mixture of 93% Ar, 7% CO_2 and <1000 ppm H_2O is filled in the tubes with 3 bar. The high voltage of 3080 V is applied and the drift time is at most 700 ns.

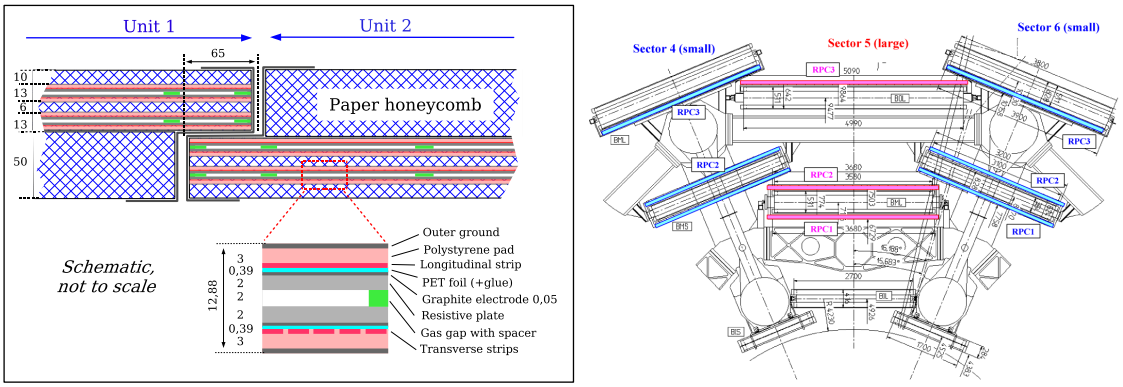

Figure 3.11: Left: Structure of an RPC layer. Right: Layout of the RPC system. The RPC is indicated with color. The middle station has two layers and the outer station has one.

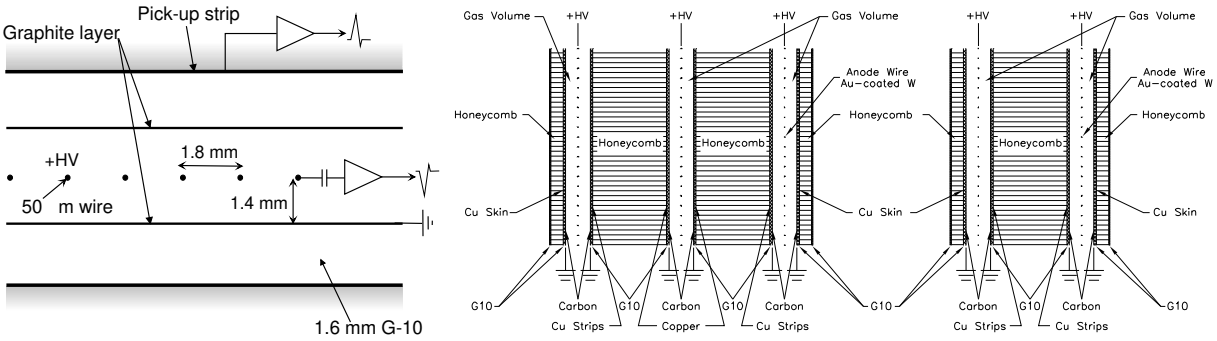

Figure 3.12: Left: Structure of Gas gap of the TGC. Right: Cross-sections of a TGC triplet and doublet modules.

In each station of the MS, 6 or 8 layers of tubes are attached on both sides of a spacer as shown in Figure 3.14. The position of a track is measured from the drift time, and a track segment is reconstructed combining tubes in a layer. The MDT provides precise measurement in the η direction, which is crucial to reconstruct the momenta of muons. The resolution of the MDT is summarized in Table 3.2.

The MDT is equipped in all the station of the MS as shown in Figure 3.10.

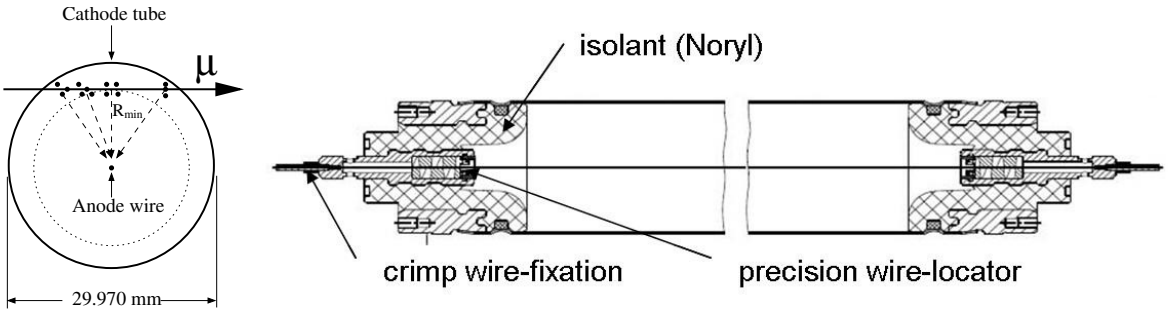

Figure 3.13: Cross-sections of an MDT tube.

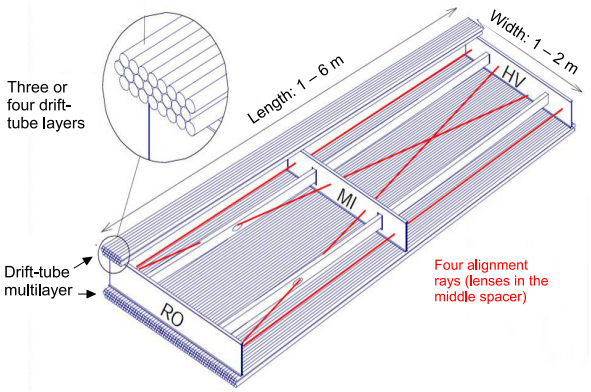

Figure 3.14: Structure of a MDT module in a station.

Cathode Strip Chamber

At the innermost layer of the MS in $2.0 < |\eta| < 2.7$, the rate of particles such as neutrons, γ-rays, and charged particles exceeds the limitation of the MDT (150 Hz/cm^2). The CSC is used instead of the MDT to provide precise measurement of tracks. This environment comes with several requirements as explained below.

The CSC is a multi-wire proportional chamber as shown in Figure 3.15. The gas mixture of 80% Ar and 20% CO_2 is filled in the gas gaps. With this gas mixture, the sensitivity of the CSC to neutrons is reduced. The high voltage of 1900 V is applied. The drift time for electrons is less than 40 ns and the time resolution is 5 ns.

Measurement is performed with cathode strips. The charge is induced in multiple cathode strips as shown in Figure 3.15. The CSC measures the position of a track by taking the barycenter of the charge. The cathode strips measuring the r and ϕ coordinates are placed on each side of the gas gap. The CSC has 4 layers of the gas gaps and provides precise tracking in $2.0 < |\eta| < 2.7$ of the inner station of the MS. With these capabilities, the CSC can operate under particle rates up to 1 kHz/cm^2, which is sufficient.

3.2.4 Trigger system

The LHC provides proton-proton collisions at 40 MHz while the capability of the ATLAS data acquisition (DAQ) system of recording data is approximately 1 kHz.

Cross-sections of processes at the LHC are shown in Figure 3.16. While the total cross-section of the proton-proton inelastic scattering is 70 nb, cross-sections of interesting processes such as the production of

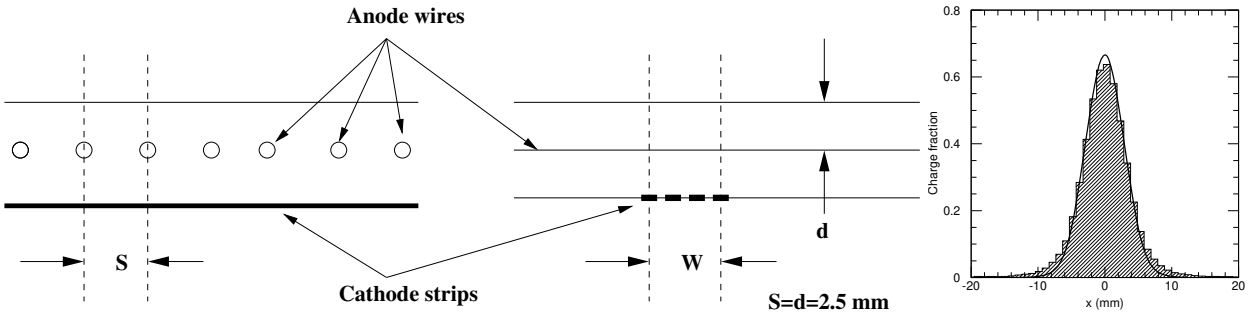

Figure 3.15: Left: Structure of anode wires and cathode strips in a CSC gas gap. Right: Charge distribution induced on the CSC cathode.

Table 3.2: Resolution and other parameters of measurements in chambers in the Muon Spectrometer.

		Chamber resolution (RMS) in			**Measurement/track**		**Number of**	
Type	**Function**	z/R	ϕ	time	barrel	end-cap	chambers	channels
MDT	tracking	35 μm (z)	-	-	20	20	1088 (1150)	339k (354k)
CSC	tracking	40 μm (R)	5 mm	7 ns	-	4	32	30.7k
RPC	trigger	10 mm (z)	10 mm	1.5 ns	6	-	544 (606)	359k (373k)
TGC	trigger	2-6 mm (R)	3-7 mm	4 ns	-	9	3588	318k

weak bosons, Higgs bosons, top quarks, and BSM particles are much smaller as shown in the figure. Thus, selecting a subset of events that contain those interesting processes is crucial to perform physics analyses with sufficient statistics. A system that performs the online event selection is called *trigger*.

The trigger system selects events with high p_{T} objects such as leptons, missing transverse energy $E_{\mathrm{T}}^{\mathrm{miss}}$, photons, or jets, targeting the hard-scattering processes mentioned in the previous paragraph. Since the trigger system must implement fast and precise selection, it exploits multi-step selection with hardware-based *Level-1 Trigger (L1)* and CPU-based *High Level Trigger (HLT)*. A schematic view of the ATLAS Trigger System is shown in Figure 3.17.

The L1 implements fast event selection based on information from the Calorimeter and Muon Spectrometer using dedicated hardware. The L1 reduces the event rate to approximately 100 kHz, which is the limitation of the readout electronics. The L1 defines *regions-of-interest (ROIs)* that are used in the HLT.

The HLT implements event selection based on the species, energies, and/or momenta of particles. It can also use a combination of requirements on several particles, or event topologies such as $E_{\mathrm{T}}^{\mathrm{miss}}$. The event selection at the HLT is based on precise event reconstruction equivalent to offline algorithms. To perform the offline level event reconstruction, the HLT uses information from all the detector subsystems in the ROIs. The HLT reduces the event rates to $\sim$ 1 kHz, which is determined by the size of the storage.

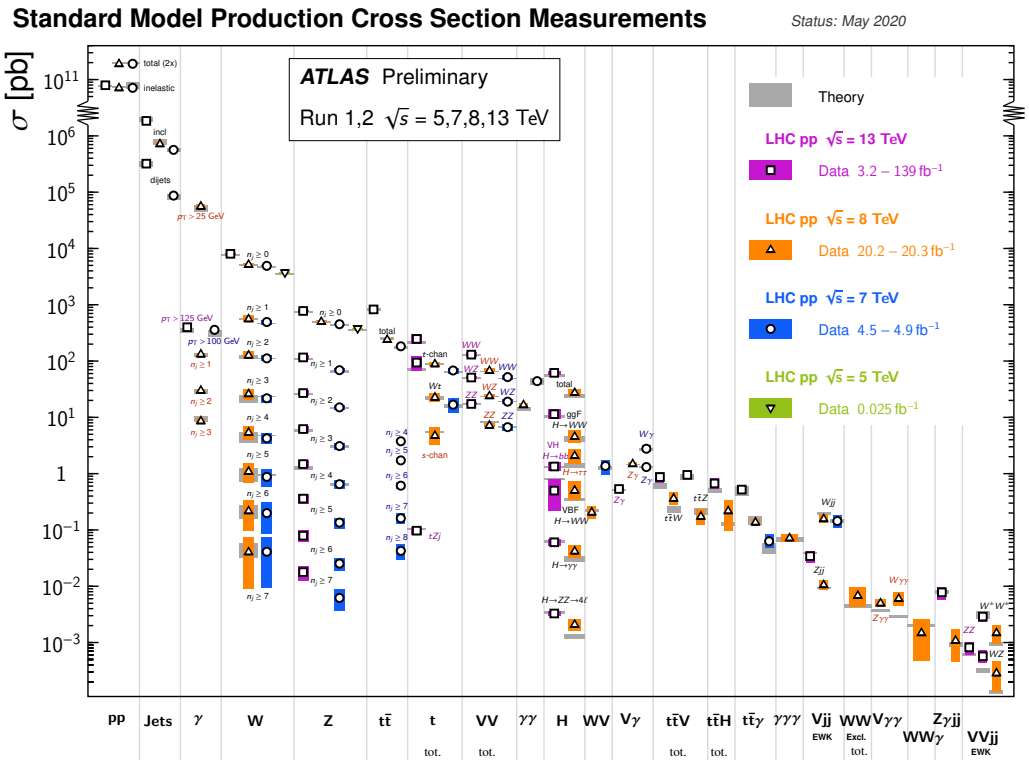

Figure 3.16: Summary of the measurements of the total cross-sections and the cross-sections in restrict phase spaces for several Standard Model processes, corrected for branching fractions, compared to the corresponding theoretical expectations [66]. In some cases, the focused phase space is different between measurements at the different center-of-mass energies $\sqrt{s}$, resulting in lower cross-section values at higher $\sqrt{s}$.

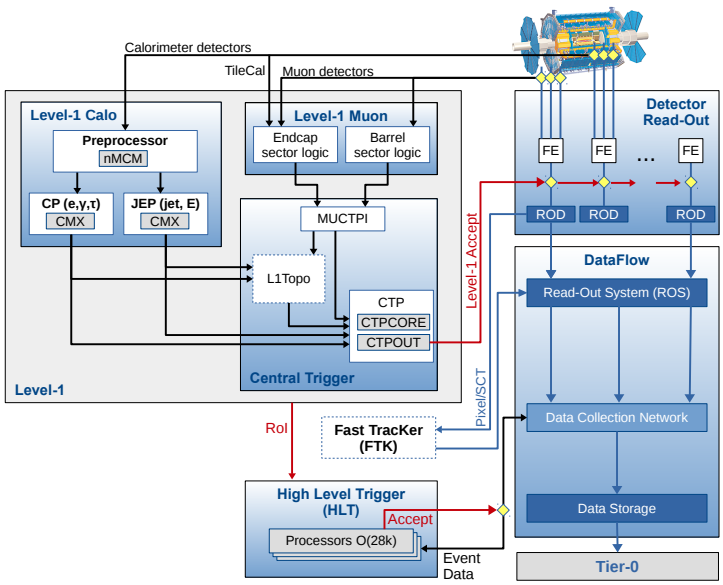

Figure 3.17: Schematic diagram of the ATLAS TDAQ system at the beginning of Run 2 [67]. L1Topo and FTK were being commissioned.

One trigger is defined as a combination of L1 and HLT selection criteria. Each trigger can run being prescaled to reduce event rates. To efficiently combine many types of the L1 Trigger and the HLT to cover important physics channels, the prescale factors for all triggers are defined, which is referred to as *Trigger Menu*. Most important triggers are used without prescaling. The main triggers in the 2018 data-taking are shown in Table 3.3.

Table 3.3: Main ATLAS triggers used with luminosities up to $2.0 \times 10^{34}\,\mathrm{cm}^{-2}\mathrm{s}^{-1}$ [68]. The observed trigger rates are reported at a luminosity of $2.0 \times 10^{34}\,\mathrm{cm}^{-2}\mathrm{s}^{-1}$ and a pileup of 55. These trigger rates include overlapping between triggers. The uncertainty of the rates is the order of a few percent. The total rate includes many more triggers than listed in this table. Electron (e), photon (γ), and tau (τ) identification of medium efficiency working point is applied. unless it is specified. An online isolation requirement is indicated as (i). Topological requirements between L1 objects are indicated as (topo). For the ditau trigger, a minimal ΔR separation between isolated L1 tau objects and L1 jet objects is imposed. A selection of flavor tagging efficiency (ϵ) working points are indicated for b-jet triggers. For B-physics triggers, dimuon vertices are required to have a positive displacement at the HLT, and dedicated selections for dimuon mass, J/ψ, B-mesons, and Υ are applied as indicated with (di-μ), (J/ψ), (B) and (Υ), respectively. the typical offline selections are determined by resolution effects. The total rates at L1 and HLT in the bottom row are the total recorded rates and account for the overlaps between individual triggers. Only a selected number of primary triggers is displayed in this table.

Trigger	**Typical offline selection**	**Trigger Selection**		**L1 Peak Rate [kHz]**	**HLT Peak Rate [Hz]**
		L1 [GeV]	HLT [GeV]	L=2.0×10^{34} $\mathrm{cm}^{-2}\mathrm{s}^{-1}$	
Single leptons	Single isolated μ, $p_{\mathrm{T}} > 27$ GeV	20	26 (i)	16	218
	Single isolated tight e, $p_{\mathrm{T}} > 27$ GeV	22 (i)	26 (i)	31	195
	Single μ, $p_{\mathrm{T}} > 52$ GeV	20	50	16	70
	Single e, $p_{\mathrm{T}} > 61$ GeV	22 (i)	60	28	20
	Single τ, $p_{\mathrm{T}} > 170$ GeV	100	160	1.4	42
Two leptons	Two μ, each $p_{\mathrm{T}} > 15$ GeV	2×10	2×14	2.2	30
	Two μ, $p_{\mathrm{T}} > 23, 9$ GeV	20	22, 8	16	47
	Two very loose e, each $p_{\mathrm{T}} > 18$ GeV	2×15 (i)	2×17	2.0	13
	One e & one μ, $p_{\mathrm{T}} > 8, 25$ GeV	20 (μ)	7, 24	16	6
	One loose e & one μ, $p_{\mathrm{T}} > 18, 15$ GeV	15, 10	17, 14	2.6	5
	One e & one μ, $p_{\mathrm{T}} > 27, 9$ GeV	22 (e, i)	26, 8	21	4
	Two τ, $p_{\mathrm{T}} > 40, 30$ GeV	20 (i), 12 (i) (+jets, topo)	35, 25	5.7	93
	One τ & one isolated μ, $p_{\mathrm{T}} > 30, 15$ GeV	12 (i), 10 (+jets)	25, 14 (i)	2.4	17
	One τ & one isolated e, $p_{\mathrm{T}} > 30, 18$ GeV	12 (i), 15 (i) (+jets)	25, 17 (i)	4.6	19
Three leptons	Three very loose e, $p_{\mathrm{T}} > 25, 13, 13$ GeV	20, 2×10	24, 2×12	1.6	0.1
	Three μ, each $p_{\mathrm{T}} > 7$ GeV	3×6	3×6	0.2	7
	Three μ, $p_{\mathrm{T}} > 21, 2 \times 5$ GeV	20	20, 2×4	16	9
	Two μ & one loose e, $p_{\mathrm{T}} > 2 \times 11, 13$ GeV	2×10 (μ)	$2 \times 10, 12$	2.2	0.5
	Two loose e & one μ, $p_{\mathrm{T}} > 2 \times 13, 11$ GeV	$2 \times 8, 10$	$2 \times 12, 10$	2.3	0.1
Signle photon	One loose γ, $p_{\mathrm{T}} > 145$ GeV	24 (i)	140	24	47
Two photons	Two loose γ, each $p_{\mathrm{T}} > 55$ GeV	2×20	2×50	3.0	7
	Two γ, $p_{\mathrm{T}} > 40, 30$ GeV	2×20	35, 25	3.0	21
	Two isolated tight γ, each $p_{\mathrm{T}} > 25$ GeV	2×15 (i)	2×20 (i)	2.0	15
Single jet	Jet ($R = 0.4$), $p_{\mathrm{T}} > 435$ GeV	100	420	3.7	35
	Jet ($R = 1.0$), $p_{\mathrm{T}} > 480$ GeV	111 (topo: $R = 1.0$)	460	2.6	42
	Jet ($R = 1.0$), $p_{\mathrm{T}} > 450$ GeV, $m_{\mathrm{jet}} > 45$ GeV	111 (topo: $R = 1.0$)	420, $m_{\mathrm{jet}} > 35$	2.6	36
$b-$jets	One b ($\epsilon = 60\%$), $p_{\mathrm{T}} > 285$ GeV	100	275	3.6	15
	Two b ($\epsilon = 60\%$), $p_{\mathrm{T}} > 185, 70$ GeV	100	175, 60	3.6	11
	One b ($\epsilon = 40\%$) & three jets, each $p_{\mathrm{T}} > 85$ GeV	4×15	4×75	1.5	14
	Two b ($\epsilon = 70\%$) & one jet, $p_{\mathrm{T}} > 65, 65, 160$ GeV	$2 \times 30, 85$	$2 \times 55, 150$	1.3	17
	Two b ($\epsilon = 60\%$) & two jets, each $p_{\mathrm{T}} > 65$ GeV	4×15, $\lvert\eta\rvert < 2.5$	4×55	3.2	15
Multijets	Four jets, each $p_{\mathrm{T}} > 125$ GeV	3×50	4×115	0.5	16
	Five jets, each $p_{\mathrm{T}} > 95$ GeV	4×15	5×85	4.8	10
	Six jets, each $p_{\mathrm{T}} > 80$ GeV	4×15	6×70	4.8	4
	Six jets, each $p_{\mathrm{T}} > 60$ GeV, $\lvert\eta\rvert < 2.0$	4×15	6×55, $\lvert\eta\rvert < 2.4$	4.8	15
$E_{\mathrm{T}}^{\mathrm{miss}}$	$E_{\mathrm{T}}^{\mathrm{miss}} > 200$ GeV	50	110	5.1	94
B-physics	Two μ, $p_{\mathrm{T}} > 11, 6$ GeV, $0.1 < \mathrm{m}(\mu, \mu) < 14$ GeV	11, 6	11, 6 (di-μ)	2.9	55
	Two μ, $p_{\mathrm{T}} > 6, 6$ GeV, $2.5 < \mathrm{m}(\mu, \mu) < 4.0$ GeV	2×6 (J/ψ, topo)	2×6 (J/ψ)	1.4	55
	Two μ, $p_{\mathrm{T}} > 6, 6$ GeV, $4.7 < \mathrm{m}(\mu, \mu) < 5.9$ GeV	2×6 (B, topo)	2×6 (B)	1.4	6
	Two μ, $p_{\mathrm{T}} > 6, 6$ GeV, $7 < \mathrm{m}(\mu, \mu) < 12$ GeV	2×6 (Υ, topo)	2×6 (Υ)	1.2	12
Main Rate				86	1750
B-physics and Light States Rate					200

4 Data and simulations

Both data and simulation samples are needed in the analysis. The data samples corresponding to the full ATLAS Run2 dataset are described in Section 4.1. The simulations for the signal and background processes are described in Section 4.2.

4.1 Data sample

Data used in the analysis are collected using unprescaled single-lepton and $E_{\mathrm{T}}^{\mathrm{miss}}$ triggers in 2015-2018 [68–71]. These triggers are listed in Table 4.1 with the criteria.

The analysis uses only the data in the periods in which the detector subsystems were operating good condition. The amounts of these *good data* are 3.2, 33.0, 44.3 and 58.9 fb^{-1} for 2015, 2016, 2017 and 2018,

Table 4.1: Single-lepton and $E_{\mathrm{T}}^{\mathrm{miss}}$ triggers used for the analysis. These triggers are unprescaled triggers operated in indicate periods [68–71] The electron and muon triggers adopt the transverse momenta of leptons for the thresholds while the $E_{\mathrm{T}}^{\mathrm{miss}}$ triggers use the magnitude of $E_{\mathrm{T}}^{\mathrm{miss}}$. The electron and muon triggers with lower thresholds also include requirement of *likelihood identification* and *isolation*. See Sections 5.2 and 5.3 for these requirements.

Year	Threshold [GeV]	Additional requirements	ATLAS terminology
		$E_{\mathrm{T}}^{\mathrm{miss}}$ trigger	
2015	70	-	HLT_xe70_L1XE50
2016	90	-	HLT_xe90_mht_L1XE50
	110	-	HLT_xe110_mht_L1XE50
2017	110	-	HLT_xe110_pufit_L1XE50
2018	70	-	HLT_xe110_pufit_xe70_L1XE50
		Electron trigger	
2015	24	Likelihood based identification	HLT_e24_lhmedium_L1EM20VH
	60	Likelihood based identification	HLT_e60_lhmedium
	120	Likelihood based identification	HLT_e120_lhloose
2016-2018	26	Likelihood based identification & Isolation	HLT_e26_lhtight_nod0_ivarloose
	60	Likelihood based identification	HLT_e60_lhmedium(_nod0)
	140	Likelihood based identification	HLT_e140_lhloose(_nod0)
2018	300	-	HLT_e300_etcut
		Muon trigger	
2015	24	Isolation	HLT_mu24_iloose_L1MU15
2016-2018	26	Isolaion	HLT_mu26_ivarmedium
2015-2018	50	-	HLT_mu50

respectively, and 139 fb^{-1} in total. The accumulation of the good data compared to the data delivered by the LHC and recorded by ATLAS is shown in Figure 4.1.

There are multiple proton-proton collisions in bunch crossings in addition to hard scatterings focused in the analysis. These extra interactions are referred to as *pile-up*. The average number of interactions per bunch crossings ($\langle\mu\rangle$) is shown in Figure 4.2 for each year. As indicated in this figure, the average $\langle\mu\rangle$ in 2015-2018 is 33.7.

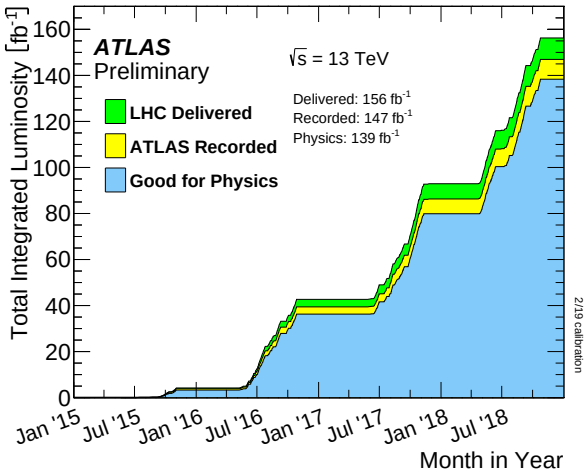

Figure 4.1: Integrated luminosity available in physics analyses compared to the integrated luminosity provided by the LHC and recorded by the ATLAS detector [72].

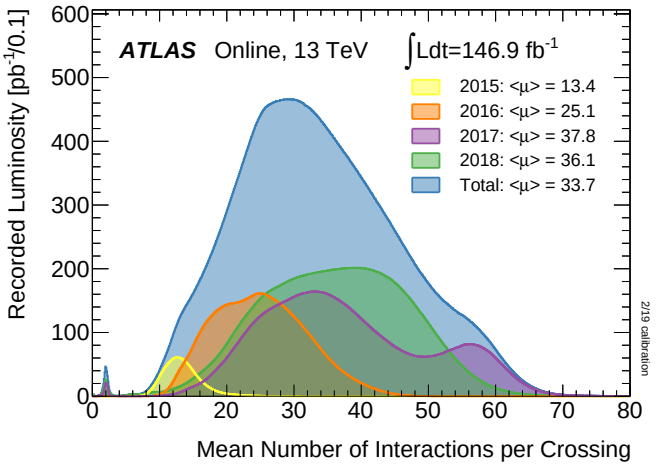

Figure 4.2: Number of interactions per crossing in each year [72].

4.2 Signal and background processes and the simulations

4.2.1 Flow of the simulation

In Monte Carlo simulations, events are generated based on theoretical calculations. This part of the simulation is summarized in Section 4.2.2. Response of the detector is simulated using the ATLAS detector simulation software [73] based on GEANT 4 [74]. As explained in Section 4.1, there are effects from the pile-up. The pile-up is simulated by the soft QCD process using PYTHIA 8.186 [75] with the A3 tune [76] and NNPDF2.3LO [77], and the contribution is overlaid after the detector simulation with GEANT 4.

4.2.2 Relevant processes and physics simulations

Simulated events are prepared using programs called *event generators*. These event generators provide differential distributions typically based on next-to-leading-order (NLO) perturbative calculation in QCD. On the other hand, the total cross-sections are often available at higher accuracy, typically next-to-next-to-leading-order (NNLO). In this case, samples are normalized using the best available theoretical calculation. Thus, event generators and the cross-sections of relevant physics processes are described in the following sections.

All generated samples, except SHERPA samples [78], are processed with EvtGen [79] to simulate the decays of heavy flavor particles such as B and C mesons.

Higgs boson production in association with a vector boson (VH signal)

As shown in Figure 4.3, three production modes $qq \to WH$, $qq \to ZH$ and $gg \to ZH$, and the decay modes $W \to \ell\nu$ and $Z \to ee/\mu\mu/\tau\tau/\nu\nu$ are considered. The quark-initiated processes are simulated using POWHEG-BOX-v2 [80] with GOSAM [81], the MINLO (Multiscale Improved NLO) correction [82, 83] and the NNPDF3.0NLO PDF [84]. The events are passed to the PYTHIA 8.212 [75] generator with the AZNLO tune [85] and the NNPDF3.0NLO PDF set [84]. The gluon-initiated ZH contribution is simulated by LO QCD prediction using POWHEG-BOX-v2 with PYTHIA 8.212 with the AZNLO tune and NNPDF3.0NLO.

The samples are normalized using the best available theoretical calculations for the cross-sections. The cross-sections for WH and ZH are calculated at NNLO (QCD) and NLO (EW) [86–92]. The gluon-induced subprocess of ZH (the rightmost diagram in Figure 4.3) appears at NNLO ($O(\alpha_S^2)$). The cross-section of this $gg \to ZH$ process is calculated in the limit of infinite top-quark and vanishing bottom quark masses. The cross-section also includes photon-initiated processes [93] whose contribution is about

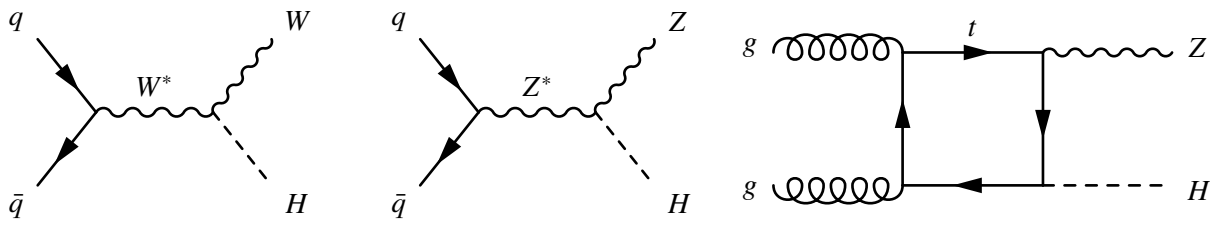

Figure 4.3: Feynman diagrams for the Higgs production in association with a vector boson (VH).

$O(5\%)$ for WH and $O(1\%)$ for ZH. The cross-section of WH is $\sigma_{WH} = 1.37 \pm 0.04\,\text{pb}$. The total ZH cross-section is $\sigma_{ZH} = 0.88^{+0.04}_{-0.03}\,\text{pb}$ (NNLO in QCD and NLO in EW). The $gg \to ZH$ samples are normalized using calculation at NLO+NLL in QCD ($O(\alpha_S^3)$) [94–98]. The $gg \to ZH$ cross-section is $\sigma_{gg\to ZH} = 0.12\,\text{pb}$. The $qq \to ZH$ samples are normalized using the cross-section defined as: $\sigma_{qq\to ZH} = \sigma_{ZH} - \sigma_{gg\to ZH} = 0.76\,\text{pb}$. The accuracy of this quantity is NNLO in QCD ($O(\alpha_S^2)$).

As already mentioned, the cross-section of VH includes the NLO electroweak correction. The spectrum of the transverse momentum of the vector boson is corrected to the NLO accuracy in the electroweak interaction using HAWK [93, 99].

Single boson production

The single boson production (V + jets) backgrounds are expressed by the Feynman diagrams shown in Figure 4.4. These processes are simulated using SHERPA 2.2.1 [78, 100–103] with NNPDF3.0NNLO [84]. SHERPA calculates the matrix elements including 0 or 1 additional parton at NLO (QCD) and 2 or 3 additional partons at LO (QCD).

The cross-sections for V + jets are available at NNLO in QCD [104]. Thus, the samples are scaled to the NNLO predictions. The scale factors for W + jets ($W \to \ell\nu$), Z + jets ($Z \to \ell\ell$) and Z + jets ($Z \to \nu\nu$) are $k^W = 0.9072$, $k^{Z\to\ell\ell} = 0.9751$ and $k^{Z\to\nu\nu} = 0.9728$. These numbers are taken from Ref. [105].

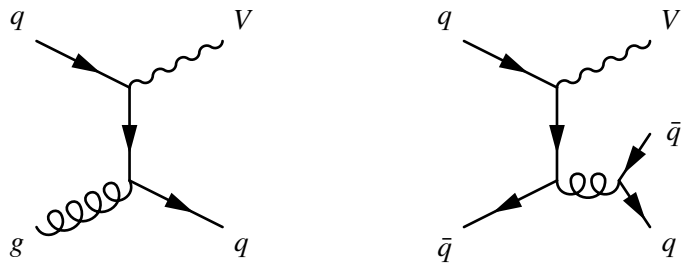

Figure 4.4: Feynman diagrams for the single boson production (V + jets).

Top-quark pair production

The Feynman diagrams for the top-quark pair production ($t\bar{t}$) background are shown in Figure 4.5. The $t\bar{t}$ process is simulated using the POWHEG-BOX-v2 NLO matrix element generator [106] with the NNPDF3.0NLO PDF set [84]. The events are further processed using PYTHIA 8.230 [75] with the A14 tune [107] and NNPDF2.3LO [77]. Detailed tuning parameters used in the simulation can be found in Ref. [108].

The cross-sections of the $t\bar{t}$ process is calculated at NNLO+NNLL in QCD [109]. The calculated cross-section is $\sigma_{t\bar{t}} = 831.76^{+40}_{-46}\,\text{pb}$. The uncertainties include the PDF and α_S uncertainties calculated using the PDF4LHC prescription [44].

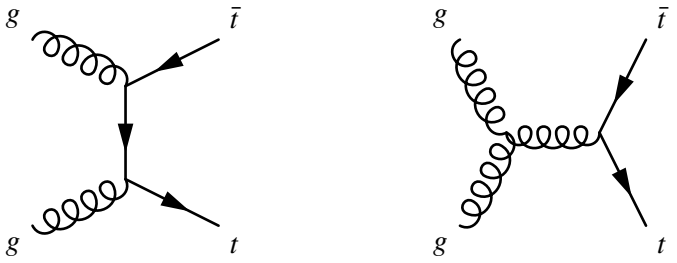

Figure 4.5: Feynman diagrams for the top-quark pair ($t\bar{t}$) production.

Single top production

The Feynman diagrams of single-top productions in Wt-, s- and t-channels are shown in Figures 4.6 and 4.7. All the production channels are simulated using Powheg-Box-v2 [110, 111] with the NNPDF3.0NLO PDF set [84]. The generated events are further processed with Pythia 8.230 with the A14 tune [107] and NNPDF2.3LO [77].

The cross-section of the Wt channel is available from an approximate NNLO calculation [112] with 172.5 GeV for the top-quark mass and MSTW2008 NNLO PDFs [112]. The calculated cross-section is $\sigma_{Wt} = 71.7^{+3.8}_{-3.8}$ pb. The uncertainty includes the PDF and α_S uncertainties calculated using the PDF4LHC prescription [44]. The cross-sections for the single top production in the s- and t-channels is calculated at NLO (QCD) with 172.5 GeV for the top-quark mass using Hathor v2.1 [113, 114]. The cross-sections of the s-channel are $\sigma_t = 6.35^{+0.2}_{-0.2}$ pb for the top-quark and $\sigma_{\bar{t}} = 3.97^{+0.19}_{-0.17}$ pb for the anti-top-quark. The cross-sections of the t-channel are $\sigma_t = 136.02^{+5.4}_{-4.6}$ pb for the top-quark and $\sigma_{\bar{t}} = 80.95^{+4.1}_{-3.6}$ pb for the anti-top-quark. These uncertainties include the PDF and α_S uncertainties calculated with the PDF4LHC prescription [44].

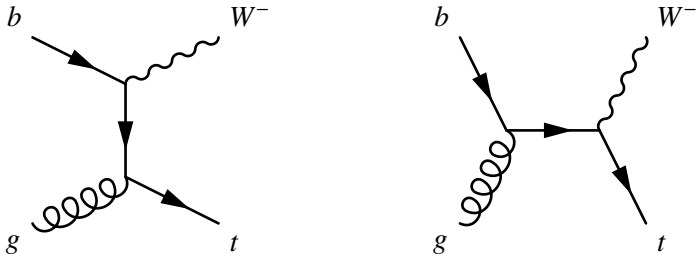

Figure 4.6: Feynman diagrams for the single-top production in the Wt channel.

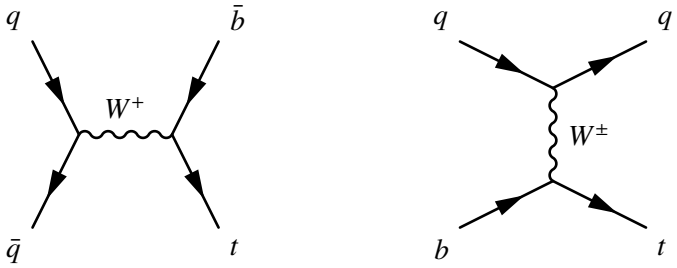

Figure 4.7: Feynman diagrams for the single top production in the s- and t-channels.

Diboson production

As shown in Figure 4.8, diboson productions include quark- and gluon-initiated processes. A Feynman diagram for diboson production is shown in Figure 4.8. The quark-initiated processes are simulated using SHERPA 2.2.1 [78, 100, 101] with the NNPDF3.0NNLO PDF set [84] while the gluon-initiated processes are simulated using SHERPA 2.2.2 with NNPDF3.0NLO [84]. As mentioned for the V + jets processes, these event generators calculate the matrix element including 0 or 1 additional parton with NLO (QCD) and 2 or 3 additional partons at LO (QCD). The diboson processes are normalized using the cross-sections provided by the SHERPA generators.

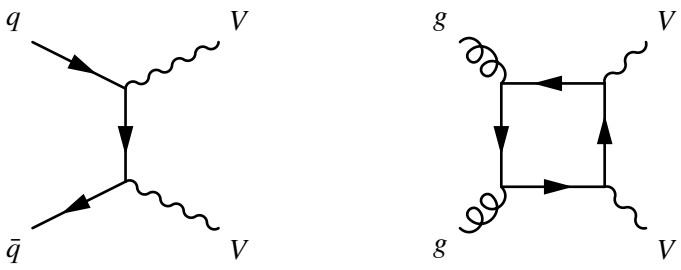

Figure 4.8: Feynman diagrams for the diboson production.

5 Object reconstruction and identification

The analysis relies on the reconstruction of objects such as electrons, muons, jets, and missing transverse momentum. The reconstruction of these objects is summarized in Sections 5.1-5.5. The analysis also much relies on the b-jet identification (*b-tagging*). The treatment of the b-jets are explained in Section 5.6.

5.1 Constituents of physics objects

5.1.1 Tracks

Charged particles left *hits* (charge such as ionized/excited electrons and holes/ions) in the inner detectors. The trajectories of these particles are reconstructed from these hits and referred to as *tracks*. The track reconstruction algorithm is presented in detail in Ref. [115] and outlined below.

The charge is often collected by multiple adjacent pixels or strips in Pixel and the Silicon Microstrip Tracker (SCT). This charge is grouped to form *clusters*. The clusters in Pixel and combination of the clusters from the *axial* and *stereo strips* in SCT represent three-dimensional measurements referred to as *space-points*. *Track seeds* are formed from three space-points. A combinatorial Kalman filter [116] is used to form *track candidates* by extrapolating the track seeds adding space-points in other Pixel and SCT layers. A track can be double-counted by two or more track candidates with the procedure above. This overlap is resolved to favor tracks with high quality defined with the number of clusters, missing space-points, χ^2 of the track fit, and the momentum of the tracks. Track candidates are rejected in this step if they fail any of the following conditions:

- $p_{\mathrm{T}} > 400$ MeV,
- $|\eta| < 2.5$,
- Minimum of 7 Pixel and SCT cluster,
- Maximum of either one shared Pixel clusters or two shared SCT clusters on the same layer,
- No more than two holes in Pixel and SCT,
- No more than one hole in Pixel,
- $|d_0| < 2.0\,\mathrm{mm}$,
- $|z_0 \sin\theta| < 3.0\,\mathrm{mm}$,

where d_0 and z_0 are defined using the position of the closest approach to the beam axis (*perigee*). d_0 is the distance between the perigee and the beam axis, and z_0 is the difference in the z coordinate between the perigee and a *primary vertex*. d_0 and z_0 are referred to as *transverse* and *longitudinal impact parameters*, respectively. To reconstruct primary vertices, these conditions for tracks are slightly modified [117] (see the next section). To improve the performance of the resolution of the overlap, clusters shared by multiple tracks are identified using a neural network algorithm [118]. Finally, precise track fitting is performed to reconstruct tracks.

5.1.2 Primary vertices

Particles emerge from the positions of initial pp collisions or decays of particles. These positions are reconstructed from tracks and referred to as *vertices*.

A vertex reconstruction algorithm is presented in Ref. [117] and outlined below. Tracks are selected with criteria described in Ref. [117]. A seed vertex position is selected from the selected tracks. The tracks and the seed position is used in vertex fitting to determine the position of the vertex. The vertex fitting is an iterative procedure that removes incompatible tracks in each iteration. The procedure is repeated to the remaining tracks that are not included in any of the vertices. The vertex with the highest sum of p_{T} of the tracks is defined as the *primary vertex*.

5.1.3 Topo-clusters

Topo-clusters [119] are constructed from the cells of the calorimeters. The topo-clusters are used as constituents of all objects that rely on measurements in the calorimeters: electrons (Section 5.2), jets (Section 5.4), and missing transverse energy (Section 5.5), in this thesis. Energies measured in the cells are calibrated assuming electromagnetically interacting particles. Cells with significant energies compared to electronic and pile-up noise are used to construct topo-clusters in the following way. Cells with the energies above a "seed" threshold form *proto-clusters* of topo-clusters. Neighboring cells of the proto-clusters with the energies above a "neighbor" threshold are added to the proto-clusters. The proto-clusters can be merged in this step. Neighboring cells of the proto-clusters with the energies above a "cell" threshold are included in the clusters. For topo-clusters densely reconstructed, it is desired that cell energies can be shared by two clusters in the following algorithm. Local maxima are searched for in the topo-clusters, and one topo-cluster can be split when it includes multiple maxima. The cells used in the previous steps are again added to the proto-clusters. Cells adjacent to more than one proto-clusters are shared by the two most energetic clusters and the cell energy is shared according to:

$$w_1 = \frac{e^{-d_1} E_1}{e^{-d_1} E_1 + e^{-d_2} E_2}, \; w_2 = \frac{e^{-d_2} E_2}{e^{-d_1} E_1 + e^{-d_2} E_2}, \tag{5.1}$$

where $E_{1,2}$ are the energies of the two proto-clusters and $d_{1,2}$ are the distances of the shared cell to the two proto-cluster centroids in the unit of a typical EM-shower scale ($\sim$ 5 cm).

5.2 Electrons

5.2.1 Reconstruction, identification, isolation and calibration of electrons

Electron reconstruction

Electrons are defined as combinations of tracks and clusters of energy deposits in the calorimeters called *super-clusters*. A detailed procedure is described in Ref. [120]. Only an outline is presented in this section.

Along with the reconstruction of electrons, a converted photon is defined as a cluster matched to a conversion vertex. An unconverted photon is defined as a cluster that is matched neither to an electron track nor to a conversion vertex. However, due to non-zero fake contribution to conversion vertices and imperfect efficiency of tracks, the discrimination between electrons and photons is ambiguous. The electrons and the photons are independently reconstructed allowing the overlap.

Energy deposits in the electromagnetic calorimeter are clustered employing the topo-clustering algorithm introduced in Section 5.1.3 instead of fixed-size clusters, which are used before [121]. There are additional requirements on topo-clusters for the electron reconstruction. Electron reconstruction uses EM topo-clusters that only take into account the energy from the electromagnetic calorimeter, except in $1.37 < |\eta| < 1.63$, where the energy measured in the presampler and the scintillator between the calorimeter cryostats is added. Clusters are considered to reconstruct electrons if their energies measured in the electromagnetic calorimeter (EM energy) are greater than 400 MeV. EM fraction, the ratio of the EM energy to the total measured energy, should be greater than 0.5 to suppress hadronic jets.

Although fixed-size clusters (called sliding-window [121]) are replaced with the topo-clusters, the fixed-size clusters are still used when tracks are searched for. A unit area of the EM calorimeter is defined as $\Delta\eta \times \Delta\phi = 0.025 \times 0.025$ corresponding to the granularity of the second layer of the EM calorimeter. The sliding-window algorithm creates clusters with a size of 3×5 in the unit area of the EM calorimeter.

Standard track reconstruction is performed in all the regions of the inner detector. The fixed-size clusters in the EM calorimeter compatible with EM showers define regions-of-interest (ROIs). If the standard tracking fails in an ROI, a modified pattern recognition algorithm based on the Kalman filter [122] is used to allowing 30% energy loss in the material. The found candidates in the ROIs are re-fitted using a Gaussian sum filter algorithm to improve the estimation of track parameters. The re-fitted tracks are then matched to the EM topo-clusters instead of the fixed-size clusters.

A super-cluster consists of a seed cluster and satellite clusters that exist close to the seed cluster. The satellite clusters for electrons are likely to be caused by bremsstrahlung. Super-clusters are constructed independently for electrons and photons with different criteria. To be a seed cluster for an electron, an EM topo-cluster must have $E_{\mathrm{T}} > 1$ GeV and matched to a track with at least four hits in the silicon detectors. The algorithm searches for satellite clusters around a seed cluster. A cluster is considered as a satellite if it is within a window with a size of $\Delta\eta \times \Delta\phi = 0.075 \times 0.125$ around the seed cluster's barycenter. For electrons, a cluster within a window $\Delta\eta \times \Delta\phi = 0.125 \times 0.300$ around a seed cluster is considered as a satellite if its best-matched track is also the best-matched track for the seed cluster. Cells from the presampler and the first three LAr calorimeter layers are assigned to super-clusters. The energy measured in the scintillator between the calorimeter cryostats in $1.4 < |\eta| < 1.6$ is also added.

After super-clusters are built, tracks are matched to the super-clusters instead of the ME topo-clusters. Since electrons and photons are reconstructed independently, one seed cluster can create both an electron and a photon. The procedure shown in Figure 5.1 is applied to discriminate electrons and photons. For objects clearly identified as electrons (photons), the results of the reconstruction for photons (electrons) are discarded. For ambiguous objects, both results for electron and photon are kept, and different analyses can design specific choice of objects.

Electron identification

A discriminant for the electron identification is constructed to separate prompt isolated electrons from hadronic jets, converted photons, and real electrons from heavy-flavor hadrons. Discriminating variables are summarized in Table 5.1, and can be categorized into groups:

- Leakage in the hadronic calorimeter
- Shower shape in the EM calorimeter
- Conditions about tracks
- Track-cluster matching

The distributions of the discriminating variables are smoothed by an adaptive kernel density estimator [123] implemented in the TMVA framework [124], and the probability density functions (PDFs) for signal and backgrounds are denoted by P_S and P_B. The likelihoods for the signal and the backgrounds are denoted by L_S and L_B and defined as:

$$L_{S(B)}(\mathbf{x}) = \prod_{i=1}^{n} P^i_{S(B)}(x_i), \tag{5.2}$$

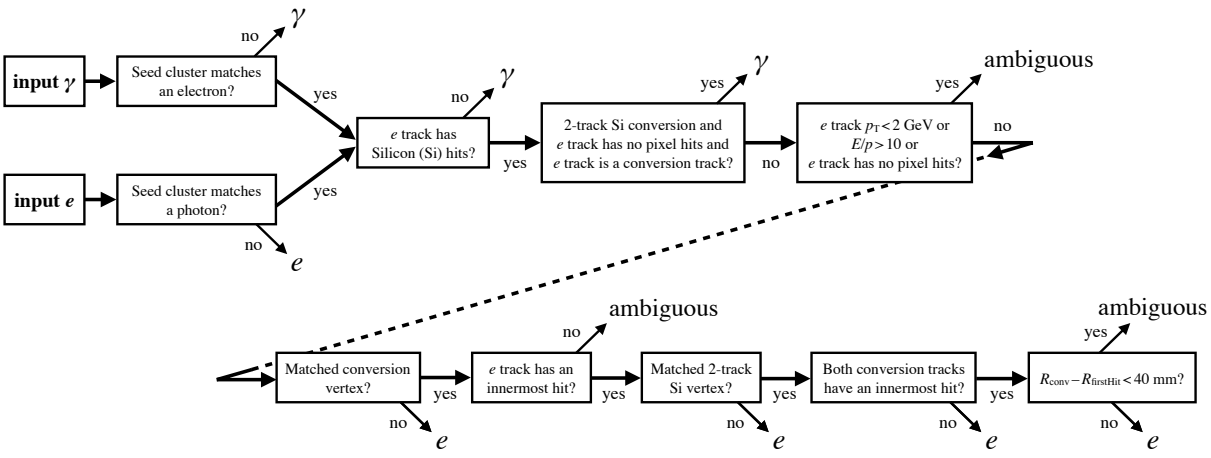

Figure 5.1: Flowchart for the resolution of the ambiguity of particles reconstructed as both electrons and photons. An innermost hit represents a hit in the closest layer of the Pixel to the beam-line. E/p is the ratio of the super-cluster energy to the measured momentum of the matched track. R_{conv} is the distance of the conversion vertex from the beam-line. R_{firstHit} is the radial position of the closest hit to the beam-line in tracks that form a conversion vertex. This figure is taken from Ref. [120].

where $P^i_{S(B)}(x_i)$ is the PDF associated to the ith discriminating variable x_i. The discriminant is defined as the logarithm of the ratio of the two likelihoods:

$$d_L = \log[L_S(\mathbf{x})/L_B(\mathbf{x})]. \tag{5.3}$$

Several cut points for the identification are defined with the likelihood discriminant and some other variables. *Loose*, *Medium* and *Tight* criteria are defined to maintain the efficiency of 93%, 88% and 80% on average, and the efficiency gradually increases in high p_{T}. These thresholds are optimized as a linear function of the number of primary vertices (N_{PV}) since the dependence of the efficiency on the pile-up is observed.

Electron isolation

Charged leptons are produced either by prompt productions such as decays of electroweak bosons or by non-prompt decays of heavy-flavor hadrons. Since the non-prompt leptons (from heavy-flavor hadrons) are produced within jets, activity around a candidate of charged lepton provides good discrimination between prompt and non-prompt contributions. Isolation variables used in the analysis are the following. The super-scripts "coneX" in the isolation variables denote a cone with the size of $R = 0.01 \times X$.

- $E_{\mathrm{T}}^{\mathrm{topoconeX}}$: sum of the transverse energies (E_{T}) of the topo-clusters in the given cone
- $p_{\mathrm{T}}^{\mathrm{coneX}}$: sum of the transverse momenta of the tracks satisfying the criteria in Table 5.2 in the given cone.
- $p_{\mathrm{T}}^{\mathrm{varconeX}}$: sum of the transverse momenta of the tracks satisfying the criteria in Table 5.2 in the given cone. The size of the cone is dependent on the p_{T} and expressed by $\min(10/p_{\mathrm{T}}[\mathrm{GeV}], X)$ for $p_{\mathrm{T}}^{\mathrm{varconeX}}$. Thus, the $p_{\mathrm{T}}^{\mathrm{varconeX}}$ uses the same cone size as the $p_{\mathrm{T}}^{\mathrm{coneX}}$ for low-p_{T} tracks.
- $p_{\mathrm{T}}^{\mathrm{varconeX}}$ _TightTTVALooseCone_pt1000: same as $p_{\mathrm{T}}^{\mathrm{varconeX}}$ except that only tracks loosely matched to the primary vertex are used.

These variables are summarized in Table 5.2.

Isolation working points are defined using the isolation variables in Table 5.2. Working points used in the analysis are called *FCLoose* and *FixedCutHighPtCaloOnly*, which are summarized in Table 5.3.

Efficiency calibration for electrons

The efficiency is split into parts as:

$$\epsilon_{\mathrm{total}} = \epsilon_{\mathrm{EMclus}} \times \epsilon_{\mathrm{reco}} \times \epsilon_{\mathrm{id}} \times \epsilon_{\mathrm{iso}} \times \epsilon_{\mathrm{trig}} = \left(\frac{N_{\mathrm{cluster}}}{N_{\mathrm{all}}}\right) \times \left(\frac{N_{\mathrm{reco}}}{N_{\mathrm{cluster}}}\right) \times \left(\frac{N_{\mathrm{id}}}{N_{\mathrm{reco}}}\right) \times \left(\frac{N_{\mathrm{iso}}}{N_{\mathrm{id}}}\right) \times \left(\frac{N_{\mathrm{trig}}}{N_{\mathrm{iso}}}\right). \tag{5.4}$$

$\epsilon_{\mathrm{EMclus}}$ is the efficiency of the reconstruction of EM cluster with respect to all the electrons in simulation. ϵ_{reco} is defined as the number of the reconstructed electrons divided by the number of the EM cluster candidates. Similarly, the efficiency of the identification, the isolation, and the trigger is defined by the other factors in Eq.5.4. The efficiency $\epsilon_{\mathrm{EMclus}}$ is determined entirely from MC simulation. The other factors of the efficiency are determined both in data and simulation employing a method called tag & probe using $Z \to ee$ events. The tag & probe method requires a pair of electron candidates, one of which is called "tag electron" and imposed requirements to achieve good purity of $Z \to ee$ events. More importantly, the tag

Table 5.1: Discriminating variables for the identification of electrons and photons. The transverse impact parameter d_0 is the distance of the perigee of a track from the beam-line. This table is taken from Ref. [120].

Category	Description	Name	Target object
Hadronic leakage	Ratio of E_{T} in the first layer of the hadronic calorimeter to E_{T} of the EM cluster (used over the ranges $\lvert\eta\rvert < 0.8$ and $\lvert\eta\rvert > 1.37$)	R_{had_1}	e/γ
	Ratio of E_{T} in the hadronic calorimeter to E_{T} of the EM cluster (used over the range $0.8 < \lvert\eta\rvert < 1.37$)	R_{had}	e/γ
EM third layer	Ratio of the energy in the third layer to the total energy in the EM calorimeter	f_3	e
EM second layer	Ratio of the sum of the energies of the cells contained in 3×7 $\eta\times\phi$ rectangle (measured in cell units) to the sum of the cell energies in a 7×7 rectangle, both centered in the most energetic cells	R_η	e/γ
	Lateral shower width, $\sqrt{(\sum E_i\eta_i^2)/(\sum E_i) - ((\sum E_i\eta_i)/(\sum E_i))^2}$, where E_i is the energy and η_i is the pseudorapidity of cell i and the sum is calculated in within a window 3×5 cells	w_{η_2}	e/γ
	Ratio of the sum of the energies of the cells contained in a 3×3 $\eta\times\phi$ rectangle (measured in cell units) to the sum of the cell energies in a 3×7 rectangle, both centred around the most energetic cell	R_ϕ	e/γ
EM first layer	Total lateral shower width, $\sqrt{(\sum E_i(i-i_{\mathrm{max}})^2)/(\sum E_i)}$, where i runs over all cells in a window of $\Delta\eta \approx 0.0625$ and i_{max} is the index of the highest-energy cell	$w_{s_{\mathrm{tot}}}$	e/γ
	Lateral shower width, $\sqrt{(\sum E_i(i-i_{\mathrm{max}})^2)/(\sum E_i)}$, where i runs over all cells in a window of 3 cells around the highest-energy cell	w_{s3}	γ
	Energy fraction outside core of three central cells, within seven cells	f_{side}	γ
	Difference between the energy of the cell associated with the second maximum, and the energy reconstructed in the cell with the smallest value found between the first and second maxima	ΔE_s	γ
	Ratio of the energy difference between the maximum energy deposit and the energy deposit in a secondary maximum in the cluster to the sum of these energies	E_{ratio}	e/γ
	Ratio of the energy measured in the first layer of the electromagnetic calorimeter to the total energy of the EM cluster	f_1	e/γ
Track conditions	Number of hits in the innermost pixel layer	$n_{\mathrm{innermost}}$	e
	Number of hits in the pixel detector	n_{pixel}	e
	Total number of hits in the pixel and SCT detectors	n_{Si}	e
	Transverse impact parameter relative to the beam-line	d_0	e
	Significance of transverse impact parameter defined as the ratio of d_0 to its uncertainty	$\lvert d_0/\sigma(d_0)\rvert$	e
	Momentum lost by the track between the perigee and the last measurement point divided by the momentum at the perigee	$\Delta p/p$	e
	Likelihood probability based on transition radiation in the TRT	eProbabilityHT	e
Track-cluster matching	$\Delta\eta$ between the cluster position in the first layer of the EM calorimeter and the extrapolated track	$\Delta\eta_1$	e
	$\Delta\phi$ between the cluster position in the second layer of the EM calorimeter and the momentum-rescaled track, extrapolated from the perigee, times the charge q	$\Delta\phi_{\mathrm{res}}$	e
	Ratio of the cluster energy to the measured track momentum	E/p	e

Table 5.2: Definitions of variables used to define isolation criteria for leptons.

Isolation variable	Definition	Used tracks
$E_{\mathrm{T}}^{\mathrm{topocone20}}$ ($E_{\mathrm{T}}^{\mathrm{topocone30}}$)	Sum of the transverse energies of the topo-clusters in the cone with the size $R = 0.2(0.3)$	-
$p_{\mathrm{T}}^{\mathrm{cone30}}$	Sum of the p_{T} of the tracks in the cone with the size $R = 0.3$	$p_{\mathrm{T}} > 1$ GeV, $\lvert z_0 \sin\theta \rvert < 3$ mm
$p_{\mathrm{T}}^{\mathrm{varcone20}}$ ($p_{\mathrm{T}}^{\mathrm{varcone30}}$)	Sum of the p_{T} of the tracks in the cone with the size $R = \max(0.2(0.3), 10/p_{\mathrm{T}}(\text{ GeV}))$	$p_{\mathrm{T}} > 1$ GeV, $\lvert z_0 \sin\theta \rvert < 3$ mm
$p_{\mathrm{T}}^{\mathrm{varcone30}}$ _TightTTVALooseCone_pt1000	Sum of the p_{T} of the tracks in the cone with the size $R = \max(0.3, 10/p_{\mathrm{T}}(\text{ GeV}))$	$p_{\mathrm{T}} > 1$ GeV, $\lvert z_0 \sin\theta \rvert < 3$ mm Loose vertex association

Table 5.3: Definitions of isolation criteria for electrons. The variables to define the criteria are summarized in Table 5.2.

Isolation name	cut
FCLoose	$E_{\mathrm{T}}^{\mathrm{topocone20}}/p_{\mathrm{T}}^{e} < 0.2$
	$p_{\mathrm{T}}^{\mathrm{varcone30}}$ _TightTTVALooseCone_pt1000$/p_{\mathrm{T}}^{e}$ <0.15
HighPtCaloOnly	$E_{\mathrm{T}}^{\mathrm{topocone20}} < \max(0.015 \times p_{\mathrm{T}}^{e}, 3.5)$ GeV

electron must fire the single electron trigger used for the data-taking to avoid a bias caused by the online event selection. The other electron candidates are called "probe electrons" and provide an unbiased sample of electrons that can be used to measure the efficiency. $J/\psi \rightarrow ee$ events are also used to measure the efficiency of the identification of low p_{T} electrons. These events can not be used for the measurement of the reconstruction efficiency because of large background with the "electron+EM cluster" selection and difficulty to design a trigger to collect events that can be used for the study.

Energy calibration for electrons

The differences in the energy scale and the resolution in between data and simulation are denoted by α_i and c_i as

$$E^{\mathrm{data,corrected}} = E^{\mathrm{data}}/(1+\alpha_i), \tag{5.5}$$

$$\left(\frac{\sigma_E}{E}\right)^{\mathrm{MC,corr}} = \left(\frac{\sigma_E}{E}\right)^{\mathrm{MC}} \oplus c_i, \tag{5.6}$$

where i corresponds to different regions of η, and $\oplus$ denotes the sum in quadrature. The corrections to the mass scale and the resolution are expressed as

$$m_{ij}^{\mathrm{data,corr}} = m_{ij}^{\mathrm{data}}/(1+\alpha_{ij}), \tag{5.7}$$

$$(\sigma_m/m)_{ij}^{\mathrm{MC,corr}} = (\sigma_m/m)_{ij}^{\mathrm{MC}} \oplus c_{ij}, \tag{5.8}$$

where $\alpha_{ij} = (\alpha_i + \alpha_j)/2$ and $c_{ij} = (c_i \oplus c_j)/2$. α_{ij} and c_{ij} are determined by a fit in each (i, j) η-region. To determine each α_i and c_i, a simultaneous fit in all categories is performed.

5.2.2 Selection criteria for electrons in the analysis

The analysis presented in this thesis defines three selection criteria called *VH-Loose*, *ZH-Signal* and *WH-Signal*, which are explained below. These criteria are summarized in Table 5.4.

VH-Loose electrons are defined to maximize the efficiency of the electron reconstruction. The requirements are listed below:

- p_{T} >7 GeV and $|\eta| < 2.47$.
- Significance of the impact parameter d_0 ($d_0/\sigma(d_0)$) is smaller than 5.0.
- $|\Delta z_0 \sin\theta| < 0.5$ mm to reject pile-up and cosmic muons.
- *Loose* criteria of the likelihood-based discriminant.
- *FCLoose* isolation criteria.

ZH-Signal electrons are requested in the 2-lepton channel (introduced in Section 6.3). In addition to the *VH-Loose* criteria, p_{T} >27 GeV is required corresponding to the threshold of the single electron trigger.

WH-Signal criteria are tighter requirements needed for the 1-lepton channel (introduced in Section 6.3) to suppress the multijet background. The *Tight* likelihood identification and the *FixedCutHighPtCaloOnly* isolation are required.

5.3 Muons

5.3.1 Reconstruction, identification, isolation and calibration of muons

Preparation of reconstructed muons for analyses is presented in detail in Ref. [125]. Only an outline is presented in this section.

Table 5.4: Definitions of the selection criteria for electrons used in the analysis.

Criteria	VH-Loose	ZH-Signal	WH-Signal
p_{T}	> 7 GeV	> 27 GeV	> 27 GeV
η	$\lvert\eta\rvert < 2.47$	$\lvert\eta\rvert < 2.47$	$\lvert\eta\rvert < 2.47$
ID	Loose	Loose	Tight
d_0^{sig} wrt to the beam-line	<5	<5	<5
$\lvert\Delta z_0 \sin\theta\rvert$	<0.5 mm	<0.5 mm	< 0.5 mm
Isolation	FCLoose	FCLoose	FixedCutHighPtCaloOnly

Reconstruction in the Muon Spectrometer (MS)

Three layers of the MS provide information on local trajectories (*segments*) of muons. In each layer of the Monitored Drift Tubes (MDTs) and the trigger chambers, i.e. Resistive Plate Chambers (RPCs) and Thin Gap Chambers (TGCs), a Hough transformation is performed to search for hits aligned on a trajectory. To reconstruct a segment, a straight-line fit is performed to the hits in each layer. The MDTs provide precision measurements of tracks in the η coordinate, while the trigger chambers provide measurements both in the η and ϕ coordinates. Segments in the Cathode Strip Chambers (CSCs) are measured both in the η and ϕ directions.

Track candidates are built by fitting the hits in the segments using a global χ^2. A track candidate is accepted if the χ^2 of the fit satisfies a criterion. Hits that have a large contribution to the global χ^2 are removed from the track. Conversely, hits that are not included in the segments can also be used if they are consistent with the track candidate.

Combined muon reconstruction

The combined reconstruction of muons uses the inner detector (ID) as well as the MS. As explained below, there are four types of muons: *combined muons, segment-tagged muons, calorimeter-tagged muons* and *extrapolated muons*.

Combined muon Independent tracks are reconstructed in the ID and the MS. The hits of tracks in the ID and MS tracks are refitted.

Segment-tagged muon A track in the ID is extrapolated to the MS. If the track is matched to at least one segment in the MDTs or the CSCs, the track is classified as a *segment-tagged* muon.

Calorimeter-tagged muon If a track in the ID matched to an energy deposit in the calorimeters consistent with a minimum-ionizing particle, the track is classified as a *calorimeter-tagged* muon. This reconstruction method has the lowest purity of the four types, but it provides muon reconstruction in η-ϕ regions where the muon chambers are only partially instrumented.

Extrapolated muons An MS track is extrapolated backward to the interaction point taking into account the energy deposit in the calorimeters. If the origin of the track is compatible with the interaction point, the MS track is thought of as an *extrapolated muon*. This reconstruction algorithm requires segments in at least two layers of the MS. Extrapolated muons are used in $2.5 < |\eta| < 2.7$ which is not covered by the ID, but where the MS can provide tracks.

When different reconstruction methods share an ID track, which likely to mean a muon is reconstructed as different types, priority is given to combined, then segment-tagged, and finally calorimeter-tagged. An extrapolated muon is prioritized when it provides a better fit quality and uses a larger number of hits than other types.

Muon identification

To obtain good purity of muons, the corresponding ID tracks must satisfy the following conditions:

- The track includes at least one Pixel hit.
- The track includes at least five SCT hits.
- The track has fewer Pixel or SCT holes than three. An active sensor is considered as a hole when a track candidate traverses but it has no hits.
- At least 10% of the TRT hits originally included in the track are used in the final fit. This criterion is only considered in the acceptance of the TRT, $0.1 < |\eta| < 1.9$.

With the requirements on MS tracks in addition to the requirements on ID tracks above, four identification criteria, *Loose*, *Medium*, *Tight* and *High-*p_T are prepared. The *Loose* and *Medium* criteria are used in the analysis and explained in this section.

The *Medium* criteria are defined to minimize the systematic uncertainties associated with the reconstruction and the calibration [1]. Only combined and extrapolated muons are used for the criteria. Combined muons are required to have three or more hits in at least in two MDT or CSC layers except in $|\eta| < 0.1$ where the coverage of the MDTs are limited. There are several criteria used to quantify the quality of muon candidates, but only the parameter, q/p *significance* is used to define the *Medium* criteria, where the q/p significance should be smaller than 7.

The *Loose* criteria are defined to maximize the efficiency. All (combined and extrapolated) muons accepted by the medium criteria are included in the loose criteria. Segment-tagged and calorimeter-tagged muons are also accepted but restricted in the region $|\eta| < 0.1$.

Muon isolation

The isolation for muons uses a track-based variable, $p_T^{varcone30}$, and a calorimeter-based variable, $E_T^{topocone30}$, which are already introduced in Section 5.2 for the isolation of electrons. The analysis presented in this thesis uses *FixedCutLoose* and *FixedCutHighPtTrackOnly* criteria for the isolation of muons. Requirements defined by these criteria are summarized in Table 5.5.

Table 5.5: Definition of isolation criteria for muons. The variables used to define the criteria are summarized in Table 5.2.

Isolation name	cut
FixedCutLoose	$E_{\mathrm{T}}^{\mathrm{topocone20}}/p_{\mathrm{T}}^{\mu} < 0.3$ $p_{\mathrm{T}}^{\mathrm{varcone30}}/p_{\mathrm{T}}^{\mu} < 0.15$
FixedCutHighPtTrackOnly	$p_{\mathrm{T}}^{\mathrm{cone20}} < 1.25$ GeV

[1] It is not clearly explained in references, but it is interpreted that too loose criteria bring large background contribution in the calibration while too tight requirements cause systematic uncertainties relevant to the modeling of processes and detectors used in the calibration.

Efficiency calibration for muons

The tag & probe method using $Z \to \mu\mu$ ($J/\psi \to \mu\mu$) events is employed to measure the efficiency of the reconstruction of muons. The method requires a pair of muon candidates, one of which is called "tag muon" and imposed requirements to ensure good purity for the $Z \to \mu\mu$ (or $J/\psi \to \mu\mu$) process. More importantly, the tag muons must fire the single muon trigger used in the data-taking to avoid a bias caused by the online event selection. The other muon candidate is called "probe muon", and a track in the ID or a calorimeter-tagged muon (a track in the MS) is used to measure the efficiency of the track reconstruction in the MS (ID). While the purity of the probe muons is good due to the requirement on the tag muons and the invariant mass of the pair, the probes still provide an unbiased sample of muons that can be used in the measurement. $Z \to \mu\mu$ and $J/\psi \to \mu\mu$ events are used for muons with $p_{\mathrm{T}} > 10$ GeV and $p_{\mathrm{T}} < 10$ GeV, respectively.

Since the region, $|\eta| > 2.5$, is not covered by the ID, the measurement of the reconstruction efficiency of the MS track using ID tracks is not possible. To estimate the efficiency of the extrapolated muons in this region, the ratio of the number of reconstructed muons in $|\eta| > 2.5$ to $2.2 < |\eta| < 2.5$ is calculated both for data and simulation applying all the known corrections for the efficiency in $|\eta| < 2.5$. The correction factor (scale factor) for the efficiency is derived as the double ratio of the two ratios.

Momentum calibration for muons

The momentum scales of muons in ID or MS are corrected according to

$$p_{\mathrm{T}}^{\mathrm{Cor,Det}} = \frac{p_{\mathrm{T}}^{\mathrm{MC,Det}} + \sum_{n=0}^{1} s_n^{\mathrm{Det}}(\eta,\phi)\left(p_{\mathrm{T}}^{\mathrm{MC,Det}}\right)^n}{1 + \sum_{m=0}^{2} \Delta r_m^{\mathrm{Det}}(\eta,\phi)\left(p_{\mathrm{T}}^{\mathrm{MC,Det}}\right)^{m-1} g_m}, \tag{5.9}$$

where "Det" denotes ID or MS, and $p_{\mathrm{T}}^{\mathrm{MC,Det}}$ is the uncorrected transverse momentum in simulation, s_n^{Det} and $\Delta r_m^{\mathrm{Det}}$ describe the correction of the momentum scale and the resolution smearing, and g_m are normally distributed random numbers for smearing. s_n^{Det} and $\Delta r_m^{\mathrm{Det}}$ are determined by a maximum-likelihood fit using $m_{\mu\mu}^{\mathrm{Det}}$ and $\rho = (p_{\mathrm{T}}^{\mathrm{MS}} - p_{\mathrm{T}}^{\mathrm{Cor,ID}})/p_{\mathrm{T}}^{\mathrm{Cor,ID}}$ distributions.

5.3.2 Selection criteria for muons in the analysis

The analysis defines three selection criteria for muons, *VH-Loose*, *ZH-Signal* and *WH-Signal*, which are summarized in Table 5.6 and explained below.

VH-Loose is a baseline selection for muons that maximizes the efficiency. This requires the following:

- $p_{\mathrm{T}} > 7$ GeV and $|\eta| < 2.7$.
- The significance of the transverse impact parameter d_0 ($|d_0|/\sigma(d_0)$) is smaller than 3.0.
- $|\Delta z_0 \sin\theta| < 0.6$ mm to reject pile-up and cosmic muons.
- The *Loose* identification criteria.
- The *FixedCutLoose* isolation criteria.

ZH-Signal muons are used in the 2-lepton channel (introduced in Section 6.3). This selection requires $p_{\mathrm{T}} > 27$ GeV and $|\eta| < 2.5$ in addition to the *VH-Loose* selection. These requirements ensure that a focused muon fires the trigger used for online event selection.

WH-Signal muons are used in the 1-lepton channel (introduced in Section 6.3). These muons are required to have $p_{\mathrm{T}} > 25$ GeV and $|\eta| < 2.5$. The *Medium* identification criteria and the *FixedCutHighPtTrackOnly* isolation criteria must be satisfied.

5.4 Jets

After the reconstruction of the topo-clusters, they are clustered to form jets using the *anti-k_t algorithm* [126] implemented in the FastJet package [127]. In the algorithm, distance parameters are defined as

$$d_{ij} = \min(k_{ti}^{2p}, k_{tj}^{2p}) \frac{\Delta_{ij}^2}{R^2}, \tag{5.10}$$

$$d_{iB} = k_{tj}^{2p}, \tag{5.11}$$

where $\Delta_{ij}^2 = (y_i - y_j)^2 + (\phi_i - \phi_j)^2$ and k_{ti}, y_i and ϕ_i is the transverse momentum, the rapidity and the azimuthal angle of the ith constituent. d_{ij} is the distance of the ith and jth constituents. d_{iB} is the distance of the ith constituent to the beam (B). The anti-k_t algorithm searches for jets in the following way. Two constituents with the smallest distance are merged into one new constituent. The procedure is repeated until no constituent is left in the event.

The anti-k_t algorithm is realized by setting $p = -1$ in the Eqs. 5.10 and 5.11, and it is widely adopted in physics analyses in the ATLAS experiment since it has following good characteristics. Kinematic properties of jets, such as the center and the area of jets, are resilient to the soft parton emission (*infrared-safe*), and collinear splitting of partons (*collinear-safe*).

A technique called *Jet Vertex Tagger (JVT)* [128, 129] are used to discriminate hard-scattering jets from pile-up jets. The probability of a jet to be a hard-scattering jet rather than a pile-up jet is derived as a function of two variables using information of tracks, *corrJVF* and R_{pT}:

$$\mathrm{corrJVF} = \frac{\sum_m p_{\mathrm{T},m}^{\mathrm{track}}(\mathrm{PV}_0)}{\sum_l p_{\mathrm{T},l}^{\mathrm{track}}(\mathrm{PV}_0) + \frac{\sum_{n\geq 1}\sum_l p_{\mathrm{T},l}^{\mathrm{track}}(\mathrm{PV}_n)}{k \cdot n_{\mathrm{track}}^{\mathrm{PU}}}}, \tag{5.12}$$

Table 5.6: Definitions of the selection criteria for muons used in the analysis.

Criteria	VH-Loose	ZH-Signal	WH-Signal
p_{T}	> 7 GeV	> 27 GeV	> 25 GeV
η	$\|\eta\| < 2.7$	$\|\eta\| < 2.5$	$\|\eta\| < 2.5$
ID	Loose	Loose	Medium
d_0^{sig} wrt to the beam-line	<3	<3	<3
$\|\Delta z_0 \sin\theta\|$	<0.5 mm	<0.5 mm	< 0.5 mm
Isolation	FixedCutLoose	FixedCutLoose	FixedCutHighPtTrackOnly

$$R_{\mathrm{pT}} = \frac{\sum_k p_{\mathrm{T},k}^{\mathrm{track}}(\mathrm{PV}_0)}{p_{\mathrm{T}}^{\mathrm{jet}}}, \tag{5.13}$$

where PV_0 and PV_n are the primary and other vertices, respectively. By using tracks, jets can be associated with the primary vertices. Thus, it provides some discrimination between hard-scattering and pile-up jets. The likelihood associated with the probability is used as a discriminant. JVT is applied to jets with $p_\mathrm{T} < 120$ GeV and $|\eta| < 2.5$ where information from the ID is available.

5.4.1 Energy correction for jets

A generic calibration chain for the energy of jets is presented in detail in Ref. [130, 131]. The procedure performs *origin correction*, *pileup correction*, *jet energy scale calibration* and *global sequential calibration*. Those steps are outlined in this section.

The origin correction recalculates the four-momenta of jets to use the primary vertices as the origin instead of the center of the detector. This improves the resolution in η keeping the energy constant.

The Pile-up correction is broken down into an *area-based correction* and *residual corrections*. The area-based correction uses the momentum density ρ of pile-up that is explained below. Jets are reconstructed with the k_t algorithm ($p = 1$ in Eqs. 5.10 and 5.11) with the radius parameter $R = 0.4$ including low p_T jets. The area A of a jet is calculated with a ghost-association algorithm [132] where virtual particles with 0 momenta are included in the jet and the area is estimated from the number of particles ghost-associated with the jet. The momentum density ρ is defined as the median of p_T/A of the jets in the event. The area-based pile-up correction is expressed as:

$$p_{\mathrm{T}}^{\mathrm{corr}} = p_{\mathrm{T}}^{\mathrm{reco}} - \rho \times A, \tag{5.14}$$

where A is the area of the corrected jet.

Residual pile-up dependence in the p_T response is observed. The effects are parametrized by the number of primary vertices (N_PV) and the average number of hard-scattering per bunch crossing (μ), which correspond to the *in-time pile-up* and the *out-of-time pile-up*, respectively. The final pile-up correction including the area based correction is expressed by:

$$p_{\mathrm{T}}^{\mathrm{corr}} = p_{\mathrm{T}}^{\mathrm{reco}} - \rho \times A - \alpha \times (N_{\mathrm{PV}} - 1) - \beta \times \mu, \tag{5.15}$$

where α and β are fitted parameters dependent on $|\eta|$.

After the origin and pile-up corrections, jets are corrected using the *truth jets*. The truth jets are defined with the anti-k_t algorithm run on truth semi-stable particles (with the lifetimes longer than 10 ps) including neither muons nor neutrinos and with the radius parameter $R = 0.4$. The energy and the η of jets are corrected. The correction factor is derived as a function of the energy and $|\eta_{\mathrm{det}}|$. $|\eta_{\mathrm{det}}|$ is the direction of a jet before the origin correction since the η dependence is caused by hardware such as the gap of the calorimeter technologies and the non-uniform granularity of the calorimeters.

After the calibration of the jet energy scale, residual dependencies of the response on features of jets are observed. For example, quark-initiated jets often include hadrons that carry a higher fraction of the energy, while gluon-initiated jets typically contain more particles with low momenta, which leads to lower responses of the calorimeters and wider transverse profiles. Five observables are found that they improve the resolution of jet energies, and they are:

- The fraction of jet energy measured in the first layer of the hadronic Tile calorimeter (used in $|\eta_{\text{det}}| < 1.7$).
- The fraction of jet energy measured in the third layer of the electromagnetic LAr calorimeter (used in $|\eta_{\text{det}}| < 3.5$).
- The number of tracks with $p_{\text{T}} > 1$ GeV that are ghost-associated with the jet (used in $|\eta_{\text{det}}| < 2.5$)
- The average p_{T}-weighted transverse distance in the η-ϕ plane between the jet axis and tracks with $p_{\text{T}} > 1$ GeV that are ghost associated with the jet (used in $|\eta_{\text{det}}| < 2.5$)
- the number of muon track segments, $n_{\text{segements}}$, ghost-associated with the jet (used in $|\eta_{\text{det}}| < 2.7$). The $n_{\text{segements}}$ is a proxy of punch-through particles in jets, which are not absorbed in the calorimeter.

The sequential correction based on the five observables is called *Global Sequential Calibration (GSC)*.

5.4.2 Selection criteria of jets in the analysis

Jets reconstructed in the following acceptance are used in the analysis presented in this thesis. Jets in the central region, $|\eta| < 2.5$, are required to have $p_{\text{T}} > 25$ GeV and the medium JVT score that gives 92% efficiency for hard-scattering jets. Jets in the forward region, $|\eta| > 2.5$, are required to have $p_{\text{T}} > 30$ GeV. The higher requirement on p_{T} is necessary to suppress pile-up jets because inner detector tracks and JVT are not available in the forward region. The selection criteria are summarized in Table 5.7.

5.5 Missing transverse energy

Neutrinos do not interact with the detector. The experimental signature of these neutrinos is missing momentum in the transverse plane since the vector sum of the transverse momenta (p_{T}) of all particles including the neutrinos is zero. The magnitude of the missing p_{T} is referred to as *missing transverse energy* ($E_{\text{T}}^{\text{miss}}$).

$E_{\text{T}}^{\text{miss}}$ is defined as the magnitude of the negative vector sum of p_{T} of *hard objects* and *track-based fort term* [135]. The hard objects consist of electrons, muons, photons, and τ leptons. The electrons and muons are selected with the VH-Loose criteria defined in Tables 5.4 and 5.6. The photon and hadronic τ leptons

Table 5.7: Selection criteria for jets used in the analysis. Jet cleaning refers to a procedure that removes jets in regions with either calorimeter noise or beam-induced fake jets [133, 134].

Jet Category	Selection Requirements
Forward Jets	jet cleaning $p_{\text{T}} > 30\,\text{GeV}$ $2.5 \leq \|\eta\| < 4.5$
Central Jets	jet cleaning $p_{\text{T}} > 20\,\text{GeV}$ $\|\eta\| < 2.5$ JVT cut corresponding to 92% efficiency for $p_{\text{T}} < 120\,\text{GeV}$

are selected with the criteria described in Ref. [135]. Criteria for jets are slightly different from Table 5.7, and summarized in Table 5.8. The track-based soft term is defined as the negative vector sum of tracks not matched to the hard objects. The tracks are included if the criteria in Table 5.9 is satisfied.

5.6 Reconstruction of *b*-jets

5.6.1 *b*-tagging discriminant

The *b*-tagging algorithm provides a multivariate discriminant that uses the impact parameters of tracks, the secondary vertex, and the relationship between the primary and secondary vertices [136]. The final discriminant is a BDT trained with the information above, whose distributions are shown in Figure 5.2. The discriminant for *b*-tagging is named *MV2c10*.

5.6.2 Pseudo-continuous *b*-tagging

The analysis uses the cut on the discriminating variable (MV2c10) for each jet. The cut is defined as the quantile of 70%, jets with greater MV2c10 values are classified as *b*-jets. This criterion is referred to as 70% *working point (WP)*. Since this approach recognizes all jets with MV2c10 values greater than the quantile as *b*-jets, this is also called *cumulative b-tagging* in contrast to the approach introduced in the next paragraphs.

In addition to the cut on the MV2c10 discriminant on jets, the analysis further uses the MV2c10 values to separate backgrounds including *c*-jets. Since the calibration of the full continuous spectrum of the MV2c10 discriminant is not easy, a compromised approach called *pseudo-continuous b-tagging* is adopted

Table 5.8: Selection criteria for jets used in the calculation of the $E_{\mathrm{T}}^{\mathrm{miss}}$.

Jet Category	Selection Requirements
Forward Jets	jet cleaning $p_{\mathrm{T}} > 30\,\mathrm{GeV}$ $2.4 \leq \lvert\eta\rvert < 4.5$
Central Jets	jet cleaning $p_{\mathrm{T}} > 20\,\mathrm{GeV}$ $\lvert\eta\rvert < 2.5$ JVT cut corresponding to 92% efficiency for $p_{\mathrm{T}} < 60\,\mathrm{GeV}$

Table 5.9: Selection criteria for tracks used in the calculation of the track-based $E_{\mathrm{T}}^{\mathrm{miss}}$ soft term. d_0 and z_0 are the transverse and longitudinal impact parameters, and the θ is the direction of tracks. $\sigma(d_0)$ is the resolution of d_0.

Transverse momentum	$p_{\mathrm{T}} > 0.4\,\mathrm{GeV}$
Pseudo rapidity	$\lvert\eta\rvert < 2.5$
Significance of the transverse impact parameter	$\left\lvert\frac{d_0}{\sigma(d_0)}\right\rvert < 2$
Longitudinal impact parameter	$\lvert z_0 \sin\theta\rvert < 3.0\,\mathrm{mm}$

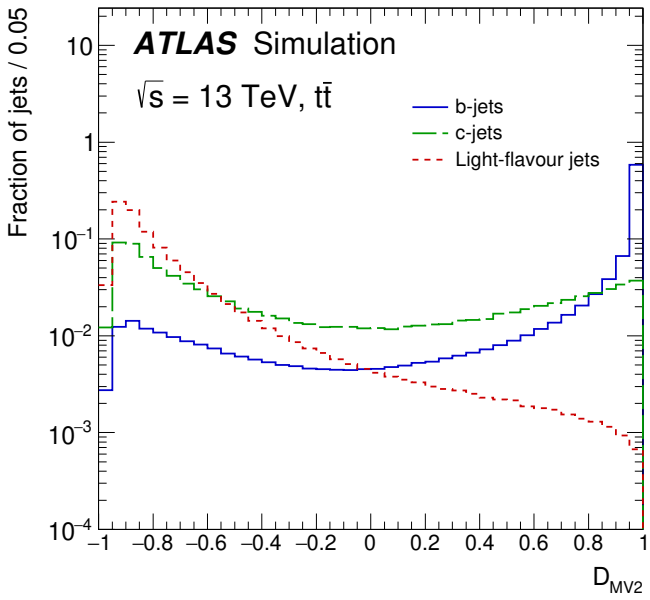

Figure 5.2: Distributions of the b-tagging discriminant (MV2c10) for jets with indicated flavors in $t\bar{t}$ simulated events.

as the following. The *quantiles* of the MV2c10 discriminant for 100%, 85%, 77%, 70%, 60% and 0% are derived, and the bins of the discriminant is defined with the quantiles as the intervals [100,85], [85,77], [77,70], [70,60], [60,0]. The distribution of the binned MV2c10 value is shown in Figure 5.3. Jets are classified into the bins according to their MV2c10 values and the bins [70,60] and [60,0] are used in the analysis. The binned scores ([70,60] or [60,0]) are used to separate backgrounds including c-jets.

5.6.3 Truth *b*-tagging

c- and light-jets are strongly suppressed by the b-tagging algorithm. Thus, the statistical uncertainty of MC events is large. This is problematic in the training of a BDT discriminant, and the uncertainty caused by the MC statistical error has a large contribution to the measurement. To increase the statistics of such processes, a method called *truth b-tagging* is introduced in contrast to *direct b-tagging* which cuts jets and events based on the MV2c10 values. In this method, events are not rejected even if they are not tagged, but the method accepts them by applying event weights based on the probability of the events to be tagged. The probability is derived from the b-tagging efficiency per jet as a function of p_{T} and η of the jets.

Since the implementation of the truth b-tagging is slightly technical, the details of the algorithm and the efficiency maps are presented in Appendix B.

5.6.4 Energy correction for *b*-jets

The Global Sequential Calibration is not optimal for b-jets since they show unique features of b-hadrons such as the semi-leptonic decay, the secondary vertex, and the mass of the hadrons. Therefore, dedicated

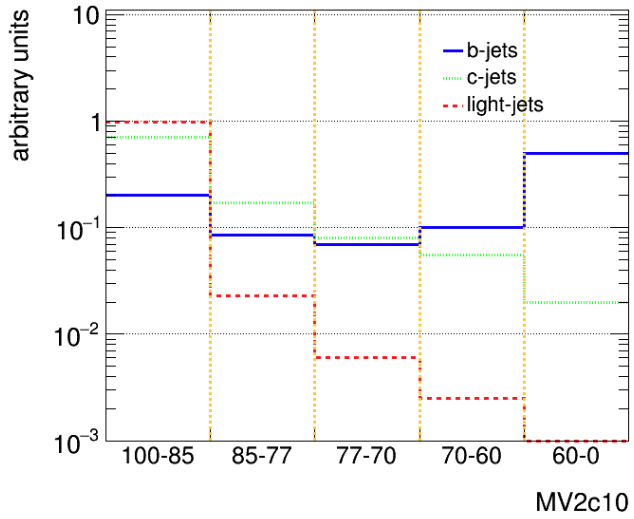

Figure 5.3: Binned distributions of the *b*-tagging discriminant (MV2c10) for *b*-, *c*- and light-jets. The bins "X-Y" indicate the intervals of the discriminant defined with the X and Y% quantiles.

energy corrections are applied for *b*-jets to improve the resolution of the invariant mass of the Higgs boson candidates. The correction procedure employs *muon-in-jet correction*, *PtReco correction* and *Kinematic Fit*, which are described in this section.

Muon-in-jet correction

About 10% of *b*-jets contain reconstructed muons from the semi-leptonic decay of the *b*-hadrons. Since muons pass through the calorimeters giving only a few GeV of their energies, such events show lower reconstructed energy. The momenta of such muons can be added to the *b*-jets to recover the true energy. The procedure is called *muon-in-jet correction*.

The selection of muons used in the muon-in-jet correction is as follows:

- $p_{\mathrm{T}} > 4$ GeV, $|\eta| < 2.7$
- Medium quality (Section 5.3)
- $\Delta R(j, \mu) < \min(0.4, 0.04 + 10/p_{\mathrm{T}}^{\mu}\ (\mathrm{GeV}))$
- The closest muon to the *b*-jet

PtReco correction

p

b-hadrons have significant mass and longer lifetime. These features lead to the p_{T}-dependent out-of-cone effect where the energy leaks out of the cone of the jet. The semi-leptonic decays of *b*-hadrons contain neutrinos which make a part of the energy of the original hadrons invisible. Thus, an energy correction factor dependent on the p_{T} and the decay mode improves the resolution of the invariant mass of Higgs

boson candidates. The correction factor scales the energies of b-jets after the muon-in-jet correction to *truth jets* that are formed with truth particles *including muons and neutrinos*. This energy correction is called *PtReco correction*, and applied in the 0- and 1-lepton channels. The 2-lepton channel utilizes *kinematic fitting* introduced in the next section.

Kinematic Fitting (KF)

In the 2-lepton channel, all objects are reconstructed in signal events. Thus, it is possible to impose the momentum balance of the objects in the transverse plane. The typical resolution of the p_{T} measurement for leptons is $\sim 1\%$, while the typical resolution for jets is $\sim 10\%$. Thus, the requirement of the p_{T} balance means that it is possible to correct and constrain the energies of the b-jets. This correction is called *kinematic fit (KF)*. The correction is implemented as the minimization of the negative log-likelihood:

$$-2\ln L = \sum_{\text{objects}} \frac{(p_{\mathrm{T}} - p_{\mathrm{T}}^{\mathrm{fit}})^2}{\sigma^2} - \sum_{\text{jets}} 2\ln L(p_{\mathrm{T}}, p_{\mathrm{T}}^{\mathrm{fit}}) + \frac{\sum_{\text{objects}}(p_x^2 + p_y^2)}{\sigma^2_{\text{balance}}} + 2\ln\{(m_{\ell\ell}^2 - m_Z^2)^2 + m_Z^2\Gamma_Z^2\}. \quad (5.16)$$

In Eq. 5.16, the p_{T} of all the final state objects are corrected. The first term represents the resolution of each object. The second term expresses constraints on the energies of the b-jets. They are derived from the distribution of $E_{b\text{-jet}}^{\text{muon-in-jet}} - E_{b\text{-jet}}^{\text{truth}}$, thus the term allows the energies to be scaled up to those of truth jets, which take into account the out-of-cone effect and the missing energy carried by neutrinos. The third term represents the constraints required by the p_{T} balance. The fourth term expresses the constraint on the p_{T} of the leptons imposing the Z mass.

The KF is applied to events with 2 or 3 jets. But for events with more than 3 jets, the PtReco correction is used since no improvement is observed by using the KF.

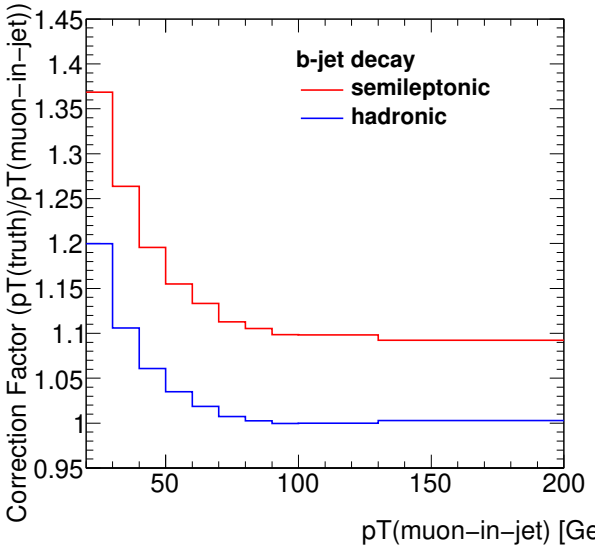

Figure 5.4: Correction factor for the PtReco correction is shown for b-jets that include a hadronic (blue) and semi-leptonic (red) decay of b-hadrons. The correction factor scales muon-in-jet corrected p_{T} of a b-jet up to the p_{T} of truth jets that include muons and neutrinos so that it recovers the missing energy either carried by the leptons (visible in the red line) or the energy that leaks out of jets (visible in the low p_{T} region).

Performance

The resolution of the invariant mass of the pair of b-jets in signal events ($qq \rightarrow ZH$ and $gg \rightarrow ZH$) is shown in Figures 5.5 and 5.6. For example, the resolution after the corrections is 16.3 (GSC), 14.3 (muon-in-jet), 13.8 (PtReco) and 9.5 GeV (KF) for the $qq \rightarrow ZH$ signal with 2 jets and $150 \leq p_{\mathrm{T}}^{V} < 250$ GeV.

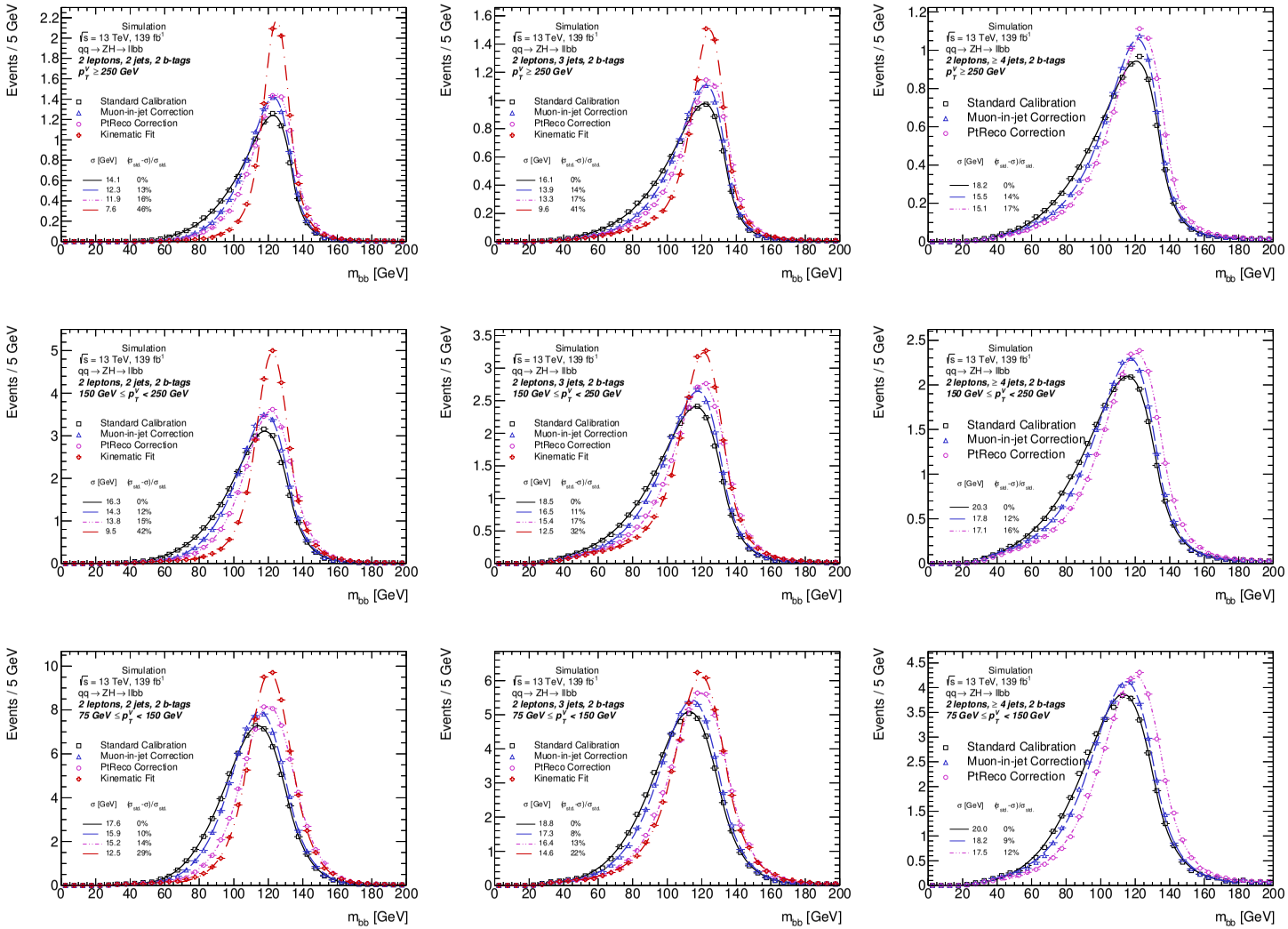

Figure 5.5: Resolution in the invariant mass of a pair of b-jets ($m_{b\bar{b}}$) in the $qq \rightarrow ZH \rightarrow \ell^+\ell^- b\bar{b}$ signal after each b-jet energy correction. As indicated in the plots, they show the distributions of $m_{b\bar{b}}$ in events with 2 jets (left), 3 jets (middle), and more than 3 jets (right); $p_{\mathrm{T}}^V \geq 250$ GeV (top), $150 \leq p_{\mathrm{T}}^V < 250$ GeV (middle), and $75 \leq p_{\mathrm{T}}^V < 150$ GeV (bottom). The black, blue, purple, and red plots show the distributions after GSC, muon-in-jet, PtReco, and KF, respectively. Each histogram is fitted with a Bukin function, and the extracted resolution is reported in the plots.

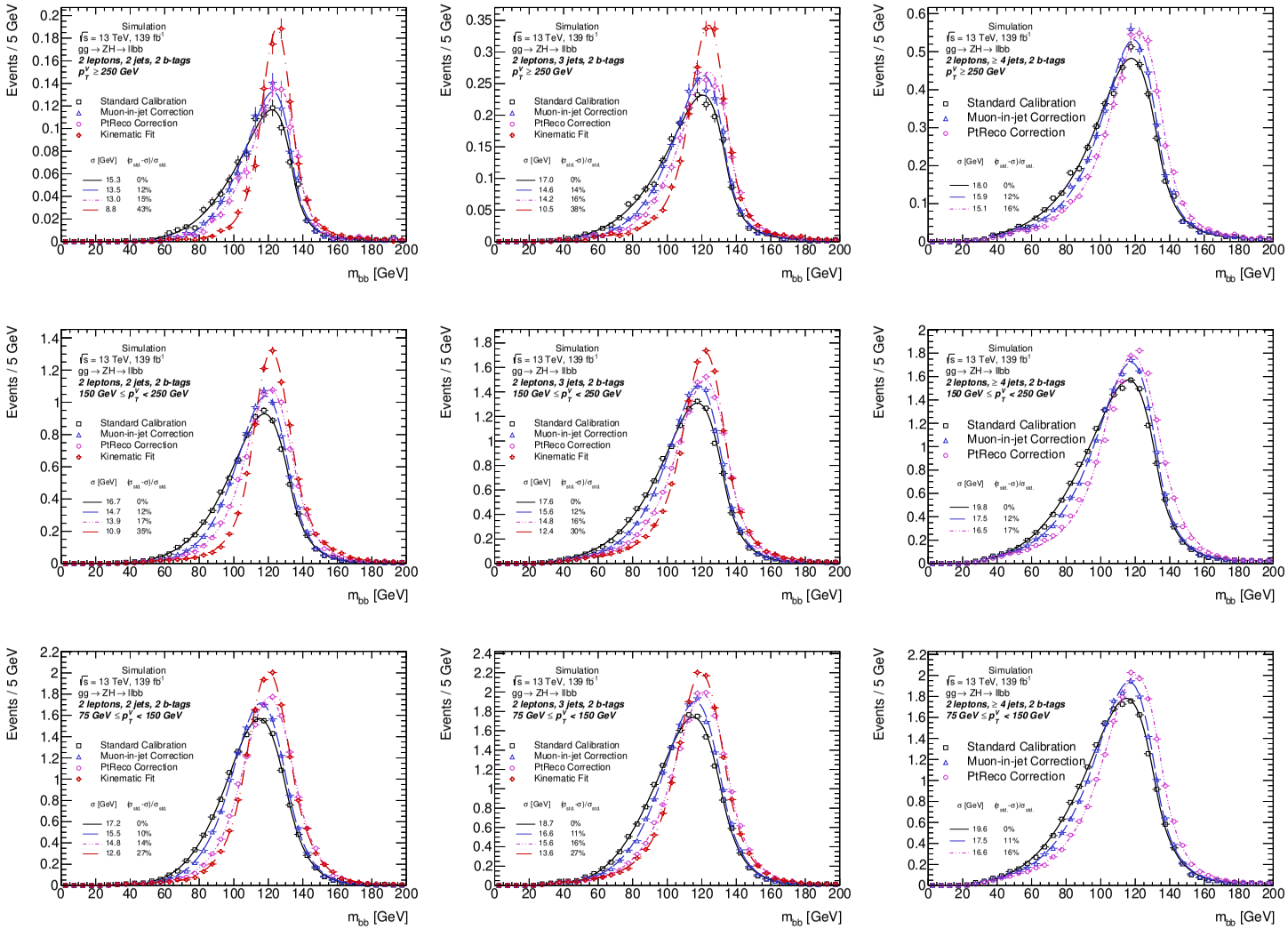

Figure 5.6: Resolution in the invariant mass of a pair of b-jets ($m_{b\bar{b}}$) in the $gg \rightarrow ZH \rightarrow \ell^+\ell^- b\bar{b}$ signal after each b-jet energy correction. As indicated in the plots, they show the distributions of $m_{b\bar{b}}$ in events with 2 jets (left), 3 jets (middle), and more than 3 jets (right); $p_{\mathrm{T}}^V \geq 250$ GeV (top), $150 \leq p_{\mathrm{T}}^V < 250$ GeV (middle), and $75 \leq p_{\mathrm{T}}^V < 150$ GeV (bottom). The black, blue, purple, and red plots show the distributions after GSC, muon-in-jet, PtReco, and KF, respectively. Each histogram is fitted with a Bukin function, and the extracted resolution is reported in the plots.

6 Analysis strategy

The overall strategies of the analysis: the targets of the measurement, the event selection and the categorization, the optimization of the analysis, and the validation, are introduced in this chapter.

6.1 Measurement of the differential cross-section

Possible effects from physics beyond the Standard Model (BSM) will be expressed by higher dimensional operators in the effective Lagrangian [26]. As explained in Section 2.4 (and will be explained in Section 11.1), the dimension-6 interactions affect the cross-section of the VH production in the phase space with high transverse momentum of the vector boson (p_{T}^{V}). The goal is to measure the differential cross-section of the VH production as a function of p_{T}^{V}.

Since the signal strength is defined as the ratio of the cross-section times the branching ratio to the Standard Model prediction ($\sigma \times B/(\sigma \times B)_{\mathrm{SM}}$), the theoretical uncertainties on the prediction are folded into its measurement. The theoretical uncertainties are divided into two categories: the uncertainties on the cross-section, and the uncertainties on the fraction of the signal events which are caught by the analysis the analysis phase space. This fraction is referred to as *acceptance*. It is necessary to consider the uncertainties on the acceptance (*acceptance uncertainties*) because the modeling of the acceptance relies on the differential distributions provided by Monte Carlo simulation and the simulation has uncertainties. In a cross-section measurement instead of the signal strength measurement, only the acceptance uncertainties are relevant.

The differential cross-section measurement performed in this thesis adopts the Simplified Template Cross Section approach [137, 138]. It is preferred that the measured phase spaces are synchronized to the analysis acceptance to avoid folding large acceptance uncertainties into the measurement. The derivation of relevant systematic uncertainties and the implementation of statistical analysis are explained in Sections 8.2.2 and 9.2.3, respectively.

In this thesis, the cross-sections of the WH and ZH productions are measured separately. The $qq \to ZH$ and $gg \to ZH$ processes are merged into the single ZH process since the analysis sensitivity is currently insufficient to distinguish the two processes. The p_{T}^{V} defined in the event generator is denoted as *truth* p_{T}^{V} ($p_{\mathrm{T}}^{V,\mathrm{truth}}$) in contrast to the *reconstructed* p_{T}^{V} ($p_{\mathrm{T}}^{V,\mathrm{reco}}$). Signal categories based on truth variables and reconstructed variables are called *truth categories* and *reconstructed categories*, respectively. There is event migration caused by detector effects such as resolution or identification efficiency of leptons, jets, and so on. The estimation of the signal in a reconstructed category is dependent on the performance of detectors, thus the measurement is not theoretically well-defined. In order to compare measurements with theories, the cross-sections in truth categories are measured. A method for the extraction of the theoretically well-defined cross-sections is further explained in Section 9.2.3. The phase space is divided into 2 WH bins and 3 ZH bins based on the $p_{\mathrm{T}}^{V,\mathrm{truth}}$: 150 GeV $< p_{\mathrm{T}}^{V,\mathrm{truth}} \leq$ 250 GeV, $p_{\mathrm{T}}^{V,\mathrm{truth}} >$ 250 GeV for WH, and 75 GeV $< p_{\mathrm{T}}^{V,\mathrm{truth}} \leq$ 150 GeV, 150 GeV $< p_{\mathrm{T}}^{V,\mathrm{truth}} \leq$ 250 GeV, $p_{\mathrm{T}}^{V,\mathrm{truth}} >$ 250 GeV for ZH.

The analysis is not sensitive to ZH in $p_{\mathrm{T}}^{V,\mathrm{truth}} < 75$ GeV and WH in $p_{\mathrm{T}}^{V,\mathrm{truth}} < 150$ GeV due to the small acceptance of the processes in the regions (See Sections 6.3 and 6.4). Thus, these signals are not measured but constrained to the Standard Model prediction within the theoretical uncertainty during the analysis. The binning is summarized in Figure 6.1 and Table 6.1.

6.2 Strategy of signal and background estimation

The main goal of the analysis is to estimate the yield of the signal precisely from the data. Technically, it is essential to select events that contain signal events with good purity because the expected significance of an excess from a background distribution is given by $\sigma = \sqrt{(S+B)\ln(1+S/B)) - S}$, where S and B are the expected yields of the signals and the backgrounds, respectively, when only the statistical uncertainty is taken into account. This point is further discussed in Sections 6.3 and 6.4.

Another main goal of the analysis is to estimate contributions from the background processes in the selected events using data. The distributions of the backgrounds predicted by the simulations have their systematic uncertainties as well as the statistical uncertainty. Thus, it is necessary to define special selection criteria called "control regions" to correct and validate the estimation of the backgrounds using data in those regions. Details are discussed in Section 6.5.

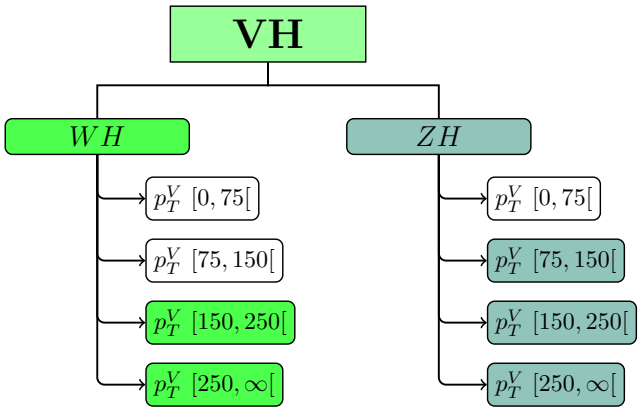

Figure 6.1: Schematic diagram for the binning of the differential cross-section.

Table 6.1: Binning for the cross-section measurement, and the corresponding analysis categories.

Bin for the cross-section measurement		Corresponding reconstructed analysis categories		
Process	$p_{\mathrm{T}}^{V,\mathrm{truth}}$ interval	Number of leptons	p_{T}^{V} interval	Number of jets
WH	$150 \le p_{\mathrm{T}}^{V} < 250$ GeV	1	$150 \le p_{\mathrm{T}}^{V} < 250$ GeV	2, 3
WH	$p_{\mathrm{T}}^{V} \ge 250$ GeV	1	$p_{\mathrm{T}}^{V} \ge 250$ GeV	2, 3
ZH	$75 \le p_{\mathrm{T}}^{V} < 150$ GeV	2	$75 \le p_{\mathrm{T}}^{V} < 150$ GeV	2, ≥ 3
ZH	$150 \le p_{\mathrm{T}}^{V} < 250$ GeV	0	$150 \le p_{\mathrm{T}}^{V} < 250$ GeV	2, 3
		2	$150 \le p_{\mathrm{T}}^{V} < 250$ GeV	2, ≥ 3
ZH	$p_{\mathrm{T}}^{V} \ge 250$ GeV	0	$p_{\mathrm{T}}^{V} \ge 250$ GeV	2, 3
		2	$p_{\mathrm{T}}^{V} \ge 250$ GeV	2, ≥ 3

To achieve good sensitivity, we use variables that can distinguish the signals and the backgrounds. Significance of an excess in a distribution with multiple bins is given by the following equation, $\sqrt{\sum_i \sigma_i^2} = \sqrt{\sum_i [(S_i + B_i)\ln(1 + S_i/B_i) - S_i]} \simeq \sqrt{\sum_i S_i^2/B_i}$. This indicates that we can achieve better significance if the signal and the background have a more different shape. An obvious example of such variables is the invariant mass of b-jets from the Higgs boson, which forms a narrow peak around 125 GeV. To achieve better sensitivity, we take more detailed differences of the signals and the backgrounds into account exploiting a multivariate technique. It is discussed in Section 6.6.

6.3 Event selection

We focus on the leptonic decay channels of the vector boson produced in association with H. This is because the hadronic decay channel of the VH productions ($Z \to qq, H \to b\bar{b}$) only consist of jets in the final state, and suffers from the huge multi-jet background. By selecting the leptonic decay of the vector boson, the multi-jet background is significantly reduced and the signal over background ratio is improved.

In order to measure the WH and ZH signals independently, events are categorized into three channels depending on the number of charged leptons in the final states targeting $ZH \to \nu\bar{\nu}b\bar{b}$, $WH \to \ell\nu b\bar{b}$ and $ZH \to \ell^+\ell^- b\bar{b}$ in *0-, 1-, and 2-lepton channels*, respectively. This categorization also disentangles the backgrounds that include W and Z bosons, and allows us to constrain these multiple component backgrounds including the top productions separately.

Single lepton and $E_{\mathrm{T}}^{\mathrm{miss}}$ triggers are used to take the signals that contain charged leptons or neutrinos. The triggers are almost fully efficient in the phase spaces sensitive to the signals. Additionally, the selection of the triggers efficiently reduces the multi-jet background.

The spectra of p_{T}^V of the signal and the background processes are compared in the 0-, 1- and 2-lepton channels in Figure 6.2, where we can see that the signals have higher in p_{T}^V than the backgrounds. Thus, a common approach among three lepton channels is taken to exploit the better S/N ratio in the phase space with high p_{T}^V. Specifically, the analysis takes into account events with $p_{\mathrm{T}}^V \geq 150$ GeV in the 0- and 1-lepton channels and with $p_{\mathrm{T}}^V \geq 75$ GeV in the 2-lepton channel. The lower bound of the selection in p_{T}^V for lepton channel is determined by several limitations discussed in a later part of this section.

The specific event selection criteria are described in the rest of this section.

Common event selection for lepton channels

In all lepton channels, events are required to have exactly two b-tagged jets (b-jets). p_{T} of at least one b-jet should be greater than 45 GeV. This pair of b-jet forms a Higgs boson candidate. Events with additional jets that are not b-tagged are accepted to increase the acceptance of the signal. In counting jets, the *central* and *forward* jets, defined in Section 5.4, are taken into account. In the 0- and 1-lepton channels, events with more than 3 jets are not included in the analysis because there is large contribution from the semi-leptonic $t\bar{t}$ background as shown in Figure 6.3. In the 2-lepton channel, the S/N is also high for the events with more than 3 jets as shown in Figure 6.3 because the $t\bar{t}$ background is dominated by the full-leptonic decay channel due to the requirement of two charged leptons. Thus, those events are included to improve the acceptance of the signal.

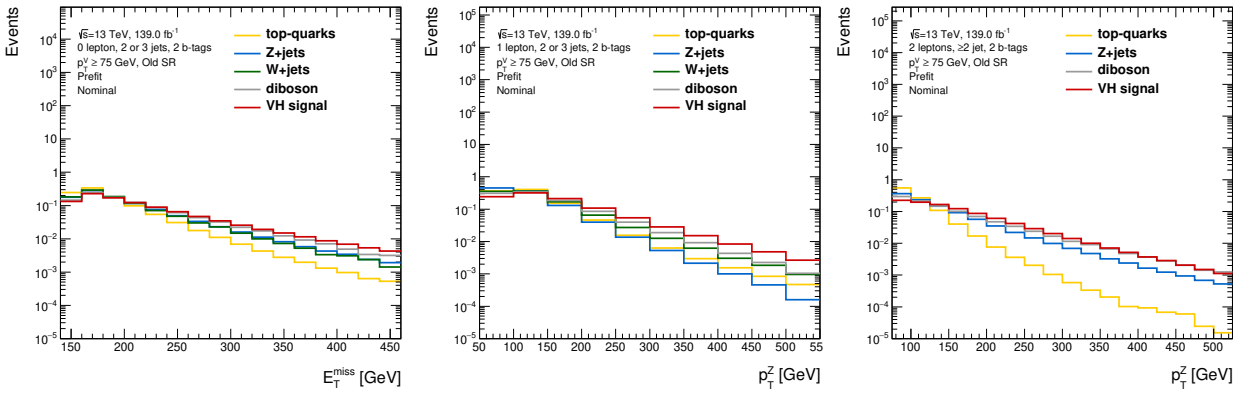

(a) 0-lepton (b) 1-lepton (c) 2-lepton

Figure 6.2: Distributions of the transverse momentum of the Z or W boson in the signal and the background processes in each lepton channel. For the 0- (a) and 1-lepton (b) channels, distributions with events with two or three jets are shown. For the two lepton channel (c), distribution with events with two or more jets are shown.

Zero lepton specific selection

In the 0-lepton channel, p_{T}^{V} corresponds to $E_{\mathrm{T}}^{\mathrm{miss}}$ of the events since the Z decays to a pair of neutrinos. Thus, the signal events are collected by the $E_{\mathrm{T}}^{\mathrm{miss}}$ triggers whose thresholds varied from 70 GeV to 110 GeV in the 2015 and 2018 data taking periods. $E_{\mathrm{T}}^{\mathrm{miss}}$ is required to be greater than 150 GeV in the offline analysis, and events are vetoed when they contain the *VH-Loose* charged leptons defined in Sections 5.2 and 5.3.

The efficiency of the $E_{\mathrm{T}}^{\mathrm{miss}}$ trigger reaches its plateau at $E_{\mathrm{T}}^{\mathrm{miss}} = 200$ GeV, and in a turn-on region[1] the efficiency slightly depends on the number of jets. A cut on the scalar sum of the transverse momenta of the jets, $H_{\mathrm{T}} > 120$ GeV (2 jets), 150 GeV (3 jets), is applied to remove the small phase space that is affected by the dependence on the number of jets.

The multi-jet background has a high $E_{\mathrm{T}}^{\mathrm{miss}}$ when the energy of jets is mismeasured. In order to reduce this background, these cuts defined using angular variables of the jets and $E_{\mathrm{T}}^{\mathrm{miss}}$ as following are imposed:

- $|\mathrm{min}\Delta\phi(E_{\mathrm{T}}^{\mathrm{miss}}, \mathrm{jet})| \begin{cases} > 20^\circ \text{ (2 jets)} \\ > 30^\circ \text{ (3 jets)} \end{cases}$, where min indicates the smallest value among jets.
- $|\Delta\phi(E_{\mathrm{T}}^{\mathrm{miss}}, h)| > 120^\circ$, where h is the Higgs candidate.
- $|\Delta\phi(\mathrm{jet1,jet2})| < 140^\circ$, where jet1 and jet2 are the leading and sub-leading jets, respectively.
- $|\Delta\phi(E_{\mathrm{T}}^{\mathrm{miss}}, E_{\mathrm{T,\,trk}}^{\mathrm{miss}})| < 90^\circ$

Here the $E_{\mathrm{T,\,trk}}^{\mathrm{miss}}$ is defined as the negative vector sum of the transverse momenta of the tracks reconstructed in the inner detector and originating from the primary vertex.

[1] Range of $E_{\mathrm{T}}^{\mathrm{miss}}$ around the threshold of the $E_{\mathrm{T}}^{\mathrm{miss}}$ trigger where the efficiency rises as $E_{\mathrm{T}}^{\mathrm{miss}}$ increases.

One lepton specific selection

In the 1-lepton channel, since the W decays to a pair of a charged lepton and a neutrino, the p_{T}^{V} is reconstructed as the vector sum of the $E_{\mathrm{T}}^{\mathrm{miss}}$ and the p_{T} of the lepton. Since muons are not included in the calculation of $E_{\mathrm{T}}^{\mathrm{miss}}$ in the trigger system, events in the muon sub-channel, $W \to \mu\nu$, with $p_{\mathrm{T}}^{V} \geq 150$ GeV are collected using the $E_{\mathrm{T}}^{\mathrm{miss}}$ triggers as the 0-lepton channel. Events in the electron sub-channel are collected using the single electron triggers whose thresholds varied from 24 to 26 GeV during the data taking periods. Events are required to have exactly one *VH-tight* charged lepton defined in Sections 5.2 and 5.3, and events that contain *VH-Loose* charged leptons are vetoed. The muon must have $p_{\mathrm{T}} > 25$ GeV, and the electron must have $p_{\mathrm{T}} > 27$ GeV.

The phase space with $75 \leq p_{\mathrm{T}}^{V} < 150$ GeV can be included by using the single muon triggers. However, attempts did not succeed because the fit (Chapter 9) was not manageable due to the high statistics and large systematic uncertainties of the backgrounds. Thus, the 1-lepton channel only considers events with $p_{\mathrm{T}}^{V} \geq 150$ GeV. Furthermore, events in the electron sub-channel are required to have $E_{\mathrm{T}}^{\mathrm{miss}} > 30$ GeV.

Two lepton specific selection

In the 2-lepton channel, the Z boson decaying to a pair of charged leptons is fully reconstructed. Events are required to contain exactly two *VH-Loose* leptons (see Sections 5.2 and 5.3) of the same flavor, and events with additional *VH-Loose* leptons are rejected. A cut on the invariant mass of the dilepton system is imposed: $81 < m_{\ell\ell} < 101$ GeV. The two muons are required to have opposite charges while the requirement is not imposed for the electron sub-channel because of the higher rate of charge misidentification [120].

The single lepton triggers are employed for both the muon and electron sub-channels. The thresholds of the single muon triggers varied from 20 to 26 GeV during the data taking periods, Thus, at least one lepton must have $p_{\mathrm{T}} > 27$ GeV.

The event selection for all the lepton channels are summarized in Table 6.2.

6.4 Categorization

In general, the S/N ratio is dependent on phase spaces. For instance, phase space with higher p_{T}^{V} gives a better S/N ratio than ones with lower p_{T}^{V}. Similarly, the S/N ratio is higher in the phase spaces with a small number of jets than in the ones with many jets as shown in Figure 6.3.

On the other hand, the signals have a larger cross-section in the phase spaces with low p_{T}^{V} or high jet multiplicity.

In order to maximize the sensitivity, we separate the events into *categories* to take full advantage of the *high purity* of event sets and the *high statistics* of other event sets. As explained in the previous paragraphs, we define three categories based on p_{T}^{V}: $75 \leq p_{\mathrm{T}}^{V} < 150$ GeV, $150 \leq p_{\mathrm{T}}^{V} < 250$ GeV, and $p_{\mathrm{T}}^{V} \geq 250$ GeV, and two categories based on the number of jets: 2 jets and more than 2 jets for the 2-lepton channel. As discussed in Section 6.3, events with $150 \geq 150$ GeV and 2 or 3 jets are included for the 0- and 1-lepton analyses. The defined categories are summarized in Table 6.3.

Table 6.2: Summary of the signal event selection in the 0-, 1- and 2-lepton analyses.

Common Selections	
Jets	≥ 2 signal jets
b-jets	2 b-tagged signal jets
Leading b-tagged-jet p_{T}	> 45 GeV
0 lepton	
Trigger	$E_{\mathrm{T}}^{\mathrm{miss}}$ triggers
Leptons	0 *VH-Loose* lepton
$E_{\mathrm{T}}^{\mathrm{miss}}$	> 150 GeV
H_{T}	> 120 (2 jets), >150 GeV (3 jets)
$\lvert\min\Delta\phi(E_{\mathrm{T}}^{\mathrm{miss}}, \mathrm{jet})\rvert$	$> 20°$ (2 jets) , $> 30°$(3 jets)
$\lvert\Delta\phi(E_{\mathrm{T}}^{\mathrm{miss}}, h)\rvert$	$> 120°$
$\lvert\Delta\phi(\mathrm{jet1,jet2})\rvert$	$< 140°$
$\lvert\Delta\phi(E_{\mathrm{T}}^{\mathrm{miss}}, E_{\mathrm{T,\,trk}}^{\mathrm{miss}})\rvert$	$< 90°$
p_{T}^{V}	$p_{\mathrm{T}}^{V} \geq 150$ GeV
1 lepton	
Trigger	e channel: single electron trigger μ channel: $E_{\mathrm{T}}^{\mathrm{miss}}$ trigger
Leptons	1 *VH-Tight* lepton > 1 *VH-Loose* lepton veto
$E_{\mathrm{T}}^{\mathrm{miss}}$	> 30 GeV (e channel)
p_{T}^{V}	$p_{\mathrm{T}}^{V} \geq 150$ GeV
2 lepton	
Trigger	Single lepton triggers
Leptons	2 *VH-Loose* leptons Same flavor, opposite-charge for $\mu\mu$
$m_{\ell\ell}$	$81 < m_{\ell\ell} < 101$ GeV
p_{T}^{V}	$p_{\mathrm{T}}^{V} \geq 75$ GeV

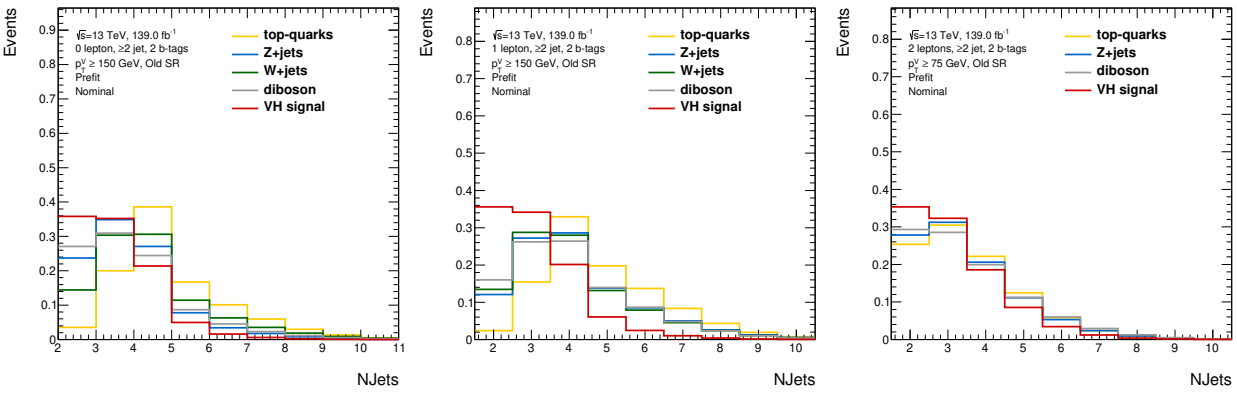

Figure 6.3: The distribution of the number of jets in events for the signals and the backgrounds in each lepton channel. The phase spaces with $p_{\mathrm{T}}^{V} \geq 150$ GeV are shown since they are the events that are analyzed.

Table 6.3: Summary of the categorization for the 0-, 1- and 2-lepton analyses.

Number of leptons	Number of jets	p_{T}^{V}
0-lepton 1-lepton	2 jets, 3 jets	$150 \leq p_{\mathrm{T}}^{V} < 250$ GeV, $p_{\mathrm{T}}^{V} \geq 250$ GeV
2-leptons	2 jets, $\geq$ 3 jets	$75 \leq p_{\mathrm{T}}^{V} < 150$ GeV $150 \leq p_{\mathrm{T}}^{V} < 250$ GeV, $p_{\mathrm{T}}^{V} \geq 250$ GeV

The categorization using p_{T}^{V} as well as the number of charged leptons also allows us to measure the differential cross-section of the VH production in the bins with $75 \leq p_{\mathrm{T}}^{V} < 150$ GeV, $150 \leq p_{\mathrm{T}}^{V} < 250$ GeV, and $p_{\mathrm{T}}^{V} \geq 250$ GeV for ZH and $150 \leq p_{\mathrm{T}}^{V} < 250$ GeV and $p_{\mathrm{T}}^{V} \geq 250$ GeV for WH.

The categorization based on p_{T}^{V} allows us to measure the differential cross-section of the VH production in the bins discussed in Section 6.1. The predicted fraction of the signal in each reconstructed category is shown in Figure 6.4. The predicted fraction of the signal in each reconstructed category is also shown in Figure 6.4.

6.5 Signal regions and control regions

For the background estimation, we categorize events into signal-rich regions and background-rich regions. They are named *signal regions* and *control regions*. Control regions called *high-ΔR control regions* and *low-ΔR control regions* are defined to get sets of events that have small contamination of the signals as discussed in Section 6.5.1. Special control regions called *$e\mu$ control regions* are defined to estimate the $t\bar{t}$ background in the 2-lepton channel as discussed in Section 6.5.2.

6.5.1 Definitions by angles

The signal processes are resonant processes that have a narrow peak in the distribution of the invariant mass of the pair of b-jets. In other words, they distribute on a narrow band in the $\Delta R_{b\bar{b}}$-p_{T}^{V} plane as shown in Figures 6.5, 6.6 and 6.7. This fact allows us to define a signal region in the p_{T}^{V}-$\Delta R_{b\bar{b}}$ plane. The functional form of the continuous cuts we employ is

$$\Delta R_{b\bar{b}} \lessgtr \alpha + \exp\left(\beta - \gamma \times p_{\mathrm{T}}^{V}\right) \qquad \begin{pmatrix} > : \text{upper cut} \\ < : \text{lower cut} \end{pmatrix}, \tag{6.1}$$

and the parameters α, β and γ are tuned in the 1-lepton channel as follows: The upper cut sets the parameters to have the efficiency of the $WH \to \ell\nu b\bar{b}$ signal to be better than 95% in the 2-jets category and 85% in the 3-jets category, and the lower cut sets the parameters to have the efficiency of the diboson ($WZ \to \ell\nu b\bar{b}$) process to be better than 90% in both the 2-jets and 3-jets categories. The optimized parameters are summarized in Table 6.4, and the defined curves are shown in Figures 6.5, 6.6 and 6.7 as the white curves. The regions above the upper cut and below the lower cut define control regions called *high-ΔR control regions* (*high-ΔR-CRs*) and *low-ΔR control regions* (*low-ΔR-CRs*), respectively. The same set of cuts is used also in the 0- and 2-lepton channels.

The signal regions and the control regions have yields of processes as shown in Tables C.1-C.7. It should be emphasized that these yields of the backgrounds are corrected to reproduce the distributions in data of

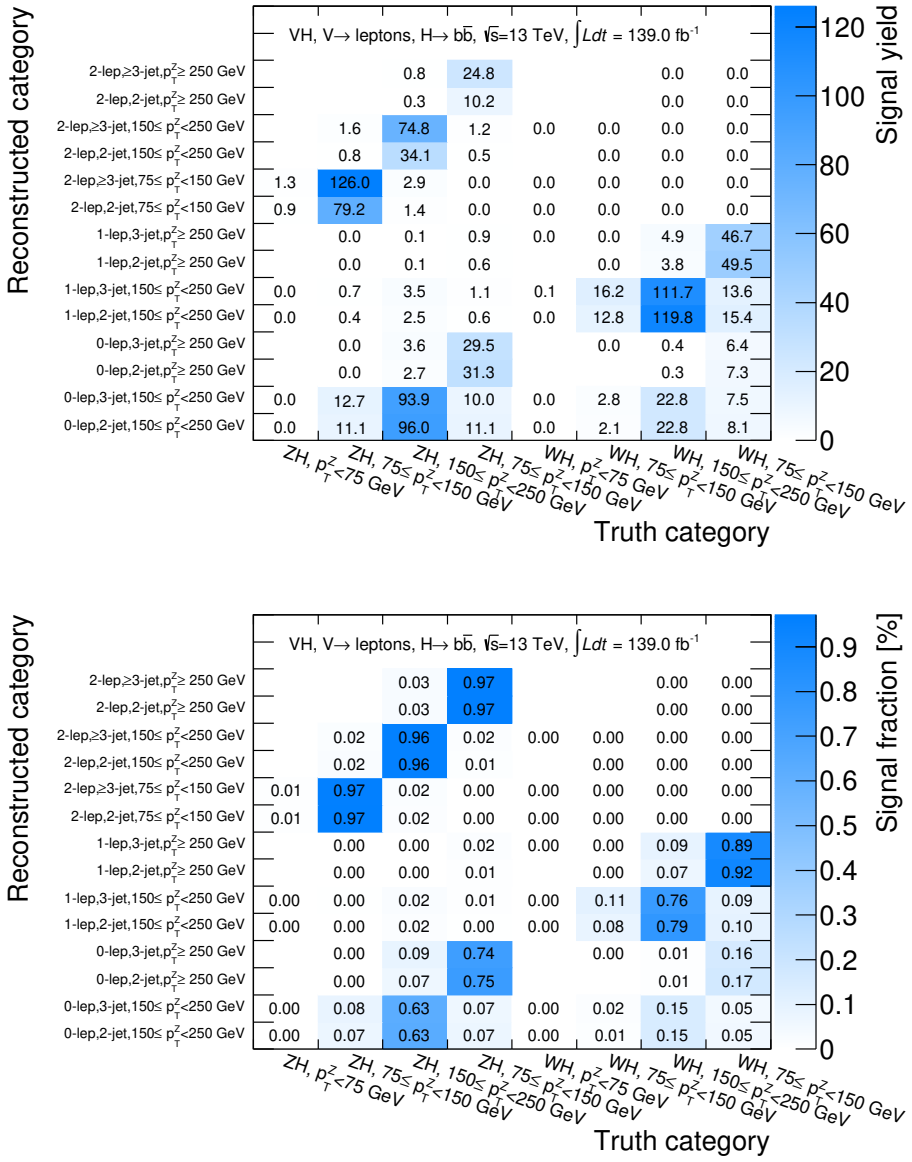

Figure 6.4: Top: the expected yields of the signal events from the indicated truth phase spaces (x-axis) in the categories defined in this section (y-axis). Bottom: the expected fraction of the signals from indicated truth phase spaces in the categories.

the signal regions and the control regions. This procedure is called *fit*, and discussed in Chapter 9. The fraction of each background component is checked and shown in Figure 6.8. In the 1-lepton channel, the control regions are designed so that the high-ΔR-CRs is enriched in the $t\bar{t}$ and single top backgrounds, and the low-ΔR-CRs is enriched in the W + jets background. In the 2-lepton channel, two control regions are enriched in the Z + jets background with a smaller contribution from the top background. Special control regions are defined for that background and explained in Section 6.5.2. Thus, it is likely to be possible to estimate one background component in one control region. On the other hand, the background in the control regions of the 0-lepton channel is a mixture of Z + jets, W + jets, and top. This means that it is necessary to use the information from the 1- and 2-lepton channels for constraining each background in the 0-lepton channel. This is implemented in a *simultaneous fit* discussed in Chapter 9.

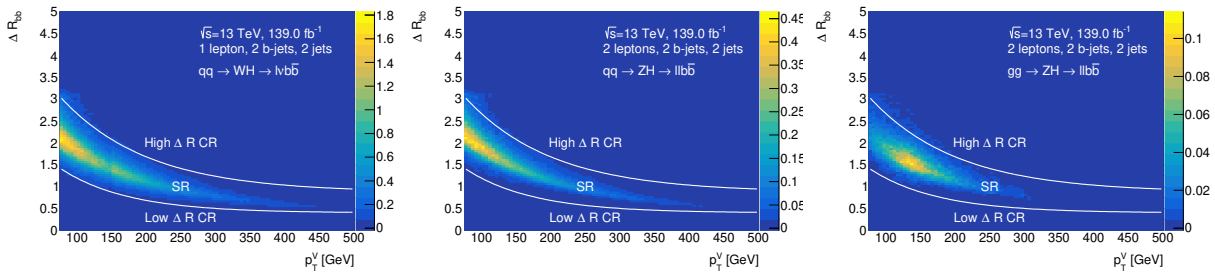

Figure 6.5: Two dimensional distributions of the signal processes, WH (left), $qq \to ZH$ (middle), $gg \to ZH$ (right) in the $\Delta R_{b\bar{b}}$-p_{T}^{V} plane in the events selected with the criteria given in Section 6.3 and in the two jet category. The plot for the WH signal shows the distribution in the 1-lepton channel, while the ones for $qq \to ZH$ and $gg \to ZH$ show the distributions in the 2-lepton channel.

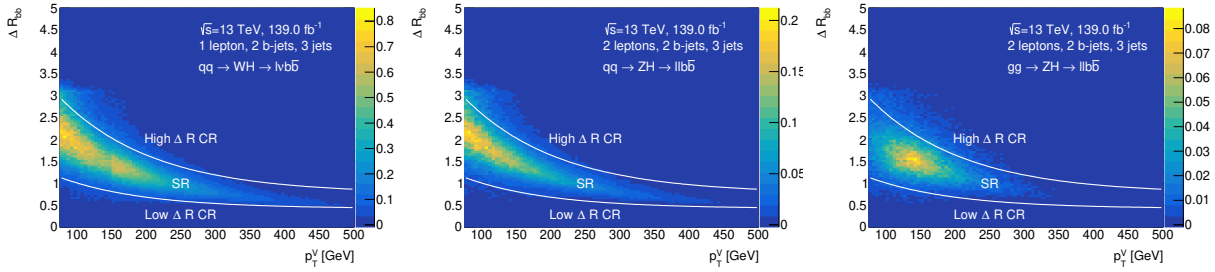

Figure 6.6: Two dimensional distributions of the signal processes, WH (left), $qq \to ZH$ (middle), $gg \to ZH$ (right) in the $\Delta R_{b\bar{b}}$-p_{T}^{V} plane in the events selected with the criteria given in Section 6.3 and in the three jet category. The plot for the WH signal shows the distribution in the 1-lepton channel, while the ones for $qq \to ZH$ and $gg \to ZH$ show the distributions in the 2-lepton channel.

Table 6.4: Cuts that define the high-ΔR-CRs and the low-ΔR-CRs for the 2 and ≥ 3 jets categories.

Number of jets	Cuts for the high-ΔR-CRs	Cuts for the low-ΔR-CRs
2-jets	$\Delta R > 0.87 + \exp\left(1.38 - 0.00795 \times p_{\mathrm{T}}^{V}\right)$	$\Delta R > 0.76 + \exp\left(1.33 - 0.0073 \times p_{\mathrm{T}}^{V}\right)$
≥ 3-jets	$\Delta R < 0.40 + \exp\left(0.788 - 0.01023 \times p_{\mathrm{T}}^{V}\right)$	$\Delta R < 0.42 + \exp\left(0.268 - 0.00809 \times p_{\mathrm{T}}^{V}\right)$

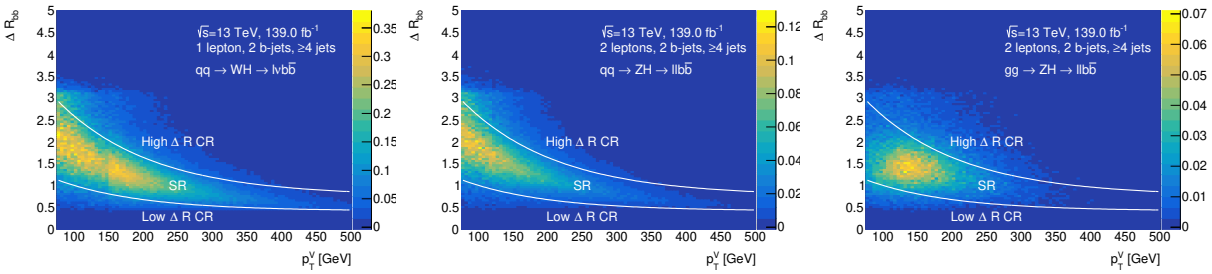

Figure 6.7: Two dimensional distributions of the signal processes, WH (left), $qq \rightarrow ZH$ (middle), $gg \rightarrow ZH$ (right) in the $\Delta R_{b\bar{b}}$-p_{T}^{V} plane in the events selected with the criteria given in Section 6.3 and in the three jet category. The plot for the WH signal shows the distribution in the 1-lepton channel, while the ones for $qq \rightarrow ZH$ and $gg \rightarrow ZH$ show the distributions in the 2-lepton channel.

6.5.2 Top-$e\mu$ control region in the 2-lepton channel

The top backgrounds, $t\bar{t}$ and Wt, contain two W bosons either directly produced or appearing in the decay of a top-quark. In the 2-lepton channel, the final states from these background processes have the same branching fraction for the same flavor leptons (e^+e^- or $\mu^+\mu^-$) and the different flavor leptons ($e^-\mu^+$ or $e^+\mu^-$) have the same branching fraction. This character of the top backgrounds is expressed as *flavor symmetry*. The other backgrounds and the signals in the 2-lepton channel contain a Z boson which decays to a pair of the same flavor leptons. Thus, in order to enhance the top backgrounds, events are selected with the same criteria as the signal regions except for the combination of the flavor of the leptons. These regions contain the top backgrounds with the purity of more than 99%, as shown in Tables C.8, C.9, C.10 and Figure 6.9. These control regions are called *$e\mu$ control regions*.

Since the continuous cuts defined in Section 6.5.1 are also applied to the eμ control regions, each of these control regions is corresponding to one of the same flavor regions: the signal regions, the high-ΔR control regions and the low-ΔR control regions of the 2-lepton channel. Due to the same kinematic selection applied to the signal regions and eμ control regions, and the flavor symmetry of the top backgrounds, the same number of events and same kinematic distributions are expected between the same flavor regions and the eμ control regions. This behavior plays a crucial role in a top background estimation method, as discussed later in Section 7.2.2. We apply to the eμ control regions the requirement for the opposite charge, which is applied to the muon sub-channel but not to the electron sub-channel. This difference has a minor effect on the method, and it is also discussed.

6.5.3 Prefit comparisons of the data and Monte-Carlo

The distributions of $m_{b\bar{b}}$ in the data and the MC predictions are shown in Figures 6.10, 6.11 and 6.12. The $t\bar{t}$ background in the 2-lepton channel is modeled using a special method that is discussed in Section 7.2.2 instead of the MC prediction shown here. It should be emphasized that these MC predictions are corrected in the fitting procedure discussed in Chapter 9.

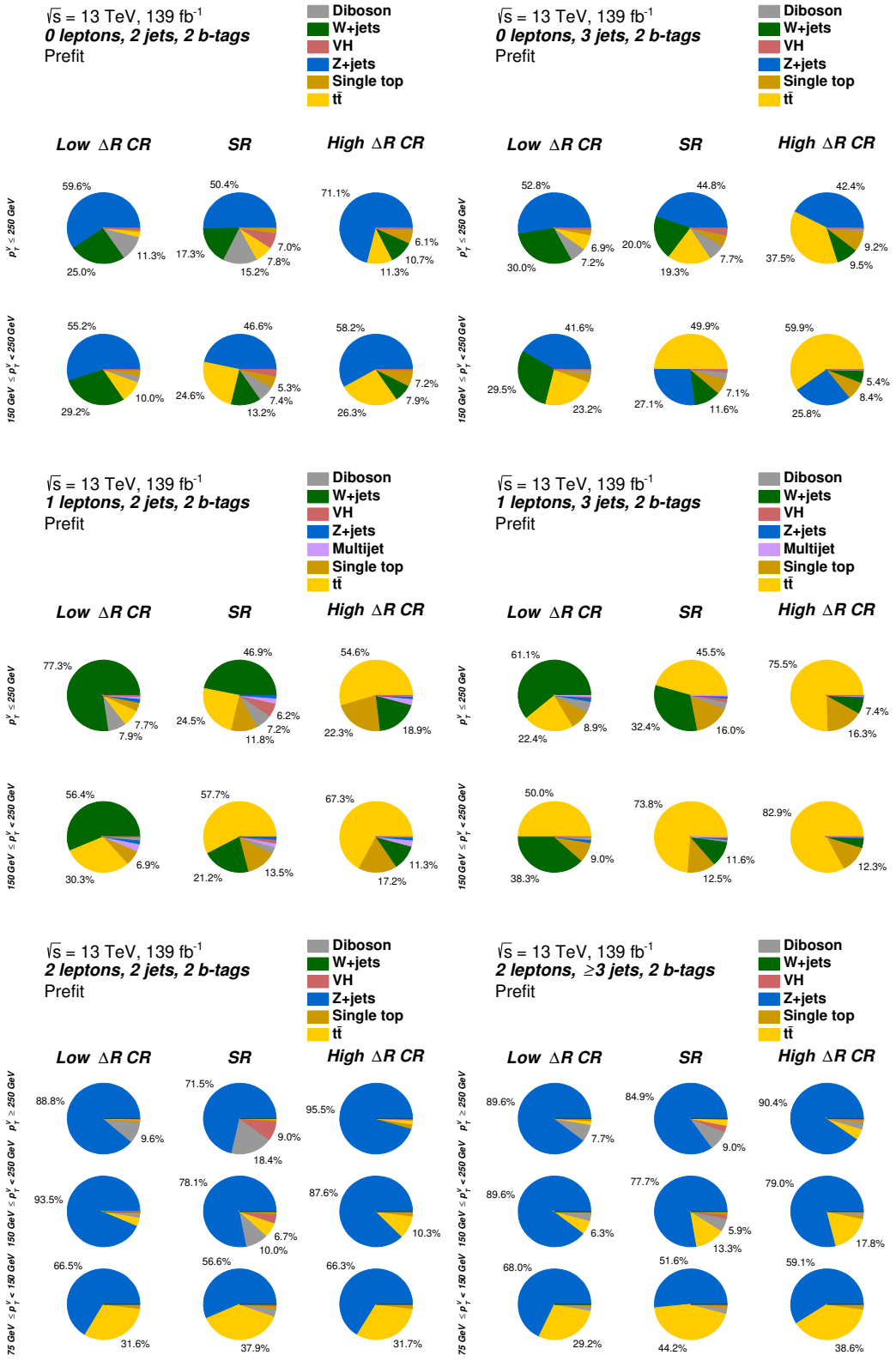

Figure 6.8: Pie-charts showing the background fraction in the indicated regions before fitting in each analysis region of each lepton channel.

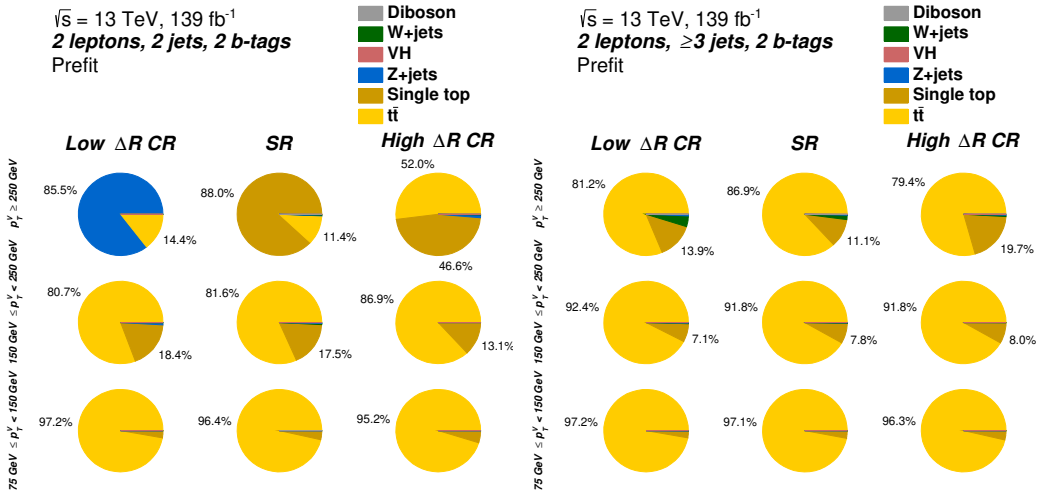

Figure 6.9: Pie-charts showing the background fractions in the indicated regions before fitting in the eμ control regions.

6.6 Multivariate analysis

As discussed in Section 6.2, one essential task of the analysis is to maximize the S/N ratio of sensitive bins. As well as the invariant mass of the pair of b-jets, p_{T}^{V}, $\Delta R_{b\bar{b}}$, angles of objects are different for the signal and the backgrounds due to the spin structure of bosons (vector bosons such as W, Z, gluons and the scaler boson such as the Higgs boson). These differences allow improving the separation of the signals and the backgrounds. As known well, multiple cuts on many variables are not efficient. Thus, it is motivated to use a multivariate technique to optimize cuts in a multidimensional space.

6.6.1 Boosted Decision Tree and setups for training

Boosted Decision Trees (BDTs) are implemented to separate signal and background events using the TMVA framework [124].

Training of BDT is done using the MC samples of the signals and the backgrounds. If a BDT discriminant is evaluated for events used in the training, it can be overtuned to separate the training samples based on differences created by statistical fluctuation. The BDT trained by MC can show different behaviors when it is applied to a statistically independent dataset, i.e. the data. This is called *overtraining*. It is problematic because, in this case, the distributions of BDT score are mismodeled, thus the signal can be mismeasured. To avoid the problem, it is necessary to apply BDTs to statistically independent samples. To maximize the size of samples used to train BDT while assuring the independence of training and applied samples, MC events are split into two parts based on *even* and *odd* of an event number, meaning that the events are split randomly. Two sets of BDTs, *even BDTs* and *odd BDTs*, are trained, and when they are used in the analysis, the even BDTs are applied to the events with odd event numbers and vice versa.

We trained two sets of BDTs for different purposes. The first set (BDT_{VH}) is trained to separate the VH signals from the other backgrounds. This is used for the main analysis, which measures the VH signal.

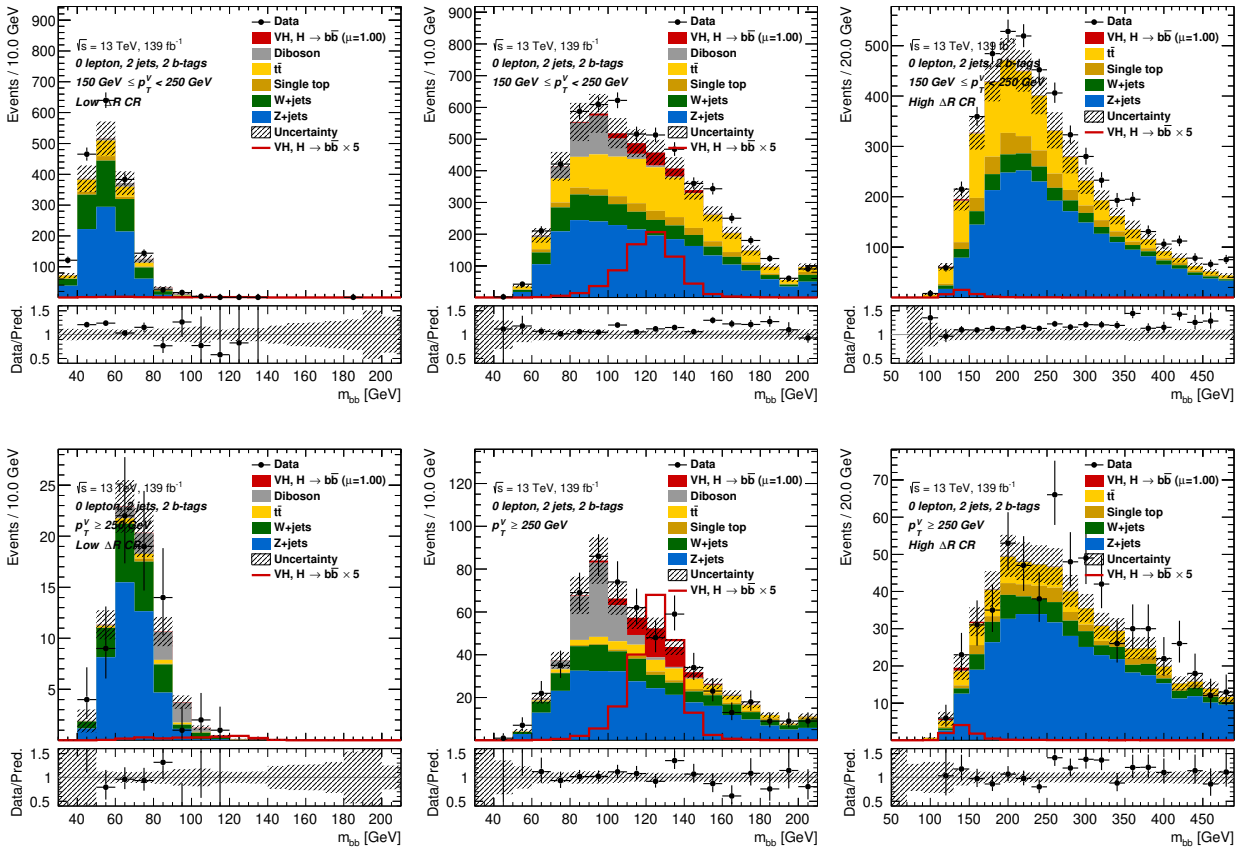

Figure 6.10: Comparisons of the data and the prediction in the distributions of $m_{b\bar{b}}$ in the signal regions and the control regions of the 0-lepton channel. These distributions are obtained before the fitting. The red unstacked and unfilled histograms show the Higgs signals with the scale factors indicated in the legend. The lower panels in each plot show the ratio of the data and the predictions of the signals and the backgrounds. The hatched bands in the upper and lower panels show the total uncertainty, which includes the statistical and systematic uncertainties. Each plot shows the region indicated in the plot.

The second set (BDT_{VZ}) is trained to separate the diboson processes from other processes including VH. This is used for an auxiliary measurement that estimates the diboson processes for a cross-check of the main analysis.

The event selection discussed in Section 6.3, and the categorization based on the number of jets are applied before training. For the categories based on p_{T}^{V}, $150 \leq p_{\mathrm{T}}^{V} < 250$ GeV and $p_{\mathrm{T}}^{V} \geq 250$ GeV are merged but the categories of the 2-lepton channel with $75 \leq p_{\mathrm{T}}^{V} < 150$ GeV are separated. As well as the categories of p_{T}^{V}, the signal, the high-ΔR, and low-ΔR control regions are merged for the training. These categorizations are determined because these separation does not improve the sensitivity, and the training can be more robust against overtraining because of the larger statistics for training. Thus, one BDT discriminant is constructed for one category based on the numbers of leptons and jets, and p_{T}^{V} as summarized in Table 6.5.

The BDT discriminants are trained with the hyper-parameters listed in Table 6.6. The BDT discriminants are tuned to provide the best expected significance by testing with various parameters.

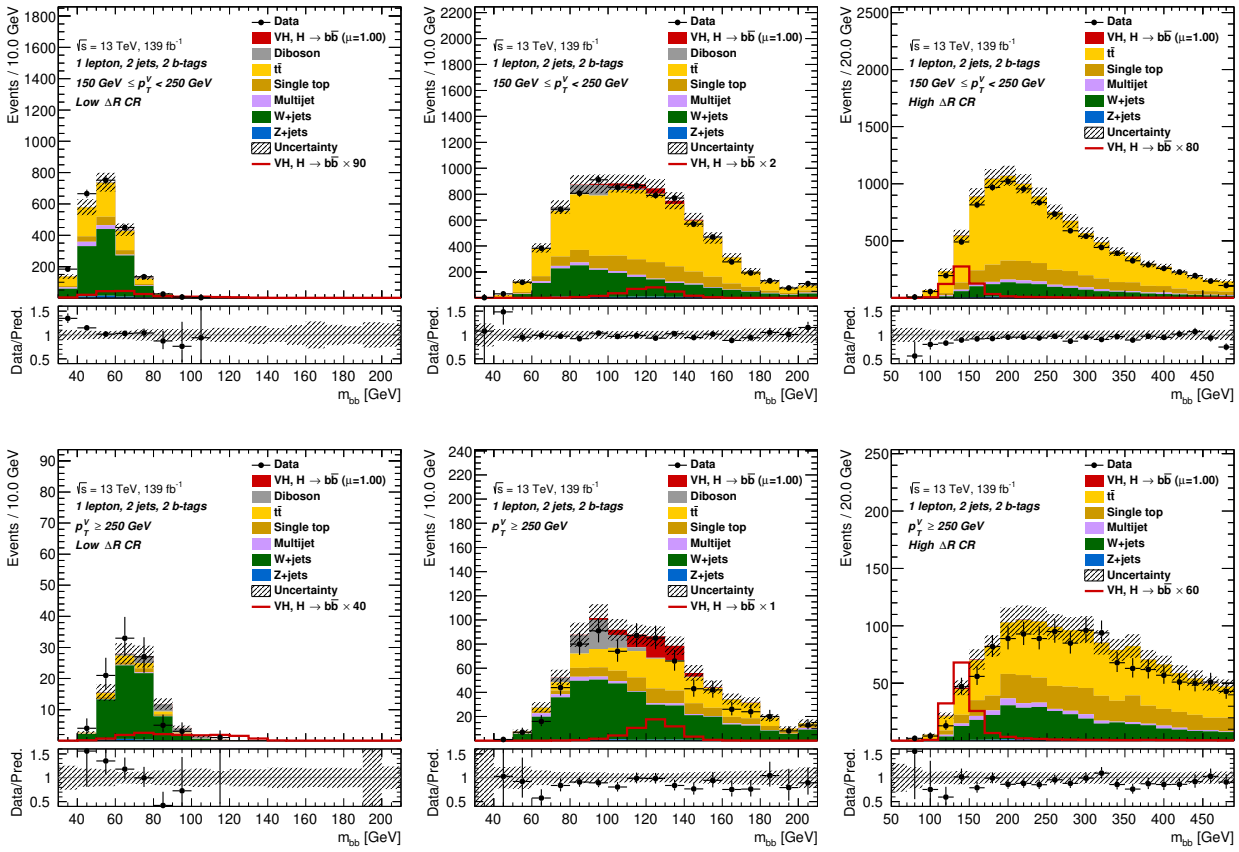

Figure 6.11: Comparisons of the data and the prediction in the distributions of $m_{b\bar{b}}$ in the signal regions and the control regions of the 1-lepton channel. These distributions are obtained before the fitting. The red unstacked and unfilled histograms show the Higgs signals with the scale factors indicated in the legend. The lower panels in each plot show the ratio of the data and the predictions of the signals and the backgrounds. The hatched bands in the upper and lower panels show the total uncertainty, which includes the statistical and systematic uncertainties. Each plot shows the region indicated in the plot.

Table 6.5: Summary of the categories defined to train BDTs.

Number of leptons	Number of jets	p_{T}^V
0-lepton 1-lepton	2 jets, 3 jets	$p_{\mathrm{T}}^V \geq 150$ GeV
2-leptons	2 jets, $\geq$ 3 jets	$75 \leq p_{\mathrm{T}}^V < 150$ GeV, $p_{\mathrm{T}}^V \geq 150$ GeV

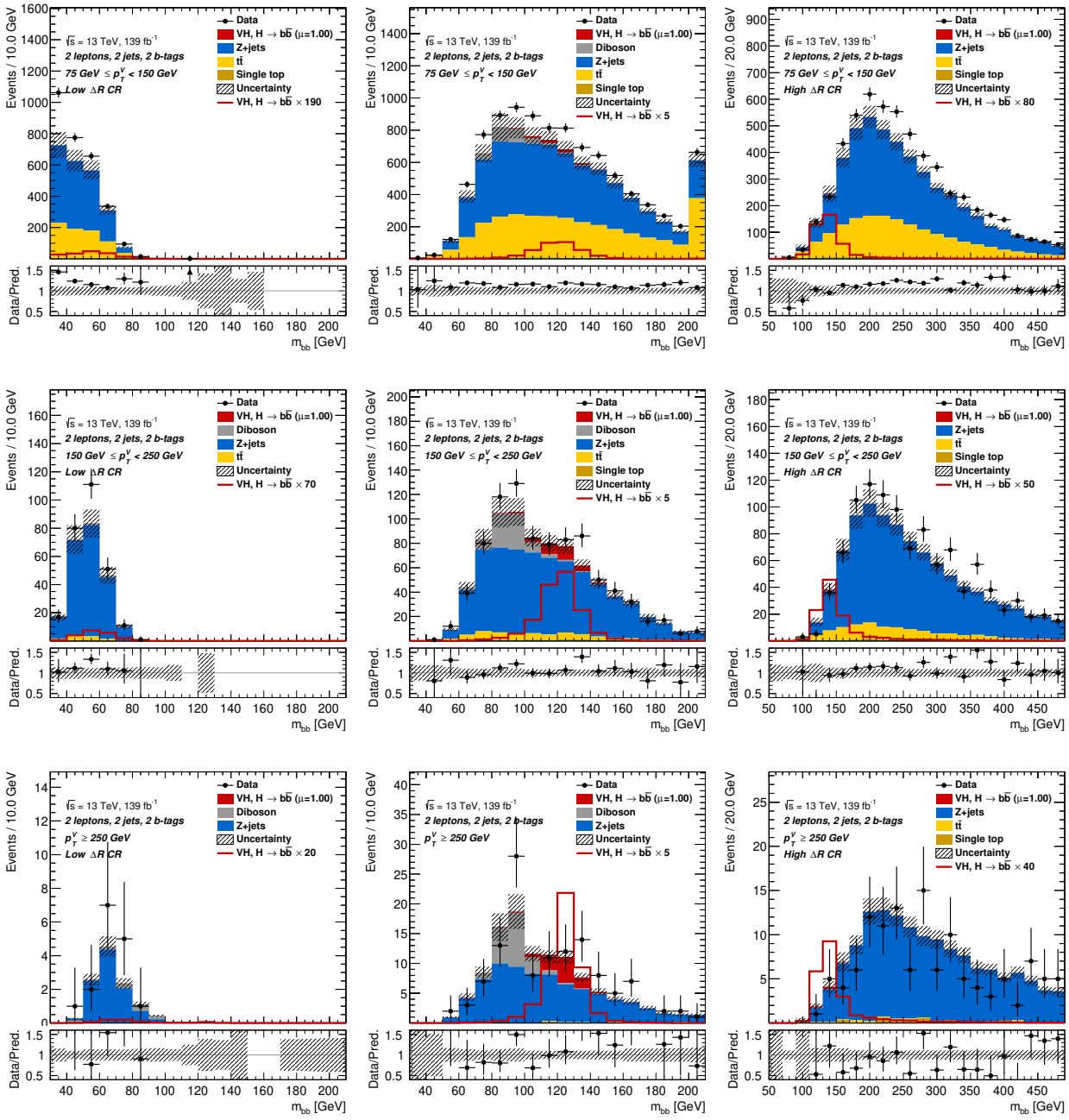

Figure 6.12: Comparisons of the data and the prediction in the distributions of $m_{b\bar{b}}$ in the signal regions and the control regions of the 2-lepton channel. These distributions are obtained before the fitting. The red unstacked and unfilled histograms show the Higgs signals with the scale factors indicated in the legend. The lower panels in each plot show the ratio of the data and the predictions of the signals and the backgrounds. The hatched bands in the upper and lower panels show the total uncertainty, which includes the statistical and systematic uncertainties. Each plot shows the region indicated in the plot.

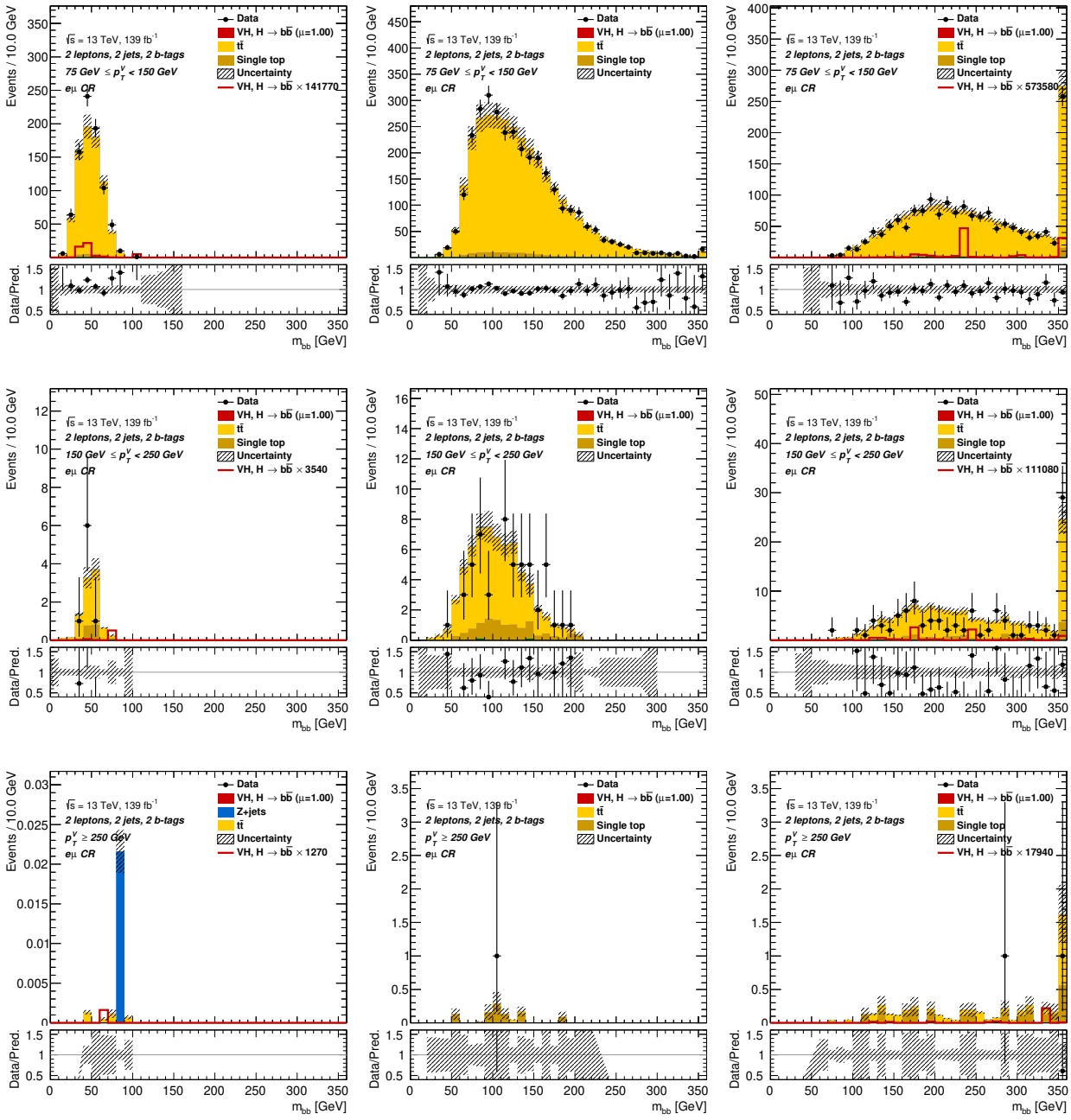

Figure 6.13: Comparisons of the data and the prediction in the distributions of $m_{b\bar{b}}$ in the signal regions and the eμ control regions of the 2-lepton channel. These distributions are obtained before the fitting. The red unstacked and unfilled histograms show the Higgs signals with the scale factors indicated in the legend. The lower panels in each plot show the ratio of the data and the predictions of the signals and the backgrounds. The hatched bands in the upper and lower panels show the total uncertainty, which includes the statistical and systematic uncertainties. Each plot shows the region indicated in the plot.

Table 6.6: List of the hyper-parameters used to train the BDTs for all channels. Exceptions for the 1-lepton VH and diboson training are given in brackets.

TMVA Setting	Value	Definition
BoostType	gradient boosting	Boost procedure
Shrinkage	0.5	Learning rate
SeparationType	Gini index	Node separation gain
PruneMethod	No Pruning	Pruning method
NTrees	200 (600 for 1-lepton VH)	Number of trees
MaxDepth	4 (2 for 1-lepton diboson)	Maximum tree depth
nCuts	100	Number of equally spaced cuts tested per variable per node
nEventsMin	5%	Minimum number of events in a node (% of total events)

6.6.2 Input variables

In this section, kinematic variables used in the training of the BDTs are described. The list of input variables for the BDT trainings is shown in Table 6.7.

Variables used in the previous result [16]

The following variables are also used in all the lepton channels in the analysis in this thesis:

- $m_{b\bar{b}}$: invariant mass of the dijet system constructed from the two b-tagged jets
- $\Delta R_{b\bar{b}}$: distance in η and ϕ between the two b-tagged jets
- $p_{\mathrm{T}}^{b_1}$: transverse momentum of the b-tagged jet with the higher p_{T} in the dijet system
- $p_{\mathrm{T}}^{b_2}$: transverse momentum of the b-tagged jet with the lower p_{T} in the dijet system
- p_{T}^{V}: transverse momentum of the vector bosons; given by the $E_{\mathrm{T}}^{\mathrm{miss}}$ in the 0 lepton channel, the vectorial sum of $E_{\mathrm{T}}^{\mathrm{miss}}$ and the transverse momentum of the lepton in the 1 lepton channel, and the vectorial sum of the transverse momenta of the pair of leptons in the 2 lepton channel
- $\Delta\phi(\boldsymbol{V}, \boldsymbol{bb})$: distance in ϕ between the vector boson candidate and the Higgs boson candidate. The vector boson candidate is the $E_{\mathrm{T}}^{\mathrm{miss}}$ in the 0 lepton channel, the vectorial sum of the $E_{\mathrm{T}}^{\mathrm{miss}}$ and the lepton in the 1 lepton channel and the di-lepton system in the 2 lepton channel. The Higgs candidate is reconstructed with the two b-tagged jets.
- $p_{\mathrm{T}}^{\mathrm{jet}_3}$: transverse momentum of the jet with the highest transverse momentum among central jets that are not b-tagged. The *central jet* is defined in Section 5.4. Only used for events with 3 or more signal jets.
- $m_{b\bar{b}j}$: invariant mass of the two b-tagged jets and the jet with the highest transverse momentum among central jets that are not b-tagged; only used for events with 3 or more signal jets.

The 0-lepton channel uses five variables in addition to the common variables:

- $|\Delta\eta(\boldsymbol{b}_1, \boldsymbol{b}_2)|$: distance in pseudo-rapidity η between the two b-tagged jets
- m_{eff} : scalar sum of $E_{\mathrm{T}}^{\mathrm{miss}}$, the p_{T} of the two b-jets and the p_{T} of the third jet if it is present

The 1-lepton channel uses seven variables in addition to the common variables:

- $E_{\mathrm{T}}^{\mathrm{miss}}$: missing transverse energy of the event
- $\min[\Delta\phi(\boldsymbol{\ell}, \boldsymbol{b})]$: distance in ϕ between the lepton and the closest b-tagged jet
- m_{T}^{W}: transverse mass of the W boson candidate, which is defined as $m_{\mathrm{T}}^{W} = \sqrt{2p_T^{\ell}E_{\mathrm{T}}^{\mathrm{miss}}(1-\cos(\Delta\phi(\ell, E_{\mathrm{T}}^{\mathrm{miss}})))}$
- $|\Delta y(\boldsymbol{V}, \boldsymbol{bb})|$: difference in rapidity between the Higgs boson candidate and the W boson candidate
- m_{top}: reconstructed mass of the leptonically decaying top quark

The last two variables require the p_z of a neutrino candidate (p_z^{ν}) to be determined, using m_W as a constraint to solve the quadratic equation:

$$p_z^{\nu} = \frac{1}{2(p_T^l)^2}\left[p_z^l X \pm E_l\sqrt{X^2 - 4(p_T^l)^2(E_{\mathrm{T}}^{\mathrm{miss}})^2}\right], \tag{6.2}$$

where

$$X = m_W^2 + 2p_x^l E_x^{\mathrm{miss}} + 2p_y^l E_y^{\mathrm{miss}}. \tag{6.3}$$

m_{top} is then reconstructed by selecting a jet from the two b-tagged jets, and a solution to Eq. 6.2 which minimizes m_{top}. If p_z^{ν} has an imaginary solution (i.e. $X^2 < 4(p_T^l)^2(E_{\mathrm{T}}^{\mathrm{miss}})^2$), the magnitude of $E_{\mathrm{T}}^{\mathrm{miss}}$ is corrected so that the discriminant in Eq 6.3 is equal to zero.

The 2-lepton channel uses four additional variables in addition to the common variables:

- $|\Delta\eta(\boldsymbol{V}, \boldsymbol{bb})|$: distance in η between the dilepton and dijet system of the b-tagged jets,
- $E_{\mathrm{T}}^{\mathrm{miss}}/\sqrt{S_{\mathrm{T}}}$: quasi-significance of the $E_{\mathrm{T}}^{\mathrm{miss}}$ in the event, defined with S_{T}, which is the scalar sum of the p_{T} of the leptons and the jets in the event,
- $m_{\ell\ell}$: invariant mass of the dilepton system.

The distributions of the input variables are shown in Figures 6.14, 6.15 and 6.16, comparing the processes: the VH signal, W + jets, Z + jets, diboson and $t\bar{t}$.

6.6.3 Performances compared to the dijet mass distribution

Significance that only takes into account the statistical uncertainty is improved by using BDT_{VH} with respect to the $m_{b\bar{b}}$ distributions as shown in Figure 6.17 and summarized in Table 6.8. The gain in the significance is 30%-60% depending on the channels.

The inclusion of the variable for Z-polarization improves the significance as shown in Table 6.9. The gain of the improvement is about 7%.

6.6.4 New variables added in the analysis

In addition to the variables brought from the previous result, the following new variables are introduced to the analysis.

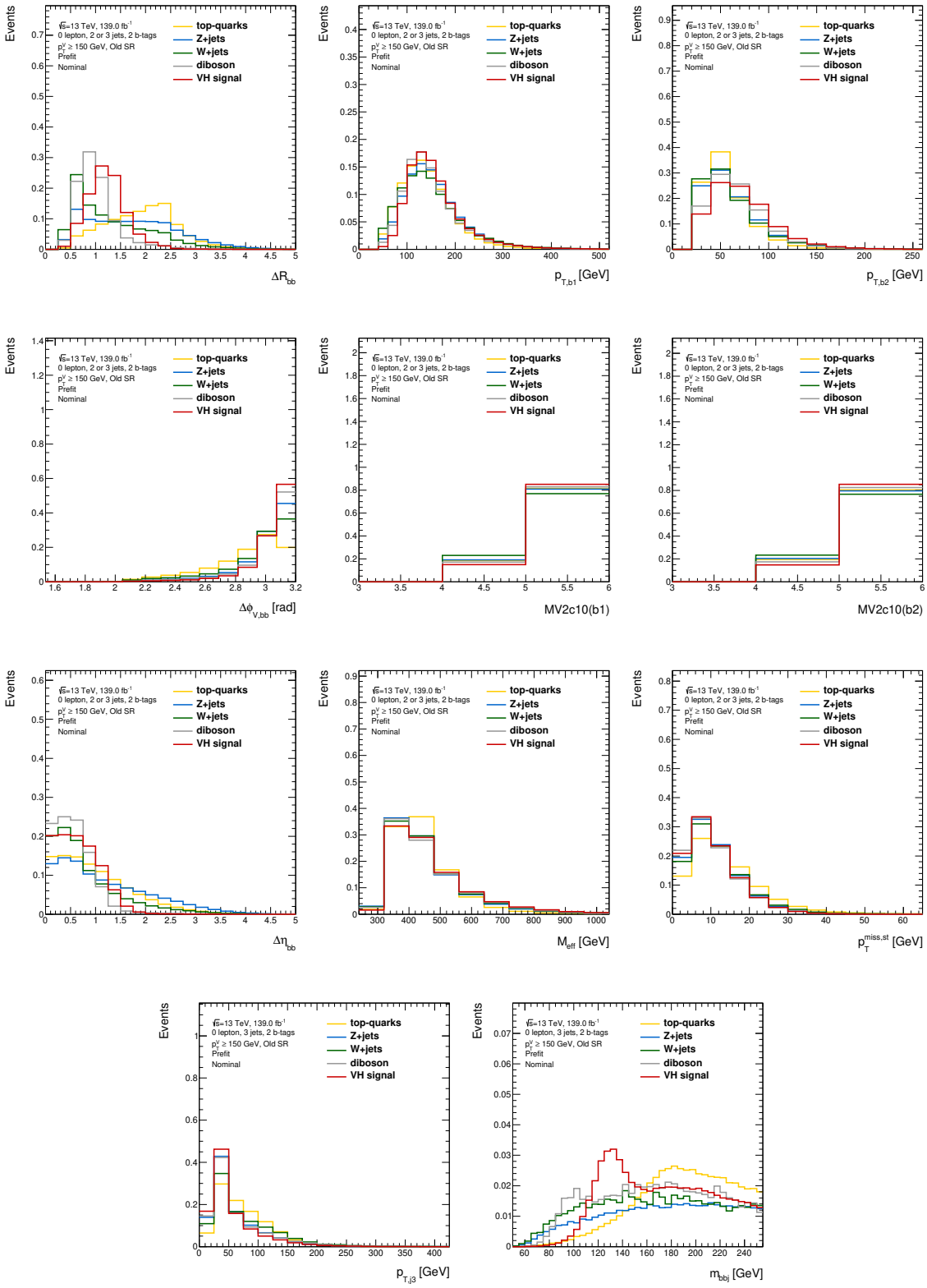

Figure 6.14: Distributions of input variables used in the 0-lepton channel for the signals and the backgrounds. The plots show the distributions summed for the signal and control regions of the categories with either two or three jet, and $p_{\mathrm{T}}^{V} \geq 150$ GeV except for the variables m_{bbj} and $p_{\mathrm{T},j3}$. These two variables are only defined in the three jet categories and shown in those regions.

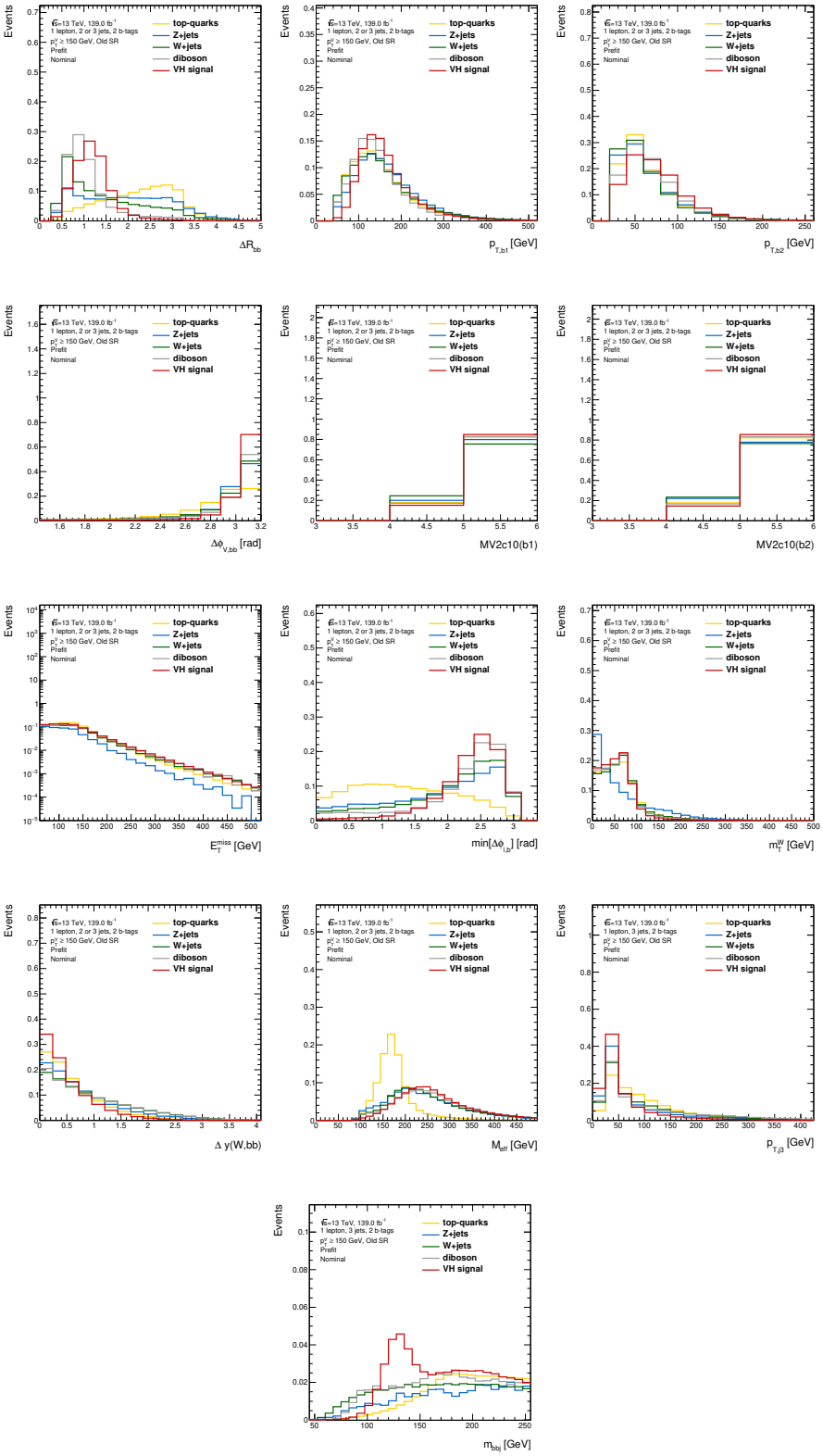

Figure 6.15: Distributions of input variables used in the 1-lepton channel for the signals and the backgrounds. The plots show the distributions summed for the signal and control regions of the categories with either two or three jet, and $p_{\mathrm{T}}^{V} \geq 150$ GeV except for the variables m_{bbj} and $p_{\mathrm{T},j3}$. These two variables are only defined in the three jet categories and shown in those regions.

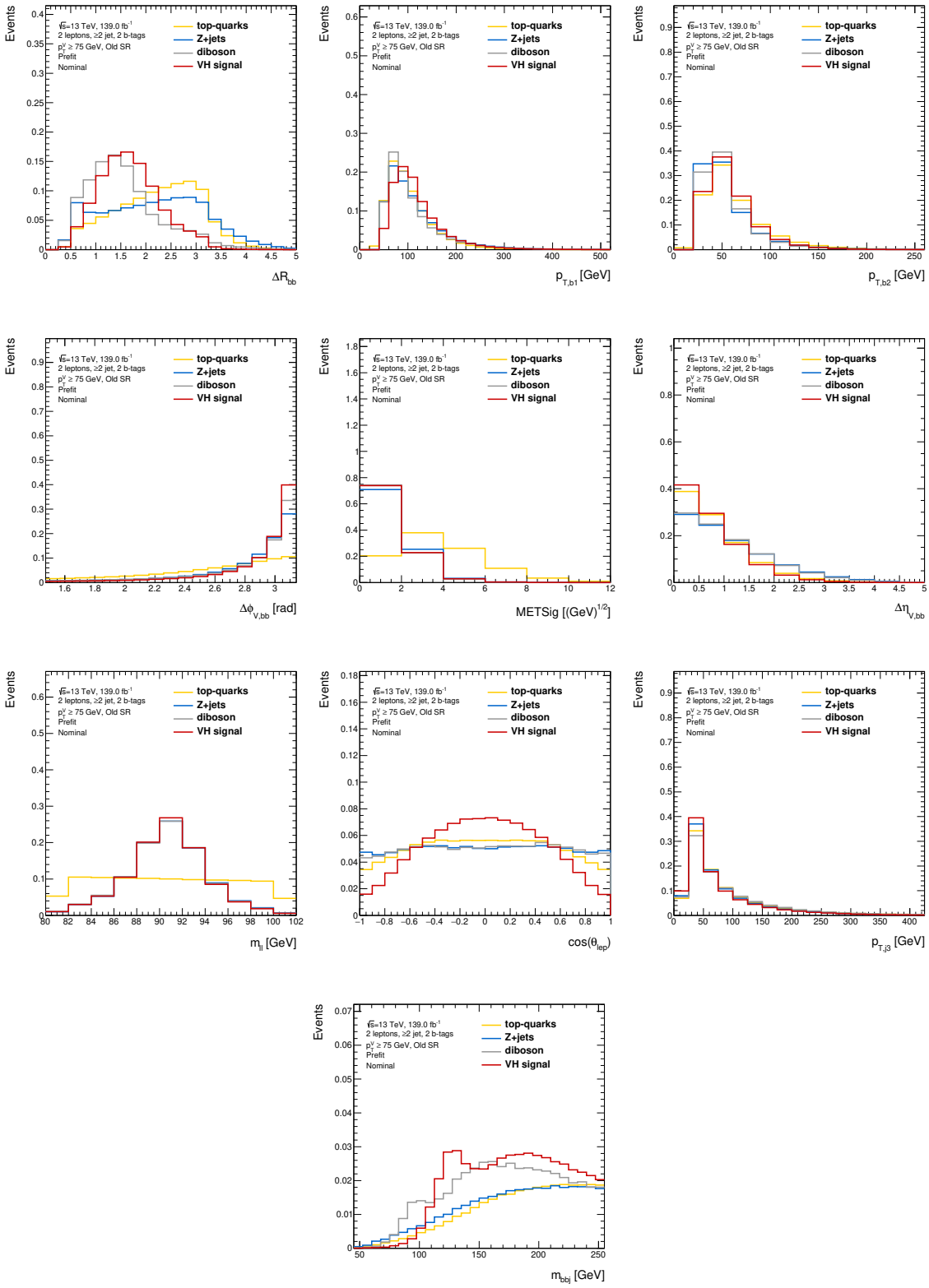

Figure 6.16: Distributions of input variables used in the 2-lepton channel for the signals and the backgrounds. The plots show the distributions summed for the signal and control regions of the categories with either two or three jet, and $p_{\mathrm{T}}^{V} \geq 75$ GeV except for the variables m_{bbj} and $p_{\mathrm{T},j3}$. These two variables are only defined in the three jet categories and shown in those regions.

Table 6.7: List of the input variables used to train the BDTs for the 0-, 1- and 2-lepton channels, where the × symbol indicates the inclusion of a variable.

Variable	0-lepton	1-lepton	2-lepton
$m_{b\bar{b}}$	×	×	×
$\Delta R_{b\bar{b}}$	×	×	×
$p_{\mathrm{T}}^{b_1}$	×	×	×
$p_{\mathrm{T}}^{b_2}$	×	×	×
p_{T}^{V}	×	×	×
$\Delta\phi(\boldsymbol{V}, \boldsymbol{bb})$	×	×	×
MV2c10(b_1)	×	×	
MV2c10(b_2)	×	×	
$E_{\mathrm{T}}^{\mathrm{miss}}$	$\equiv p_{\mathrm{T}}^{V}$	×	
$\lvert\Delta\eta(\boldsymbol{b_1}, \boldsymbol{b_2})\rvert$	×		
m_{eff}	×		
$p_{\mathrm{T}}^{\mathrm{miss,st}}$	×		
$\min[\Delta\phi(\boldsymbol{\ell}, \boldsymbol{b})]$		×	
m_{T}^{W}		×	
$\lvert\Delta y(\boldsymbol{V}, \boldsymbol{bb})\rvert$		×	
m_{top}		×	
$\lvert\Delta\eta(\boldsymbol{V}, \boldsymbol{bb})\rvert$			×
$E_{\mathrm{T}}^{\mathrm{miss}}/\sqrt{S_{\mathrm{T}}}$			×
$m_{\ell\ell}$			×
$\cos\theta(\boldsymbol{\ell^-}, \boldsymbol{Z})$			×
	Only in 3-jet events		
$p_{\mathrm{T}}^{\mathrm{jet_3}}$	×	×	×
m_{bbj}	×	×	×

Track-based soft $E_{\mathrm{T}}^{\mathrm{miss}}$ term

As introduced in Section 5.5, the track based soft $E_{\mathrm{T}}^{\mathrm{miss}}$ term [135] is the vector sum of the p_{T} of all tracks in the events that are not associated with any reconstructed objects in the 0-lepton channel. This variable improves the expected significance by 1% to 3% in the 1-lepton channel depending on the analysis regions.

Scores of the b-tagging discriminant

Binned distribution of the MV2c10 b-tagging discriminant for the leading and sub-leading b-tagged jets is added in the input variables for the 0- and 1-lepton channels. The bins in this distribution are identical with ones defined for the pseudo-continuous b-tagging working point explained in Section 5.6. These variables improve the discrimination power by rejecting the c-jet component in the $t\bar{t}$ and single top Wt-channel backgrounds in the 0- and 1-lepton channels, where a top quark decays as $t \to bW$ ($W \to cq$), and the c-jet is misidentified as a b-jet. The gain by including these variables is 7% in the 0-lepton channel and 10% in the 1-lepton channel in the expected significance.

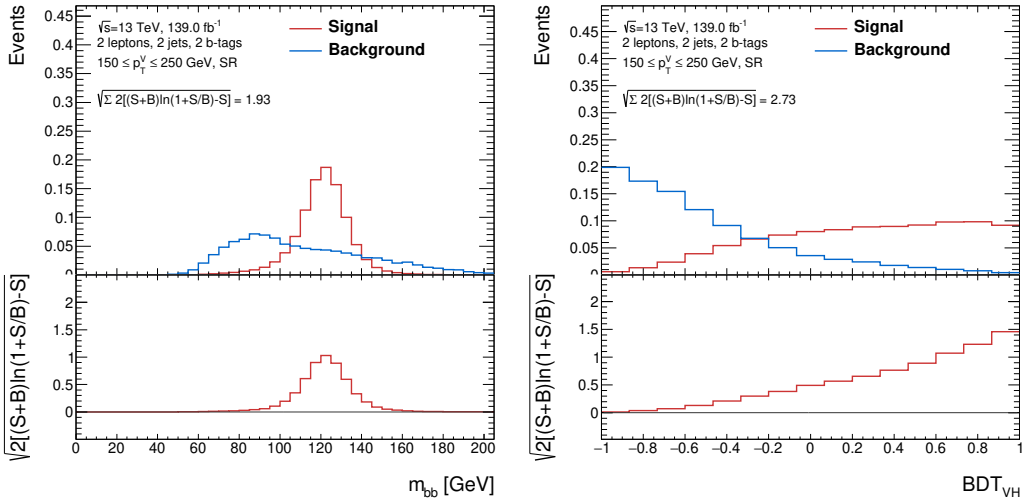

Figure 6.17: Comparison of the signal and background processes in the $m_{b\bar{b}}$ and BDT$_{VH}$ shapes in the signal region of the 2-lepton channels with $150 \leq p_{\mathrm{T}}^{V} < 250$ GeV and 2 jets. The significance is computed including only the statistical uncertainty by using the formula: $\sqrt{\sum_{\mathrm{bin}}[(S+B)\ln(1+S/B)) - S]}$.

Table 6.8: Comparison of the expected significance obtained from the $m_{b\bar{b}}$ and BDT$_{VH}$ distributions in each category and channel.

Channel	Category		Significance		
			$m_{b\bar{b}}$	BDT$_{VH}$	Gain
0 lepton	$150 \leq p_{\mathrm{T}}^{V} < 250$ GeV	2 jets	2.77	3.80	37%
		3 jets	1.53	2.46	61%
	$p_{\mathrm{T}}^{V} \geq 250$ GeV	2 jets	2.53	3.27	29%
		3 jets	1.51	2.04	35%
	Combination		4.32	5.94	38%
1 lepton	$150 \leq p_{\mathrm{T}}^{V} < 250$ GeV	2 jets	2.07	3.60	74%
		3 jets	0.91	2.05	125%
	$p_{\mathrm{T}}^{V} \geq 250$ GeV	2 jets	2.55	3.78	48%
		3 jets	1.23	2.17	76%
	Combination		3.62	6.02	66%
2 leptons	$75 \leq p_{\mathrm{T}}^{V} < 150$ GeV	2 jets	1.28	2.03	59%
		≥3 jets	1.06	1.76	66%
	$150 \leq p_{\mathrm{T}}^{V} < 250$ GeV	2 jets	1.93	2.73	41%
		≥3 jets	1.65	2.47	50%
	$p_{\mathrm{T}}^{V} \geq 250$ GeV	2 jets	1.91	2.28	19%
		≥3 jets	1.40	1.95	39%
	Combination		3.85	5.46	42%

Polarization of the Z-boson

$\cos\theta(\boldsymbol{\ell}^{-}, \boldsymbol{Z})$ is defined in the 2-lepton channel as the angle between the negatively charged lepton and the flight direction of the Z-boson in the rest-frame of the Z-boson as shown in Figure 6.18. This variable makes use of the difference in the polarization of the Z-boson between the signal and the Z+jets background as suggested in [139]. The polarization of the Z boson is almost 100% longitudinal for both the $qq \to ZH$ and $gg \to ZH$ signal whereas the polarization is transverse for the background processes, Z + jets and ZZ. This means that, in the rest frame of the Z boson, the decay leptons come in the transverse (longitudinal) direction with respect to the flight direction of the Z boson for the signal (background) as shown in Figure 6.19. The distributions of this variable for the signal, the backgrounds, and the data are shown in Figure 6.20. These distributions show the difference between the signal and the backgrounds as well as the data are described well by the Monte Carlo simulations.

A significant gain by 7% in the 2 lepton training performance is observed with this variable.

6.6.5 Prefit comparisons of the data and Monte-Carlo

The distributions of the data and the MC predictions in the BDT output are shown in Figures 6.21, 6.22 and 6.23. It should be mentioned that the $t\bar{t}$ background in the 2-lepton channel is modeled with a special

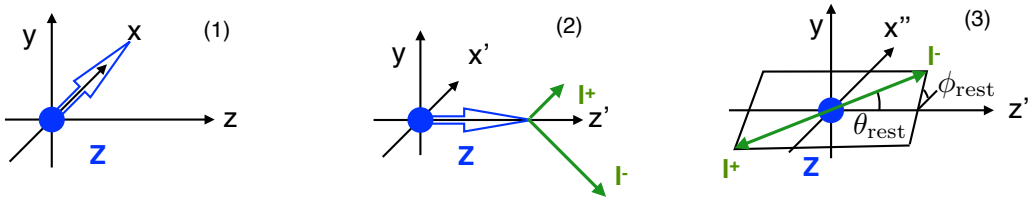

Figure 6.18: Definition of the angular variable $\phi_{\rm lep}$ in the ZH production. To define $\phi_{\rm lep}$, the following steps are needed: (1) Lorentz boost along the z-axis and spatial rotation with respect to the z-axis are applied to the coordinate frame where the Z boson is moving to the x-axis. (2) Rotation with respect to the y-axis is applied moving to the frame where the Z boson is flying along the z'-axis. (3) Lorentz boost along z'-axis is applied moving to the rest frame of the Z boson. The $\theta_{\rm lep}$ angle is defined as the angle between the negatively charged lepton and the z'-axis. The $\phi_{\rm lep}$ angle is defined as the angle between the decay plane and the $x''z'$-plane.

Table 6.9: Expected significance with improvement by the Z-polarization variable. The significance is computed including only the statistical uncertainty by using the formula: $\sqrt{\sum_{\rm bin}[(S+B)\ln(1+S/B)) - S]}$.

Channel	Category		Significance		
			w/o Z-polarization	w/ Z-polarization	Gain
2 leptons	$75 \le p_{\rm T}^{V} < 150$ GeV	2 jets	1.62	1.68	3.7%
		≥3 jets	1.59	1.66	4.4%
	$150 \le p_{\rm T}^{V} < 250$ GeV	2 jets	2.10	2.26	7.6%
		≥3 jets	2.11	2.30	9.0%
	$p_{\rm T}^{V} \ge 250$ GeV	2 jets	1.82	1.98	8.9%
		≥3 jets	1.66	1.81	9.0%
	Combination		4.48	4.81	7.4%

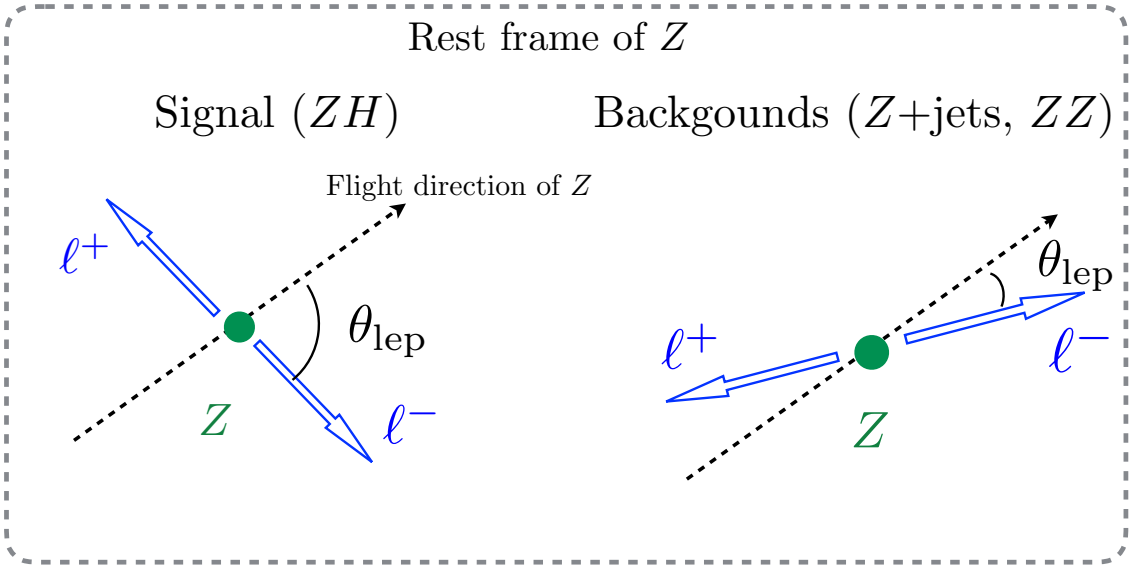

Figure 6.19: Typical decay angles of $Z \to \ell^+\ell^-$ for the signal and the backgrounds, Z + jets and ZZ. The leptons decay in the transverse (longitudinal) direction for the signal (backgrounds) regarding the flight direction of the Z boson in the rest frame of Z.

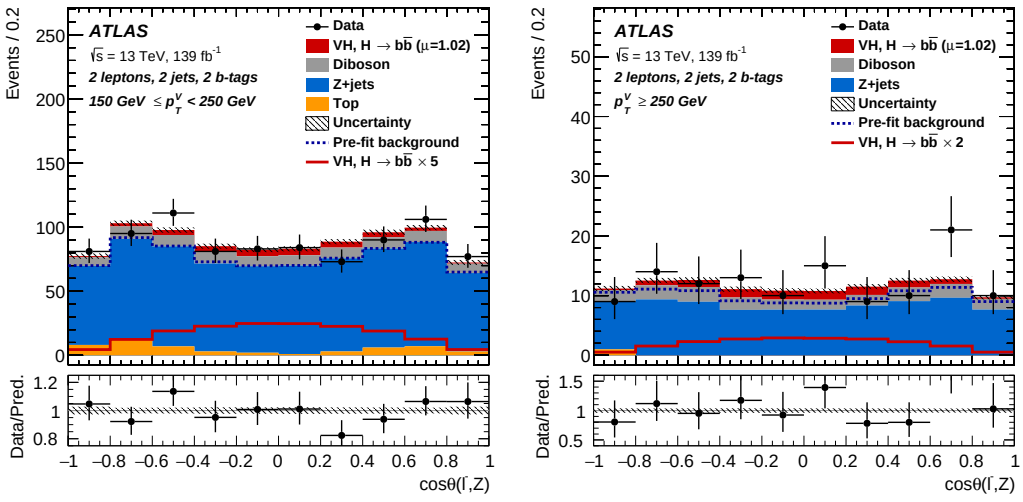

Figure 6.20: Distribution of $\cos\theta(\boldsymbol{\ell^-}, \boldsymbol{Z})$ for the signal, the backgrounds, and the data in the 2 jets, $150 \leq p_{\mathrm{T}}^V < 250$ GeV and $p_{\mathrm{T}}^V \geq 250$ GeV categories. The stacked histograms show the prediction after the fitting. The red unstacked and unfilled histograms show the VH signals with the scale factors indicated in the legend. The lower panels show the ratio of the data and the prediction of the signals and the backgrounds. The hatched bands in the lower and upper panels show the total uncertainty that includes only the systematic uncertainties.

method that is discussed in Section 7.2.2 instead of the MC prediction shown here. These MC predictions are corrected in the fitting procedure discussed in Chapter 9.

6.7 Analysis validations

Diboson processes that include $Z \to b\bar{b}$ and either $Z \to \ell\ell, \nu\nu$ or $W \to \ell\nu$ are backgrounds with a similar kinematics to the Higgs signals. As already mentioned in Section 6.6.1, it is possible to construct an analysis to measure these diboson processes by training special BDTs (BDT_{VZ}), regarding them as the signal. This

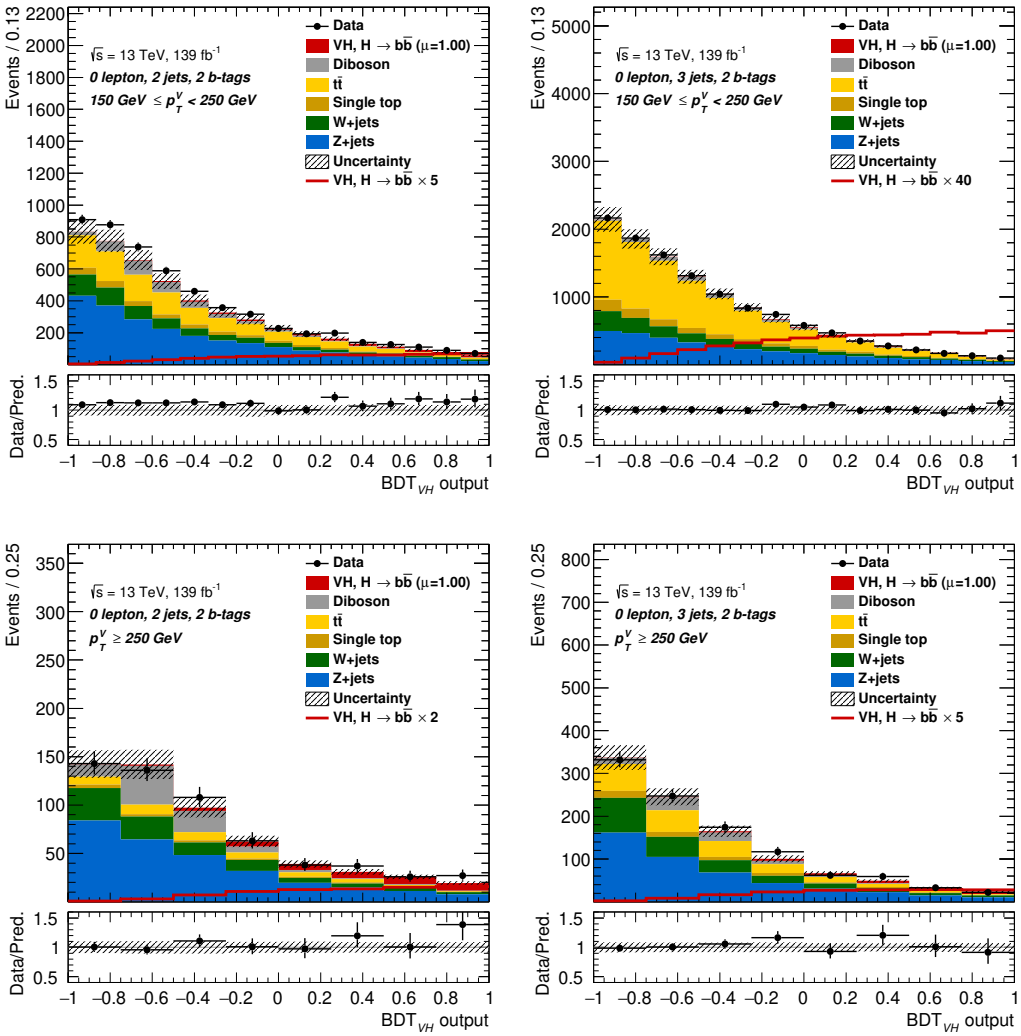

Figure 6.21: Comparisons of the data and the prediction in the distributions of BDT_{VH} in the four signal regions of the 0-lepton channel. These distributions are obtained before the fitting. The red unstacked and unfilled histograms show the Higgs signals with the scale factors indicated in the legend. The lower panels in each plot show the ratio of the data and the predictions of the signals and the backgrounds. The hatched bands in the upper and lower panels show the total uncertainty, which includes the statistical and systematic uncertainties.

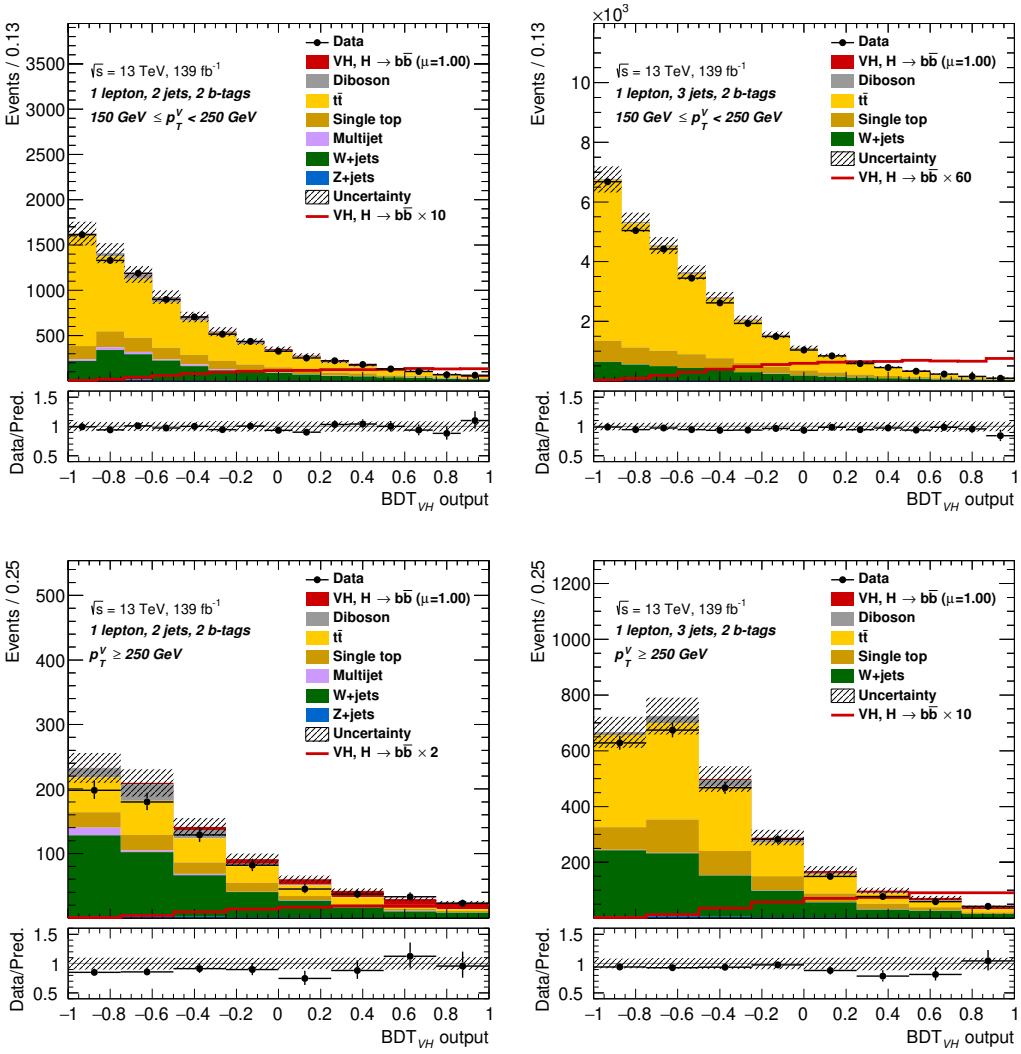

Figure 6.22: Comparisons of the data and the prediction in the distributions of BDT_{VH} in the four signal regions of the 1-lepton channel. These distributions are obtained before the fitting. The red unstacked and unfilled histograms show the Higgs signals with the scale factors indicated in the legend. The lower panels in each plot show the ratio of the data and the predictions of the signals and the backgrounds. The hatched bands in the upper and lower panels show the total uncertainty, which includes the statistical and systematic uncertainties.

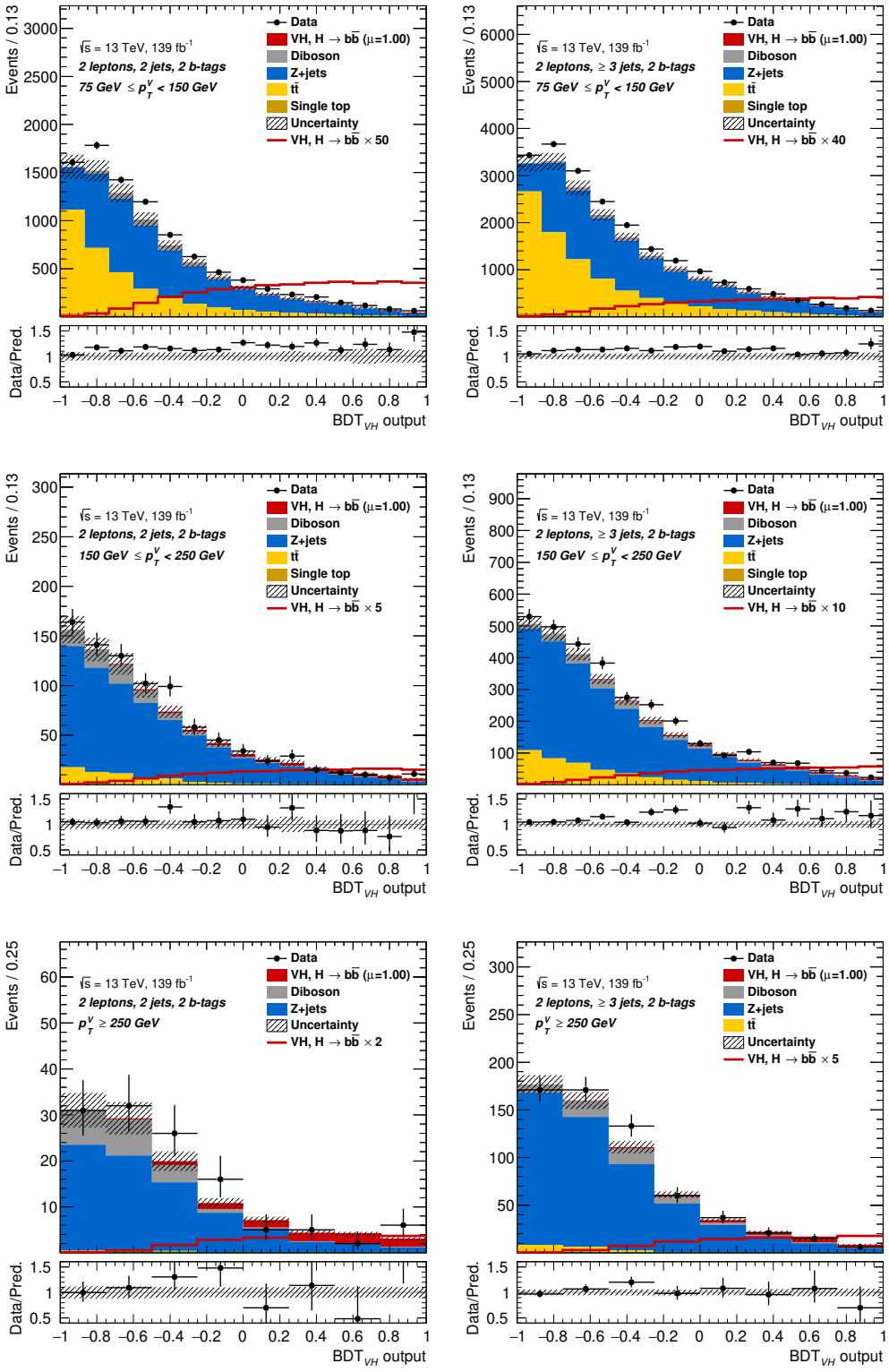

Figure 6.23: Comparisons of the data and the prediction in the distributions of BDT_{VH} in the six signal regions of the 2-lepton channel. These distributions are obtained before the fitting. The red unstacked and unfilled histograms show the Higgs signals with the scale factors indicated in the legend. The lower panels in each plot show the ratio of the data and the predictions of the signals and the backgrounds. The hatched bands in the upper and lower panels show the total uncertainty, which includes the statistical and systematic uncertainties.

method should work as a validation of the background estimation (supposing that the diboson processes do not deviate from the Standard Model). Results of this validation are shown in Section 10.2.1.

Another naive strategy to estimate the signal is to fit the $m_{b\bar{b}}$ distribution where Higgs forms a peak. It is actually possible to perform such an analysis with 30% lower sensitivity as shown in Section 6.6.3. It provides another opportunity for validation of results, especially to confirm that there is no mistake in the usage of the BDT. Results of this cross-check is shown in Section 10.2.2.

7 Background estimation

In order to estimate the backgrounds, both Monte Carlo-based estimation and data-driven estimation are employed depending on the processes.

7.1 MC-based estimation

The normalization and the shape of the backgrounds, W + jets, Z + jets, $t\bar{t}$ (in the 0- and 1-lepton channels), the single top production and the diboson production, are modeled based on Monte Carlo simulation. The Monte Carlo simulation involves systematic uncertainties affecting both the normalization and the shape of distributions. The considered uncertainties are discussed in Chapter 8. It is desired to adopt an approach without relying MC simulation too much for the dominant backgrounds, W + jets, Z + jets and $t\bar{t}$. The dominant backgrounds, W + jets, Z + jets and $t\bar{t}$, should be compared and corrected to the data in the control regions defined in Section 6.5 without relying on the simulation too much. These comparison and correction are automatically performed in statistical analysis (*fit*) discussed in Chapter 9.

7.2 Data-driven estimation

7.2.1 Estimation of multi-jet background

QCD induced multijet background is involved after the final event selection defined in Section 6.3 due to mismeasurement of jet energy (0-lepton) and *fake leptons* (1-, 2-lepton). The fake leptons arise either due to jets making similar clusters to electrons in the electromacnetic calorimeter or non-prompt electrons and muons from the decays of heavy hadrons. Since it is difficult to simulate such events accurately, data-driven approaches are adopted for all the lepton channels.

Since the multijet background is negligible in the 0- and 2-lepton channels as evaluated in Ref. [16], a short argument is given here. In the 0-lepton channel, the additional cuts are used when defining the signal regions (SRs) to reduce the multijet (see Section 6.3). It is negligible in the 2-jet categories and O(1%) in the 3-jet categories. In the 2-lepton channel, the requirement of existence of two isolated leptons that form the invariant mass consistent with a Z boson significantly reduces the multijet background. A study is performed using events with same sign leptons, and shows that it is negligible.

The multijet background is also small in the 1-lepton channel, but it has a non-negligible contribution. A method called template method is performed as well as Ref. [16]. The description can be found in Appendix D.

7.2.2 Data driven estimation of the top background in the 2 lepton channel

The $t\bar{t}$ modeling uncertainty is one of the leading systematic sources in the previous work [16]. The uncertainties on the shape of the distribution have approximately a 10% effect as shown later. In order to reduce the impact of the modeling and increase the robustness of the analysis, a data-driven estimation of $t\bar{t}$ and single top backgrounds in the 2 lepton channel is adopted. Distributions of data as a function of a variable in the eμ control regions (eμCR) introduced in Section 6.5.2 can directly be used as a template for the top background ($t\bar{t}$ and single top) in the signal regions (SR). The schematic diagram of this method is shown in Figure 7.1. As expressed by the equation:

$$N^{\mathrm{SR}}_{\mathrm{top,\,data}} = \frac{N^{\mathrm{e}\mu\mathrm{CR}}_{\mathrm{top,\,data}}}{N^{\mathrm{e}\mu\mathrm{CR}}_{\mathrm{top,\,MC}}} \times N^{\mathrm{SR}}_{\mathrm{top,\,MC}} = \frac{N^{\mathrm{SR}}_{\mathrm{top,\,MC}}}{N^{\mathrm{e}\mu\mathrm{CR}}_{\mathrm{top,\,MC}}} \times N^{\mathrm{e}\mu\mathrm{CR}}_{\mathrm{top,\,data}}\,, \tag{7.1}$$

the fundamental concept of the method is to estimate the top background in the signal regions by deriving two quantities, $N^{\mathrm{SR}}_{\mathrm{top,\,MC}}/N^{\mathrm{e}\mu\mathrm{CR}}_{\mathrm{top,\,MC}} (\equiv \alpha)$ and $N^{\mathrm{e}\mu\mathrm{CR}}_{\mathrm{top,\,data}}$. Due to the very high purity of the top background in the eμCRs (99.5-99.9% depending on the categories, see Section 6.5.2), the $N^{\mathrm{e}\mu\mathrm{CR}}_{\mathrm{top,\,data}}$ can be considered as the distribution of data in the eμCR. The extrapolation factor α can be estimated in Monte Carlo simulations.

An important aspect of this approach is the uncertainties of α. Most of the systematic uncertainties on the extrapolation factor α, especially theoretical modeling and jet-related systematic uncertainties, are canceled because the same kinematic selections are applied to both the SRs and eμCRs, and $t\bar{t}$ and single top backgrounds are flavor symmetric. Thus, in this data-driven background estimation, elimination of the following two uncertainties are focused on:

(i) Experimental systematics related to the calibration of the object reconstruction and the identification: the energy calibration of jets and the b-tagging.

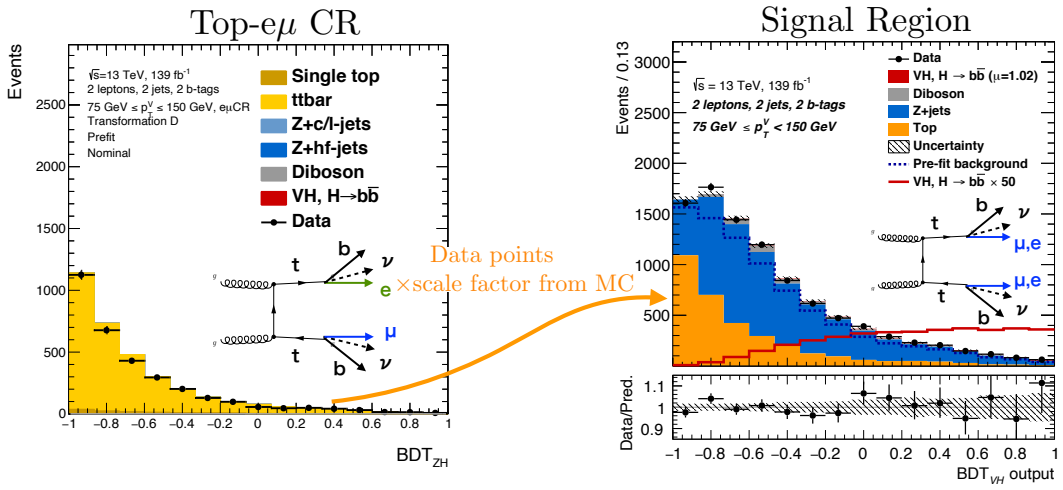

Figure 7.1: Schematic diagram of the data-driven estimation of the top background. The data points are taken from the eμ control region, and embedded in the signal regions as the template of the top background by multiplying the scale factor derived from the Monte Carlo simulation. The Feynman diagrams shown in the plots indicate the decay channels contributing to the two regions.

(ii) Theoretical systematics from modeling and MC dependence.

Since the dominant source of the uncertainties in the data-driven background estimation is the statistics of the data, the statistical uncertainties derived from the eμCRs data are included in the final fit of the analysis. The mathematical implementation of this statistical uncertainty is discussed in Section 9.2.

This method relies on the assumption that the shapes of the $t\bar{t}$ and single top backgrounds in the SR are the same as those in the eμCR. Validation studies are performed in the following to show that α does not depend on any kinematic variables i.e. the distribution of the top background in the SRs and the eμCRs agree within statistical uncertainty.

The benefit, i.e. the cancellation of the systematic uncertainties in the extrapolation factor, is demonstrated in the following sections by comparing systematic uncertainties on shapes in the SRs and the eμCRs.

The derivation of the extrapolation factors and the result are presented in the last part of this section. The extrapolation factors are derived from the top background without the separation by p_{T}^{V}. Individual values are calculated by taking into account the number of jets.

Comparison of distributions in between signal and eμ control regions

In this section, the p_{T}^{V} and BDT_{VH} distributions in the SRs and the eμCRs are compared using the processes listed in Table 7.1, in order to validate the assumption that the top background in the eμCRs is kinematically identical to those in the SRs. The final discriminant, BDT_{VH}, is compared in Figure 7.2, which shows the agreement of the SRs and the eμCRs within the statistical uncertainties in the categories with $75 \leq p_{\mathrm{T}}^{V} < 150$ GeV and with 2 jets or $\geq$3 jets.

In order to investigate the dependence of α on p_{T}^{V}, the same comparison is performed for the p_{T}^{V} distributions for the events with 2 jets or $\geq$3 jets separately. As shown in Figure 7.3 no dependence on p_{T}^{V} is found.

Cancellation of systematics

The cancellation of systematics results from the same systematic variations in the SRs and the eμCRs. We can confirm that both of the uncertainties create the same variations in the SRs and the eμCRs in Figures 7.4 and 7.5, and systematic uncertainties on α are consistently canceled, not depending on these variables.

The method can be applied to all the sources of systematic uncertainties. To demonstrate that, the impacts from every source of the systematic uncertainties on the yields of the SR and the eμCR and on the ratio of the yields are computed, as shown in Figures 7.6 and 7.7. Similar values of impact for each uncertainty are found in the SR and the eμCR, and therefore the uncertainty is canceled when the ratio is taken.

Table 7.1: The top MC samples used in the comparison between the SRs and the eμCRs, to assess the extrapolation factor.

Production process	Decay mode
$t\bar{t}$	full-leptonic decays
$t\bar{t}$	semi-leptonic decays
single top (Wt, s and t-channel)	full- and semi-leptonic decay

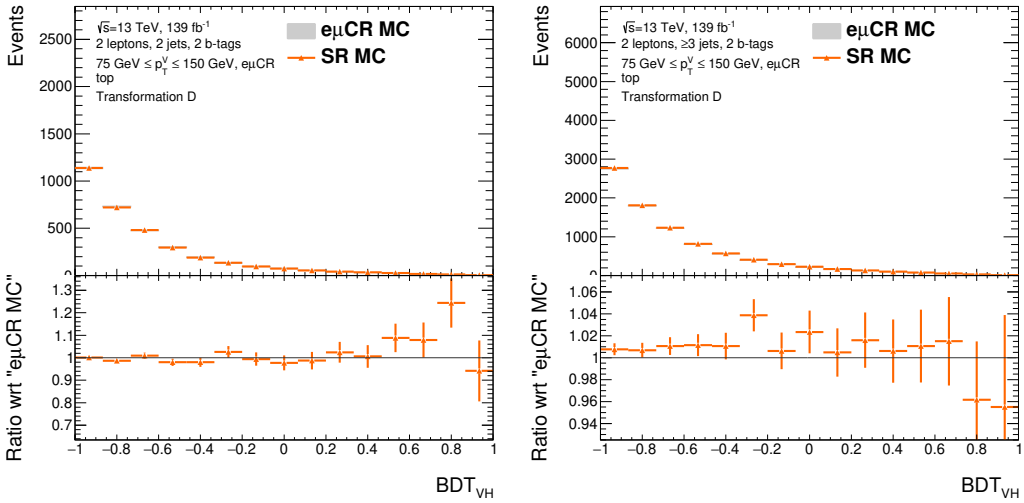

Figure 7.2: Comparison of the BDT distributions in the SRs and the eμCRs in the 2-jet (left) and $\geq$ 3-jet (right) categories for the events with $75 \leq p_{\mathrm{T}}^{V} < 150$ GeV. The distributions are the sum of the processes listed in Table 7.1.

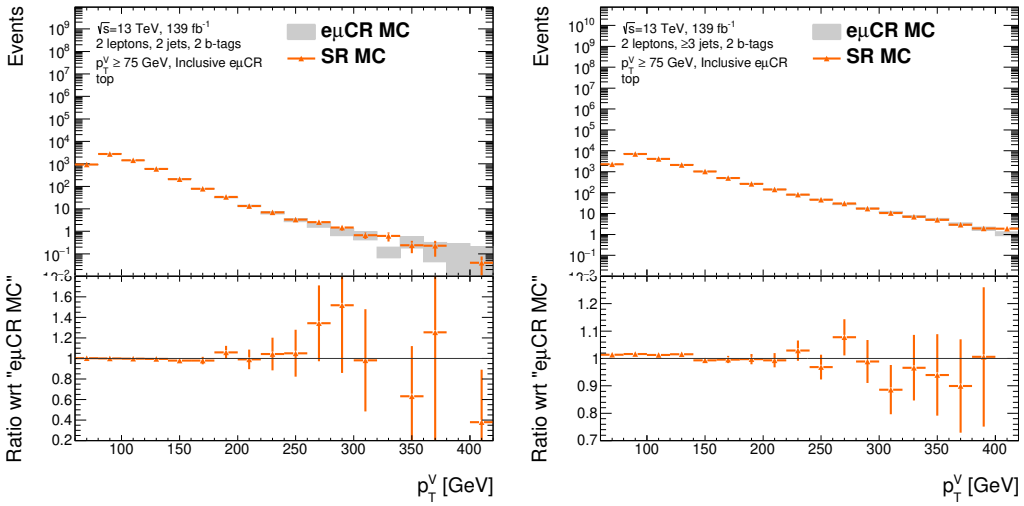

Figure 7.3: Comparison of the p_{T}^{V} distributions in the SRs and the eμCRs in the 2-jet (left) and $\geq$ 3-jet (right) categories. The distributions are the sum of the processes listed in Table 7.1. In these plots, the "SR" indicates the sum of the SRs, the low-ΔR-CRs, and the high-ΔR-CRs. The "eμCR" indicates the $e\mu$ regions corresponding to these same-flavor SRs and CRs.

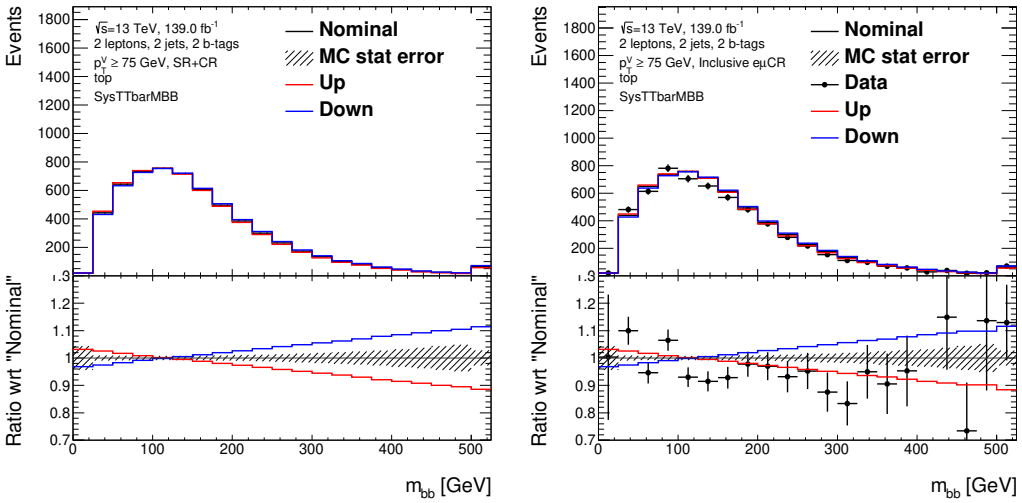

Figure 7.4: Systematic uncertainty on the $m_{b\bar{b}}$ shape in the SR (left) and the eμCR (right) in the 2-jet, $p_{\mathrm{T}}^{V} \geq 75$ GeV category. Events in each distribution are the sum of the processes listed in Table 7.1. In these plots, the "SR" indicates the sum of the SRs, the low-ΔR-CRs, and the high-ΔR-CRs. The "eμCR" indicates the $e\mu$ regions corresponding to these same-flavor SRs and CRs.

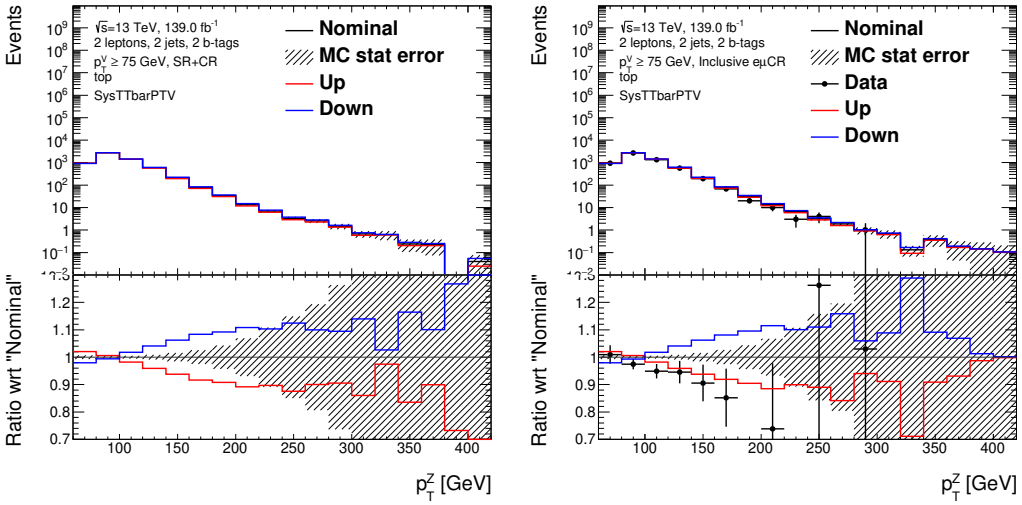

Figure 7.5: Systematic uncertainty on the p_{T}^{V} shape in the SR (left) and the eμCR (right) in the 2-jet, $p_{\mathrm{T}}^{V} \geq 75$ GeV category. Events in each distribution are the sum of the processes listed in Table 7.1. In these plots, the "SR" indicates the sum of the SRs, the low-ΔR-CRs, and the high-ΔR-CRs. The "eμCR" indicates the $e\mu$ regions corresponding to these same-flavor SRs and CRs.

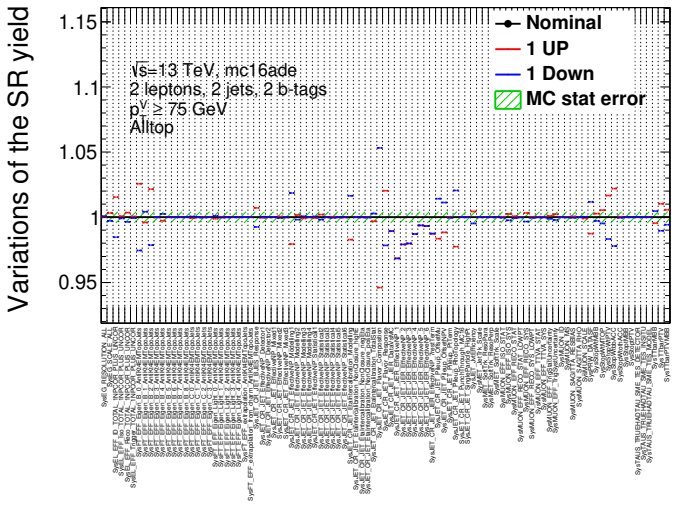

(a) SR

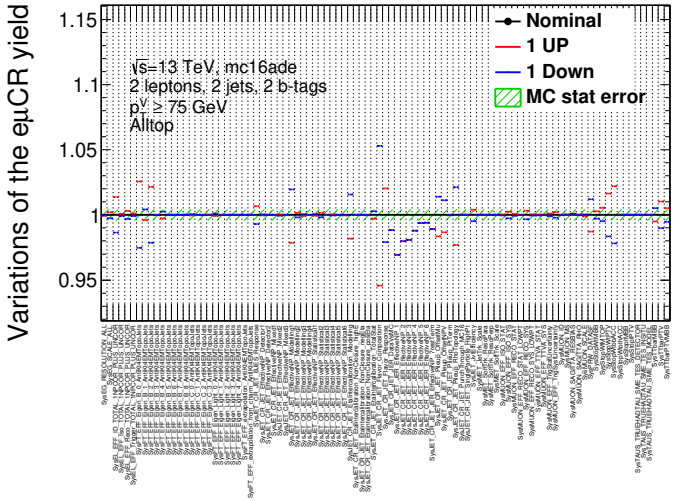

(b) eμCR

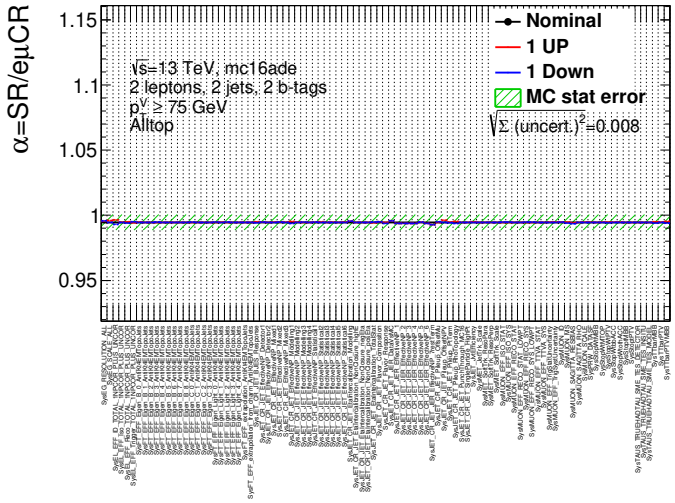

(c) Ratio

Figure 7.6: All systematic uncertainties on the yield of the SR (top) and the eμCR (middle) in the 2-jet category, and the uncertainties on the ratio, α (bottom). All the systematic uncertainties are listed in the x-axis. In these plots, the "SR" indicates the sum of the SRs, the low-ΔR-CRs, and the high-ΔR-CRs. The "eμCR" indicates the $e\mu$ regions corresponding to these same-flavor SRs and CRs.

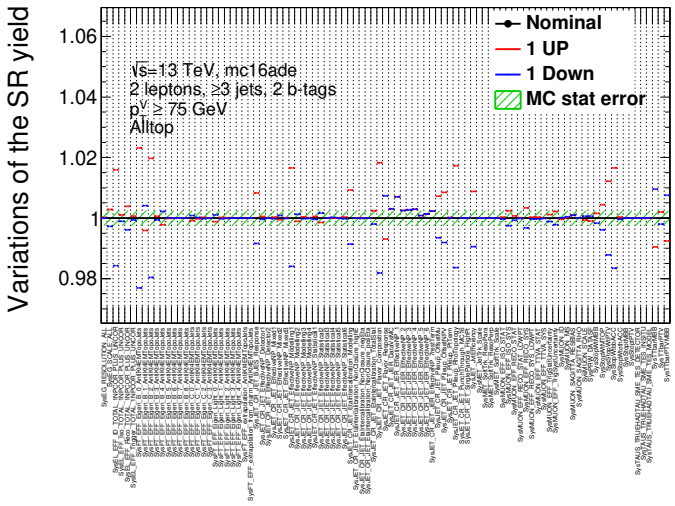

(a) SR

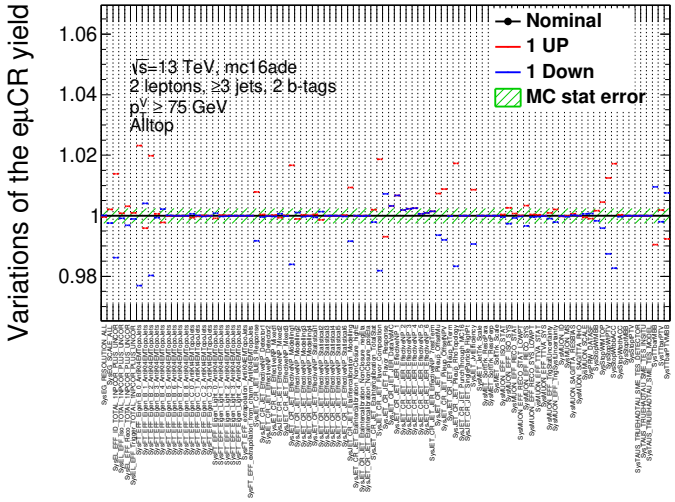

(b) eμCR

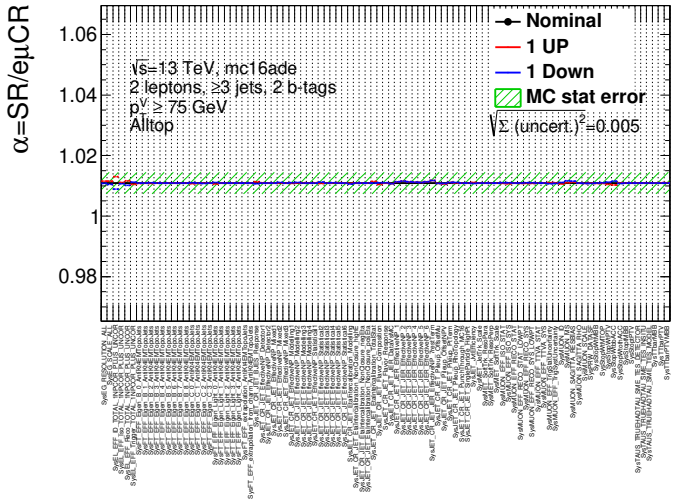

(c) Ratio

Figure 7.7: All systematic uncertainties on the yield of the SR (top) and the eμCR (middle) in the ≥3-jet category, and the uncertainties on the ratio, α (bottom). All the systematic uncertainties are listed in the x-axis. In these plots, the "SR" indicates the sum of the SRs, the low-ΔR-CRs, and the high-ΔR-CRs. The "eμCR" indicates the $e\mu$ regions corresponding to these same-flavor SRs and CRs.

Scale factors in each sample

To check the consistency of the scale factors between the MC samples listed in Table 7.1, the comparisons of the BDT output in the SR and the eμCR are made for the samples separately.

The comparisons of the BDT in the full-leptonic $t\bar{t}$, semi-leptonic $t\bar{t}$ and full- and semi-leptonic single top (Wt, s and t-channel) samples are shown in Figures 7.8, 7.9 and 7.10, respectively. While the ratios for the full-leptonic $t\bar{t}$ and single top are around 1, they are, for the semi-leptonic $t\bar{t}$ events, around 1.5 in the ≥ 3 jet category rather than 1 due to contribution from the same sign ee events in the signal region.

This scale factor of 1.5 can be explained by the following argument. $f(qqbb \to e^{\pm}bbj)$ and $f(qqbb \to \mu^{\pm}bbj)$ are defined as the fake rates of the $qqbb$ partonic final state reconstructed as $ebbj/\mu bbj$ including fake e/μ. $N(e^{\pm}qqbb)$ and $N(\mu^{\pm}qqbb)$ are defined as the number of events at truth level. The true/reconstructed final states and the expected yields in the SRs and the eμCRs are summarized as shown in Table 7.2.

Since the number of events for events including a true electron and muon are the same ($N(e^{\pm}qqbb) = N(\mu^{\pm}qqbb) = N(\ell^{\pm}qqbb)$), the expected yields of events are:

$$\text{SRs}: \quad N(\ell^{\pm}qqbb) \cdot [f(qqbb \to e^{\mp}bbj) + f(qqbb \to \mu^{\mp}bbj)] + N(\ell^{\pm}qqbb) \cdot f(qqbb \to e^{\pm}bbj), \tag{7.2}$$

$$e\mu\text{CRs}: \quad N(\ell^{\pm}qqbb) \cdot [f(qqbb \to e^{\mp}bbj) + f(qqbb \to \mu^{\mp}bbj)]. \tag{7.3}$$

The second term of the equation 7.2 expresses the same-sign ee events and explains the origin of the scale factor of ≥ 1 when we measure it using the semi-leptonic $t\bar{t}$ events.

The fake events from the semi-leptonic $t\bar{t}$ are much less in the 2 jets category due to the small probability of the parton level final state, $\ell^{\pm}qqbb$, to be reconstructed as a 2-jet event. Thus, the scale factors are different in the categories with 2 and more than 2 jets as discussed in the last part of this section. Since the impact on the shapes by including the semi-leptonic $t\bar{t}$ sample is confirmed to be smaller than the statistical uncertainty, it is enough to have individual extrapolation factors for 2 and ≥ 3 jets.

Derivation of the extrapolation factors

The extrapolation factors for 2-jets and $\geq$ 3-jets are shown in the bottom plots of Figures 7.6 and 7.7, respectively. The central value of each extrapolation factor is identified as the ratio of the nominal yields in the SRs to that in the eμCRs. The uncertainty is separated into the MC statistical uncertainty and the others remaining systematic uncertainties, and expressed as:

$$\text{Uncertainty} = \sqrt{(\text{MC stat. unc.})^2 + \sum_{s \in \text{systematics}} \sigma_s^2} \tag{7.4}$$

Table 7.2: Summary of true and reconstructed final states of semi-leptonic ttbar events, and their expected yields.

Region	True →reconstructed final states	Expected yields
SR	$e^{\pm}qqbb \to e^{\pm}ebbj\mu^{\pm}$ $\mu^{\pm}qqbb \to \mu^{\pm}\mu^{\mp}bbj$	$N(e^{\pm}qqbb)f(qqbb \to ebbj)$ $N(\mu^{\pm}qqbb)f(qqbb \to \mu^{\mp}bbj)$
eμ control region	$e^{\pm}qqbb \to e^{\pm}\mu^{\mp}bbj$ $\mu^{\pm}qqbb \to \mu^{\pm}e^{\mp}bbj$	$N(e^{\pm}qqbb)f(qqbb \to \mu^{\mp}bbj)$ $N(\mu^{\pm}qqbb)f(qqbb \to e^{\mp}bbj)$

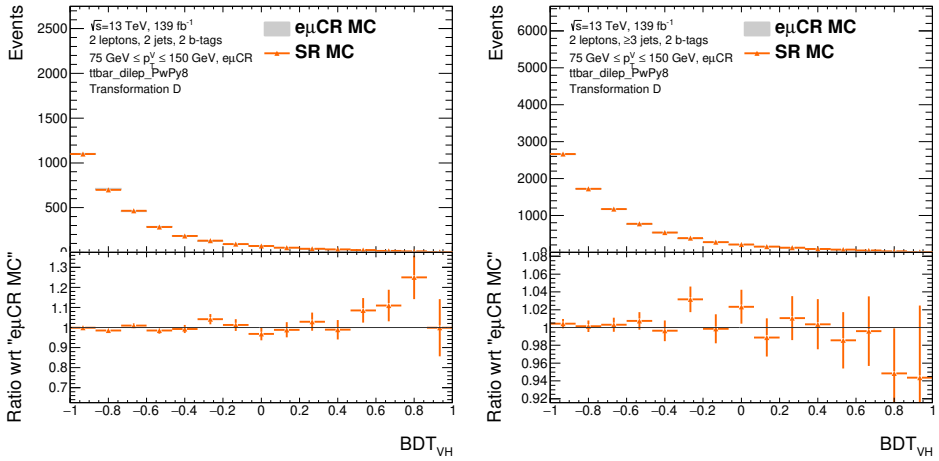

Figure 7.8: Comparison of the BDT distribution in the SR and the eμCR in the categories with 2 jets (left) and more than 2 jets (right) for the fully leptonic $t\bar{t}$ events with $75 \leq p_{\mathrm{T}}^{V} < 150$ GeV.

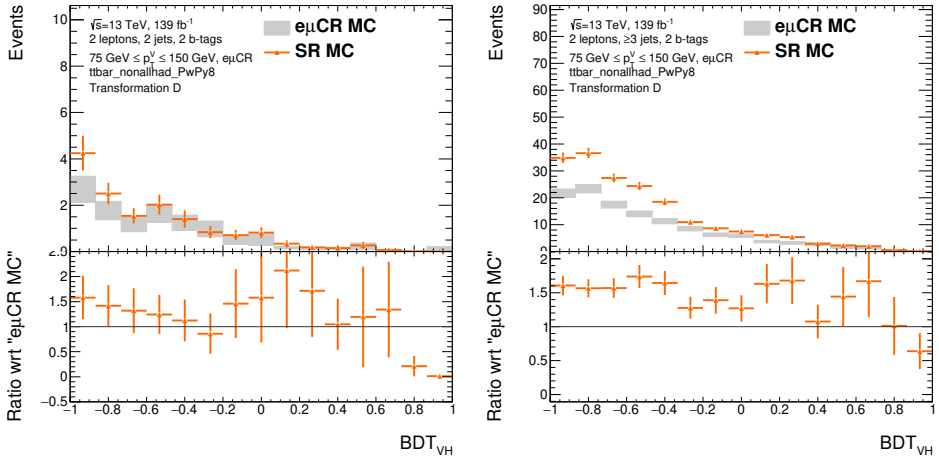

Figure 7.9: Comparison of the BDT distribution in the SR and the eμCR in the categories with 2 jets (left) and more than 2 jets (right) for the semi-leptonic $t\bar{t}$ events with $75 \leq p_{\mathrm{T}}^{V} < 150$ GeV.

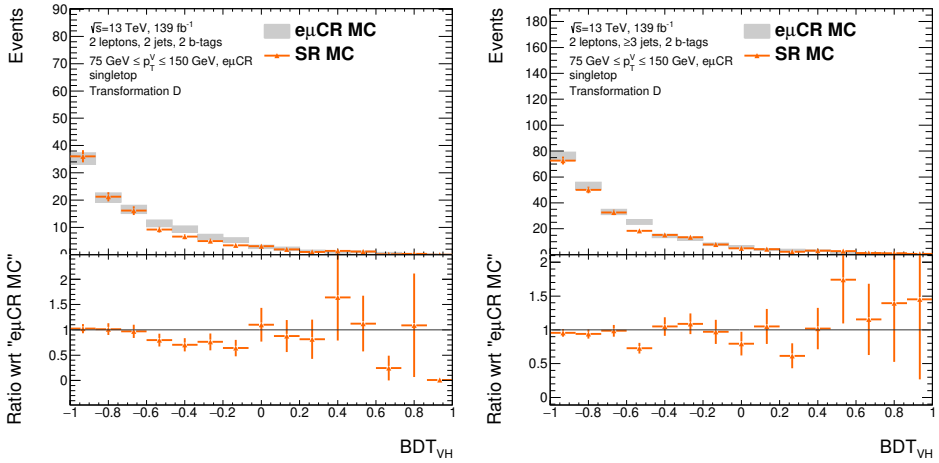

Figure 7.10: Comparison of the BDT distribution in the SR and the eμCR in the categories with 2 jets (left) and more than 2 jets (right) for the single top events with $75 \leq p_{\mathrm{T}}^{V} < 150$ GeV.

As shown in these plots, the leading component of the uncertainties is the statistical uncertainty of the MC samples. The systematic uncerainties both from experimental and theoretical sources are eliminated as mentioned at the beginning of this section.

From the comparison of p_{T}^{V} distribution in the SR and the CR (Figure 7.3), it is understood that it is not necessary to have different extrapolation factors for the p_{T}^{V} categories. However, following the argument around Eqs. 7.2 and 7.3, it is expected that different extrapolation factors should be used in the categories with 2 jets and more than 2 jets. The measured extrapolation factors in Figures 7.6 (2 jets) and 7.7 indeed show difference between the categories. Eventually, the derived extrapolation factors are 0.995 ± 0.008 for 2 jets and 1.011 ± 0.005 for more than 2 jets.

8 Systematic uncertainties

Systematic uncertainty is categorized into *detector systematic uncertainties* and *theoretical (modelling) uncertainties*. The detector systematic uncertainties are uncertainties of experimental techniques such as the object reconstruction, identification, and the b-tagging, and the calibration of energy measurement. The theoretical uncertainties are uncertainties in the physics simulations (Section 4.2.2) related to missing higher-order correction, PDF+α_S uncertainties, and uncertainties in the modeling of parton shower and underlying events.

The uncertainties on the efficiency of the b-tagging and the uncertainties on the jet energy calibration have large impacts on the measurement among the experimental systematic uncertainties. The modeling uncertainties for both the signal and the backgrounds also have impacts on the measurement.

8.1 Detector related systematics

8.1.1 Electrons

Uncertainties relevant to electrons are divided into two parts: uncertainties in the calibration of the energy scale and resolution, and uncertainties on the efficiency of the reconstruction, the identification, the isolation and the trigger. These are studied in detail in Refs. [120, 140], and outlined in this section. However, these uncertainties have small impact on the result presented in this thesis.

Calibration of the energy scale/resolution measurement for electrons is performed by fitting m_{ee} distribution in $Z \to ee$ events as explained in Section 5.2.1. The uncertainties in the energy scale calibration have contributions from imperfect description of detector material and modelling of the response of the measurement to the pile-up. The uncertainties on the energy resolution have contributions from difference of pile-up noise between the data and the simulation, and difference between two methods used to extract the energy resolution correction.

Calibration of the efficiency is performed with a tag & probe method using $Z \to ee$ and $J/\psi \to ee$ events as described in Section 5.2.1. Uncertainties on the efficiency of the identification is dominated by the subtraction of backgrounds in low p_T region. The dependence of the efficiency on the E_T limits the precision in high p_T region. Uncertainties on the efficiency of the isolation are evaluated by varying details of the background subtraction and the event selection.

8.1.2 Muon

Uncertainties relevant to muons are categorized into two parts: uncertainties in the energy scale/resolution calibration, and uncertainties on the efficiency of the reconstruction, the identification, the isolation and the

trigger. Similar to the uncertainties for electrons, these uncertainties have small impact on the analysis. A detailed description is presented in Ref. [125], while only outline is presented in this section.

Calibration of the momentum scale of muons is performed by fitting variables such as $m_{\mu\mu}$ in $Z \to \mu\mu$ and $J/\psi \to \mu\mu$ events as described in Section 5.3.1. Uncertainties have contributions from the stability against a variation of the event selection used in the calibration, and uncertainties relevant to the background subtraction and the assumption of the functional form used in the extraction of the momentum scale. Alignment of chambers in the muon spectrometer also contributes to the uncertainty. This is studied with special data when the toroidal magnet is turned off, where the trajectories of muons are straight not depending on the momenta.

Calibration of the efficiency of the reconstruction, the identification, the isolation and the trigger is performed with the tag & probe method as described in Section 5.3.1. The uncertainties have contributions from the background subtraction performed in the analysis and modelling of the signal process. Efficiency using true muons defined in MC simulations as the denominator is also derived. The difference from the tag & probe method is included in the total uncertainty. The breakdown of the uncertainty on the efficiency of the identification is shown in Figure 8.1. The uncertainties on the efficiency of the isolation have contributions from a variation of the background subtraction and the event selection in low p_{T}, where backgrounds are important. The uncertainty is dominated by the statistical component in high p_{T} region.

8.1.3 Jet

In the analysis presented in this thesis, the energy scale of jets are corrected with the *Global Sequential Calibration* as described in Section 5.4. The corrected jet energies are measured in data using *in situ* techniques described below, and the uncertainties in the energy correction is derived. The detailed description of the measurement of the jet energy is presented in Refs. [131, 141], while only outline is

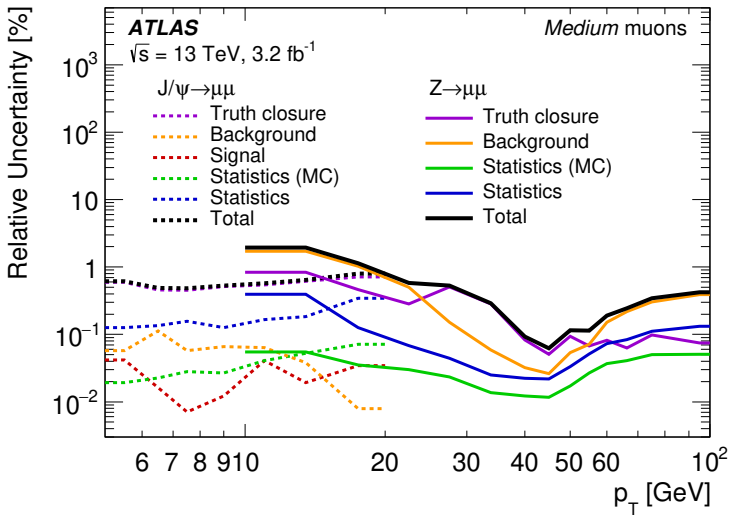

Figure 8.1: Systematic uncertainties on the efficiency scale factor of the *Medium* muon identification [125]. The uncertainties as functions of p_{T} are derived from the tag and probe method using $Z \to \mu\mu$ events (solid lines) and $J/\psi \to \mu\mu$ events (dashed lines). The total uncertainty (black lines) is the sum in quadrature of the components.

presented in this section. The *in situ* methods impose the p_{T} balance of a focused jet with a reference object such as $Z \rightarrow \ell\ell$, γ and a multi-jet system which are well measured. The measurement using Z+jet events provides calibration of the jet energy in 20 GeV $< p_{\mathrm{T}}^{j} <$ 400 GeV and in $|\eta| < 0.8$. The measurement using γ+jet events provides calibration of the jet energy in 40 GeV $< p_{\mathrm{T}}^{j} <$ 950 GeV and in $|\eta| < 0.8$. The measurement using multijet events provides calibration of the jet energy in 300 GeV $< p_{\mathrm{T}}^{j} <$ 2000 GeV and $|\eta| < 1.2$. Reference multijet system is made up of jets calibrated with the *in situ* methods using Z/γ+jet events. These methods are referred to as *Z+jet, γ+jet* and *multi-jet balance*. Dijet events are used to measure the jet energy in the forward region, $0.8 < |\eta| < 4.5$, using well measured jets in the central region, $|\eta| < 0.8$, as reference objects (referred to as *η-inter calibration*). These *in situ* measurements are combined and the result is shown in Figure 8.2.

The uncertainties in the jet energy measurement account for:

- uncertainties in the modelling of the physics process.
- uncertainties in the measurement of the reference objects.
- uncertainties on a potential bias caused by the event selection applied in the calibration analyses.

The contributions to the systematic uncertainties on the measurements of the jet energy are summarized in Table 8.1. The correlation among the derived systematic uncertainties are resolved and the uncertainties are redefined in terms of uncorrelated components. These uncertainties are independently taken into account in a statistical analysis introduced in Chapter 9.

The efficiency of Jet Vertex Tagging explained in Section 5.4 is studied with a tag & probe method using $Z \rightarrow \mu\mu$+jets event. The efficiency in data and MC agrees within statistical uncertainty. In addition to

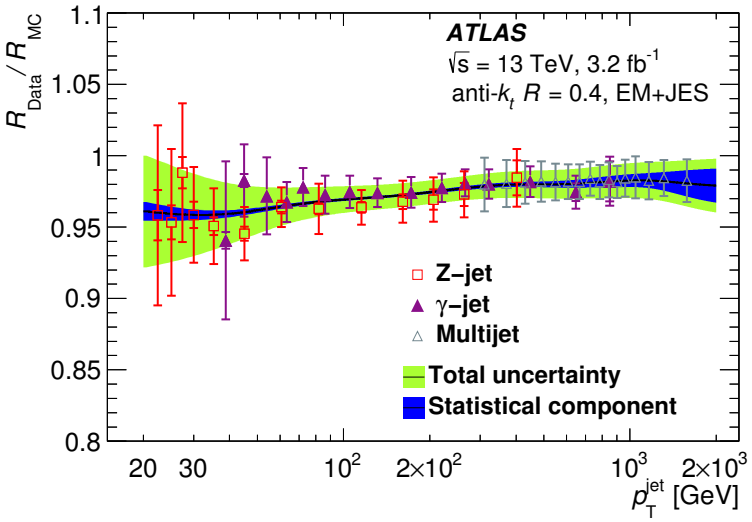

Figure 8.2: Ratio of response of the jet energy as a function of jet p_{T} [131]. The response is defined as $R = \left\langle p_{\mathrm{T}}^{j} / p_{\mathrm{T}}^{\mathrm{reference}} \right\rangle$, where the bracket represents the statistical average. The responses derived in the *in situ* measurements are shown by the red (Z+jet balance), purple (γ+jet balance) and light blue (multi-jet balance) points. The combined results of the measurement is shown in the black curve, and the statistical and total uncertainties are shown as the dark blue and green area.

Table 8.1: Summary of the systematic uncertainties considered in the *in situ* measurements of the jet energy [131].

Name	Description
Z+jet	
Electron scale	Uncertainty in the electron energy scale
Electron resolution	Uncertainty in the electron energy resolution
Muon scale	Uncertainty in the muon momentum scale
Muon resolution (ID)	Uncertainty in muon momentum resolution in the ID
Muon resolution (MS)	Uncertainty in muon momentum resolution in the MS
MC generator	Difference between MC event generators
JVT	Jet vertex tagger uncertainty
$\Delta\phi$	Variation of $\Delta\phi$ between the jet and Z boson
2nd jet veto	Radiation suppression through second-jet veto
Out-of-cone	Contribution of particles outside the jet cone
Statistical	Statistical uncertainty over 13 regions of jet p_{T}
γ+jet	
Photon scale	Uncertainty in the photon energy scale
Photon resolution	Uncertainty in the photon energy resolution
MC generator	Difference between MC event generators
JVT	Jet vertex tagger uncertainty
$\Delta\phi$	Variation of $\Delta\phi$ between the jet and γ
2nd jet veto	Radiation suppression through second-jet veto
Out-of-cone	Contribution of particles outside the jet cone
Photon purity	Purity of sample in γ+jet balance
Statistical	Statistical uncertainty over 15 regions of jet p_{T}
Multijet balance	
α^{MJB} selection	Angle between leading jet and recoil system
β^{MJB} selection	Angle between leading jet and closest subleading jet
MC generator	Difference between MC event generators
$p_{\mathrm{T}}^{\mathrm{asymmetry}}$ selection	Second jet's p_{T} contribution to the recoil system
Jet p_{T} threshold	Jet p_{T} threshold
Statistical components	Statistical uncertainty over 16 regions of $p_{\mathrm{T}}^{\mathrm{leading}}$
η-intercalibration	
Physics mismodeling	Envelope of the MC, pile-up, and event topology variations
Non-closure	Non-closure of the method in the $2.0 < \lvert\eta_{\mathrm{det}}\rvert < 2.6$ region
Statistical component	Statistical uncertainty
Pile-up	
μ offset	Uncertainty of the μ modeling in MC simulation
N_{PV} offset	Uncertainty of the N_{PV} modeling in MC simulation
ρ topology	Uncertainty of the per-event p_{T} density modeling in MC simulation
p_{T} dependence	Uncertainty in the residual p_{T} dependence
Jet flavor	
Flavor composition	Uncertainty in the jet composition between quarks and gluons
Flavor response	Uncertainty in the jet response of gluon-initiated jets
b-jet	Uncertainty in the jet response of b-quark-initiated jets
Punch-through	Uncertainty in GSC punch-through correction
AFII non-closure	Difference in the absolute JES calibration using AFII
Single-particle response	High-p_{T} jet uncertainty from single-particle and test-beam measurements

the statistical components, systematic uncertainties are added to account for the differences in efficiency derived in SHERPA and POWHEG+PYTHIA8, and mismodelling in a kinematic distribution.

8.1.4 *b*-tagging

Calibration of the efficiency of the *b*-tagging and the systematic uncertainties are separately derived for *b*-jets, *c*-jets and light-jets (based on the *truth* label introduced in Section 5.6.3) as described in this section. The derived systematic uncertainties are decomposed into uncorrelated components that can be used independently in the statistical analysis in Chapter 9.

Calibration of the *b*-tagging efficiency for *b*-jets

The procedure of calibration of the *b*-tagging efficiency detailed in Ref. [136] is outlined in this section. The calibration of the *b*-tagging efficiency for *b*-jets utilizes the dileptonic decay channel of the $t\bar{t}$ production selected by requiring an electron, a muon and two jets. The two jets are not required to be *b*-tagged to avoid a bias on the measurement of the efficiency of the *b*-tagging. Signal regions and control regions for this calibration are defined as following. Each lepton is paired with a jet, and the invariant masses of the pairs are denoted by $m_{j_1,\ell}$ and $m_{j_2,\ell}$. There are two permutations of pairs of the jets and the leptons. The permutation that gives lower value of $m^2_{j_1,\ell} + m^2_{j_2,\ell}$ is chosen. If the lepton and the jet in a given pair come from one top-quark decay, $m_{j,\ell}$ is less than the mass of a top-quark, $m_t = 172.5$ GeV, due to the missing energy carried by neutrino. Thus, a signal region can be defined by the condition $m_{j_1,\ell}, m_{j_2,\ell} < 172.5$ GeV so that the region contain *b*-jets with relatively high purity. Control regions are defined by inverting the cut on $m_{j_1,\ell}$ and $m_{j_2,\ell}$. These control regions contain *b*-jets with lower fraction. The signal region is further classified into the intervals of MV2c10 introduced in Section 5.6. The event yield in the control regions are expressed as

$$\nu_{\mathrm{CR}}(T^m, T^n) = c^{m,n}_{bb}\nu^{m,n}_{\mathrm{CR},bb} + c^{m,n}_{bl}\nu^{m,n}_{\mathrm{CR},bl} + c^{m,n}_{lb}\nu^{m,n}_{\mathrm{CR},lb} + c^{m,n}_{ll}\nu^{m,n}_{\mathrm{CR},ll}, \tag{8.1}$$

where T^m, T^n represent the p_{T} bins, $\nu^{m,n}_{\mathrm{CR},bb}, \nu^{m,n}_{\mathrm{CR},bl}, \nu^{m,n}_{\mathrm{CR},lb}, \nu^{m,n}_{\mathrm{CR},ll}$ are the expected yields of the indicated flavor component in the p_{T} bins. $c^{m,n}_{bb}, c^{m,n}_{bl}, c^{m,n}_{lb}, c^{m,n}_{ll}$ are the correction factors for the yields. These correction factors are constrained in the control regions and extrapolated to the signal regions. The yield in the signal regions are parametrized as

$$\begin{aligned}\nu_{\mathrm{SR}}(T^m, T^n, O^k, O^p) = {} & c^{m,n}_{bb}\nu^{m,n}_{\mathrm{SR},bb}P_b(O^k|T^m)P_b(O^p|T^n) \\ & + c^{m,n}_{bl}\nu^{m,n}_{\mathrm{SR},bl}P_b(O^k|T^m)P_l(O^p|T^n) \\ & + c^{m,n}_{lb}\nu^{m,n}_{\mathrm{SR},lb}P_l(O^k|T^m)P_b(O^p|T^n) \\ & + c^{m,n}_{ll}\nu^{m,n}_{\mathrm{SR},ll}P_l(O^k|T^m)P_l(O^p|T^n),\end{aligned} \tag{8.2}$$

where T^m and $c^{m,n}_{bb}, c^{m,n}_{bl}, c^{m,n}_{lb}, c^{m,n}_{ll}$ are the same parameters as Eq. 8.1. $\nu^{m,n}_{\mathrm{SR},bb}, \nu^{m,n}_{\mathrm{SR},bl}, \nu^{m,n}_{\mathrm{SR},lb}, \nu^{m,n}_{\mathrm{SR},ll}$ are the expected yields of the indicated flavor components in the p_{T} bins of the signal regions (l stands for *c*- and light jets). O^k represents the MV2c10 bins. $P_b(O^k|T^m)$ and $P_l(O^p|T^n)$ are the probabilities of *b*-jets and jets of other flavor to be tagged in the indicated p_{T} and MV2c10 bins. $P_b(O^k|T^m)$ are determined by fitting the control regions and the signal regions. $P_l(O^k|T^m)$ are taken from other analysis (i.e. the calibration for *c*- and light-jets described below). Contributions to the uncertainty on the scale factors are shown in Table 8.2.

Table 8.2: Breakdown of the contributions to the systematic uncertainty on the efficiency of the b-tagging in the individual MV2c10 bins [136]. The uncertainties for b-jets with 110 GeV $\leq p_{\mathrm{T}}^{b} <$ 140 GeV are shown. "$t\bar{t}$ modeling" and "single top modelling" include uncertainties in parton shower, hadronization model, initial-state and final-state radiation and PDF for the $t\bar{t}$ and single-top productions. "Other souces" account for residual uncertainties: the resolution of jet energy, performance of the electron and muon reconstruction, b-tagging efficiency for c- and light-jets, the performance of the *JVT*, the profile of the pile-up, and the modelling uncertainties for the diboson and Z + jets productions.

Source of uncertainty	Impact on $\mathcal{P}_b$ [%] per pseudo-continuous OP				
	100%–85%	85%–77%	77%–70%	70%–60%	60%–0%
Data statistics	4.2	3.0	3.2	2.6	0.7
MC statistics	1.4	0.5	0.3	0.3	0.2
Jet energy scale	1.0	0.2	0.2	0.2	0.1
$t\bar{t}$ modelling	7.2	0.9	0.8	0.9	0.9
Single top modelling	2.4	0.5	0.3	0.2	0.3
Fake leptons modelling	0.1	0.1	< 0.1	< 0.1	< 0.1
Other sources combined	2.1	0.5	0.5	2.2	0.1
Total	9.1	3.3	3.3	3.2	1.2

Calibration of the b-tagging efficiency for c- and light-jets

The calibration of the b-tagging for c- and light-jets are too much detail. The description is presented in Appendix E.

8.1.5 $E_{\mathrm{T}}^{\mathrm{miss}}$

The uncertainties in the calibration of the energy scale of electrons, the momentum of muons and jets are propagated into the uncertainty of $E_{\mathrm{T}}^{\mathrm{miss}}$. Uncertainties on the modelling of the underlying events and performances of the tracking are also included [135, 142].

8.1.6 Other experimental uncertainties

There are other experimental systematic uncertainties taken into account. Uncertainties on the efficiency scale factor of the $E_{\mathrm{T}}^{\mathrm{miss}}$ trigger are evaluated and included for the 0- and 1-lepton channels. Uncertainties on the integrated luminosity of the data, which is evaluated as 1.7% [143, 144], are considered. The profile of the average number of interaction per bunch crossing is corrected based on the analysis in Ref. [145], and the uncertainties are taken into account.

8.2 Theoretical uncertainties

8.2.1 General description of methodologies

Predictions with Monte Carlo simulations are kind of approximations of phenomena caused by the Standard Model (or some phenomenological models for hadronization and so on). Thus, systematic uncertainties of

the simulations should be considered.

The systematic uncertainty would be broken down into uncertainties on the cross-sections and residual uncertainties such as acceptance uncertainties relevant to extrapolation between channels and categories, flavor composition uncertainties and uncertainties on the shapes of kinematic distributions. They are outlined in this section.

Cross-section uncertainty

For the sample normalization, best available cross-section are used as nominal theoretical predictions. Event generation is typically done with theoretical calculations at the NLO accuracy in QCD. while the total cross-section is often available at the NNLO accuracy.

The uncertainty on the total cross-section computed at the NNLO is often estimated by checking stability against variations of the renormalization and factorization scale, PDF, α_S, and so on. This method is adopted for the singnals and the diboson and single-top productions. The V + jets backgrounds containing bb, bc bl, cc jets (referred to as Z + hf-jets) are modelled with the method described below whereas the other flavor components ($V + cl$ and $V + ll$) are modelled in this way.

It is however preferred that the normalization for important backgrounds are estimated using data without relying on the theoretical cross-sections. Practically, the cross-section values are not of interest for the backgrounds, but it is sufficient to just get the normalization factors that make the MC predictions describe the data well. The normalization factors of the dominant backgrounds, W + jets, Z + jets and $t\bar{t}$, are estimated with such approach by defining the control regions discussed in Section 6.5.

Acceptance / extrapolation uncertainty

Although assumptions on the overall cross-sections of the dominant backgrounds are mostly removed, *acceptance uncertainties* still need to be considered to account for differences of the normalization factors (or acceptance correction) among the categories and the channels due to the different kinematic selections used. Thus, the acceptance uncertainty would also be called *extrapolation uncertainty*. The acceptance uncertainties relevant to a "category A" and a "category B" are evaluated using the nominal MC sample and an alternative sample according to:

$$\frac{\text{Acceptance[CategoryA](Nominal)}}{\text{Acceptance[CategoryB](Nominal)}} \Big/ \frac{\text{Acceptance[CategoryA](Alternative)}}{\text{Acceptance[CategoryB](Alternative)}} \,. \tag{8.3}$$

And it is applied to the category B. Note that the impact from the difference of the overall normalization between the two MC samples are removed from Eq.8.3 by definition.

For the single-top and diboson backgrounds, they are normalized relying on the theoretical cross-sections. In this case, not only uncertainties on the difference of the acceptances but the those for "absolute acceptance" need to be considered.

Flavor composition uncertainties

Flavor composition uncertainties need to be considered because distributions may differ depending on flavor components. If theoretical uncertainty on the flavor fraction of partons at the truth level is large, in particular for V + jets, a systematic uncertainty should be assigned to change the fraction, which in turn may varies kinematic distributions and the relative acceptance across regions. The variation of distributions is possible because, for example for the V + jets backgrounds, the $b\bar{b}$ final state consists of large contribution from the $g \to b\bar{b}$ process while the final state including b and c quarks is caused by other diagrams. Thus, the fraction of the flavors component changes the overall kinematic distribution. For the $t\bar{t}$ background, since the flavor of final state particles are governed by the weak interaction, the theoretical flavor uncertainty may be small. However, the flavor composition uncertainty should still be taken into account because the acceptance may be different between flavors.

Shape uncertainties: one-dimensional parametrization

Uncertainties on the shapes of background distributions in fitting regions can be relevant to the measurements. Thus, uncertainties on the distributions of relevant variables such as $m_{b\bar{b}}$ and p_{T}^{V} are evaluated by comparing different MC setups. The uncertainties are derived as re-weighting functions that correct the nominal MC distributions to the alternative ones. They are considered in the statistical analysis in Chapter 9. For this method, $m_{b\bar{b}}$ is chosen as one of parametrization variables because it is the most important variable in the final discriminants (BDTs) and the fit is sensitive to the modelling of the variable. p_{T}^{V} is is chosen as another parametrization variable because the p_{T}^{V} spectrum of the signal is measured using the binning with this variable and the fit is also sensitive to it. The One dimensional parametrization is adopted for the signal, Z + jets, the single top production, and the diboson production as shown in Table 8.3.

Shape uncertainties: multi-dimensional parametrization

Uncertainties on the shapes of the background distributions in the fitting regions can also be parameterized using several kinematic variables in a method explained below. A new BDT classifier, $\mathrm{BDT_{sys}}$, is trained to separate *the nominal MC and alternative MC samples* using the input variables of the BDTs of the main analysis (let us call this classification BDT). *One should be careful not to confuse this* $\mathrm{BDT_{sys}}$ *with the classification BDT used as the final discriminant of the main analysis, which is trained separate the signals and the backgrounds.* The output of the $\mathrm{BDT_{sys}}$ is evaluated for the two MC samples. A re-weighting factor as a binned or analytic function of the $\mathrm{BDT_{sys}}$ score is derived. So, this method parameterizes the uncertainties as functions of the $\mathrm{BDT_{sys}}$ scores while the one-dimensional parametrization above uses functions of $m_{b\bar{b}}$, p_{T}^{V} or some other variables. The nominal MC sample is re-weighted to define the systematic variation. The procedure is illustrated in Figure 8.3. This evaluation of systematic variation is called *multi-dimensional parametrization*. This method is adopted for the W + jets and $t\bar{t}$ backgrounds in the 0- and 1-lepton channels as shown in Table 8.3. For Z + jets, the theoretical uncertainties of this background is derived using the data in the side band of the $m_{b\bar{b}}$ distribution. The multi-dimensional parametrization is not adopted because the data events with $m_{b\bar{b}} \sim 125$ GeV can not be used to train $\mathrm{BDT_{sys}}$.

A problem in the multidimensional parametrization mentioned above is related to the nature of two point systematic. It can make a shape that is expressed by interpolation of the two samples since it is associated to one nuisance parameter even though it considers multiple variables to define systematic variations, and

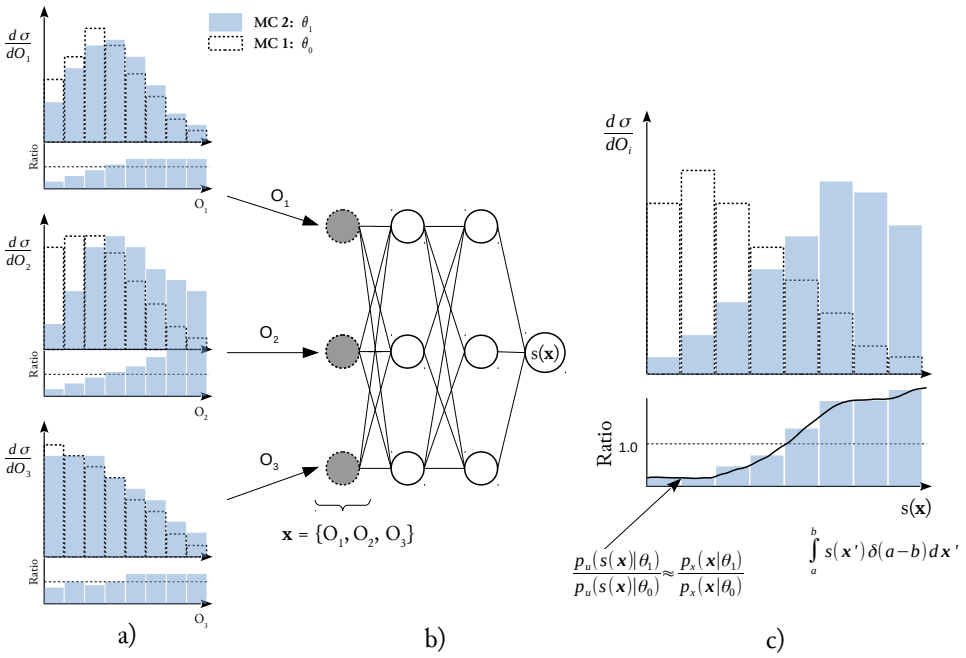

Figure 8.3: Illustration of the multidimensional parametrization. In this example, a) indicates comparison of "MC1" and "MC2" in three input variables $x = [O_1, O_2, O_3]$ for an MVA classifier $s(x)$. is trained using the three variables, O_1, O_2, O_3. c) shows comparison of MC1 and MC2 in the $s(x)$ variable. The black curve in c) indicates the derived systematic variation.

the data is not necessarily reproduced. Thus, it is desired to define multiple shape variations from one systematic source. In practice, comparison of the two samples is performed to evaluate uncertainty on the p_{T}^V shape and the nominal samples are re-weighted prior to the training of BDTs. In training with the re-weighted samples, the $\mathrm{BDT}_{\mathrm{sys}}$ is not sensitive to the difference of the p_{T}^V distributions between the two samples. Thus, the variation in p_{T}^V is factorized out from the variation parametrized with multidimensional variables. This multi-dimensional parametrization that includes the factorization of the p_{T}^V variation is called *hybrid multidimensional parametrization*. Procedure is illustrated in Figure 8.4.

8.2.2 Signal uncertainties

The uncertainties of the signal modelling are summarized in Table 8.4. These are presented in detail in [146], and outlined in this section.

Table 8.3: Summary of the parametrization methods for systematic uncertainties on the shapes for the signal and the background processes.

Type	Process
One dimensional	signal, Z + jets, single top production, diboson production
Multi-dimensional	$t\bar{t}$ (0- and 1-lepton), W + jets

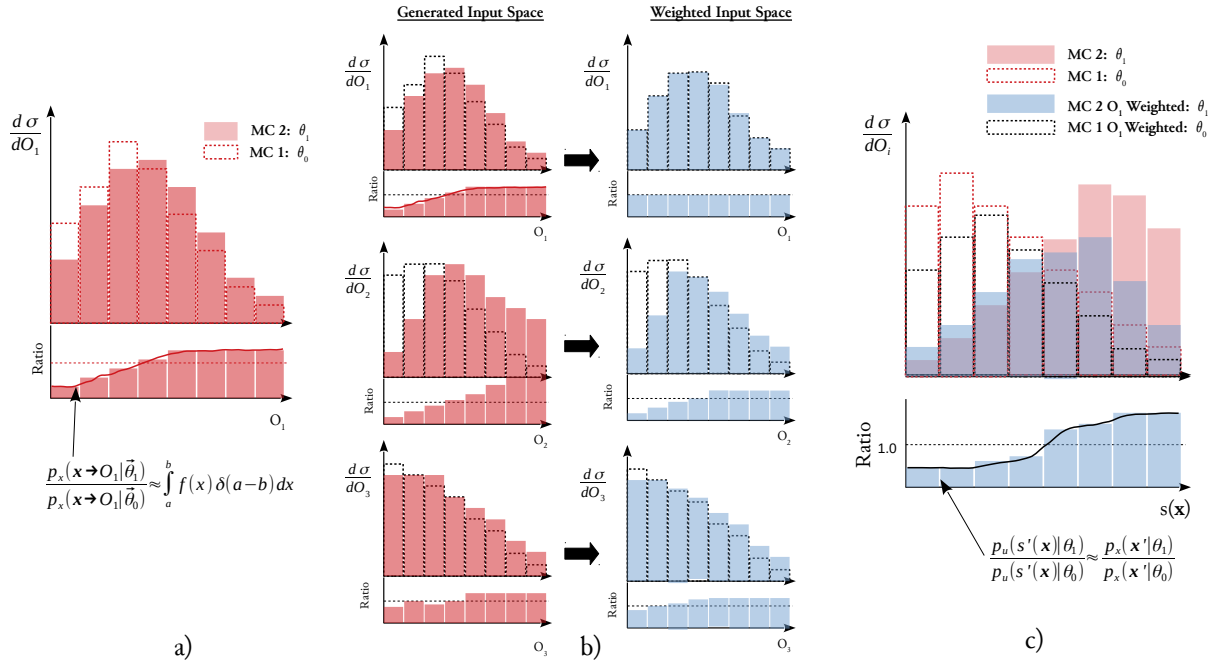

Figure 8.4: Illustration of the hybrid multidimensional parametrization. a) indicates the derivation of the O_1 shape from comparison of MC1 and MC2. In b), input variables $x = [O_1, O_2, O_3]$ are re-weighted by the function derived in a), and the O_1 shape effect is factorized out from the input variables. The black curve in c) represents the parametrized systematic variation (O_1 factorized multidimensional parametrization). In this example, $x = [O_1, O_2, O_3]$ are input variables for the classification BDTs, and O_1 is factorized out from the multi-dimensional parametrization.

Table 8.4: Summary of the systematic uncertainties on the signal modelling. The symbol XS indicates that the uncertainties are used in the differential cross-section measurement. The ranges for these uncertainties shows that they depend on the bins.

Description	Size or implementation
Cross-section (scale)	0.7% ($qq \to VH$), 25% ($gg \to ZH$)
$H \to b\bar{b}$ branching fraction	1.7%
Scale variations (XS)	3.0%-3.9% ($qq \to WH$), 6.7%-12% ($qq \to ZH$), 37%-100% ($gg \to ZH$)
PS/UE variations (XS)	1%-5% ($qq \to VH$), 5%-20% ($gg \to ZH$)
PDF+α_S variations (XS)	1.8%-2.2% ($qq \to WH$), 1.4%-1.7% ($qq \to ZH$), 2.9%-3.3% ($gg \to ZH$)
$m_{b\bar{b}}$ shape (scale)	Migration and shape
$m_{b\bar{b}}$ shape (PS/UE)	Migration and shape
$m_{b\bar{b}}$ shape (PDF+α_S)	Migration and shape
p_T^V from the NLO EW correction	Migration and shape

Cross-section (overall normalization)

The cross-sections of WH and ZH are obtained at NNLO in QCD [87, 89] ($O(\alpha_S^2)$) and NLO in the electroweak interaction [147] including gluon induced heavy-quark loop mediate subprocess for ZH ($gg \rightarrow ZH$) [94]. The WH sample is normalized to the NNLO (QCD) and NLO (EW) prediction. The $gg \rightarrow ZH$ sample is normalized to the NLO+NLL calculation in QCD ($O(\alpha_S^3)$). The cross-section of $qq \rightarrow ZH$ is obtained as the subtraction of the $gg \rightarrow ZH$ cross-section from the overall ZH cross-section, thus it is a quantity of $O(\alpha_S^2)$.

To obtain the QCD scale uncertainty separately for $qq \rightarrow ZH$ and $gg \rightarrow ZH$, it is assumed the uncertainty on $qq \rightarrow ZH$ is the same as those for $qq \rightarrow WH$. Then, the uncertainty on $gg \rightarrow ZH$ is derived so that the quadratic sum of the $qq \rightarrow ZH$ and $gg \rightarrow ZH$ uncertainties reproduces the uncertainty on the overall ZH production cross-section. Uncertainty on the $H \rightarrow b\bar{b}$ branching ratio considers higher order effects of QCD and the electroweak interaction, uncertainties on the b-quark mass and α_S [45].

Migration uncertainties

As mentioned in Section 6.1, the differential cross-sections are measured for the p_T^V categories defined with the truth p_T^V (*truth categories*). Theoretical uncertainties need to be considered to account for either the event migration across regions or the acceptance correction of the individual regions of signal events. QCD scale uncertainties, PDF uncertainties and uncertainties relevant to the parton shower (PS) and underlying event (UE) modelling are considered. These are discussed below.

The QCD scale uncertainties are evaluated varying the renormalization scale (μ_R) and the factorization scale (μ_R) to account for the acceptance of the truth category. Six scale variations are tested: $(\mu_R, \mu_F) = (0.5, 1), (1, 0.5), (2, 1), (1, 2), (0.5, 0.5), (2, 2)$, and the largest variation is used. The QCD scale uncertainties are derived following the Stewart-Tackman method [148]. These uncertainties cause the migration across p_T^V and n-jet boundaries, and they are evaluated using the NLO samples They are defined so that they do not change the overall cross-section since the overall cross-section is normalized to the NNLO calculation. The uncertainties associated to the p_T^V boundaries are evaluated in inclusive n-jet regions while the uncertainties associated to the n-jet boundaries evaluated in the individual p_T^V regions, which means the n-jet uncertainties are implemented as the internal variations in the p_T^V regions. Regions affected by each systematic uncertainty are shown in Tables 8.5 and 8.6. When the uncertainties are used in the statistical analysis, the uncertainties for $qq \rightarrow ZH$ and WH are correlated.

Table 8.5: Relative impact of scale variations Δ_X associated to a boundary X on the truth categories indicated in the left column. The $\sigma_{[X_1,X_2[}$ denominators represent the cross section for the categories $X_1 \leq p_T^V < X_2$ in GeV including the $|y^{\text{Higgs}}| \leq 2.5$ selection. Thus, the variations associated to $X = 75, 150, 250, 400$ do not affect the overall cross-section. Δ^y represents the variation of the overall acceptance of the $|y^{\text{Higgs}}| < 2.5$ cut.

p_T^V bin [GeV]	Δ^y	Δ_{75}	Δ_{150}	Δ_{250}	Δ_{400}
p_T^V [0, 75[	$+\Delta^y/\sigma_{[0,\infty[}$	$-\Delta_{75}/\sigma_{[0,75[}$	0	0	0
p_T^V [75, 150[	$+\Delta^y/\sigma_{[0,\infty[}$	$+\Delta_{75}/\sigma_{[75,\infty[}$	$-\Delta_{150}/\sigma_{[75,150[}$	0	0
p_T^V [150, 250[	$+\Delta^y/\sigma_{[0,\infty[}$	$+\Delta_{75}/\sigma_{[75,\infty[}$	$+\Delta_{150}/\sigma_{[150,\infty[}$	$-\Delta_{250}/\sigma_{[150,250[}$	0
p_T^V [250, 400[	$+\Delta^y/\sigma_{[0,\infty[}$	$+\Delta_{75}/\sigma_{[75,\infty[}$	$+\Delta_{150}/\sigma_{[150,\infty[}$	$+\Delta_{250}/\sigma_{[250,\infty[}$	$-\Delta_{400}/\sigma_{[250,400[}$
p_T^V [400, ∞[	$+\Delta^y/\sigma_{[0,\infty[}$	$+\Delta_{75}/\sigma_{[75,\infty[}$	$+\Delta_{150}/\sigma_{[150,\infty[}$	$+\Delta_{250}/\sigma_{[250,\infty[}$	$+\Delta_{400}/\sigma_{[400,\infty[}$

Table 8.6: Relative impact of scale variations Δ^1 and Δ^2 associated to the 1 and 2 additional jets boundaries. σ_i indicate the cross-sections in the indicated phase spaces including the $|y^{\text{Higgs}}| \leq 2.5$ selection. Both the variations do not affect the overall cross-section. The Δ^2 variation provides a finer split in the N-jets$\geq$ 1 phase space.

N-jets bin	Δ^1	Δ^2
N-jets=0	$-\Delta^1/\sigma_{\text{n-jets}<1}$	
N-jets=1	$+\Delta_1/\sigma_{\text{n-jets}\geq 1}$	$-\Delta^2/\sigma_{\text{n-jets}=1}$
N-jets$\geq$ 2	$+\Delta_1/\sigma_{\text{n-jets}\geq 1}$	$+\Delta^2/\sigma_{\text{n-jets}\geq 2}$

To evaluate the PDF uncertainties, PDF4LHC15_30 set is used to follow the "PDF4LHC recommendations for LHC Run II" [84, 149–154]. The first sample of the PDF4LHC15_30 set (PDF0) is used as the nominal. Systematic variations are defined as

$$\text{Var}_i = \frac{y_{\text{PDF}i} - y_{\text{PDF0}}}{y_{\text{PDF0}}}, \tag{8.4}$$

where Var_i represents the relative variation of the yield. For PDF α_S uncertainties, $\alpha_S(m_Z^2) = 0.118$ is used as the nominal while two variations, $\alpha_S(m_Z^2) = 0.1165$ and $\alpha_S(m_Z^2) = 0.1195$, are used to define

$$\text{Var}_{\alpha_S} = \frac{|\text{Var}_{\alpha_S=0.01165}| + |\text{Var}_{\alpha_S=0.01195}|}{2} \tag{8.5}$$

All the variations are derived for the truth categories and used in the statistical analysis.

The PS/UE uncertainties are introduced to account for the uncertainties on the acceptance of the reconstructed categories for the signal classified in the truth categories. The nominal Powheg+Pythia8 sample is compared to AZNLO tune variations and Powheg+Herwig7, and the uncertainties are:

$$\sigma_S^{C,I} = \frac{N_S(C,I)}{N_S(I)} \Bigg/ \frac{N_{\text{nominal}}(C,I)}{N_{\text{nominal}}(I)}, \tag{8.6}$$

where N_x are the yield of the nominal and the systematic variations, S represents a source of a systematic, C is the event selection used in the reconstructed level analysis and I represents a category based on truth information.

The nominal p_T^V distribution is first evaluated at LO (EW) and corrected to the NLO calculation of the electroweak interaction using HAWK [93, 99]. The difference between the leading order prediction and the NLO prediction is considered as an uncertainty.

Elimination of the systematic uncertainties for the signals

Elimination of the signal uncertainties in the differential cross-section measurement is briefly mentioned in Section 6.1. It is formularized below. The measurement is performed in the five p_T^V bins, but the systematic uncertainties are derived for regions with finer split. To discuss the elimination of the systematic uncertainties, the uncertainties for the merged regions need to be factorized into the uniform effect on the normalization in the bin and residual effects on the internal shape. The uniform effect is defined as:

$$\delta_{\text{merged-bin}} = \frac{\sum_{t \in \text{merged-bin}} \delta_t \sigma_t}{\sum_{t \in \text{merged-bin}} \sigma_t}, \tag{8.7}$$

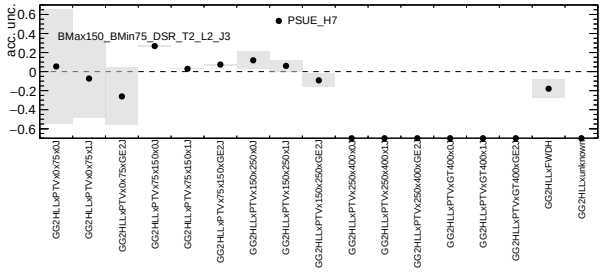

(a) $gg \to ZH \to \ell^+\ell^- b\bar{b}$,3-jets,$75 \leq p_{\mathrm{T}}^V < 150$ GeV

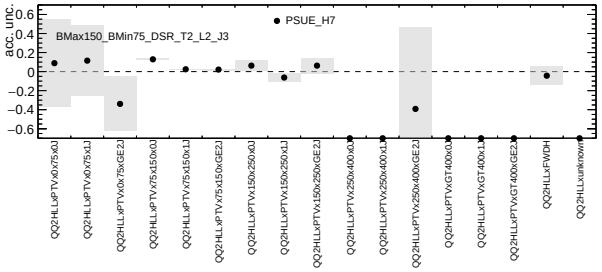

(b) $qq \to ZH \to \ell^+\ell^- b\bar{b}$,3-jets,$75 \leq p_{\mathrm{T}}^V < 150$ GeV

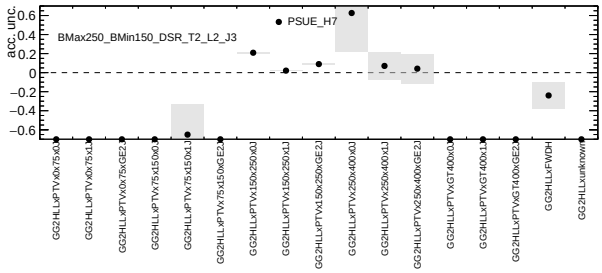

(c) $gg \to ZH \to \ell^+\ell^- b\bar{b}$,3-jets,$150 \leq p_{\mathrm{T}}^V < 250$ GeV

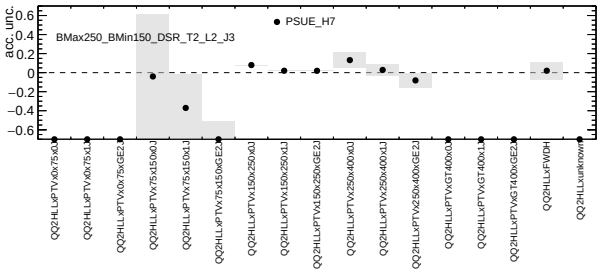

(d) $qq \to ZH \to \ell^+\ell^- b\bar{b}$,3-jets,$150 \leq p_{\mathrm{T}}^V < 250$ GeV

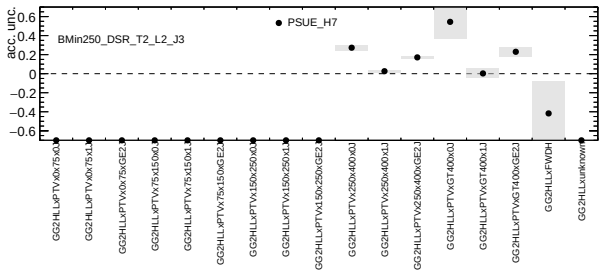

(e) $gg \to ZH \to \ell^+\ell^- b\bar{b}$,3-jets,$p_{\mathrm{T}}^V > 250$ GeV

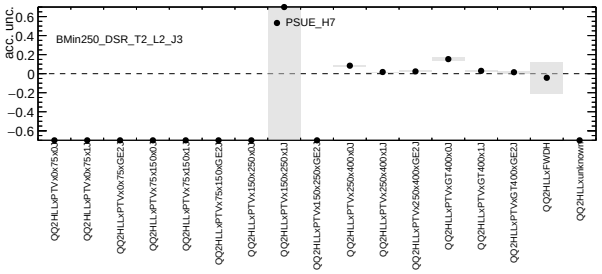

(f) $qq \to ZH \to \ell^+\ell^- b\bar{b}$,3-jets,$p_{\mathrm{T}}^V > 250$ GeV

Figure 8.5: Acceptance corrections and their uncertainties for each truth category (listed in the x-axes) and each reconstructed category ((a)-(f)). In the x-axes of the plots, "GG2HLL" and "QQ2HLL" represents "gg→$ZH \to \ell^+\ell^- b\bar{b}$" and "qq→$ZH \to \ell^+\ell^- b\bar{b}$"; "PTVxAxB" represents the p_{T}^V categories $A \leq p_{\mathrm{T}}^V < B$; "NJ" represents the N-jets.

where σ_t and δ_t are the cross-section and the uncertainty in a bin t, respectively. The uncertainty $\delta_{\text{merged-bin}}$ uniformly affects the bins in the "merged bins". $\delta_{\text{merged-bin}}$ is eliminated when the cross-section of the merged-bin is measured. The residual uncertainties are defined as:

$$\delta_{t,\text{residual}} = \delta_t - \delta_{\text{merged-bin}} = \frac{\sum_{s\in\text{merged-bin}}(\delta_t - \delta_s)\sigma_s}{\sum_{s\in\text{merged-bin}}\sigma_s}. \tag{8.8}$$

These uncertainties affect each bin, and are not eliminated in the measurement.

The QCD scale uncertainties for the signal strength measurement and the cross-section measurement in all the truth categories are shown in Figure 8.6. It can be seen in the bottom plot that uncertainties for the WH process is almost eliminated in the cross-section measurement while those for the ZH processes are not fully eliminated. This feature is confirmed in Appendix F conducting the calculation in Eq. 8.8 for some examples.

Uncertainties on the $m_{b\bar{b}}$ shape

The PS/UE uncertainties (Powheg+Pythia8 vs Powheg+Herwig7) on $m_{b\bar{b}}$ shape are derived in the 1-lepton, 2-jet region by a truth level analysis and the same shape uncertainties are applied to all the regions. The QCD scale uncertainties are derived by varying the renormalization and factorization scales in the 2-jet and 3-jet categories separately using a Powheg+MiNLO+Pythia8 sample. The same shape is used for $qq \to ZH$ and $gg \to ZH$ but treated as independent nuisance parameters in the statistical analysis.

8.2.3 Background uncertainties

The modeling uncertainties are derived following the method described in Section 8.2.1 for all the background components, W + jets, Z + jets, $t\bar{t}$, the single-top production, and the diboson production. The detailed description of these background modeling uncertainties is presented in Appendix G.

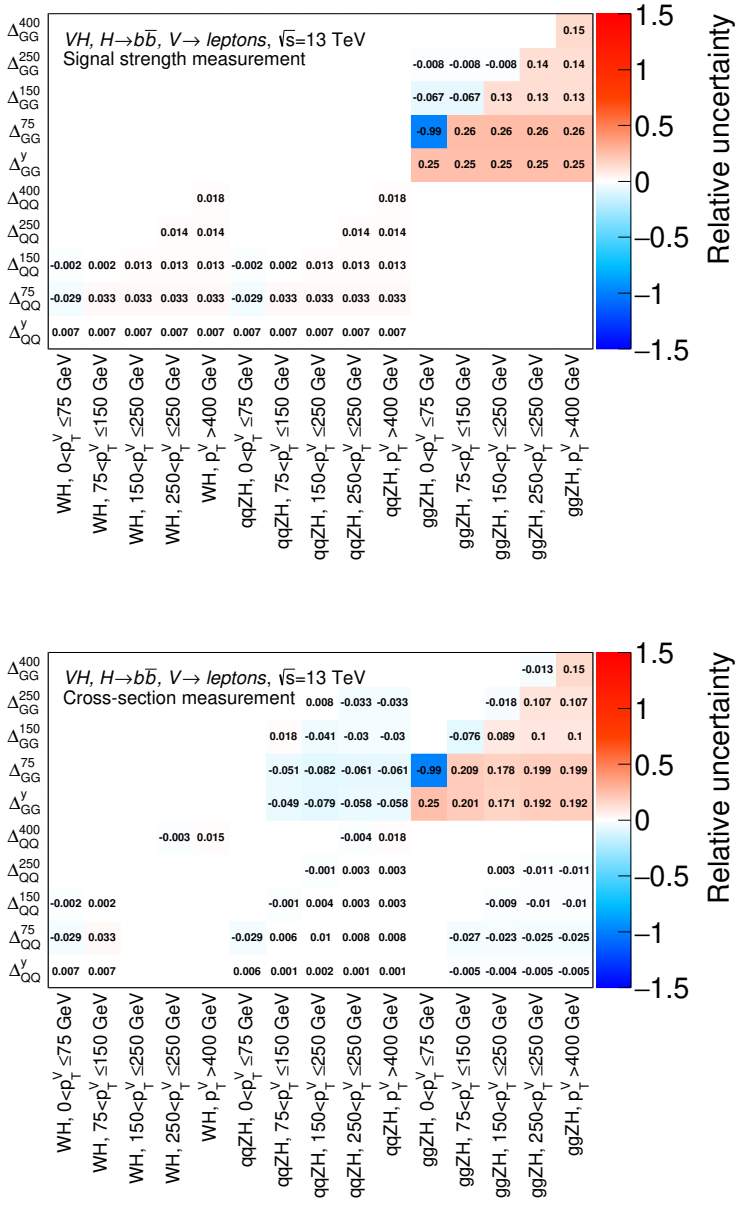

Figure 8.6: QCD scale uncertainties associated to the p_{T}^{V} boundaries and their effects on the truth categories. The top plot shows the uncertainties used in the signal strength measurement, and the bottom plot shows the uncertainties used in the differential cross-section measurement in the 5 p_{T}^{V} categories defined in Section 6.1. Δ_i^j represents the uncertainties on the signal i associated to the boundaries j. The x-axes indicates the phase spaces of the signal that are affected. The full systematic uncertainties are considered in the signal strength measurement. In the differential cross-section measurement, the most of the scale uncertainties are eliminated for WH while they are not fully eliminated for ZH as confirmed in Eqs. F.7 and F.7

9 Statistical analysis

Statistical methods used in the analysis are described in this chapter. General aspects of the proile-likelihood fit are explained in Section 9.1. Analysis-specific configurations are introduced in Section 9.2.

9.1 General description of the profile likelihood fit

9.1.1 Construction of likelihood functions

Profile-likelihood fits are performed to estimate parameters such as *signal strength (μ)* defined as a ratio of the observed cross-section times the branching fraction to the prediction of the Standard Model, underlying parameters of models like coupling constants, and so on. The estimation of parameters (*fit*) is done by maximizing a likelihood as a function of parameters of interest and others called nuisance parameters, which are introduced later. The likelihood function is constructed from a dataset, a probability density function (PDF) of a model that describes the data and systematic uncertainties of the model. The likelihood function consists of two parts: *likelihood terms* and *constraint terms*, which are explained in the following sections.

Likelihood terms

The likelihood terms describe the agreement of data and a model that predicts distributions of the data. It is defined as a product of Poisson probabilities of all the bins of the PDF:

$$L(\{x_i\}|\{\theta_k\}) = \prod_{j \in \text{bins}} \frac{F(x_j;\{\theta_k\})^{n_j}}{n_j!} e^{-F(x_j;\{\theta_k\})}, \tag{9.1}$$

where $F(x_j;\{\theta_k\})$ represents the PDF value of the jth bin, $\{\theta_k\}$ is a set of parameters[1] contained in the model, and n_j is the observed number of events in the jth bin.

Systematic uncertainties are expressed as variations of the PDF. The parameters $\{\theta_k\}$ in the Eq.9.1 are called *nuisance parameters*, and they are introduced to parameterize the systematic uncertainties. Dependence of the PDF on $\{\theta_k\}$ is expressed as:

$$F(x;\{\theta_k\}) = (1 - \sum \theta_k) f_{\text{nominal}}(x) + \sum \theta_k f_k(x), \tag{9.2}$$

where $f_k(x)$ are alternative PDFs associated to the parameters θ_k. Thus, the PDF is now also a function of the nuisance parameters.

[1] In this notation, a symbol $f(x;\{\theta_k\})$ is a function of x and $\theta_1, \cdots, \theta_n$: $f(x;\theta_1, \cdots, \theta_n)$

Constraint terms

Some systematic uncertainties are constrained within predefined sizes by calibration of experimental techniques or theoretical estimation.

The sizes of the systematic uncertainties are expressed with additional terms called *constraint terms* in the likelihood. The form of a constraint term is given as[2]:

$$\exp\left\{\frac{-(\theta_k - \theta_k^{\text{Nominal}})^2}{\sigma_k^2}\right\}, \tag{9.3}$$

where k is an index for the kth nuisance parameter in $\{\theta_k\}$. For the experimental uncertainties, σ_k are derived in the calibration processes. For the theoretical uncertainties, σ_ks are estimated by comparing nominal and alternative setups of simulation, or other methods described in Section 8.2. Practically, θ_k are redefined so that $\theta_k^{\text{Nominal}} = 0$ and $\sigma_k = 1$.

Uncertainties of statistical nature can also be implemented as nuisance parameters "γ" using the Beeston-Barlow technique [155]. Dependence of a PDF on γ is introduced by multiplying these parameters to the nominal yields. These γ factors have Poisson constraint terms of the form:

$$f(\gamma;\tau) = (\tau\gamma)^\tau e^{-\tau\gamma}, \tag{9.4}$$

where $\tau = 1/(\text{relative error})^2$. The function in Eq.9.4 has the maximum at $\gamma = 1$ and the width around the maximum is $\tau^{-1/2}$. A special case of this implementation is used in Section 9.2.2.

9.1.2 Asimov datasets

In order to study characteristics of a likelihood and extract statistical quantities, it is needed to know how parameters of interest (POIs) behave in fits and how systematic uncertainties affect the POIs. To obtain such knowledge while blinding the signal, it is useful to create pseudo datasets and then study the likelihood constructed from them. Asimov dataset is a dataset that exactly reproduces distributions of a model. For example, if an Asimov dataset is created based on the signal+background hypothesis, the fit estimates the same hypothesized signal.

9.1.3 Evaluation of statistical quantities from likelihood

Statistical significance of an excess

Statistical significance is an example of the likelihood ratio test, described in Appendix H. A *test statistic* [156] is defined as the log likelihood ratio of two hypotheses[3]:

$$q_\mu = -\Delta\ln(L) = -\ln\frac{\mathcal{L}(\{x\}|\mu,\hat{\hat{\theta}}_\mu)}{\mathcal{L}(\{x\}|\hat{\mu},\hat{\theta})}. \tag{9.5}$$

[2] The center of the Gaussian (global observable) can be an arbitrary value, but it is typically $\theta_{\text{nominal}} = 0$.
[3] A definition $q_\mu = -\Delta\ln(L)$ is often used in literature, but Eq. 9.5 is used in this thesis.

The statistical significance of an excess is $\sqrt{2q_0}(\equiv \sqrt{2q_\mu}\big|_{\mu=0})$ standard deviation. A *p-value* is defined as probability that the excess is created based on statistical fluctuation even if the background-only hypothesis is valid, and the p-value can be calculated as $\mathrm{erfc}(\sqrt{q_0})/2$. Here, the factor 1/2 is necessary since without the factor it represents the probability that either larger excess or deficit is observed.

Estimate of parameters and their uncertainties

Uncertainty of a parameter is also derived from the test statistic q_μ. Here, a method for derivation of uncertainties is explained using the signal strength μ as an example. As shown in Figure 9.1, a typical curve of a likelihood as a function of $\mu(= -\Delta\ln(L))$ has an approximately parabolic shape. The maximum likelihood estimate of the parameter μ is defined as μ that minimizes q_μ. The uncertainty of μ is defined as the interval with which q_μ gives the smaller value than 1/2.

Likelihood curves can be evaluated with full systematic uncertainties and with some nuisance parameters of interest fixed at the best-fit values. The curve evaluated with fixed parameters always gives a smaller width than the one with the full systematic uncertainties. Thus, a breakdown of contributions to the total uncertainty of μ is defined as the difference in quadrature between the total uncertainty and the uncertainty derived by fixing the relevant nuisance parameters at the best fit values. An example breakdown of contributions to the total uncertainty into experimental and theoretical components is shown in Table 9.1.

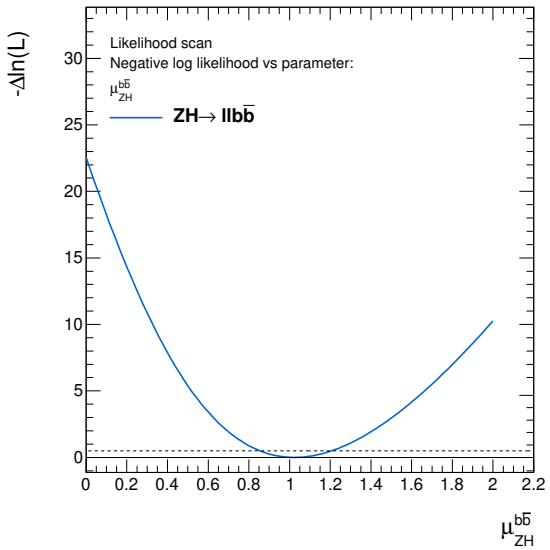

Figure 9.1: A typical curve of a log likelihood ratio ($q_\mu = -\Delta\ln(L)$) as a function of μ. The likelihood is minimized with respect to the other parameters at each given value of μ. The fit is performed only with the 2-lepton regions, and with the BDT distributions. Since the model is fitted to the Asimov dataset created with the S+B hypothesis, the NLL gives the minimum at $\mu = 1$. The dashed line indicates the y-value of 0.5 to show the 1 σ interval of μ.

Table 9.1: Example of a breakdown of the contribution to the total uncertainty. The fit is performed only in the 2-lepton regions with the BDT distributions. Since the model is fitted to the Asimov dataset created with the signal plus background hypothesis, the central value of μ is 1. The total uncertainty is computed from the likelihood scan with all nuisance parameters included. The "data statistical" uncertainty is computed from the similar likelihood scan with all nuisance parameters are fixed except floating normalization factors that are introduced in Section 9.2.1. The "systematic" uncertainty is defined as $\sqrt{(\text{total})^2 - (\text{data statistical})^2}$. "Data statistical" is computed from the likelihood scan with all nuisance parameters are fixed including the floating normalization factors. The other lines are defined by quadratically subtracting the 1 σ intervals evaluated with relevant parameters fixed at the best fit values from the total 1 σ interval.

POI		Central Value	
Signal strength μ		1	
Source of uncertainty		Impact on error	
Total		+0.187 / -0.172	±0.179
Statistical		+0.116 / -0.115	±0.116
Systematic		+0.146 / -0.128	±0.137
Statistical uncertainties			
Data statistical		+0.109 / -0.107	±0.108
$t\bar{t}$ eμ control region		+0.016 / -0.016	±0.016
Floating normalizations		+0.037 / -0.035	±0.036
Experimental systematic uncertainties			
Jets		+0.050 / -0.040	±0.045
$E_{\mathrm{T}}^{\mathrm{miss}}$		+0.014 / -0.013	±0.014
Leptons		+0.004 / -0.003	±0.004
b-tagging	b-jet	+0.047 / -0.042	±0.045
	c-jet	+0.038 / -0.033	±0.036
	light-jet	+0.011 / -0.011	±0.011
	extrap	+0.000 / -0.000	±0.000
Pile-up		+0.006 / -0.005	±0.005
Luminosity		+0.018 / -0.013	±0.016
Theoretical and modelling systematic uncertainties			
Signal		+0.058 / -0.043	±0.051
Z + jets		+0.034 / -0.031	±0.032
W + jets		+0.039 / -0.036	±0.037
$t\bar{t}$		+0.021 / -0.020	±0.020
single top quark		+0.022 / -0.021	±0.022
Diboson		+0.041 / -0.037	±0.039
Multi-jet		+0.006 / -0.006	±0.006
Luminosity		+0.018 / -0.013	±0.016
MC statistical		+0.029 / -0.030	±0.029

Correlation of measurements

The parameters are constrained in the multi-dimensional space of the parameters since a likelihood is a function of multiple parameters. To characterize the constraints, the behavior of the negative log likelihood around the minimum is represented by Hessian:

$$H_{ij} = \frac{\partial^2(-\ln \mathcal{L})}{\partial\theta_i \partial\theta_j}. \tag{9.6}$$

A *covariance matrix* is defined as the inverse matrix of *Hessian* [156]:

$$\mathrm{Cov}_{ij} = (H^{-1})_{ij} \tag{9.7}$$

Note that the following identity is hold.

$$(H^{-1})_{ij} = \frac{\int d\theta\theta_i\theta_j e^{-(-\ln \mathcal{L}_0 + H_{ij}\theta_i\theta_j)}}{\int d\theta e^{-(-\ln \mathcal{L}_0 + H_{ij}\theta_i\theta_j)}} \tag{9.8}$$

$$\simeq \frac{\int d\theta\theta_i\theta_j \mathcal{L}(\{\theta\})}{\int d\theta \mathcal{L}(\{\theta\})}. \tag{9.9}$$

In this sense, the covariance in the profiled likelihood fit has the same form as that in ordinary probability. A *correlation matrix* is defined by normalizing the diagonal components of the covariance:

$$\mathrm{Cor}_{ij} = \frac{\mathrm{Cov}_{ij}}{\sqrt{\mathrm{Cov}_{ii}\mathrm{Cov}_{jj}}}. \tag{9.10}$$

When a feature of data can be explained by several parameters, a correlation of the parameters usually takes place.

9.2 Analysis specific configurations used in the VHbb analysis

9.2.1 Treatment of the dominant backgrounds

The dominant backgrounds, W + jets, Z + jets, and $t\bar{t}$, have separate normalization factors implemented as nuisance parameters without constraint terms. These normalization factors are separately assigned to the 2-jet and (≥)3-jet categories. Thus, the analysis does not rely on theoretical predictions of the cross-sections of these backgrounds.

Each lepton channel has multi-component backgrounds. Thus, a simultaneous fit across the channels and the categories is needed to improve the estimation of backgrounds in the signal regions using the data in the control regions as briefly discussed in Section 6.5. This improvement of estimation by other fitting regions is referred to as *extrapolation*. The extrapolation needs associated systematic uncertainties, introduced in Chapter 8, since the normalization factors can be different among the fitting regions.

The extrapolation of the dominant backgrounds happens as indicated in Figure 9.2. Since the leptonic decay channel of the $t\bar{t}$ background is very pure in the eμ control regions, the normalization factor of this background can be obtained in that region. However, the analysis adopts a more advanced approach,

directly using the data distributions in the eμ control regions as templates in the signal regions. This method is detailed in Section 7.2.2. The semi-leptonic $t\bar{t}$ is mainly constrained in the high-ΔR-CRs of the 1-lepton channel, and this is correlated in the signal regions of the 0- and 1-lepton channels. The semi-leptonic $t\bar{t}$ is correlated in the high-ΔR-CRs of the 1-lepton channel and the signal regions of the 0- and 1-lepton channels. Then, the background is mainly constrained in the high-ΔR-CRs of the 1-lepton channel. The Z + jets backgrounds are pure both in the high-ΔR-CRs and the low-ΔR-CRs of the 2-lepton channel since the $t\bar{t}$ background is modeled by the data-driven method and no systematic uncertainty needs to be considered. The obtained normalization factors for the Z + jets background are extrapolated to the signal regions of the 0- and 2-lepton channels. The W + jets backgrounds are constrained in the low-ΔR-CRs of the 1-lepton channel. Then the constraints are extrapolated to the signal regions of the 0- and 1-lepton channels.

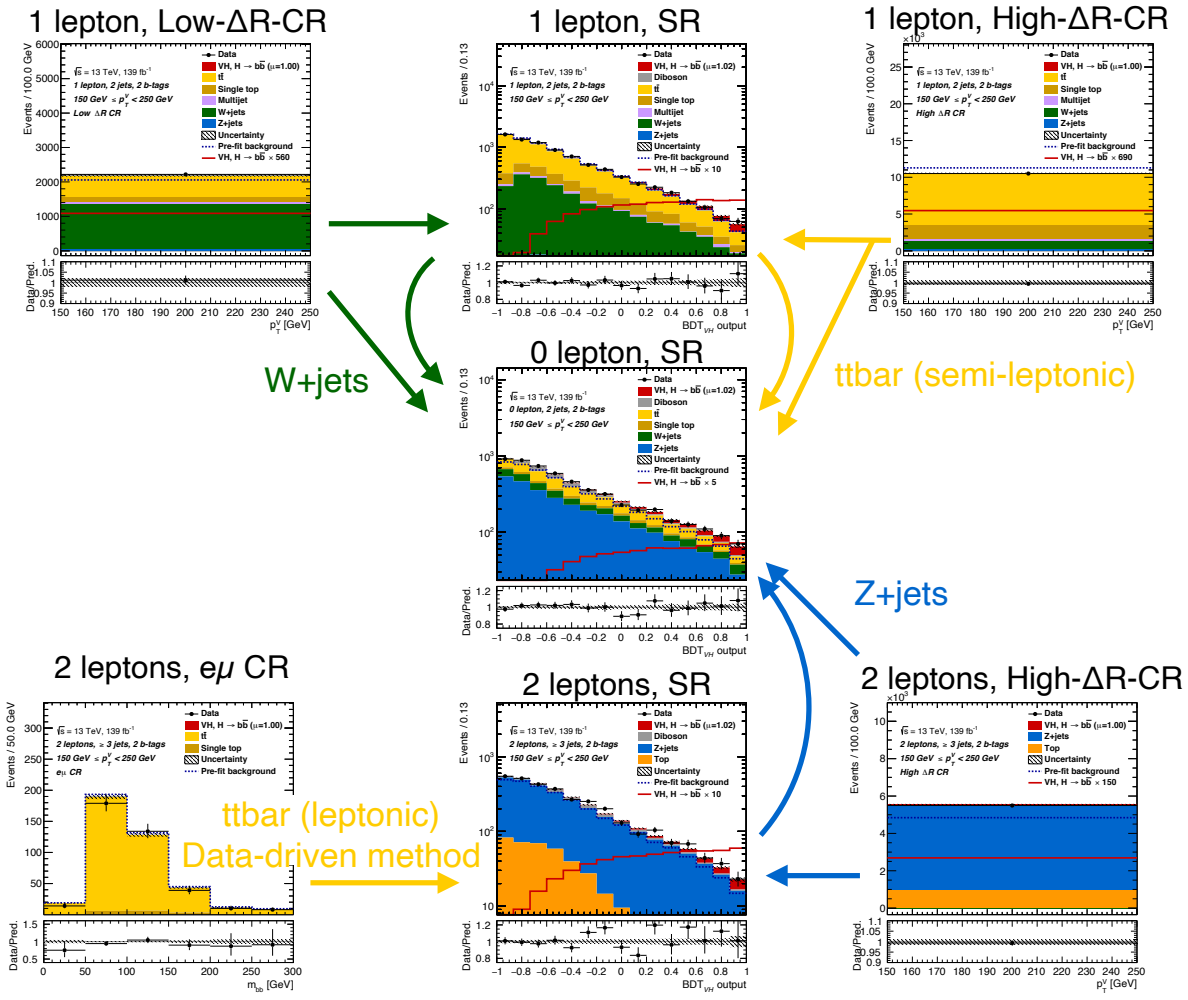

Figure 9.2: Schematic diagram of extrapolation of knowledge on the backgrounds. The arrows indicate the extrapolation of the constraints on the normalization and the shapes of the backgrounds. The blue, green, and yellow arrows explain the extrapolation of Z + jets, W + jets, and $t\bar{t}$ as indicated in the figure. The 1-, 0- and 2-lepton regions are shown in the top, middle and bottom rows. Note that the eμ control regions are actually not fitted, but the data events are directly used to construct templates in the 2-lepton regions as discussed in Sections 7.2.2 and 9.2.2.

The systematic uncertainties on the shapes of $m_{b\bar{b}}$ and so on are also considered to describe residual differences between the simulations and the data. All the systematic uncertainties explained in Chapter 8 are implemented as nuisance parameters with constraint terms. These nuisance parameters are constrained in one fitting region and extrapolated to other regions if it gives a reasonable description of the data.

9.2.2 Configurations relevant to the data-driven estimation of the $t\bar{t}$ background

Uncertainties on the data-driven estimation of the $t\bar{t}$ background (Section 7.2.2) have only two components. The first dominant component is statistical uncertainty in each bin. The second one is an overall extrapolation factor associated with the extrapolation from the eμ control regions to the signal regions. This is much smaller than the statistical one.

The extrapolation uncertainty is implemented with nuisance parameters separately in the 2-jet and ≥3-jet regions with the sizes derived in Section 7.2.2.

The statistical uncertainties are implemented by setting the independent nuisance parameters (γ) introduced in Eq. 9.4, for all the bins. The shape of the constraint term of γ for a bin where the data-driven template has one event is plotted in Figure 9.3.

The statistical uncertainties are also assigned to bins without the entry of the data-driven template according to the following argument. When N events are observed, the likelihood function for λ that is the predicted yield of an underlying model is given by Poisson probability

$$F(N|\lambda) = \frac{\lambda^N}{N!}e^{-\lambda}. \tag{9.11}$$

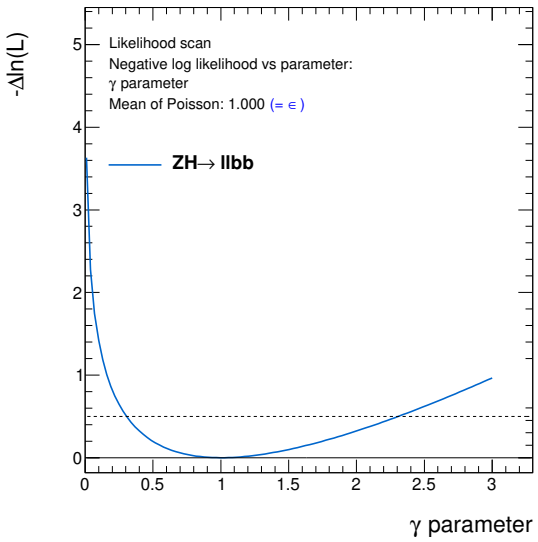

Figure 9.3: Curve of the negative log-likelihood as a function of a statistical nuisance parameter (γ) in a bin where the data-driven template has one event. The likelihood is not minimized at each given value of γ. The dashed line indicates the y-value of 0.5. The curve is driven by the constraint term of the γ parameter with an additional small contribution to the total likelihood from the bin with one event.

When no event is observed in the template, the expected yield λ and its constraint should be

$$L(\lambda) = F(0|\lambda) = e^{-\lambda}. \tag{9.12}$$

To approximate this likelihood in the RooFit framework, the nuisance parameter γ (Section 9.1.1) is used with a special configuration. The nominal yield of the bin is set to ϵ. Thus, the PDF gives the yield $\gamma\epsilon$ in that bin. In the constraint term of γ (Eq.9.4), τ is substituted with ϵ, then ϵ is set to a small number. The mathematical foundation of this operation is based on the following equation:

$$f(\gamma;\epsilon) = (\epsilon\gamma)^{\epsilon} e^{-\epsilon\gamma} \to e^{-\epsilon\gamma} \quad (\text{as } \epsilon \to 0, \epsilon\gamma \text{ is fixed}). \tag{9.13}$$

This shows that $f(\gamma;\epsilon)$ approximates Eq.9.12 for the case of 0 observed events.

The right plot of Figure 9.4 shows the shape of $-\ln f(\gamma;\epsilon)$ ($\epsilon = 0.001$). Since the yield of the PDF is $\gamma\epsilon$, $\lambda = \gamma\epsilon = 0.001\gamma$. Thus, the curve approximates Eq.9.12.

9.2.3 Truth categorization and unfolding

As briefly introduced in Section 6.1, the cross-sections in the theoretically well-defined phase spaces are measured using reconstructed variables. Aspects of the statistical analysis are explained in this section starting with a reminder of Section 6.1.

In the differential cross-section measurement, a cross-section in a physically well-defined phase space (*fiducial volume*) is extracted. Those phase spaces are defined using variables that theoretical calculations

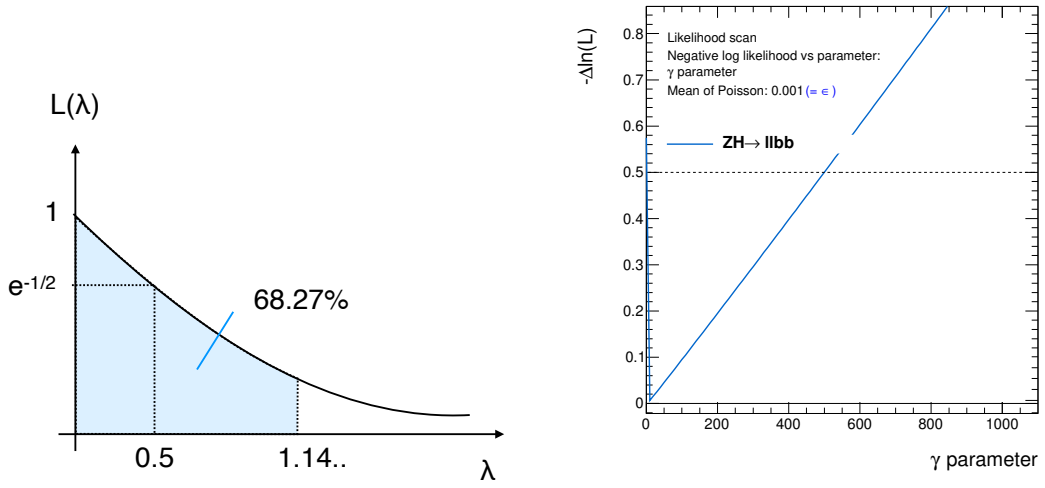

Figure 9.4: Left: Likelihood function for the predicted yield λ when 0 events are observed. $\lambda = 0.5$ gives the likelihood value of $e^{-1/2}$, which means $= \Delta\ln(L) = 0.5$, while $\lambda = 1.14$ gives 68.27% confidence interval. Right: Curve of the negative log-likelihood as a function of a statistical nuisance parameter (γ) in a bin where the data-driven template has no event and the small dummy yield $\epsilon\gamma$ ($\epsilon = 0.001$) is assigned. The likelihood is not minimized at each given value of γ. The dashed line indicates the y-value of 0.5. Since the template with $\epsilon\gamma$ events has a small contribution to the total likelihood, the curve is mainly driven by the constraint term of the γ parameter. The curve intersects with the dashed line at $\gamma \sim 500$, which means $\epsilon\gamma \sim 0.5$, thus it gives a correct 1 σ interval.

rely on in physics simulations. Such theoretically well-defined variables are called *truth variable*, and categorization based on the truth variables is called *truth categorization*. In the analysis presented in this thesis, the binning with the $p_{\mathrm{T}}^{V,\mathrm{truth}}$ for WH and ZH is an example application of the truth categorization.

In the estimation of a signal in categories based on reconstructed quantities (*reconstructed categories*), detector effects are folded. A reconstructed category can contain signal events that are not in the corresponding truth category. This event migration is caused by detector effects such as resolution or identification efficiency of leptons, jets, and so on. The estimation of the signal in the reconstructed category is dependent on the performance of detectors, thus it is not theoretically well-defined.

To extract cross-sections in fiducial volumes, the simulated signal events are classified with truth variables, and truth categories are defined. In the construction of the likelihood function, independent normalization parameters μ are assigned to the truth categories. Thus, information on the truth-reconstructed migration is encoded in the likelihood. μ are estimated by maximizing the likelihood.

The acceptance of the analysis is not the same as the fiducial volume for which the cross-section is measured. In order to measure the cross-section for the fiducial volume using events in the analysis phase space, it is necessary to consider the acceptance uncertainties which are explained in Section 8.2.2.

This process for measuring quantities defined for truth categories or fiducial volumes using reconstructed categories is often called *unfolding*.

9.2.4 Blind of the signal

We employed blind analysis following the procedures:

- Data points are not plotted in bins where the high S/N is predicted by the simulations.
- The normalization factors of the signals are fixed at the prediction of the Standard Model.
- Optimization is done with blinding both the VH and VZ processes. Thus, analysis strategies are optimized to maximize the *expected* sensitivity.
- Once all the needed systematic uncertainties are implemented and fits show reasonable behaviors, the VZ signal is unblinded and the signal strength μ_{VZ} is fitted.
- Finally, the VH signal is unblinded.

After unblinding the VZ signal, additional uncertainties for Z + jets and W + jets are added to account for the migration between the signal regions and the high-ΔR-CRs; the signal regions and low-ΔR-CRs. This is because significant tensions between these regions are found for the normalization factors of these backgrounds, and it is concluded that the impact of these tensions on the measurement can not be neglected.

10 Results

The results of the performed measurements are presented in this chapter. The measurement of the signal strengths for the VH signal are shown in Section 10.1. The analysis validations exploiting the diboson processes and the $m_{b\bar{b}}$ distributions are shown in Section 10.2. The measurement of the differential cross-section of the VH production times the branching ratio of the $H \to b\bar{b}$ decay as a function of p_{T}^{V} is presented in Section 10.3.

10.1 Signal strength measurement of the VH signal

The unblinded distributions of BDT_{VH} after fitting are shown in Figure 10.1. The unblinded distributions in the other signal regions after fitting are shown in Appendix I.1 (Figures I.1 and I.2).

The unblinded results of the signal strength (μ) measurement from the simultaneous fit with two μs for WH and ZH, and the combined fit with single-μ for VH are shown in Figure 10.2. The measurements exclude the background-only hypothesis with observed (expected) significance of 4.0 (4.1) and 5.3 (5.1) standard deviations for the WH and ZH signals. The significance of the excess under various signal hypotheses is shown in Table 10.1. The fitted μ of the WH and ZH signals are

$$\mu_{WH}^{bb} = 0.95^{+0.27}_{-0.25} = 0.95^{+0.18}_{-0.18}(\mathrm{stat.})^{+0.19}_{-0.18}(\mathrm{syst.}),$$
$$\mu_{ZH}^{bb} = 1.08^{+0.25}_{-0.23} = 1.08^{+0.17}_{-0.17}(\mathrm{stat.})^{+0.18}_{-0.15}(\mathrm{syst.}),$$

and the μ for the combined VH signal is

$$\mu_{VH}^{bb} = 1.02^{+0.18}_{-0.17} = 1.02^{+0.12}_{-0.11}(\mathrm{stat.})^{+0.14}_{-0.13}(\mathrm{syst.}).$$

The μ in the 0-, 1-, and 2-lepton channels are shown in Figure 10.3. As shown in the plot, the the 0-, 1-, and 2-lepton channels have similar sensitivity. The dependence of μ on p_{T}^{V} and the number of jets is also studied in each lepton channel. All the measurements are consistent within their uncertainties. A compatibility test is performed based on the method in Appendix H to estimate quantitative consistency among the categories (number-of-jets, p_{T}^{V}) and the consistency of the measurements with the Standard

Table 10.1: Summary of the significance of the excess by the VH signal hypotheses from the background-only hypothesis.

Signal hypothesis	Expected significance	Observed significance
VH	6.7	6.7
WH	4.1	4.0
ZH	5.1	5.3

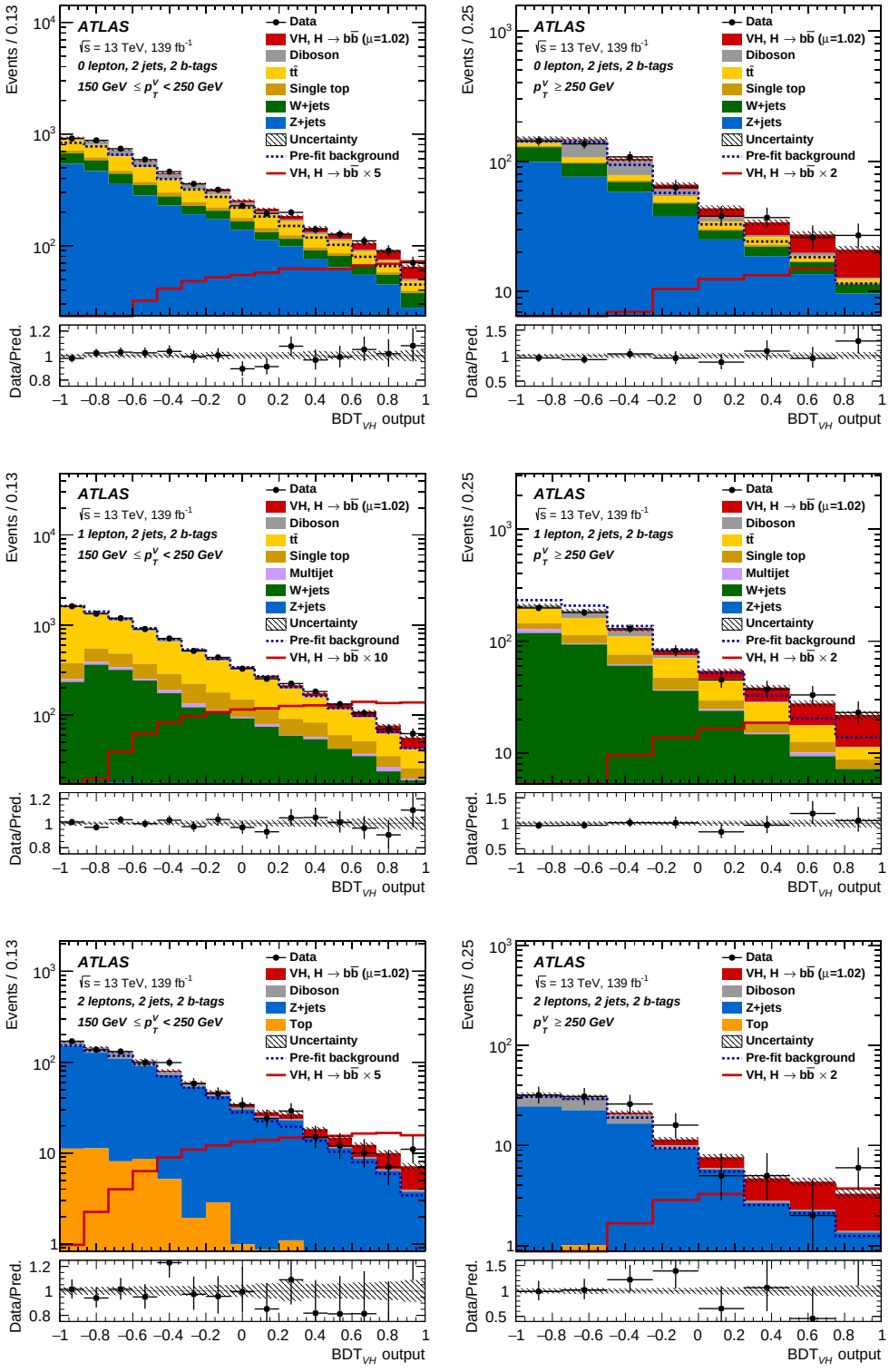

Figure 10.1: The distributions of the BDT_{VH} scores in the categories with 2 jets and $150 \leq p_{\mathrm{T}}^{V} < 250$ GeV, $p_{\mathrm{T}}^{V} \geq 250$ GeV of the 0-,1- and 2-lepton channels. The stacked histograms show the prediction after the fitting. The red unstacked and unfilled histograms show the VH signals with the scale factors indicated in the legend. The lower panels show the ratio of the data and the prediction of the signals and the backgrounds. The hatched bands in the lower and upper panels show the total uncertainty that includes both the statistical and systematic uncertainties.

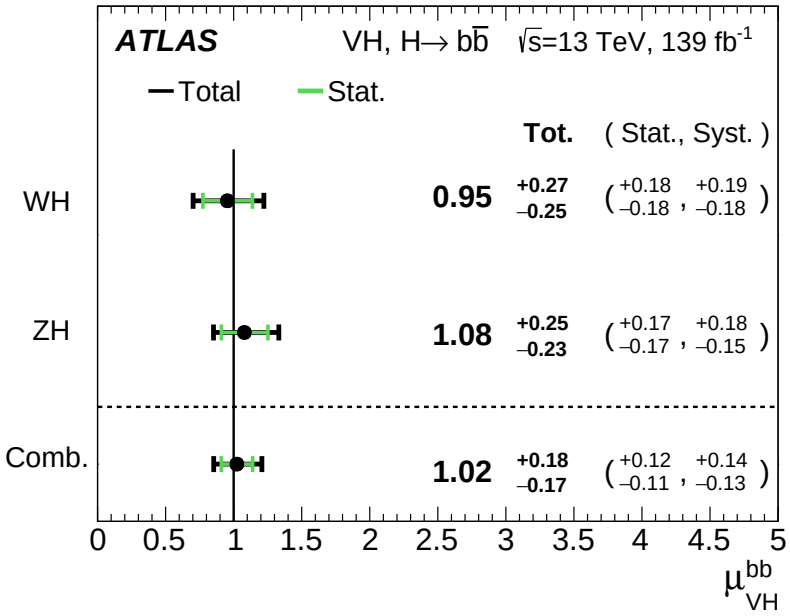

Figure 10.2: μ_{VH}^{bb} values for WH and ZH are obtained from the simultaneous fit with individual signal strengths for these signals. The combined μ_{VH}^{bb} is obtained from the fit that uses the single signal strength for both of the signals.

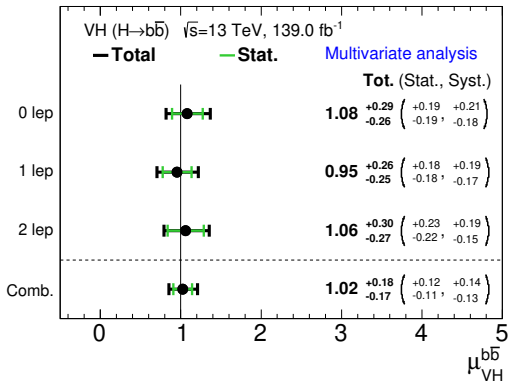

Figure 10.3: Observed signal strengths μ_{VH}^{bb} of the VH processes in the 0-, 1- and 2-lepton channels and the combination. The μ_{VH}^{bb} values for the channels are obtained from the simultaneous fits with the individual signal strengths for these channels. The combined μ_{VH}^{bb} is obtained from the fit with the single signal strength for three channels.

Model (SM) prediction. The results of the compatibility test are 71-99%. Detailed results are presented in Appendix I.1.

The breakdown of the contributions to the uncertainty on the signal strength μ is shown in Table 10.2. These numbers are defined with the method introduced in Section 9.1.3, i.e. by taking the differences in quadrature between the total 1σ width of μ and a 1σ that is derived by fixing the considered nuisance parameters to their best-fit values. For both WH and ZH, the systematic and statistical uncertainties are of similar size. Important sources of the systematic uncertainty are related to the calibration of jets, $E_{\mathrm{T}}^{\mathrm{miss}}$, flavor tagging, and the signal and background modeling. These are understood as following.

Experimental uncertainties: The uncertainties relevant to the calibration of jets and b-tagging are large for both WH and ZH. The systematic uncertainty of the jet energy calibration is relevant because the calibration affects the reconstructed distribution of kinematic variables such as $m_{b\bar{b}}$ and BDT_{VH}. The systematic uncertainties on the efficiency of the b-tagging and the $E_{\mathrm{T}}^{\mathrm{miss}}$ reconstruction are relevant because these uncertainties directly affect the efficiency and the acceptance. The uncertainties on the mis-b-tagging rate for c-jets has a significant contribution since the 1-lepton channel much relied on the rejection of c-jets in the BDT discriminant.

Theoretical uncertainties: The uncertainty on W + jets and Z + jets have a large contribution to WH and ZH, respectively, because these are the main backgrounds for these signals. The uncertainty on the $t\bar{t}$ production is much reduced in ZH compared to WH due to the data-driven technique developed in Section 7.2.2 and 9.2.2. The signal uncertainty is much larger for ZH than WH since the ZH includes $gg \to ZH$ modeled with calculation with the leading order accuracy. Contributions per nuisance parameter are shown in Appendix J with an evaluation method.

10.2 Cross-check and validation

10.2.1 Validation with the WZ and ZZ processes

The background estimation is validated by performing the analysis that considers the diboson processes as the signals as explained in Section 6.7. This analysis uses a multivariate discriminant, BDT_{VZ}, instead of BDT_{VH} for the main analysis that measures the Higgs signals. The unblinded distributions of BDT_{VZ} after fitting are shown in Figure 10.4. The unblinded distributions of BDT_{VZ} in the other signal regions after fitting are shown in Appendix I.3 (Figures I.8 and I.9). As shown in these figures, the simulation provides a reasonable description of the data, and the excess can be confirmed in the high BDT_{VZ} bins.

As shown in Figure 10.5, the fitted values of the signal strength for WZ and ZZ are

$$\mu_{WZ}^{bb} = 0.68^{+0.26}_{-0.24} = 0.68^{+0.15}_{-0.15}(\mathrm{stat.})^{+0.21}_{-0.19}(\mathrm{syst.}),$$
$$\mu_{ZZ}^{bb} = 1.00^{+0.18}_{-0.15} = 1.00^{+0.08}_{-0.08}(\mathrm{stat.})^{+0.16}_{-0.13}(\mathrm{syst.}),$$

and the one for the combined VZ signal is

$$\mu_{VZ}^{bb} = 0.93^{+0.15}_{-0.14} = 0.93^{+0.07}_{-0.06}(\mathrm{stat.})^{+0.14}_{-0.12}(\mathrm{syst.}).$$

Table 10.2: Uncertainties of the signal strength measurement for WH, ZH, and combined VH, and their breakdown of the contributions to the uncertainty. The total uncertainty is defined as the 1σ width of the signal strength. The components are defined as the differences in quadrature between the total uncertainty and the uncertainties derived by fixing the considered nuisance parameters to their best-fit values.

Source of uncertainty		Size of impacts		
		VH	WH	ZH
Total		0.177	0.260	0.240
Statistical		0.115	0.182	0.171
Systematic		0.134	0.186	0.168
Statistical uncertainties				
Data statistical		0.108	0.171	0.157
$t\bar{t}$ $e\mu$ control region		0.014	0.003	0.026
Floating normalisations		0.034	0.061	0.045
Experimental uncertainties				
Jets		0.043	0.050	0.057
$E_{\mathrm{T}}^{\mathrm{miss}}$		0.015	0.045	0.013
Leptons		0.004	0.015	0.005
b-tagging	b-jets	0.045	0.025	0.064
	c-jets	0.035	0.068	0.010
	light-flavour jets	0.009	0.004	0.014
Pile-up		0.003	0.002	0.007
Luminosity		0.016	0.016	0.016
Theoretical and modelling uncertainties				
Signal		0.052	0.048	0.072
Z + jets		0.032	0.013	0.059
W + jets		0.040	0.079	0.009
$t\bar{t}$		0.021	0.046	0.029
Single top quark		0.019	0.048	0.015
Diboson		0.033	0.033	0.039
Multi-jet		0.005	0.017	0.005
MC statistical		0.031	0.055	0.038

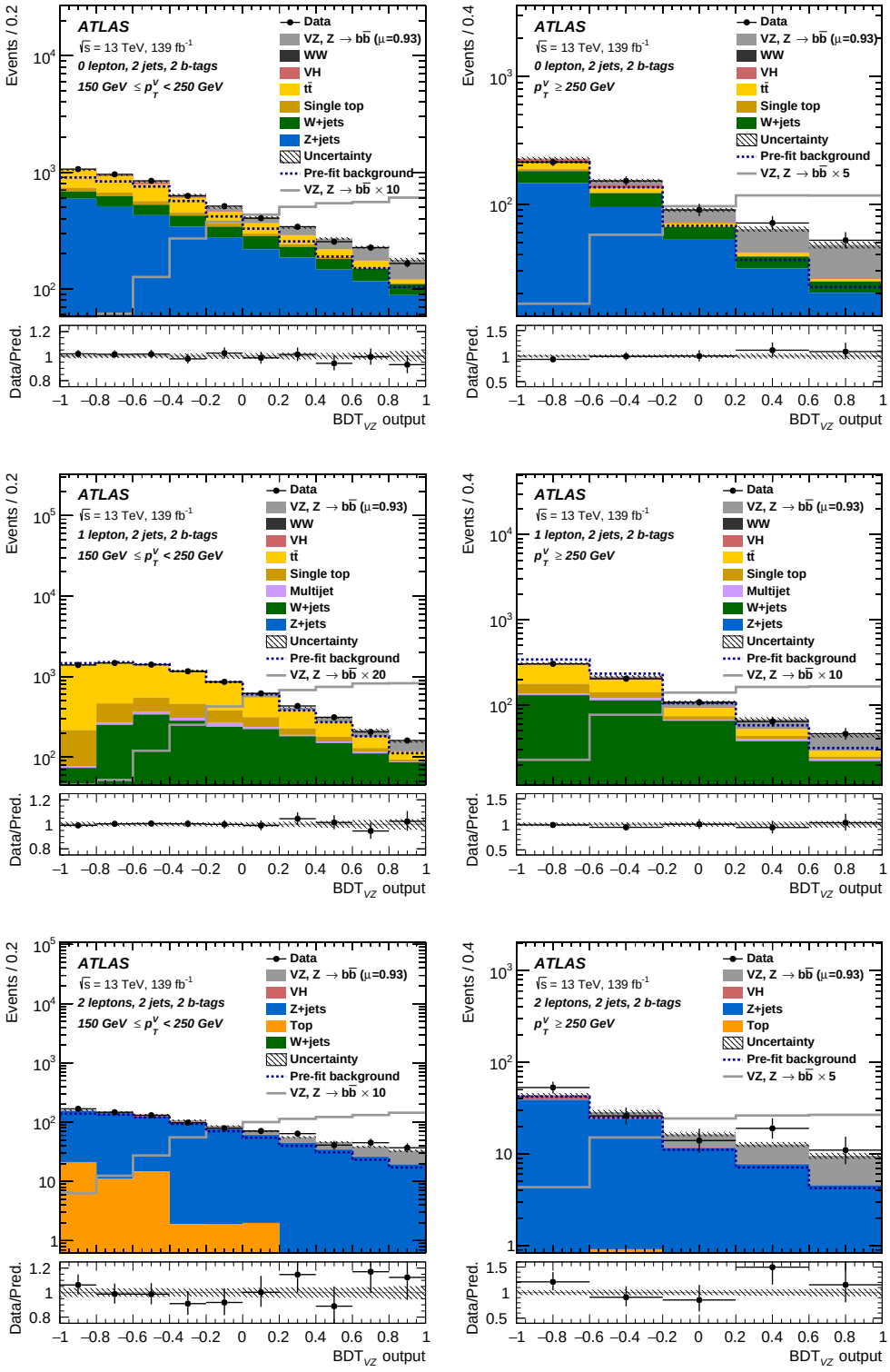

Figure 10.4: Distributions of the BDT_{VZ} scores for the prediction and the data in the categories with 2 jets and $150 \leq p_{\mathrm{T}}^{V} < 250$ GeV, $p_{\mathrm{T}}^{V} \geq 250$ GeV of the 0-,1- and 2-lepton channels. The stacked histograms show the prediction after the fitting. The gray unstacked and unfilled histograms show the diboson signals with the scale factors indicated in the legend. The lower panels show the ratio of the data and the prediction of the signals and the backgrounds. The hatched bands in the lower and upper panels show the total uncertainty that includes both the statistical and systematic uncertainties.

The fitted μ for ZZ agrees with the prediction of the SM well. On the other hand, the fitted μ for WZ is slightly lower than the SM. However, the compatibility of the SM hypothesis with the data is 48%, and this shift is not statistically significant. It is concluded that the background modeling and the simultaneous fit work correctly.

Detailed results are presented in Appendix I.3

10.2.2 Cross-check: dijet mass analysis

As explained in Section 6.7, in order to cross-check the results of the VH signal with the BDTs (Section 10.1), the unblinded distributions of $m_{b\bar{b}}$ after fitting are shown in Figure 10.6. The distributions of the other categories after fitting are shown in Appendix I.2 (Figures I.4 and I.5).

The measurements exclude the background-only hypothesis with the observed (expected) significance of 5.5 (4.9) standard deviations for the VH signal. The significance of the excess under various signal hypotheses is shown in Table 10.3. The fitted value of the signal strength μ is

$$\mu_{VH}^{bb} = 1.17^{+0.25}_{-0.23} = 1.17^{+0.16}_{-0.16}(\text{stat.})^{+0.19}_{-0.16}(\text{syst.}).$$

The results of the signal strength from the MVA-based analysis and the $m_{b\bar{b}}$-based analysis are compared in Figure 10.7, and we concluded that all the measurements show reasonable consistency, which in turn means the BDT discriminants are reliable.

Detailed results are presented in Appendix I.2.

10.3 Cross-section measurements

As discussed in Sections 6.1 and 8.2.2, the measurement of the cross-sections is performed by fitting without the theoretical uncertainties on the signal cross-sections that are measured. The residual uncertainties on

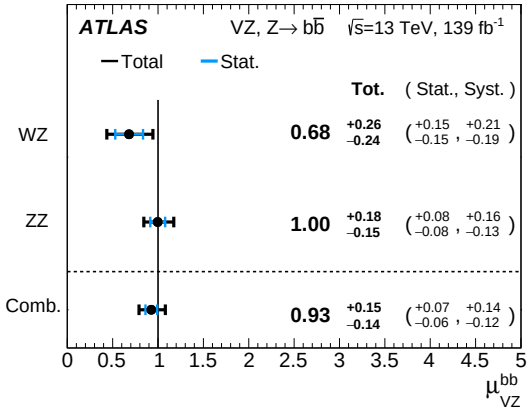

Figure 10.5: Observed signal strengths μ_{VZ}^{bb} of the diboson processes, WZ, ZZ, and the combination, VZ. The μ_{VZ}^{bb} values for WZ and ZZ are obtained from the simultaneous fit with the individual signal strengths for these signals. The combined μ_{VZ}^{bb} are obtained from the fit with single signal strength for two signals.

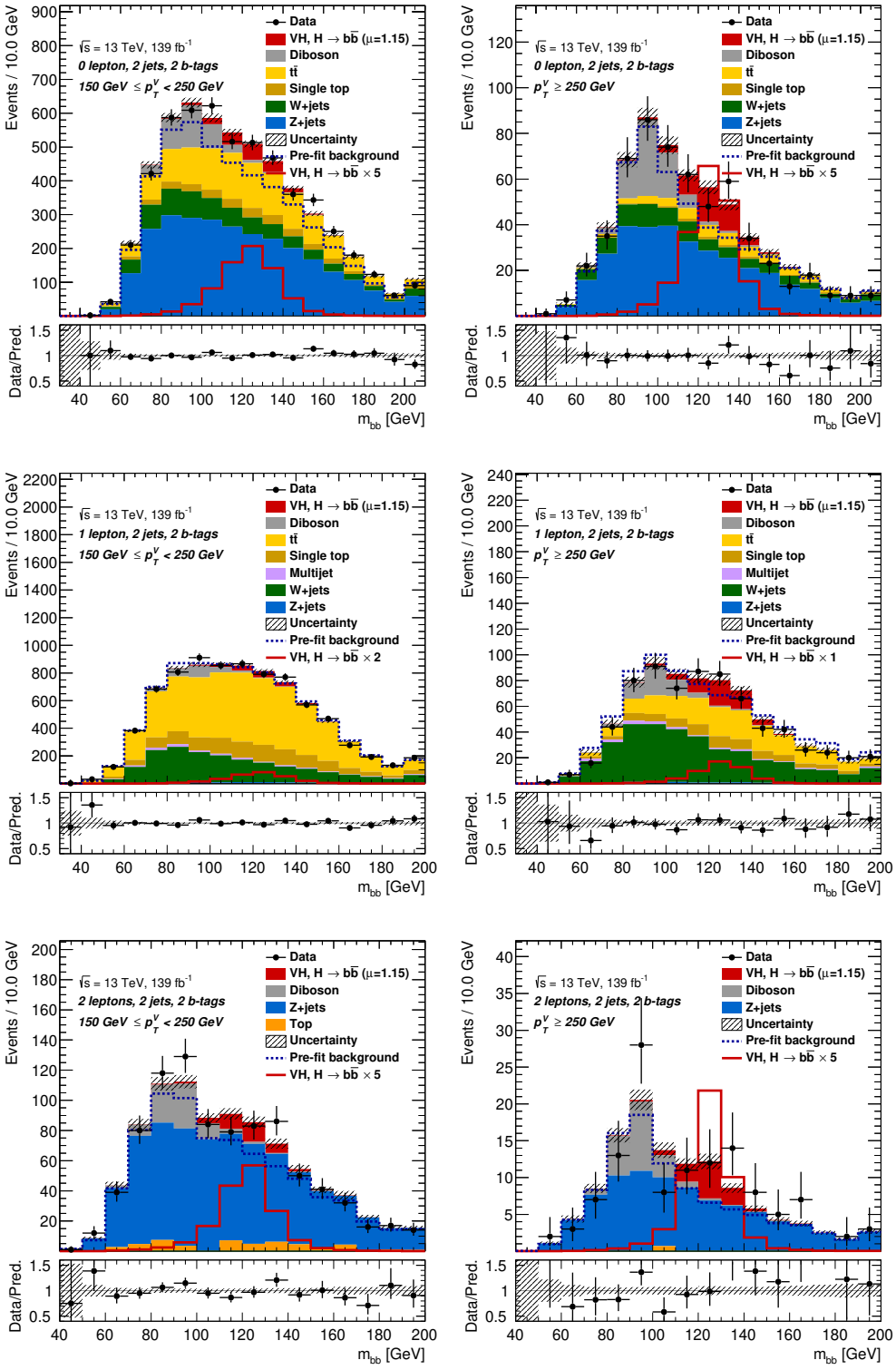

Figure 10.6: Distributions of the $m_{b\bar{b}}$ in the categories with 2 jets and $150 \leq p_{\mathrm{T}}^{V} < 250$ GeV, $p_{\mathrm{T}}^{V} \geq 250$ GeV of the 0-,1- and 2-lepton channels. The stacked histograms show the prediction after the fitting. The red unstacked and unfilled histograms show the VH signals with the scale factors indicated in the legend. The lower panels show the ratio of the data and the prediction of the signals and the backgrounds. The hatched bands in the lower and upper panels show the total uncertainty that includes both the statistical and systematic uncertainties.

Table 10.3: Summary of the significance of the excess in the dijet mass distributions by the VH signal hypotheses from the background-only hypothesis.

Signal hypothesis	Expected significance	Observed significance
0 lepton	3.3	3.5
1 lepton	2.7	3.4
2 leptons	2.9	3.5
Combined	4.9	5.5

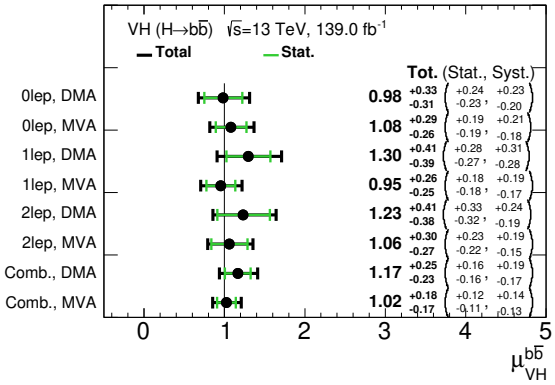

Figure 10.7: Comparison of the measured signal strengths from the MVA-based analysis (MVA) and the dijet mass analyses (DMA) the 0-, 1-, and 2-lepton channels. The individual μ_{VH}^{bb} values are obtained from the simultaneous fits with the individual signal strengths for the indicated categories. The combined μ_{VH}^{bb} is obtained from the fit with the single signal strength for the signals in all the categories.

the signal modeling are kept to describe either internal shape uncertainties in bins where the measurement are performed or the acceptance uncertainties. As discussed in Section 6.1, the measurements in the 14 signal regions are unfolded to the cross-sections in 5 bins: $150 \leq p_{\mathrm{T}}^{V} < 250$ GeV and $p_{\mathrm{T}}^{V} \geq 250$ GeV for the WH signal, and $75 \leq p_{\mathrm{T}}^{V} < 150$ GeV, $150 \leq p_{\mathrm{T}}^{V} < 250$ GeV and $p_{\mathrm{T}}^{V} \geq 250$ GeV for the ZH signal. Note that, for ZH, the cross-section of $qq \rightarrow ZH$ plus $gg \rightarrow ZH$ are measured since these two signals can not be separated with the current statistics. The uncertainty on the fraction of the qq and gg components are included by the method described in Section 8.2.2 and Appendix F. All the bins are restricted to the phase spaces with the rapidity of Higgs less than 2.5: $|y_{\mathrm{Higgs}}| < 2.5$.

The measured cross-sections are shown in Figure 10.8 and Table 10.4. All the results show agreement with the Standard Model predictions within their uncertainties. The relative uncertainty on the cross-section is about 85% in the lowest p_{T}^{V} bin and about 30% in the higher p_{T}^{V} bins. The correlations of the measurements in the bins are derived as explained in Section 9.1.3 and shown in Appendix I.4 (Figure I.11).

The breakdown of the contributions to the relative uncertainties on the signal cross-sections in the measured bins are shown in Appendix I.4 (Tables I.5 and I.6).

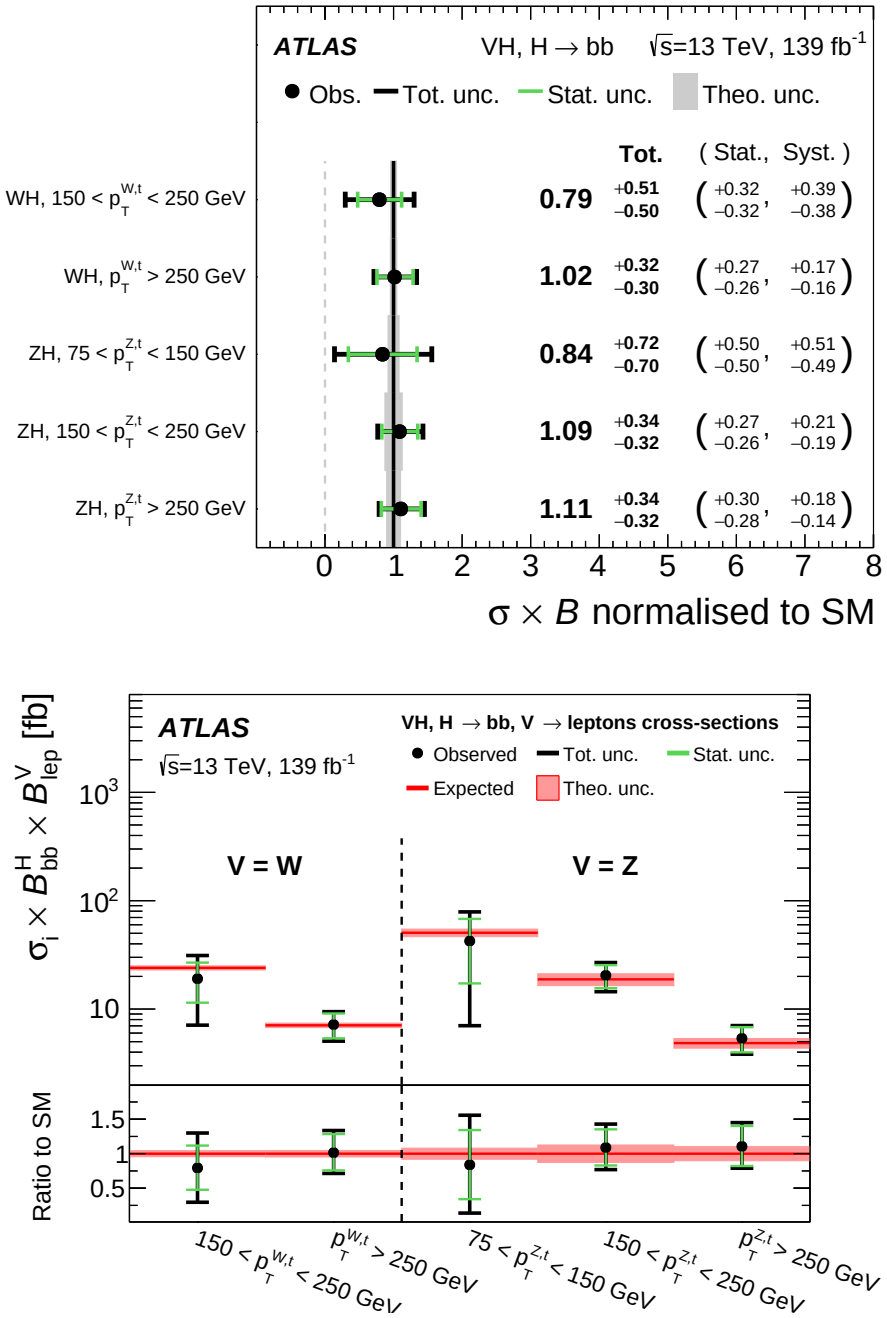

Figure 10.8: Measured cross sections of the VH production (σ) times the branching ratio of the $V \rightarrow$ leptons and $H \rightarrow b\bar{b}$ decays (B). The $\sigma \times B$ values are unfolded to the indicated bins. The top plot shows the $\sigma \times B$ normalized to the Standard Model predictions. The bottom one shows the absolute values of $\sigma \times B$.

Table 10.4: Standard Model predictions and the measured differential cross-sections of the VH production (σ) times the branching ratio of $V \to$ leptons and $H \to b\bar{b}$ decays (B) in the fiducial phase spaces. The uncertainty on $\sigma \times B$ and the breakdown into the statistical and systematic sources. The systematic uncertainty is further broken down into the theoretical uncertainties on the signal and background modeling, and the experimental ones.

STXS region		SM prediction			Result			Stat. unc.	Syst. unc. [fb]					
Process	$p_{\mathrm{T}}^{V,\,\mathrm{truth}}$ interval	[fb]			[fb]			[fb]	Th. sig.		Th. bkg.		Exp.	
$W(\ell\nu)H$	150–250 GeV	24.0	±	1.1	19.0	±	12.1	± 7.7	±	0.9	±	5.5	±	6.0
$W(\ell\nu)H$	> 250 GeV	7.1	±	0.3	7.2	±	2.2	± 1.9	±	0.4	±	0.8	±	0.7
$Z(\ell\ell/\nu\nu)H$	75–150 GeV	50.6	±	4.1	42.5	±	35.9	± 25.3	±	5.6	±	17.2	±	19.7
$Z(\ell\ell/\nu\nu)H$	150–250 GeV	18.8	±	2.4	20.5	±	6.2	± 5.0	±	2.3	±	2.4	±	2.3
$Z(\ell\ell/\nu\nu)H$	>250 GeV	4.9	±	0.5	5.4	±	1.7	± 1.5	±	0.5	±	0.5	±	0.3

11 Discussions

The interpretations of the results are discussed in this chapter. The result of the differential production cross-section of VH times the branching ratio as a function of p_{T}^{V} is interpreted using the Standard Model Effective Field Theory framework in Section 11.1. A new method for testing the CP-property of the ZH production using the decay angle of $Z \to \ell^{+}\ell^{-}$ is proposed in Section 11.2. The Higgs coupling measurement is performed combining the VH, $H \to b\bar{b}$ analysis (this thesis) with other analysis channels, and its interpretation is presented in Section 11.3.

11.1 Differential cross-section as a function of p_{T}^{V}

As described in Sections 2.4 and 6.1, the differential cross-section is interpreted using the Standard Model Effective Field Theory (SMEFT) framework.

The form of the SMEFT Lagrangian is written as:

$$\mathcal{L} = \mathcal{L}_{\mathrm{SM}} + \frac{1}{\Lambda}\sum_{k} C_k^{(5)} Q_k^{(5)} + \frac{1}{\Lambda^2}\sum_{k} C_k^{(6)} Q_k^{(6)} + O\left(\frac{1}{\Lambda^3}\right), \tag{11.1}$$

where $Q_k^{(d)}$ are field operators with dimension-d and $C_k^{(d)}$ are dimensionless Wilson coefficients of the dimension-d operators. Λ is the energy scale of BSM, and it is set to 1 TeV in the analysis. In this formalism, a theory is determined by specifying the Wilson coefficients. A set of operators (basis) could be defined in several ways. The *Warsaw* basis [26] is adopted in this thesis.

By imposing the gauge symmetry of the Standard Model ($SU(3)_{\mathrm{C}} \times SU(2)_{\mathrm{L}} \times U(1)_{\mathrm{Y}}$), there is only one allowed dimension-5 term with the form:

$$Q_{\nu\nu} = \epsilon_{jk}\epsilon_{mn}\varphi^{j}\varphi^{m}(l_p^{k})^{T} C l_r^{n} \equiv (\tilde{\varphi}^{\dagger} l_p)^{T} C (\tilde{\varphi}^{\dagger} l_r), \tag{11.2}$$

where l_p and l_r are the left handed spinors of leptons, and C is the charge conjugation operator. j, k, m, and n are the indices for the components of the $SU(2)_L$ doublets. This operator is referred to as the *Majorana mass* term and violates the lepton number. Similarly, the dimension 7 operators [157] violate the $B - L$. These interactions are not considered in this analysis because other experiments strongly constrain these dimension-5 or 7 operators by searches for the signature with the lepton or $B - L$ violation [33, 158]. In addition, dimension-8 interactions are suppressed by a factor of $1/\Lambda^4$. Therefore, the dimension-6 extension to the Standard Model Lagrangian is focused on in this study.

The total number of theoretically allowed dimension-6 terms is 2499. By imposing the gauge symmetry of the Standard Model and the baryon number conservation reduces the number to 59. The operators are presented in Ref. [26] and shown in Tables K.2 and K.3. There are 13 operators relevant to the VH production (6 for both WH and ZH, and 7 for only ZH). The Yukawa coupling is modified by the dimension-6 term, $c_{dH}Q_{dH}/\Lambda^2$. These relevant operators are summarized in Table 11.1.

Table 11.1: Dimension-6 operators and their Wilson coefficients relevant to the associated production VH and the $H \to b\bar{b}$ decay.

Wilson coefficients	Field operators	Affected processes
c_{HWB}	$\varphi^\dagger \tau^i \varphi W^i_{\mu\nu} B^{\mu\nu}$	ZH
c_{HW}	$\varphi^\dagger \varphi W^i_{\mu\nu} W^{i\mu\nu}$	WH, ZH
$c^{(3)}_{Hq}$	$(\varphi^\dagger i \overleftrightarrow{D}^i_\mu \varphi)(\bar{q}_p \tau^i \gamma^\mu q_r)$	WH, ZH
$c^{(1)}_{Hq}$	$(\varphi^\dagger i \overleftrightarrow{D}_\mu \varphi)(\bar{q}_p \gamma^\mu q_r)$	ZH
$c^{(1)}_{ll}$	$(\bar{l}_p \gamma_\mu l_r)(\bar{l}_s \gamma^\mu l_t)$	WH, ZH
$c^{(3)}_{Hl}$	$(\varphi^\dagger i \overleftrightarrow{D}^i_\mu \varphi)(\bar{l}_p \tau^i \gamma^\mu l_r)$	WH, ZH
$c^{(1)}_{Hl}$	$(\varphi^\dagger i \overleftrightarrow{D}_\mu \varphi)(\bar{l}_p \gamma^\mu l_r)$	ZH
c_{HDD}	$(\varphi^\dagger D^\mu \varphi)^* (\varphi^\dagger D_\mu \varphi)$	WH, ZH
c_{Hu}	$(\varphi^\dagger i \overleftrightarrow{D}_\mu \varphi)(\bar{u}_p \gamma^\mu u_r)$	ZH
c_{Hd}	$(\varphi^\dagger i \overleftrightarrow{D}_\mu \varphi)(\bar{d}_p \gamma^\mu d_r)$	ZH
$c_{H\Box}$	$(\varphi^\dagger \varphi)\Box(\varphi^\dagger \varphi)$	WH, ZH
c_{HB}	$\varphi^\dagger \varphi B_{\mu\nu} B^{\mu\nu}$	ZH
c_{He}	$(\varphi^\dagger i \overleftrightarrow{D}_\mu \varphi)(\bar{e}_p \gamma^\mu e_r)$	ZH
c_{dH}	$(\varphi^\dagger \varphi)(\bar{q}_p d_r \varphi)$	$H \to b\bar{b}$

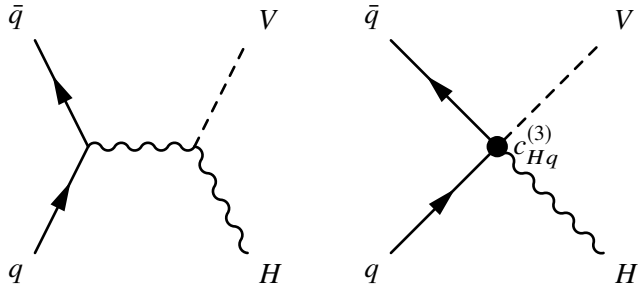

Figure 11.1: The Feynman diagrams for the associated production of a Higgs boson with a weak boson caused by the Standard Model interaction (left) and a BSM effect (right). The Wilson coefficient, $c^{(3)}_{Hq}$, is shown as an example.

Feynman diagrams of the VH production with the Standard Model interaction and an example with a dimension-6 interaction $c^{(3)}_{Hq}$ is shown in Figure 11.1. The Feynman rules for the VVH vertices in the SM are derived as:

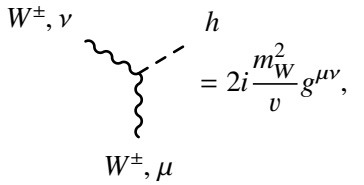

$$= 2i \frac{m_W^2}{v} g^{\mu\nu},$$

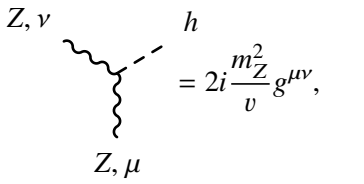

$$= 2i \frac{m_Z^2}{v} g^{\mu\nu}, \tag{11.3}$$

where μ and ν are the indices for the polarization of the vector bosons.

The scattering amplitude in the SM is expressed by:

$$\mathcal{M}_{\mathrm{SM}} = \frac{2m_Z^2}{v} g^{\mu\nu} \frac{-ig_{\nu\rho}}{p^2 - m_Z^2} J^Z_\rho \epsilon^*_\mu, \tag{11.4}$$

where J_μ^V is the femionic current for Z[1]. The Feynman rule for the Wilson coefficient, $c_{Hq}^{(3)}$, is expressed as:

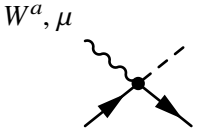

$$= -\frac{4ivc_{Hq}^{(3)}}{\Lambda^2} J_L^{a\mu}, \tag{11.5}$$

where $J_L^{a\mu}$ $(a = 1, 2, 3)$ is the left-handed fermionic current. The scattering amplitude of $qq \to ZH$ caused by this interaction is:

$$\mathcal{M}_{c_{Hq}^{(3)}} = -\frac{4vc_{Hq}^{(3)}}{\Lambda^2} \cos\theta_W \epsilon_\mu^* J_L^{3\mu}. \tag{11.6}$$

The amplitude caused by the BSM vertex is not suppressed by the propagator of the weak boson, and the polarization of the vector boson is longitudinal for both the SM and the BSM interactions. Thus, the BSM enhances events in the high p_{T}^V phase space compared to the Standard Model prediction, as it is expected in the dimensional analysis presented in Section 6.1. Thus, the cross-section measurement in high p_{T}^V is sensitive to these Wilson coefficients.

Distributions of p_{T}^V with the Standard Model interaction and some of BSM interactions are shown in Figure 11.2, where the event yields are affected by the BSM interactions in the high p_{T}^V phase space.

11.1.1 EFT parametrization of differential cross-section of the VH production

The cross-sections in the two p_{T}^V bins of the WH production and the three bins of the ZH production are parametrized as functions of the Wilson coefficients. Then, the likelihood as a function of the cross-sections is reparametrized in terms of the Wilson coefficients.

The general cross-section is expressed as

$$\sigma = \sigma_{\mathrm{SM}} + \sigma_{\mathrm{int}} + \sigma_{\text{dim-6}}, \tag{11.7}$$

where σ_{int} and $\sigma_{\text{dim-6}}$ are the terms in the cross-section for the interference and the BSM that are defined as:

$$\sigma_{\mathrm{int}}/\sigma_{\mathrm{SM}} = (\mathcal{M}_{\mathrm{int}}^* \mathcal{M}_{\mathrm{SM}} + \mathcal{M}_{\mathrm{int}} \mathcal{M}_{\mathrm{SM}}^*)/|\mathcal{M}_{\mathrm{SM}}|^2 = 2\mathrm{Re}(\mathcal{M}_{\mathrm{int}}^* \mathcal{M}_{\mathrm{SM}})/|\mathcal{M}_{\mathrm{SM}}|^2, \tag{11.8}$$

$$\sigma_{\text{dim-6}}/\sigma_{\mathrm{SM}} = |\mathcal{M}_{\text{dim-6}}|^2/|\mathcal{M}_{\mathrm{SM}}|^2. \tag{11.9}$$

As shown in these equations, the interference terms are linear in the Wilson coefficients, and the dimension-6 terms are quadratic in the Wilson coefficients. Thus, these terms are parametrized in terms of the Wilson coefficients as

$$\sigma_{\mathrm{int}}/\sigma_{\mathrm{SM}} = A_i c_i, \tag{11.10}$$

$$\sigma_{\text{dim-6}}/\sigma_{\mathrm{SM}} = B_{ij} c_i c_j. \tag{11.11}$$

[1] $J_{+\mu}^W = \frac{1}{\sqrt{2}} (\bar{\nu}_L \gamma^\mu e_L + \bar{u}_L \gamma^\mu d_L)$, $J_{-\mu}^W = \frac{1}{\sqrt{2}} (\bar{e}_L \gamma^\mu \nu_L + \bar{d}_L \gamma^\mu u_L)$,
$J_\mu^Z = \frac{1}{\cos\theta_W} \left[\bar{\nu}_L \gamma^\mu \left(\frac{1}{2}\right) \nu_L + \bar{e}_L \gamma^\mu \left(-\frac{1}{2} + \sin^2\theta_W\right) e_L + \bar{e}_R \gamma^\mu \left(\sin^2\theta_W\right) e_R \right.$
$\left. + \bar{u}_L \gamma^\mu \left(\frac{1}{2} - \frac{2}{3}\sin^2\theta_W\right) u_L + \bar{u}_R \gamma^\mu \left(-\frac{2}{3}\sin^2\theta_W\right) u_R + \bar{d}_L \gamma^\mu \left(-\frac{1}{2} + \frac{1}{3}\sin^2\theta_W\right) d_L + \bar{d}_R \gamma^\mu \left(\frac{1}{3}\sin^2\theta_W\right) d_R \right]$.

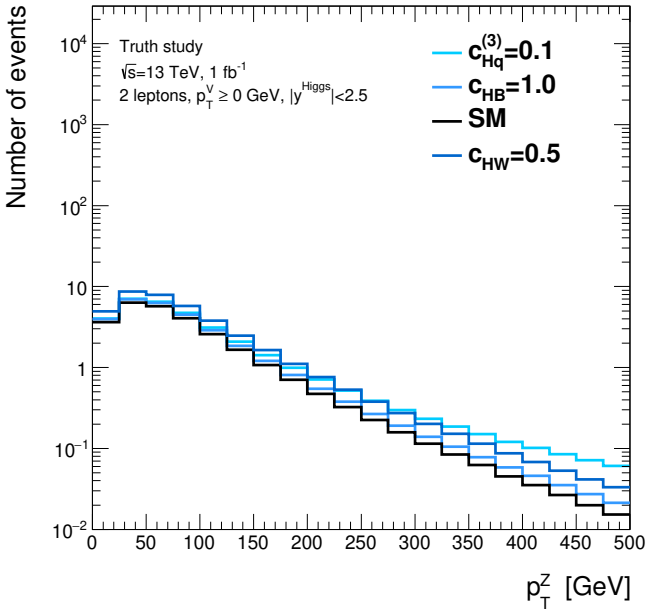

Figure 11.2: Distributions of truth p_{T}^{V} for each Wilson coefficient for the $qq \to ZH$ process. The distributions are computed with the SMEFTsim package [51] at the LO accuracy utilizing MADGRAPH 5+PYTHIA 8 [159, 160]. These distributions are normalized using the cross-section of $qq \to ZH$ times the branching ratios of $Z \to \ell\ell$ and $H \to b\bar{b}$ computed in the NNLO (QCD) and NLO (EW) prediction. The luminosity used to normalize the distributions is 1 fb^{-1}. A cut $|y^{\mathrm{Higgs,truth}}| < 2.5$ is applied.

Extraction of the parametrization is performed with generated events by the Standard Model terms and the dimension-6 terms. To extract the parameters A_i in Eq. 11.10, N samples are prepared for N Wilson coefficients considering only the interference terms in the cross-section. To extract the parameters B_{ij} in Eq. 11.11, $N(N+1)/2$ samples are separately prepared for the combinations of two Wilson coefficients from N coefficients including pairs of same operators $c_i c_i$. B_{ij} are extracted by considering only the terms caused by the dimension-6 terms, $\sigma_{\text{dim-6}}$. The events are generated with the *SMEFTsim* package [51], which internally uses MADGRAPH 5 for the computation of the matrix elements and PYTHIA 8 for showering. These calculations are all done at the leading order, and only the ratio to the Standard Model prediction is used. Examples of the derived parameters A_i and B_{ij} are shown in Table 11.2 and Figure 11.3 for Wilson coefficients, $c_{Hq}^{(3)}$ and c_{HW}. The derived parametrization of the cross-sections for the WH and ZH productions for all the relevant operators are summarized in Appendix K (Tables K.4-K.8). $gg \to ZH$ is modified by dimension-8 terms, thus this process is fixed to the Standard Model prediction in the analysis.

11.1.2 EFT parametrization of the branching ratio of the $H \to b\bar{b}$ decay

The branching fraction of the $H \to b\bar{b}$ decay has the form $\mathrm{BR}^{H\to b\bar{b}} = \Gamma^{H\to b\bar{b}}/\Gamma^{\mathrm{total}}$, where $\Gamma^{H\to b\bar{b}}$ is the partial decay width and Γ^{total} is the total width of the Higgs boson. Both of the widths are also affected by the dimension-6 terms in the Lagrangian and can be expressed as quadratic functions of the Wilson

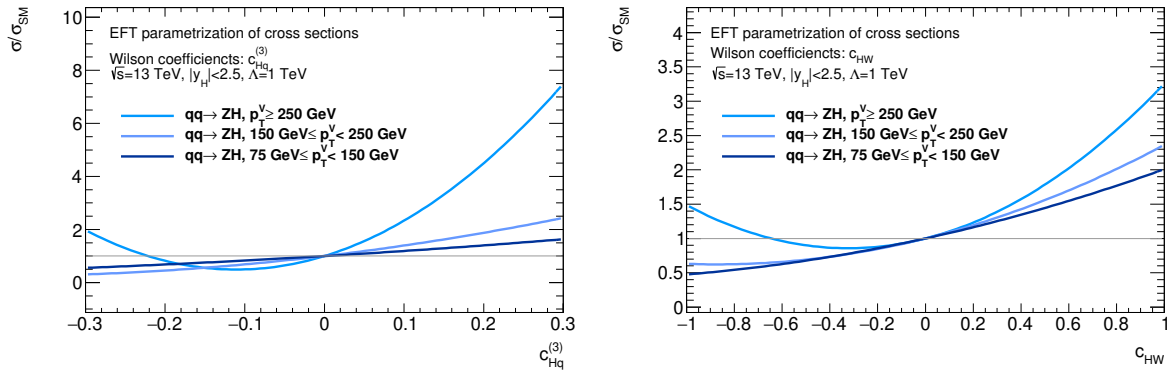

Figure 11.3: Ratio of the cross-sections of the $qq \to ZH$ production for Wilson coefficients, $c_{Hq}^{(3)}$ and c_{HW}, to predictions of the Standard Model.

Table 11.2: Parametrization of the production cross-sections of $qq \to WH$ and $qq \to ZH$ in the p_{T}^{V} bins as a function of considered Wilson coefficients $c_{Hq}^{(3)}$.

Bins	Cross-sections
$qq \to WH,\ 150 \leq p_{\mathrm{T}}^{V} < 250$ GeV	$\sigma/\sigma_{\mathrm{SM}} = 1 + 3.83\, c_{Hq}^{(3)} + 4.28 \left(c_{Hq}^{(3)}\right)^2$
$qq \to WH,\ p_{\mathrm{T}}^{V} \geq 250$ GeV	$\sigma/\sigma_{\mathrm{SM}} = 1 + 10.8\, c_{Hq}^{(3)} + 53.1 \left(c_{Hq}^{(3)}\right)^2$
$qq \to ZH,\ 75 \leq p_{\mathrm{T}}^{V} < 150$ GeV	$\sigma/\sigma_{\mathrm{SM}} = 1 + 1.8\, c_{Hq}^{(3)} + 1.04 \left(c_{Hq}^{(3)}\right)^2$
$qq \to ZH,\ 150 \leq p_{\mathrm{T}}^{V} < 250$ GeV	$\sigma/\sigma_{\mathrm{SM}} = 1 + 3.55\, c_{Hq}^{(3)} + 4.14 \left(c_{Hq}^{(3)}\right)^2$
$qq \to ZH,\ p_{\mathrm{T}}^{V} \geq 250$ GeV	$\sigma/\sigma_{\mathrm{SM}} = 1 + 9.19\, c_{Hq}^{(3)} + 41.5 \left(c_{Hq}^{(3)}\right)^2$

coefficients. Thus, the parametrization of the branching ratio is expressed as:

$$\frac{\mathrm{BR}^{H\to b\bar{b}}}{\mathrm{BR}_{\mathrm{SM}}^{H\to b\bar{b}}} = \frac{\Gamma^{H\to b\bar{b}}/\Gamma_{\mathrm{SM}}^{H\to b\bar{b}}}{\Gamma^{\mathrm{total}}/\Gamma_{\mathrm{SM}}^{\mathrm{total}}} = \frac{1 + A_i^{H\to b\bar{b}} c_i + B_{ij}^{H\to b\bar{b}} c_i c_j}{1 + A_i^{\mathrm{total}} c_i + B_{ij}^{\mathrm{total}} c_i c_j}, \tag{11.12}$$

The total and partial widths of the Higgs boson are computed with MADGRAPH 5 for the decay channels shown in Appendix K (Table 11.3). The dependence of these widths on an example coefficient, c_{dH}, is shown in Table 11.4. The derived parametrization of the total and partial widths of the Higgs boson in terms of all the Wilson coefficients are shown in Table K.9. These modifications are uniformly applied in all the p_{T}^{V} bins.

11.1.3 Constraints on the Wilson coefficients

The cross-section times the branching ratio in each bin is parametrized in terms of the Wilson coefficients c_i. after determination of the parameters A_i^{prod}, B_{ij}^{prod}, $A_i^{H\to b\bar{b}}$, $B_{ij}^{H\to b\bar{b}}$, A_i^{total}, and B_{ij}^{total}. Thus, the likelihood is also redefined as a function of the Wilson coefficients.

Table 11.3: Decay channels of the Higgs boson considered in the computation of the total decay width.

Categories	Decay mode
Fermionic decays	$H \to bb, cc, ss, \tau\tau, \mu\mu, e^+e^-$
Loop induced decay	$H \to \gamma\gamma, gg, Z\gamma$
Bosonic decays	$H \to 4j, 4\ell, 4\nu, 2j2\ell, 2j2\nu, 2j\ell\nu, 2\nu2\ell$

Table 11.4: Parametrization of the total decay width of the Higgs boson and the partial decay width of $H \to b\bar{b}$ with the Wilson coefficient $|c_{dH}|$.

Decay channel	Decay width
$H \to b\bar{b}$	$\Gamma^{H\to b\bar{b}}/\Gamma^{H\to b\bar{b}}_{\text{SM}} = 1 - 0.121\,\lvert c_{dH}\rvert + 0.00367\,(\lvert c_{dH}\rvert)^2$
$H \to$ all	$\Gamma^{\text{total}}/\Gamma^{\text{total}}_{\text{SM}} = 1 - 0.0852\,\lvert c_{dH}\rvert + 0.00258\,(\lvert c_{dH}\rvert)^2$

1-dimensional limits on the Wilson coefficients

The dependence of the negative-log-likelihood ($-\log(\mathcal{L}/\mathcal{L}_{\text{max}})$) on the Wilson coefficients is studied. Examples of the negative-log-likelihood as functions of single Wilson coefficients are shown in Figure 11.4. The limits on the Wilson coefficients are set based on the scanned values of the likelihood.

A summary of allowed intervals is shown in Figure 11.5 for Wilson coefficients on which the analysis sets constraints smaller than unity. The results for all the tested Wilson coefficients are shown in Appendix L. The coefficient constrained most strongly is $c^{(3)}_{Hq}$, which modifies the VH cross-section with the Feynman diagram in Figure 11.1. The limit is $-0.047 < c^{(3)}_{Hq} < 0.044$ at 95% confidence level. This type of deformation should be introduced by the Heavy Vector Triplets (HVT) or Minimal Composite Higgs model as described in Section 2.4. The coefficient $c^{(3)}_{Hq}$ is related to parameters in the HVT model:

$$c^{(3)}_{Hq} = -\frac{\Lambda^2}{m_V^2} g^2 c_H c_F = -\frac{\Lambda^2}{m_V^2} \cdot 4 g_H g_q. \tag{11.13}$$

The limit on $c^{(3)}_{Hq}$ can be interpreted in the HVT model including heavy resonances with the mass m_V as:

- $m_V = 7$ TeV: $-2.16 < g^2 c_H c_F = 4 g_H g_q < 2.30$,
- $m_V = 2$ TeV: $-0.176 < g^2 c_H c_F = 4 g_H g_q < 0.188$,
- $m_V = 1$ TeV: $-0.044 < g^2 c_H c_F = 4 g_H g_q < 0.047$.

If we assume $c_H = -g^2/g_V^2$, $c_F = 1$, and $g_V = 1$ (*Model A* in Refs. [23, 52, 53]), the limit on m_V is derived as:

$$m_V > \frac{\Lambda g^2}{\sqrt{0.047}} \simeq \frac{(1\text{ TeV}) \times (0.654)^2}{\sqrt{0.047}} = 1.97\text{ TeV} \quad (95\%\text{ CL}). \tag{11.14}$$

If we assume $c_H = c_F = 1$ and $g_V = 3$ (*Model B* in Refs. [23, 52, 53]), the limit on m_V is derived as:

$$m_V > \frac{\Lambda g}{\sqrt{0.047}} \simeq \frac{(1\text{ TeV}) \times (0.654)}{\sqrt{0.047}} = 3.02\text{ TeV} \quad (95\%\text{ CL}). \tag{11.15}$$

These are slightly weaker limits than the limits from direct searches, which report 3-5 TeV [52, 53]. Therefore, the indirect search with the VH production is thought be useful for scenarios with a larger mass and a strong coupling.

The Wilson coefficient c_{Hu} introduces a similar diagram to $c_{Hq}^{(3)}$, and c_{Hu} is also constrained. c_{Hu} is less constrained than one by $c_{Hq}^{(3)}$ because c_{Hu} modifies interaction of the right handed-quarks and only the ZH channel is sensitive to this operator. Other constrained Wilson coefficients are c_{HW} and c_{HWB}. These coefficients modify the VVH vertices and affect the VH cross-section. These operators create transversely polarized vector bosons whereas $c_{Hq}^{(3)}$ creates longitudinally polarized bosons. Thus, the enhancement of the VH cross-section in high p_{T} by c_{HW} and c_{HWB} is milder than $c_{Hq}^{(3)}$ [2]. The Wilson coefficient c_{dH} is also shown in Figure 11.5 since this operator modifies the $H \to b\bar{b}$ width.

2-dimensional limits are also derived by scanning the likelihood in the 2-dimensional plane of Wilson coefficients with the other coefficients set to 0. The results are shown in Appendix L.

[2] The longitudinal component of a vector boson behaves like E_V/m_V under Lorentz boost whereas the transverse components remain $O(1)$

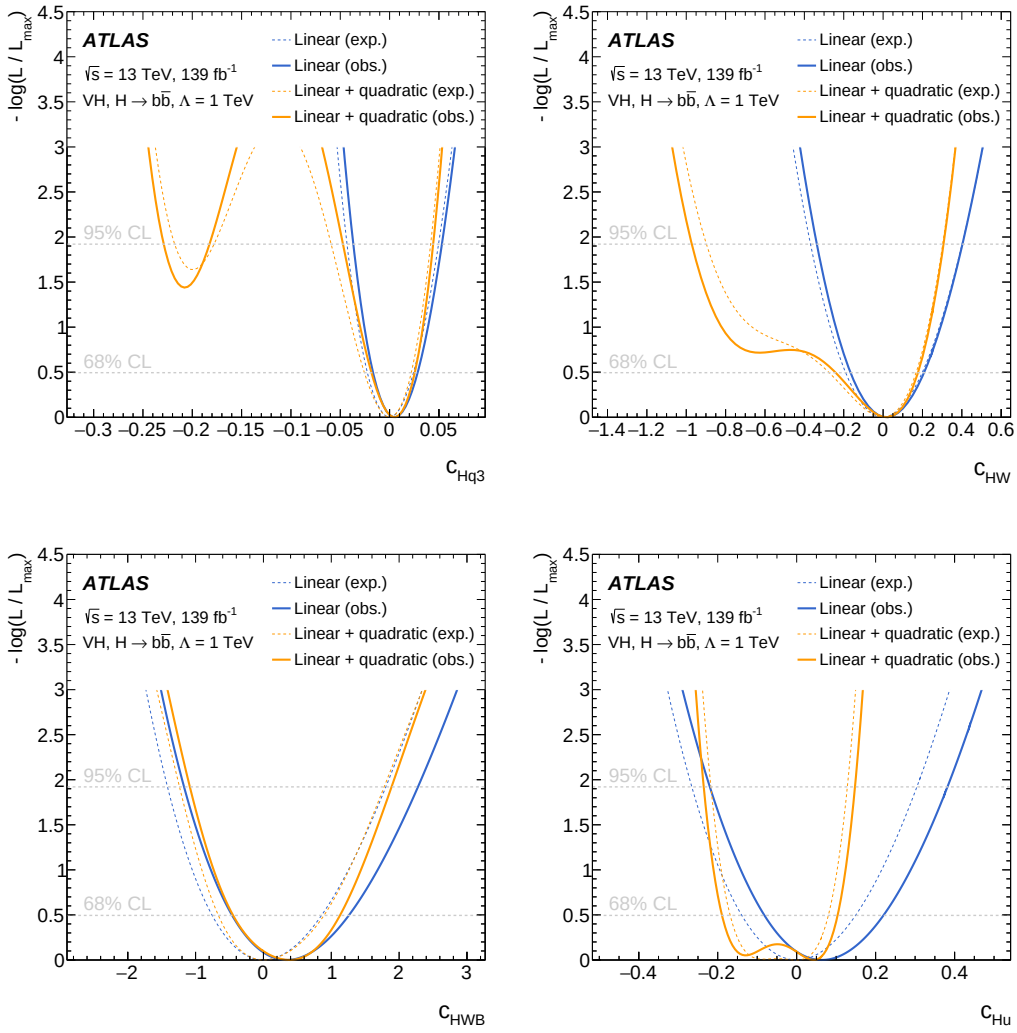

Figure 11.4: Examples of the negative-log-likelihood as a function of the indicated Wilson coefficients. The solid and dashed curves show the negative likelihood derived from the observed and expected data. The blue and orange curves represent the linear and linear+quadratic parametrization, respectively. The scale Λ is assumed to be 1 TeV .

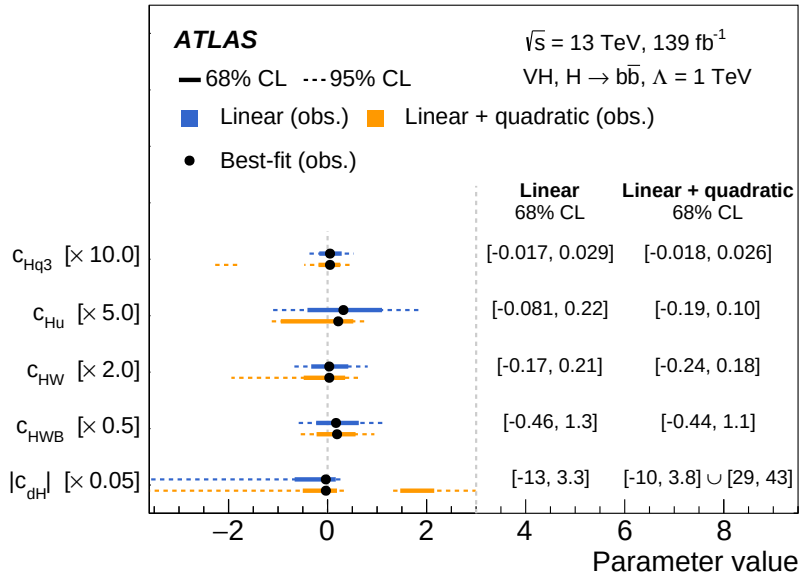

Figure 11.5: Summary of the allowed intervals for the Wilson coefficients that the analysis has sensitivity. The black points show the best fit points. The solid and dashed bars show the intervals of the 68% and 95% confidence levels. The orange and blue bars represent the results for the linear and linear+quadratic parametrization, respectively. The values of the Wilson coefficients are scaled as indicated on the y-axis. The scale Λ is assumed to be 1 TeV .

11.2 Differential cross-section as a function of the decay angle of $Z \to \ell^+\ell^-$

As introduced in Section 2.5.2, CP-odd interaction of the 125 GeV Higgs boson and the vector boson can be generated by BSM [27, 28].

11.2.1 Methodologies

CP-odd terms in the Effective Field Theory

The CP-odd bosonic operators in the effective Lagrangian are $Q_{H\widetilde{W}}$, $Q_{H\widetilde{B}}$ and $Q_{H\widetilde{W}B}$, which are summarized in Table 11.5. In those operators, the anti-symmetric tensors are defined as:

$$W^i_{\mu\nu} = \partial_\mu W^i_\nu - \partial_\nu W^i_\mu - g\epsilon^{ijk} W^j_\mu W^k_\nu, \quad \widetilde{W}^i_{\mu\nu} = \epsilon_{\mu\nu\alpha\beta} W^a_{\alpha\beta}, \tag{11.16}$$

$$B_{\mu\nu} = \partial_\mu B_\nu - \partial_\nu B_\mu, \quad \widetilde{B}_{\mu\nu} = \epsilon_{\mu\nu\alpha\beta} B_{\alpha\beta}. \tag{11.17}$$

For the fermionic operators, combinations of the form $Q - Q^\dagger$ are CP-odd, but they are not relevant to this analysis.

Observable sensitive to CP-odd interactions

The distribution of p_{T}^V with the CP-odd operators are shown in Figure 11.6. The CP-odd BSM interactions modify the p_{T}^V spectrum as well as the CP-even interactions.

The differential cross-section as a function of p_{T}^V can be modified by many BSM interactions. The CP-odd operators in Eqs. 11.16 and 11.17 can also be constrained by the measurement of the p_{T}^V spectrum. However, if a deviation of the p_{T}^V spectrum from the SM prediction is observed, the deviation may be caused by the CP-even interactions discussed in Section 11.1. Here, we construct an observable that is zero when the ZH process is purely CP-even but non-zero when the CP-odd Wilson coefficient $c_{H\widetilde{W}}$ contributes to the ZH process (*CP observable*) though the similar argument in [161]. The amplitude of the ZH process is transformed by the CP transformation as:

$$\mathcal{M}^{ZH}_{\mathrm{SM}} \xrightarrow{\mathrm{CP}} \mathcal{M}^{ZH}_{\mathrm{SM}}, \tag{11.18}$$

$$\mathcal{M}^{ZH}_{\text{CP-odd}} \xrightarrow{\mathrm{CP}} -\mathcal{M}^{ZH}_{\text{CP-odd}}, \tag{11.19}$$

where $\mathcal{M}^{ZH}_{\mathrm{SM}}$ and $\mathcal{M}^{ZH}_{\text{CP-odd}}$ are the amplitudes by the SM and a CP-odd interaction, respectively. The probabilities are computed from

$$\left|\mathcal{M}^{ZH}\right|^2 = \left|\mathcal{M}^{ZH}_{\mathrm{SM}}\right|^2 + 2\mathrm{Re}\left[\mathcal{M}^{ZH}\left(\mathcal{M}^{ZH}_{\text{CP-odd}}\right)^*\right] + \left|\mathcal{M}^{ZH}_{\text{CP-odd}}\right|^2. \tag{11.20}$$

Table 11.5: CP-odd dimension-6 operators and their Wilson coefficients relevant to the associated production VH.

Wilson coefficients	Field operators	Affected processes
$c_{H\widetilde{W}B}$	$Q_{H\widetilde{W}B} = \varphi^\dagger \tau^i \varphi \widetilde{W}^i_{\mu\nu} B^{\mu\nu}$	ZH
$c_{H\widetilde{W}}$	$Q_{H\widetilde{W}} = \varphi^\dagger \varphi \widetilde{W}^i_{\mu\nu} W^{i\mu\nu}$	WH, ZH
$c_{H\widetilde{B}}$	$Q_{H\widetilde{B}} = \varphi^\dagger \varphi \widetilde{B}_{\mu\nu} B^{\mu\nu}$	ZH

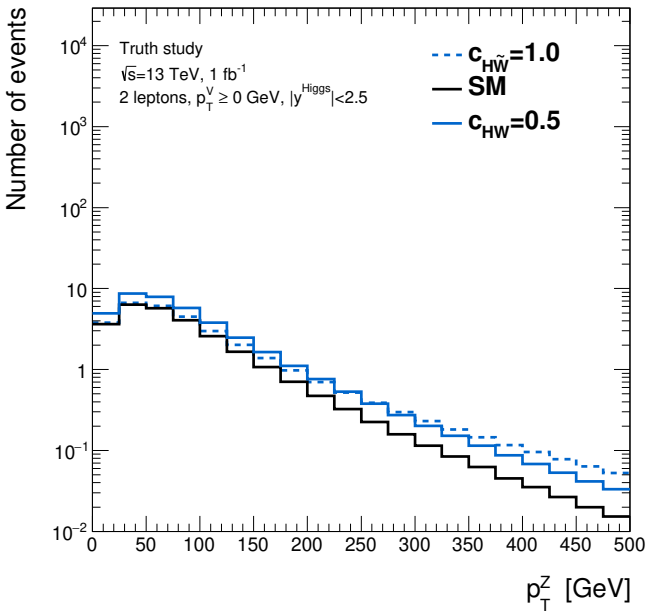

Figure 11.6: Distribution of truth p_{T}^{V} for the $qq \to ZH$ production with the CP-odd interactions in addition to the Standard Model interaction. The distributions are computed with the SMEFTsim package [51] at the LO accuracy utilizing MADGRAPH 5+PYTHIA 8 [159, 160]. These distributions are normalized using the cross-section of $qq \to ZH$ times the branching ratios of $Z \to \ell\ell$ and $H \to b\bar{b}$ computed in the NNLO (QCD) and NLO (EW) prediction. The luminosity used to normalize the distributions is 1 fb^{-1}. A cut $|y^{\mathrm{Higgs,truth}}| < 2.5$ is applied.

Each term is transformed by the CP transformation as:

$$\left|\mathcal{M}_{\mathrm{SM}}^{ZH}\right|^2 \xrightarrow{\mathrm{CP}} \left|\mathcal{M}_{\mathrm{SM}}^{ZH}\right|^2, \tag{11.21}$$

$$2\mathrm{Re}\left[\mathcal{M}^{ZH}\left(\mathcal{M}_{\text{CP-odd}}^{ZH}\right)^*\right] \xrightarrow{\mathrm{CP}} -2\mathrm{Re}\left[\mathcal{M}^{ZH}\left(\mathcal{M}_{\text{CP-odd}}^{ZH}\right)^*\right], \tag{11.22}$$

$$\left|\mathcal{M}_{\text{CP-odd}}^{ZH}\right|^2 \xrightarrow{\mathrm{CP}} \left|\mathcal{M}_{\text{CP-odd}}^{ZH}\right|^2. \tag{11.23}$$

Therefore, the interference term is an observable CP-odd quantity. On the other hand, the BSM term $\left|\mathcal{M}_{\text{CP-odd}}^{ZH}\right|^2$ is a CP-even quantity even for CP-odd operators. In order to test the CP-violation, the analysis is designed to use a variable sensitive to the interference term.

An angular variable ϕ_{lep} defined in Figure 6.18 is a candidate of such variables. The distributions of ϕ_{lep} for the interference terms $\mathrm{Re}[M_{\text{dim-6}}^{*} M_{\mathrm{SM}}]$ with c_{HW} (CP-even) and $c_{H\widetilde{W}}$ (CP-odd) are shown in Figure 11.7. In the figure, ϕ_{lep} is split into two regions named "(I)" and "(II)". Now, ϕ_{lep} is transformed under the C and P transformations as:

$$\phi_{\mathrm{lep}} \xrightarrow{P} -\phi_{\mathrm{lep}} \xrightarrow{C} -\phi_{\mathrm{lep}} + \pi, \tag{11.24}$$

meaning that events in the region (I) is transferred to the region (II) by the CP transformation. The cross-section is the same in (I) and (II) when the ZH is a CP-even process whereas the difference between the two regions indicates the CP-violation in ZH. It is also confirmed in the figure that the difference between (I) and (II) is sensitive to the interference term of $c_{H\widetilde{W}}$. Hence the difference of the cross-section between (I) and (II) is an example of the CP observable.

For completeness, the distributions of the BSM terms, $|M_{\text{dim-6}}|^2$, are shown in Figure 11.8 for c_{HW} and $c_{H\widetilde{W}}$. These terms show no difference between the (I) and (II) regions due to the CP-even nature of these BSM terms.

A strategy to utilize these angles is explained as follows. The phase space is divided into the (I) and (II) regions as indicated in Figures 11.7. The cross-section of the ZH production is measured in the (I) and (II) regions. In order to perform this, all the signal regions and the control regions are also divided into two regions based on the reconstructed ϕ_{lep}. Since the differential cross-section as a function of p_{T}^{V} can be affected by any BSM, only the difference of the cross-section between (I) and (II) is considered to derive constraints of the relevant Wilson coefficients not using the dependence of the cross-section on p_{T}^{V}. Technical aspects are described in the next paragraph.

Parametrization of the cross-sections

The dependence of the cross-section on the CP-odd Wilson coefficients is derived in the same way as Section 11.1. The derived parametrization of $\sigma/\sigma_{\text{SM}}$ is shown in Table 11.6.

For the analysis that utilizes ϕ_{lep}, the parametrization "(I)" and "(II)" are applied to the $qq \to ZH$ in the corresponding regions. The effect quadratic in $c_{H\widetilde{W}}$ (BSM term) is similar in (I) and (II) categories while the linear term (interference) is opposite in the sign as expected from Figures 11.7 and 11.8 in agreement

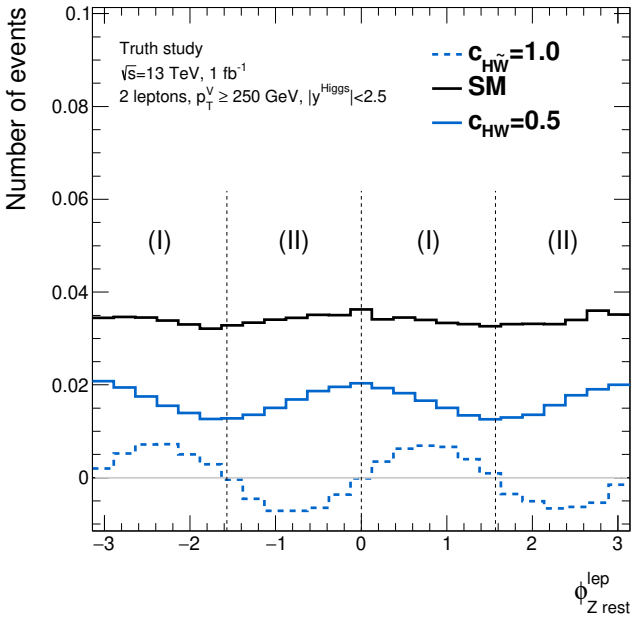

Figure 11.7: Interference terms ($2\text{Re}\left[\mathcal{M}_{\text{SM}}\mathcal{M}^{*}_{\text{dim-6}}\right]$) as functions of ϕ_{lep} for the ZH production with the CP-even and -odd interactions. The black histograms shows the distribution in the SM for comparison. The distributions are computed with MADGRAPH 5 and PYTHIA 8 at the LO accuracy considering only the interference terms of the SM and dimension-6 interaction. They are normalized using the cross-section of $qq \to ZH$ times the branching ratios of $Z \to \ell\ell$ and $H \to b\bar{b}$ computed in the NNLO (QCD) and NLO (EW) prediction. The luminosity used to normalize the distributions is 1 fb^{-1}. The cut, $|y^{\text{Higgs,truth}}| < 2.5$, is applied.

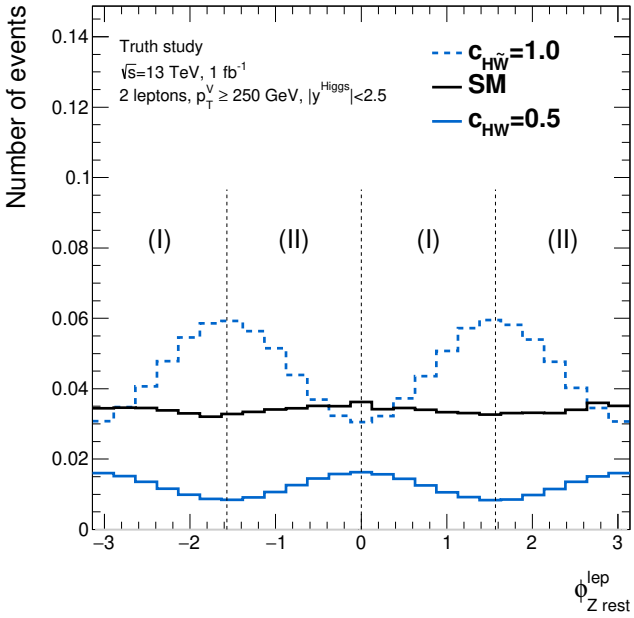

Figure 11.8: BSM terms ($|\mathcal{M}_{\text{dim-6}}|^2$) as functions of ϕ_{lep} of the ZH production with the CP-even and -odd interactions. The black histograms shows the distribution in the SM for comparison. The distributions are computed with the SMEFTsim package [51] at the LO accuracy utilizing MADGRAPH 5+PYTHIA 8 [159, 160]. These distributions are normalized using the cross-section of $qq \to ZH$ times the branching ratios of $Z \to \ell\ell$ and $H \to b\bar{b}$ computed in the NNLO (QCD) and NLO (EW) prediction. The luminosity used to normalize the distributions is 1 fb^{-1}. A cut $|y^{\text{Higgs,truth}}| < 2.5$ is applied.

with the argument in the previous paragraph. The parametrization for the angular analysis includes extra parameters $\Delta\mu_{[75,150]}$, $\Delta\mu_{[150,250]}$ and $\Delta\mu_{[250,\infty]}$. These $\Delta\mu$ are common in (I) and (II), and fully floating parameters that make the analysis not sensitive to effects on the p_{T}^V spectrum canceling the effect quadratic in $c_{H\widetilde{W}}$. Although the branching ratio of $H \to b\bar{b}$ is also affected by the term associated with $c_{H\widetilde{W}}$, the branching ratio is not parametrized but fixed at the SM prediction.

The analysis using the p_{T}^V spectrum is also performed for comparison. For this analysis, the "inclusive" parametrization of the cross-section in Table 11.6 is used. Note that the separation by ϕ_{lep} is not applied in this p_{T}^V analysis.

Systematic uncertainties

The same systematic uncertainties are considered as the results in Chapter 10 and Section 11.1. No additional systematic uncertainties are included to this interpretation.

Table 11.6: Parametrization of the cross-section in the regions (I) and (II) as functions of the Wilson coefficients associated to CP-odd operators.

Category	ϕ_{lep} bin	p_{T}^{V} bin	Parametrization of $\sigma/\sigma_{\text{SM}}$
(I)	$-\frac{\pi}{2} < \phi_{\text{lep}} < 0$ $\frac{\pi}{2} < \phi_{\text{lep}} < \pi$	$75 \leq p_{\text{T}}^{V} < 150$ GeV	$1 - 0.086c_{H\widetilde{W}} + 0.145c_{H\widetilde{W}}^{2} + \Delta\mu_{[75,150]}$
		$150 \leq p_{\text{T}}^{V} < 250$ GeV	$1 - 0.120c_{H\widetilde{W}} + 0.392c_{H\widetilde{W}}^{2} + \Delta\mu_{[150,250]}$
		$p_{\text{T}}^{V} \geq 250$ GeV	$1 - 0.137c_{H\widetilde{W}} + 1.311c_{H\widetilde{W}}^{2} + \Delta\mu_{[250,\infty]}$
(II)	$-\pi < \phi_{\text{lep}} < -\frac{\pi}{2}$ $0 < \phi_{\text{lep}} < \frac{\pi}{2}$	$75 \leq p_{\text{T}}^{V} < 150$ GeV	$1 + 0.087c_{H\widetilde{W}} + 0.145c_{H\widetilde{W}}^{2} + \Delta\mu_{[75,150]}$
		$150 \leq p_{\text{T}}^{V} < 250$ GeV	$1 + 0.120c_{H\widetilde{W}} + 0.395c_{H\widetilde{W}}^{2} + \Delta\mu_{[150,250]}$
		$p_{\text{T}}^{V} \geq 250$ GeV	$1 + 0.138c_{H\widetilde{W}} + 1.332c_{H\widetilde{W}}^{2} + \Delta\mu_{[250,\infty]}$
Inclusive	$-\pi < \phi_{\text{lep}} < \pi$ (all range)	$75 \leq p_{\text{T}}^{V} < 150$ GeV	$1 + 0.000c_{H\widetilde{W}} + 0.145c_{H\widetilde{W}}^{2}$
		$150 \leq p_{\text{T}}^{V} < 250$ GeV	$1 + 0.000c_{H\widetilde{W}} + 0.393c_{H\widetilde{W}}^{2}$
		$p_{\text{T}}^{V} \geq 250$ GeV	$1 + 0.000c_{H\widetilde{W}} + 1.322c_{H\widetilde{W}}^{2}$

11.2.2 Results

Constraints derived from the p_{T}^{V} spectrum

The allowed interval derived from a 1-dimensional scan of the likelihood is shown in Figure 11.9. This curve behaves like a quartic function around the minimum because the effect on the cross-section is quadratic.[3] The fitted $c_{H\widetilde{W}}$ is consistent with 0 within its uncertainty. The observed (expected) 95% confidence interval is $-0.87 < c_{H\widetilde{W}} < 0.87$ ($-0.9 < c_{H\widetilde{W}} < 0.9$).

Constraints derived from ϕ_{lep} as the CP observable

The signal strengths of the regions in Table 11.6 is shown in Figure 11.10. The measured signal strengths slightly look fluctuating, but they are consistent with the Standard Model prediction with compatibility of 51.6%. Hence, a limit on the Wilson coefficient $c_{H\widetilde{W}}$ is set in the next paragraph.

The allowed intervals derived from the 1-dimensional scan of the likelihood is shown in Figure 11.11. The fitted $c_{H\widetilde{W}}$ is consistent with 0 within its uncertainty. The observed (expected) 95% confidence interval is $-5.1 < c_{H\widetilde{W}} < 4.3$ ($-6.1 < c_{H\widetilde{W}} < 3.9$).

A more stringent limit is obtained when considering p_{T}^{V} than the angle. However, the p_{T}^{V} spectrum can be affected by both CP-even and CP-odd operators, but the angular analysis is sensitive only to the CP-odd operators. When a deviation from the SM prediction is found in the p_{T}^{V} spectrum, the angular analysis may be useful to distinguish which operator contributes to the deviation.

Comparison to the analysis of the Higgs decays

Since the measurements in the $H \to ZZ^{*} \to 4\ell$ and $H \to WW^{*} \to e\nu\mu\nu$ decay channels [22] are expressed in a different parametrization from the Warsaw basis, it is not straightforward to compare them

[3] The dependence of the negative-log-likelihood on a parameter is parabolic when the effect on the cross-section is linear. The signal strength μ is an example.

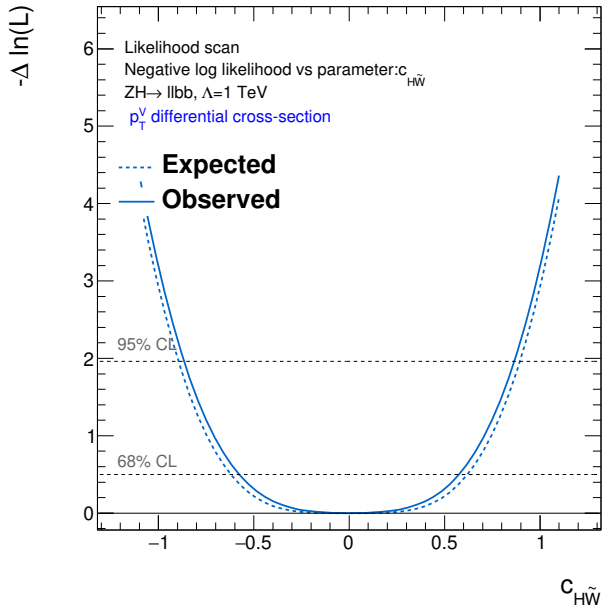

Figure 11.9: Log-likelihood ratio as a function of $c_{H\widetilde{W}}$ derived from the cross-section measurement of ZH ($Z \to \ell^+\ell^-$) considering the effect on the p_{T}^V. The 68% and 95% confidence intervals are indicated by the horizontal lines in the plot.

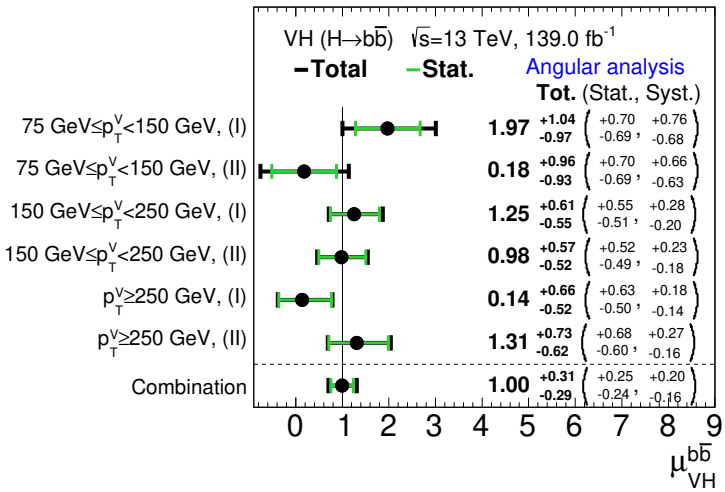

Figure 11.10: Signal strengths measured in the angular analysis. Combination indicates a fit with single signal strength for all the regions. The result is slightly different from Table 10.2 because this fit uses the regions (I) and (II).

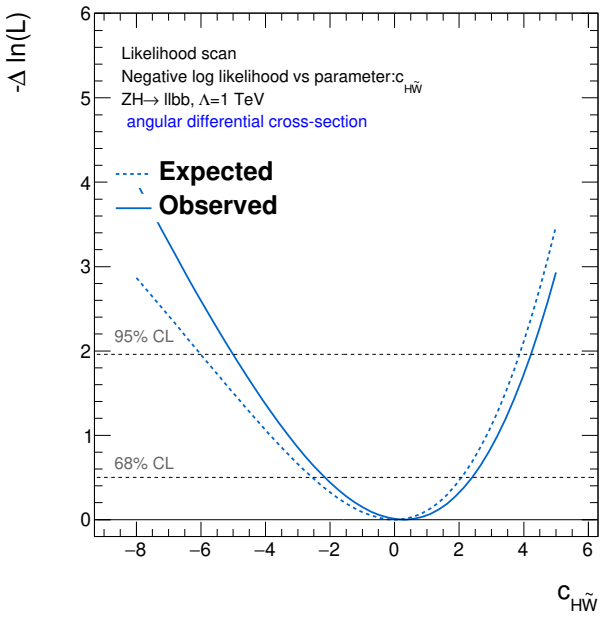

Figure 11.11: Log-likelihood ratio as a function of $c_{H\widetilde{W}}$ derived from the cross-section measurement of ZH ($Z \to \ell^+\ell^-$) considering the effect on the ϕ_{lep}. The 68% and 95% confidence intervals are indicated by the horizontal lines in the plot.

to the results in this section. However, a rough comparison of the limits is performed below. In Ref. [22], CP-odd BSM interactions are parametrized as:

$$\mathcal{L}_{VVH} = \kappa_{\text{SM}} \cos\alpha \left(-\frac{1}{v}\frac{\widetilde{\kappa}_{AZZ}}{\kappa_{\text{SM}}} \cdot \tan\alpha Z_{\mu\nu}\widetilde{Z}^{\mu\nu} - \frac{2}{v}\frac{\widetilde{\kappa}_{AWW}}{\kappa_{\text{SM}}} \cdot \tan\alpha W^+_{\mu\nu}\widetilde{W}^{-\mu\nu} \right) \cdot h. \tag{11.25}$$

By assuming $\widetilde{\kappa}_{AZZ} = \widetilde{\kappa}_{AWW} (= \widetilde{\kappa}_{AVV})$, the analysis reports the observed (expected) 95% confidence interval as $-2.18 < (\widetilde{\kappa}_{AVV}/\kappa_{\text{SM}}) \cdot \tan\alpha < 0.83$ ($-2.33 < (\widetilde{\kappa}_{AVV}/\kappa_{\text{SM}}) \cdot \tan\alpha < 2.30$). In the Warsaw basis used in this analysis, the same interactions are parametrized as:

$$\mathcal{L}_{VVH} = \frac{c_{H\widetilde{W}}}{\Lambda^2}\phi^\dagger\phi W^i_{\mu\nu}\widetilde{W}^{i\mu\nu} + \frac{c_{H\widetilde{B}}}{\Lambda^2}\phi^\dagger\phi B_{\mu\nu}\widetilde{B}^{\mu\nu} + \frac{c_{HW\widetilde{B}}}{\Lambda^2}\phi^\dagger\tau^i\phi W^i_{\mu\nu}\widetilde{B}^{\mu\nu}. \tag{11.26}$$

For example, the term with $c_{H\widetilde{W}}$ is transformed as:

$$\frac{c_{H\widetilde{W}}}{\Lambda^2}\phi^\dagger\phi W^i_{\mu\nu}\widetilde{W}^{i\mu\nu} = \frac{c_{H\widetilde{W}}}{\Lambda^2} v h W^i_{\mu\nu}\widetilde{W}^{i\mu\nu} = \frac{2}{v}\frac{c_{H\widetilde{W}}v^2}{2\Lambda^2} h W^i_{\mu\nu}\widetilde{W}^{i\mu\nu} = \frac{2}{v}\frac{c_{H\widetilde{W}}v^2}{\Lambda^2} h \left(W^+_{\mu\nu}\widetilde{W}^{-\mu\nu} + \frac{1}{2}W^3_{\mu\nu}\widetilde{W}^{3\mu\nu} \right). \tag{11.27}$$

The results from the Higgs decay, $2.18 < (\widetilde{\kappa}_{AVV}/\kappa_{\text{SM}}) \cdot \tan\alpha < 0.83$, now reads $2.18 < \frac{c_{H\widetilde{W}}}{\Lambda^2}v^2 < 0.83$. Then, for example,

$$c_{H\widetilde{W}} < 0.83 \times \frac{\Lambda^2}{v^2} \sim 0.83 \times \frac{(1000\text{ GeV})^2}{(246\text{ GeV})^2} \simeq 13.3\ . \tag{11.28}$$

The limits with the Higgs decay and the VH production are summarized in Table 11.7. Even the weaker constraints derived from the CP observable, ϕ_{lep}, are more stringent than the constraints from the Higgs decay.

Table 11.7: Summary of the limits on the Wilson coefficients for the CP-odd operators affecting the VVH vertex derived from the Higgs decays and the ZH production. As explained in the body, the "reinterpretation" of $c_{H\widetilde{W}}$ from the Higgs decay is not a precise number due to the different parametrization, but a rough estimate.

Analysis	95% confidence interval		Comments
	Observed	Expected	
$H \to ZZ^* \to 4\ell$ and	$-2.18 < \frac{\widetilde{\kappa}_{AVV}}{\kappa_{\mathrm{SM}}} \cdot \tan\alpha < 0.83$	$-2.33 < \frac{\widetilde{\kappa}_{AVV}}{\kappa_{\mathrm{SM}}} \cdot \tan\alpha < 2.30$	-
$H \to WW^* \to e\nu\mu\nu$ [22]	$-34.9 < c_{H\widetilde{W}} < 13.3$	$-37.3 < c_{H\widetilde{W}} < 36.8$	Reinterpretation
$ZH \to \ell^+\ell^- b\bar{b}$			
p_{T}^V spectrum	$-0.87 < c_{H\widetilde{W}} < 0.87$	$-0.89 < c_{H\widetilde{W}} < 0.89$	-
Angular analysis	$-5.0 < c_{H\widetilde{W}} < 4.2$	$-6.1 < c_{H\widetilde{W}} < 3.9$	-

11.3 Coupling measurement

The combined measurement of the couplings of the Higgs boson is presented in Ref. [29] using available measurements of the Higgs boson. The analysis discussed in this thesis (VH, $H \to b\bar{b}$) is also included in the coupling measurement. In this section, we study the size of the contribution of the VH, $H \to b\bar{b}$ analysis, and show that the analysis significantly contributes to constrain the whole Higgs sector.

To perform a coupling measurement, the framework used in Ref. [29] is employed. The signal yields of the production i in the decay channel j are parametrized as:

$$\sigma_i \times B_j = \sigma_i(\kappa) \times \frac{\Gamma_j(\kappa)}{\Gamma_H(\kappa)}. \tag{11.29}$$

Effective coupling modifiers κ are defined as:

$$\kappa_i^2 = \frac{\sigma_i}{\sigma_i^{\mathrm{SM}}}, \ \kappa_j^2 = \frac{\Gamma_j}{\Gamma_j^{\mathrm{SM}}}. \tag{11.30}$$

This framework using the coupling modifiers κ is called κ*-framework*. Higgs decays to invisible particles such as $H \to ZZ^* \to 4\nu$ is referred to as *invisible decays*. The *BSM* contribution to this branching ratio is denoted as B_{inv}. Higgs decays uncovered by the current analyses such as $H \to$ (top-loop) $\to gg$ is referred to as *undetected decays*. The *BSM* contribution to this branching ratio is denoted as B_{und}. The modifier of the total width of the Higgs boson Γ_H is denoted as κ_H. Using the coupling modifiers parameters, κ_H is parametrized as:

$$\kappa_H^2 = \frac{\sum_j B_j^{\mathrm{SM}} \kappa_j^2}{(1 - B_i - B_u)}. \tag{11.31}$$

The effective coupling modifiers are expressed in terms of *resolved coupling modifiers*: κ_b, κ_t, κ_W, κ_Z, κ_τ, κ_μ as shown in Table 11.8.

The results shown in this section are derived by assuming that no BSM contributes to loops and decays. Technically, this assumption is realized by setting $B_{\mathrm{inv}} = B_{\mathrm{und}} = 0$.

The goal of this measurement is to constrain six resolved coupling modifiers. To constrain these six parameters, it is necessary to combine analyses sensitive to each coupling. The input analyses are described in Ref. [29, 162], and listed in Table 11.9.

Table 11.8: Parametrization of the cross-sections and the decay widths in the κ framework [29]. In the fit, the cross-sections and the widths are parametrized in terms of the resolved coupling modifiers: κ_b, κ_t, κ_W, κ_Z, κ_τ, and κ_μ. The coupling modifiers for the second-generation quarks ($c\bar{c}$, $s\bar{s}$) are assumed to be the same as those for the third generation. The coupling modifiers for the first generation fermions are fixed at unity (SM), and they are not relevant due to the small values.

Production	Effective modifier	Resolved modifier
$\sigma(\text{ggF})$	κ_g^2	$1.040\,\kappa_t^2 + 0.002\,\kappa_b^2 - 0.038\,\kappa_t\kappa_b - 0.005\,\kappa_t\kappa_c$
$\sigma(\text{VBF})$	-	$0.733\,\kappa_W^2 + 0.267\,\kappa_Z^2$
$\sigma(qq \to ZH)$	-	κ_Z^2
$\sigma(gg \to ZH)$	$\kappa_{(ggZH)}$	$2.456\,\kappa_Z^2 + 0.456\,\kappa_t^2 - 1.903\,\kappa_Z\kappa_t$ $- 0.011\,\kappa_Z\kappa_b + 0.003\,\kappa_t\kappa_b$
$\sigma(WH)$	-	κ_W^2
$\sigma(ttH)$	-	κ_t^2
$\sigma(WtH)$	-	$2.909\,\kappa_t^2 + 2.310\,\kappa_W^2 - 4.220\,\kappa_t\kappa_W$
$\sigma(tHq)$	-	$2.633\,\kappa_t^2 + 3.578\,\kappa_W^2 - 5.211\,\kappa_t\kappa_W$
$\sigma(bbH)$	-	κ_b^2
Partial decay width		
Γ^{bb}	-	κ_b^2
Γ^{ww}	-	κ_W^2
Γ^{gg}	κ_g^2	$1.111\,\kappa_t^2 + 0.012\,\kappa_b^2 - 0.123\,\kappa_t\kappa_b$
$\Gamma^{\tau\tau}$	-	κ_τ^2
Γ^{zz}	-	κ_Z^2
Γ^{cc}	-	$\kappa_c^2\ (=\kappa_t^2)$
$\Gamma^{\gamma\gamma}$	κ_γ^2	$1.589\,\kappa_W^2 + 0.072\,\kappa_t^2 - 0.674\,\kappa_W\kappa_t$ $+0.009\,\kappa_W\kappa_\tau + 0.008\,\kappa_W\kappa_b$ $-0.002\,\kappa_t\kappa_b - 0.002\,\kappa_t\kappa_\tau$
$\Gamma^{Z\gamma}$	$\kappa_{(Z\gamma)}^2$	$1.118\,\kappa_W^2 - 0.125\,\kappa_W\kappa_t + 0.004\,\kappa_t^2 + 0.003\,\kappa_W\kappa_b$
Γ^{ss}	-	$\kappa_s^2\ (=\kappa_b^2)$
$\Gamma^{\mu\mu}$	-	κ_μ^2
Total width ($B_{\text{inv}} = B_{\text{und}} = 0$)		
Γ_H	κ_H^2	$0.581\,\kappa_b^2 + 0.215\,\kappa_W^2 + 0.082\,\kappa_g^2$ $+0.063\,\kappa_\tau^2 + 0.026\,\kappa_Z^2 + 0.029\,\kappa_c^2$ $+0.0023\,\kappa_\gamma^2 + 0.0015\,\kappa_{(Z\gamma)}^2$ $+0.0004\,\kappa_s^2 + 0.00022\,\kappa_\mu^2$

In the coupling measurement, the constraints of the six coupling modifier are derived by scanning the likelihood as a function of these κ parameters. The dependence of the negative-log-likelihood ($-\Delta \ln(L)$) on the κ parameters is shown in Figure 11.12. The corresponding 68% confidence intervals are derived and summarized in Table 11.10 and Figure 11.13. The fitted κ values are consistent with the SM within their uncertainties with and without the VH, $H \to b\bar{b}$ analysis. In Figure 11.13, the $\overline{MS}$ running masses evaluated at $m_H = 125.09$ GeV are used for quarks.

As shown in Table 11.10, the constraints on the six coupling modifiers without the VH, $H \to b\bar{b}$ analysis in the fit is worse than the constraints with the default configuration. The difference in κ_b is easy to understand because the VH, $H \to b\bar{b}$ analysis is most sensitive to the $H \to b\bar{b}$ decay. The differences in the other κ parameters are caused by the constraint on the total width Γ_H. Since the experimental observables are the branching ratios Γ_j/Γ_H, the constraints on the Γ_H, which is contributed to by the $H \to b\bar{b}$ width, is essential to constrain the κ parameters.

This result clearly shows the importance of the VH, $H \to b\bar{b}$ analysis discussed in this thesis in the context of the search for BSM scenarios that modify the Higgs couplings, such as the electroweak baryogenesis

Table 11.9: Input analyses for the coupling measurement [29], and their relevant decay and production channels. The full Run 2 data corresponds to 139 fb^{-1}. All the analyses are performed using data of pp collisions at $\sqrt{s} = 13$ TeV including the analyses with the smaller integrated luminosity.

Decay channels	Production modes	Integrated luminosity [fb^{-1}]	Ref.
$H \to \gamma\gamma$	ggF,VBF,WH,ZH,ttH, tH	139	[163]
$H \to ZZ^*$	ggF,VBF,WH,ZH,$ttH(4\ell)$	139	[164]
	ttH excl. $H \to 4\ell$	36.1	[14, 165]
$H \to WW^*$	ggF,VBF	36.1	[166]
	ttH		[14, 165]
$H \to \tau\tau$	ggF,VBF	36.1	[167]
	ttH		[14, 165]
$H \to b\bar{b}$	VBF	24.5 – 30.6	[168]
	WH, ZH	139	[169]
	ttH	36.1	[14, 170]
$H \to \mu\mu$	ggF,VBF,VH,ttH	139	[171]
$H \to$ invisible	VBF	139	[172]

Table 11.10: 68% confidence intervals for the coupling modifiers in the default configuration [29] and the configuration without the VH,$H \to b\bar{b}$ analysis.

Coupling	With VH, $H \to b\bar{b}$ [29]		Without VH, $H \to b\bar{b}$	
modifiers	Observed	Expected	Observed	Expected
κ_Z	1.02 ± 0.06	1.00 ± 0.06	$1.07^{+0.19}_{-0.18}$	1.00 ± 0.18
κ_W	$1.05^{+0.06}_{-0.05}$	1.00 ± 0.06	1.11 ± 0.18	$1.00^{+0.16}_{-0.17}$
κ_b	$0.98^{+0.14}_{-0.12}$	$1.00^{+0.15}_{-0.14}$	$1.12^{+0.48}_{-0.44}$	1.00 ± 0.43
κ_t	$0.96^{+0.09}_{-0.08}$	1.00 ± 0.09	$1.01^{+0.15}_{-0.16}$	$1.00^{+0.15}_{-0.18}$
κ_τ	$1.06^{+0.15}_{-0.14}$	1.00 ± 0.14	$1.12^{+0.24}_{-0.22}$	$1.00^{+0.22}_{-0.21}$
κ_μ	$1.12^{+0.26}_{-0.30}$	$1.00^{+0.27}_{-0.34}$	1.18 ± 0.35	$1.00^{+0.33}_{-0.37}$

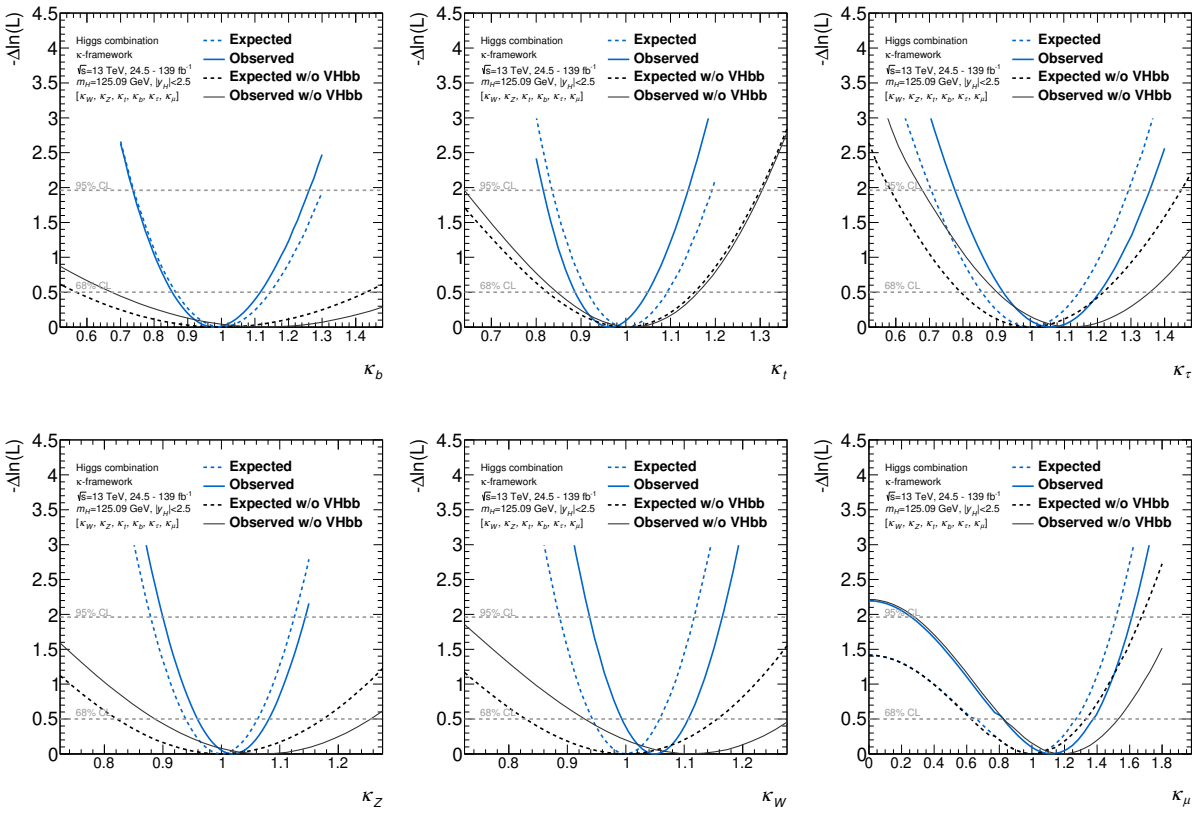

Figure 11.12: Negative-log-likelihoods ($-\Delta\ln(L)$) as functions of the coupling modifiers, κ_b, κ_t, κ_W, κ_Z, κ_τ, κ_μ. The blue curves show the values of $-\Delta\ln(L)$ when the VH, $H \to b\bar{b}$ analysis (this thesis) is included, and the same as result presented in Ref. [29]. The black curves (w/o VHbb) show the values of $-\Delta\ln(L)$ when the analysis of this thesis is not included.

explained in Section2.5.1.

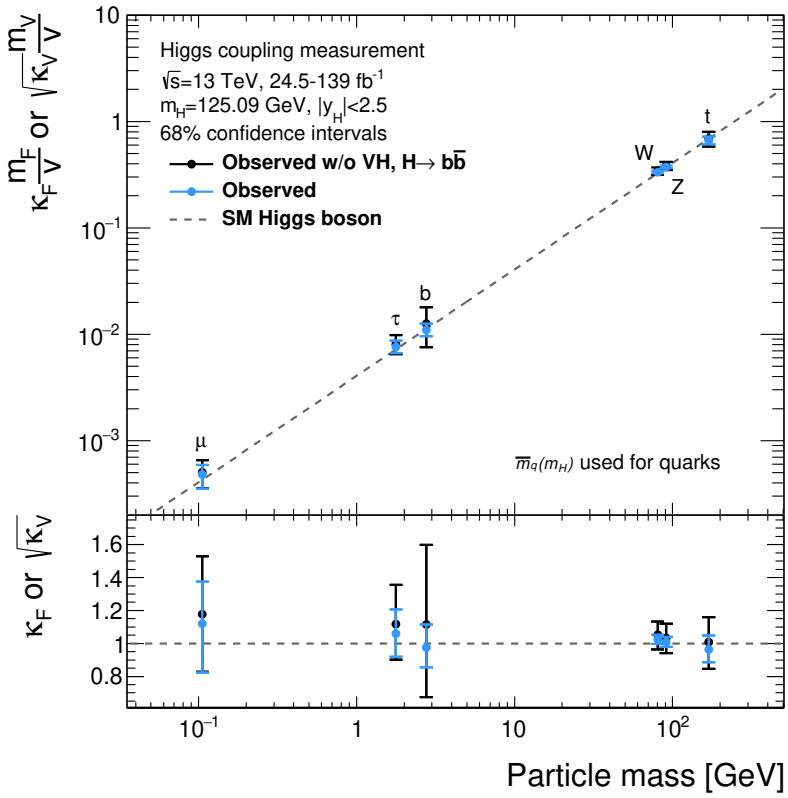

Figure 11.13: Summary of the 68% confidence intervals for the Higgs coupling measurements with and without the $VH, H \to b\bar{b}$ analysis. The light blue graph shows the default configuration including the $VH, H \to b\bar{b}$ analysis [29], and the black one shows the measurements without the $VH, H \to b\bar{b}$ analysis. The $\overline{MS}$ running masses evaluated at $m_H = 125.09$ GeV are used for quarks.

12 Conclusions

The production of the Higgs boson associated with a vector boson (VH) is studied in the $H \to b\bar{b}$ decay and the leptonic decay channels of the vector boson. The analysis is performed using the pp collision data at the center-of-mass energy of 13 TeV and with the integrated luminosity of 139 fb^{-1} collected by the ATLAS detector at the Large Hadron Collider. The signal strength and the differential cross-section of the VH production times the branching ratio of the $H \to b\bar{b}$ decay as a function of the transverse momentum of the vector boson (p_{T}^{V}) are measured.

The differential production cross-section of the VH production is affected by many types of physics beyond the Standard Model (BSM), some of which are expected to resolve the remaining issues of the Standard Model (SM). Hence, it provides an indirect search for BSM effects. The coupling measurements of the Higgs boson to the 3rd generation quarks are also important since they are sensitive to BSM models that alter the coupling. These models include the general 2 Higgs Doublet Model viable for the electroweak baryogenesis, which explains the observed baryon asymmetry of the universe.

Since there are much amount of events originating from various background processes in the analysis, several techniques are employed to reduce and control the backgrounds. In the analysis, events are separated based on the number of charged leptons so that we can measure WH and ZH individually while constraining several background components at the same time. The control regions are defined to constrain the theoretical uncertainties of the backgrounds. Multivariate analysis is used as the final discriminant to separate the signal and the backgrounds and to maximize the sensitivity. There are two improvements introduced for the 2-lepton channel targeting ZH ($Z \to \ell^{+}\ell^{-}$). One is an angular variable ($\cos\theta_{\mathrm{lep}}$), introduced to exploit the difference of the polarization of the Z boson between the signal and the backgrounds (Z + jets, ZZ, and $t\bar{t}$). By integrating $\cos\theta_{\mathrm{lep}}$ in the multivariate analysis, 7% improvement of the significance in the 2-lepton channel is confirmed. The other is the data-driven estimation of the top-quark production background in the 2-lepton channel, introduced to eliminate the systematic uncertainties on the $t\bar{t}$ production which is up to 10%. This makes the results more reliable.

The measured signal strengths are $\mu_{WH}^{bb} = 0.95^{+0.27}_{-0.25}$ for WH and $\mu_{ZH}^{bb} = 1.08^{+0.25}_{-0.23}$ for ZH. The observed significance of the signal processes is 4.0 (ZH) and 5.3 (ZH) standard deviations compared to the expected significance of 4.1 and 5.1 standard deviations. These results are the first evidence of the WH production and the first observation of the ZH production. The differential cross-section times the branching ratio as a function of p_{T}^{V} is measured to improve the sensitivity to BSM interactions that affect the cross-section in the high p_{T}^{V} phase space. The measured cross-sections are: 19.0 ± 12.1 fb ($150 \le p_{\mathrm{T}}^{W} < 250$ GeV), 7.2 ± 2.2 fb ($p_{\mathrm{T}}^{W} \ge 250$ GeV) for WH and 42.5 ± 35.9 fb ($75 \le p_{\mathrm{T}}^{Z} < 150$ GeV), 20.5 ± 6.2 fb ($150 \le p_{\mathrm{T}}^{Z} < 250$ GeV), 5.4 ± 1.7 fb ($p_{\mathrm{T}}^{Z} \ge 250$ GeV) for ZH, which agree with the Standard Model prediction. The uncertainty of the measurement is about 85% in the medium p_{T}^{V} region ($75 \le p_{\mathrm{T}}^{V} < 150$ GeV) and about 30% in the higher p_{T}^{V} regions. Since the measurement in the high p_{T}^{V} phase space, which is sensitive to the BSM, is still statistically limited, the precision of these cross-sections can be improved in future LHC runs.

In order to present the experimental limits for general BSM models, the measurement of the differential cross-section is interpreted as the limits on the Wilson coefficients of dimension-6 terms in the Standard

Model Effective Field Theory (SMEFT) Lagrangian. The Wilson coefficients, $c_{Hq}^{(3)}$, c_{Hu}, c_{HW} and c_{HWB}, are constrained. The most constrained coefficient, $c_{Hq}^{(3)}$, is thought to be sensitive to models such as the Heavy Vector Triplet (HVT) model and the Minimal Composite Higgs Model. The constraint on $c_{Hq}^{(3)}$ is interpreted as the lower mass limit of the heavy resonance in the HVT model, and the lower limits of 1.97 TeV (Model A) and 3.02 TeV (Model B) are extracted. These limits are slightly weaker than the direct searches for these heavy resonances (3-5 TeV). Therefore, the indirect search with the VH production is thought to be useful for scenarios with a larger mass and a stronger coupling.

The 125 GeV Higgs boson may be a CP-mixed particle in new physics models such as 2HDM. In that case, the CP-odd interaction between the 125 GeV scalar particle and the vector bosons (VVH vertex) can appear depending on the choice of parameters as described in Section 2.5.2. The measurement of the p_{T}^{V} spectrum is a search for general BSM and can constrain these CP-odd interactions. However, the measurement does not discriminate the CP of an anomalous VVH coupling when the anomaly is found in the p_{T}^{V} spectrum. In order to have an observable sensitive only to the CP-odd modification of the VVH vertex, the angular information of $Z \to \ell^{+}\ell^{-}$ is proposed. The constraint on the CP-odd VVH interaction from the angular analysis is weaker than the one derived from the p_{T}^{V} spectrum. However, if an anomalous VVH interaction is found, this angular analysis is useful to test the CP-structure of the interaction. The limits derived from the p_{T}^{V} spectrum and the angular distribution are better than the ones from the Higgs decays using the ATLAS Run 1 data.

The VH, $H \to b\bar{b}$ analysis is included in the global Higgs coupling measurement in Ref. [29]. The contribution of the VH, $H \to b\bar{b}$ analysis to the coupling measurement is discussed by performing the combined measurement without the work in this thesis. It is demonstrated that the VH, $H \to b\bar{b}$ analysis significantly contributes to constrain the whole Higgs sector with approximately 3 times more stringent constraints on the Higgs coupling to Z, W, and b-quark and 15-40% more stringent constraints on the coupling to t-quark, τ-lepton, and muon compared to the measurement without including the VH, $H \to b\bar{b}$ analysis. Thus, the analysis contributes to constraints of BSM scenarios that modify the Higgs couplings such as the general 2HDM capable of generating the baryon asymmetry of the universe.

Appendices

A On the renormalization scale variations

Renormalization scale variations are often used to estimate missing higher-order contributions in fixed order perturbative calculation. In this method, the renormalization scale is doubled and halved in physics simulations. This method for estimating theoretical uncertainties is not firmly backed by the field theory, but a rough understanding is presented in this appendix. Concepts used in this section are taken from Ref. [30].

When the renormalization scale is shifted, the coupling constant changes, which is referred to as *running coupling constant*. However, an amplitude does not depend on the renormalization scale because the renormalization scale is an artificial energy scale that can be chosen arbitrarily. In Feynman diagrams with loops, *counter terms* are introduced to cancel divergences (cut-off dependence) of the loop integrals. The dependence of the counter terms on the renormalization scale cancels the dependence of the amplitude on the scale through the running coupling constant. This is expressed by *Callan-Symanzik equation*:

$$M\frac{\partial}{\partial M}\mathcal{M} + \beta\frac{\partial}{\partial g}\mathcal{M} = 0, \tag{A.1}$$

where M is the renormalization scale, $\mathcal{M}$ is an amplitude of some process. β is β-function which control the evolution of the coupling constant g.

Let us expand the Callan-Symanzik equation with respect to g:

$$\mathcal{M} = \mathcal{M}^{(0)} + \mathcal{M}^{(1)} + \mathcal{M}^{(2)} + \cdots, \tag{A.2}$$

$$\beta = \beta^{(0)} + \beta^{(1)} + \beta^{(2)} + \beta^{(3)} + \cdots. \tag{A.3}$$

Here, the superscripts (n) is indicates the $O(g^n)$ term in the quantities. For QCD, the β function at the 1-loop level is given by:

$$\beta(g) = -\frac{b_0 g^3}{(4\pi)^2}, \quad \text{with } b_0 = 11 - \frac{2}{3}n_f, \tag{A.4}$$

where n_f is the number of quark flavors. Therefore,

$$\beta^0 = \beta^1 = \beta^2 = 0. \tag{A.5}$$

Each order of the Callan-Symanzik equation is given by:

$$O(g^0) : M\frac{\partial}{\partial M}\mathcal{M}^{(0)} = 0, \tag{A.6}$$

$$O(g^1) : M\frac{\partial}{\partial M}\mathcal{M}^{(1)} = 0, \tag{A.7}$$

$$O(g^2) : M\frac{\partial}{\partial M}\mathcal{M}^{(2)} = 0, \tag{A.8}$$

$$O(g^3) : M\frac{\partial}{\partial M}\mathcal{M}^{(3)} + \beta^{(3)}\frac{\partial}{\partial g}\mathcal{M}^{(1)} = 0. \tag{A.9}$$

From the last line, the dependence of $\mathcal{M}^{(1)}$ on M through the evolution of g must be canceled by the first term ($M\partial\mathcal{M}^{(3)}/\partial M$). However, if a higher-order term, $\mathcal{M}^{(3)}$ in this example, is missing in the calculation, theoretical predictions are varied by the shift of the renormalization scale. The observed difference in this "scale variation" is related to the missing higher-order terms.

B Algorithm of the truth b-tagging

The probability of jets to be tagged depends on the flavor of the jets. Thus, the analysis needs to handle the true flavors of jets defined below. Particles used in this paragraph are *truth particles* defined by Monte Carlo event generators.

- If a weakly decaying b-hadron is found within $\Delta R < R_{\text{max}} = 0.3$ of the jet axis, the jet is labeled as a b-jet.
- If a b-hadron is not found, but a weakly decaying c-hadron is found within $\Delta R < R_{\text{max}} = 0.3$ of the jet axis, the jet is labeled as a c-jet.
- If a τ-lepton is found within $\Delta R < R_{\text{max}} = 0.3$ of the jet axis, the jet is labeled as a τ-jet.
- If a hadron or τ-lepton matches more than one jets, the closest jets is considered as the parent.
- Jets that are not labeled after the procedure are labeled as a light-jet.

The event weight utilized in the truth b-tagging should be the probability of a given event to be tagged, and it is defined as below. The event selection of the analysis requires exactly two b-tagged jets (Section 6.3). If an event contains only two jets, the probability of the event to be accepted is simply the product of the two efficiencies for two jets, and it is the desired event weights. However, when there are more than two jets in an event, there is a probability of additional jets to be b-tagged. The probability of all the permutations is integrated as below. First, the probability of a given permutation of b-tagged and rejected jets are defined as the product of the efficiency for tagged jets (ϵ) and the inefficiency for rejected jets (ϵ_{in}):

$$\epsilon\left(\binom{m}{n}_i, x\right) = \prod_{j \in n} \epsilon_x^f(j), \tag{B.1}$$

$$\epsilon_{\text{in}}\left(\overline{\binom{m}{n}_i}, x\right) = \prod_{j \in m-n} (1 - \epsilon_x^f(j)), \tag{B.2}$$

where x is a given working point, and $\binom{m}{n}_i$ denotes the ith permutation when selecting n jets from m jets. $\overline{\binom{m}{n}_i}$ denotes the other jets than ones expressed by $\binom{m}{n}_i$. $j \in n$ ($j \in m - n$) indicates that the product runs over the b-tagged (rejected) jets in the given permutation. The efficiency ϵ is discussed in Section B.0.1. Then, the probability of the event to pass the event selection is the sum of the probabilities for all possible permutation of tagged and rejected jets as:

$$w = \sum_{i \in \text{permutations}} \epsilon\left(\binom{m}{n}_i\right) \cdot \epsilon_{\text{in}}\left(\overline{\binom{m}{n}_i}\right). \tag{B.3}$$

The desired final event weight is the probability derived in the previous step. To obtain kinematics of the event, a single permutation is chosen according to the probability for the ith permutation:

$$P_i = \frac{\epsilon\left(\binom{m}{n}_i, x\right) \cdot \epsilon_{\text{in}}\left(\overline{\binom{m}{n}_i}, x\right)}{w}. \tag{B.4}$$

The direct b-tagging is applied to data events.

Mis-modelling is observed in events with small $\Delta R(j, j)$ for both $t\bar{t}$ and V + jets samples as shown in Figure B.1. The cause of this issue is imagined that the truth b-tagging algorithm relies on efficiency maps for single jets, and thus the effects from nearby jets are not simulated. In the direct b-tagging algorithm, it simulates b-tagging in such a dense event topology. To overcome this issue, a hybrid approach is adopted below. The direct b-tagging is applied to all the true b-jets. Then the truth b-tagging algorithm is applied to non-b-tagged jets, and $m - n$ pseudo-tagged jets are found, where m is the required number b-tagged jets and n is the number of jets b-tagged in the previous step. By construction, events in which two true b-jets are b-tagged reproduces distributions by the direct b-tagging. For events with other combinations of true flavors, more simulated events are available.

B.0.1 b-tagging efficiency for MC and data events

Efficiency maps are needed in the truth b-tagging algorithm. The maps for each (cumulative) working point provide the b-tagging efficiency dependent on p_{T} and η. Dedicated efficiency maps are prepared for the phases space that the analysis focuses on, and separately for Powheg+Pythia8 ($t\bar{t}$) and Sherpa 2.2.1 (V + jets). The maps for the 70% working point are shown in Figures B.2 and B.3.

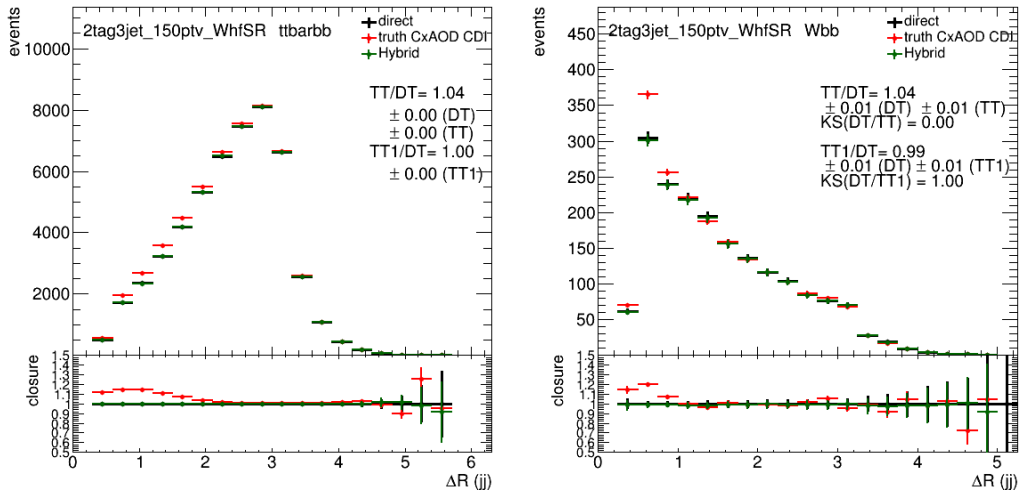

Figure B.1: $\Delta R_{b\bar{b}}$ distributions for $t\bar{t}$ (left) and $W + bb$ (right) events with the direct b-tagging (black), the truth b-tagging (red) and the hybrid truth b-tagging (green). The study is performed with events with one charged lepton (more precisely, a signal region of a 1-lepton channel defined in Section 6.3), one non-b-jet in addition to two b-jets and the reconstructed $p_{\text{T}}^{\ell+\boldsymbol{E}_{\text{T}}^{\text{miss}}}$ greater than 150 GeV are used in these plots. The plots in the bottom panes show the ratio of each method to the direct b-tagging. Non-closure is observed for the truth b-tagging, and the closure is recovered by the hybrid truth b-tagging.

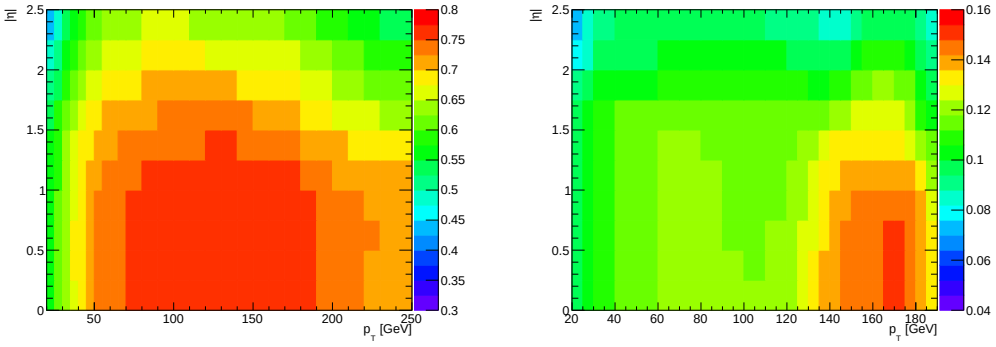

(a) b-jet (b) c-jet

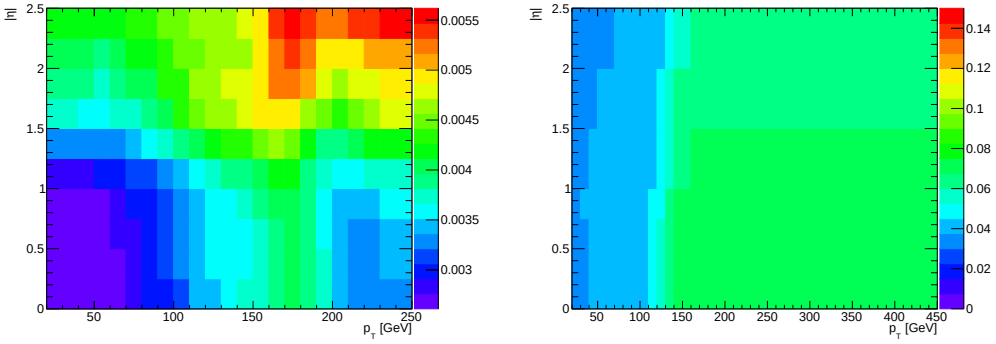

(c) τ-jet (d) light-jet

Figure B.2: Efficiency maps in the p_{T}-η plane for the b-tagging of the 70% working point in POWHEG+PYTHIA8 ($t\bar{t}$) events. The 70% working point in the cumulative b-tagging corresponds to the sum of the [70,60] and [60,0] bins used in the pseudo-continuous b-tagging.

Efficiency maps for the pseudo-continuous mode are derived by subtracting the efficiency maps of the cumulative mode shown in Figures B.2 and B.3, i.e. the efficiency for the bins of the pseudo-continuous b-tagging, [70,60] and [60,0], is defined as

$$\mathrm{MCEff}_{[70,60]} = \mathrm{MCEff}_{70\%\ \mathrm{WP}} - \mathrm{MCEff}_{60\%\ \mathrm{WP}} \tag{B.5}$$

$$\mathrm{MCEff}_{[60,0]} = \mathrm{MCEff}_{60\%\ \mathrm{WP}} \tag{B.6}$$

They give the probability of a given jet to fall in one b-tagging bin for MC events. The efficiency is multiplied by scale factors to compare the MC samples to the data:

$$\mathrm{Eff}_{\mathrm{bin}} = \mathrm{MCEff}_{\mathrm{bin}} \cdot \mathrm{SF}_{\mathrm{bin}}, \tag{B.7}$$

where the $\mathrm{SF}_{\mathrm{bin}}$ is the MC-to-data scale factor described in the next paragraph. The efficiency of the b-tagging is expressed by the sum of the probabilities for the bins [70,60], [60,0]:

$$\mathrm{Eff}_{70\%} = \sum_{\mathrm{bin}} \mathrm{Eff}_{\mathrm{bin}} = \mathrm{Eff}_{[70,60]} + \mathrm{Eff}_{[60,0]}, \tag{B.8}$$

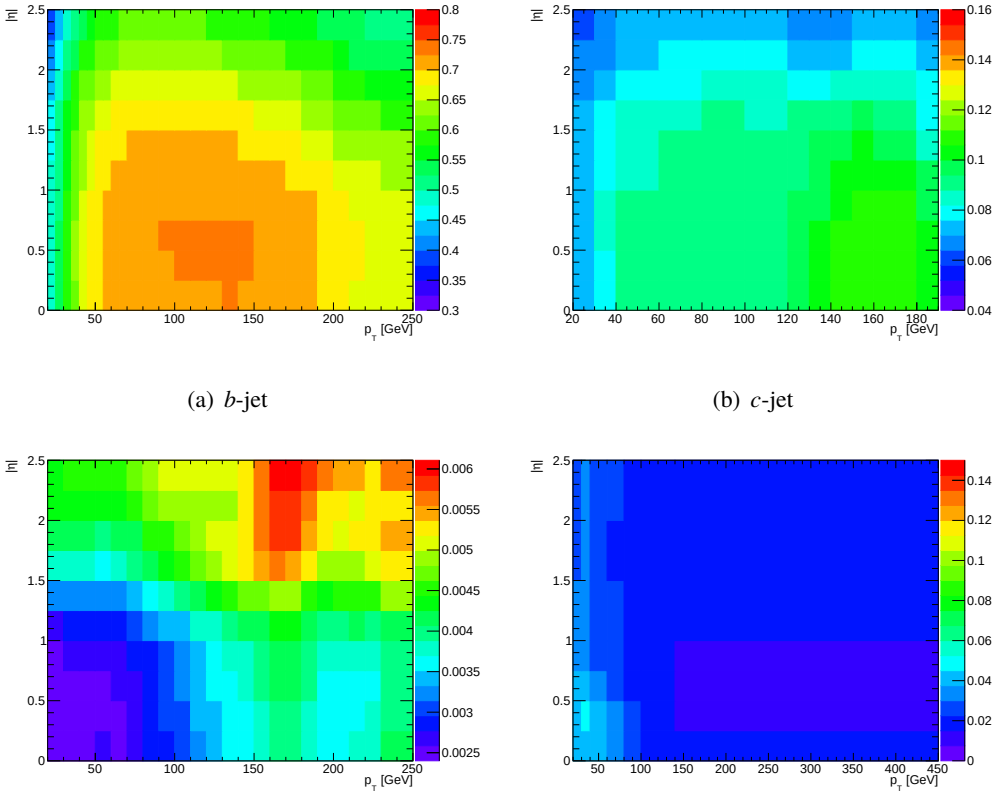

(a) b-jet (b) c-jet

(c) τ-jet (d) light-jet

Figure B.3: Efficiency maps in the p_{T}-η plane for the b-tagging of the 70% working point in SHERPA 2.2.1 (V + jets) events. The 70% working point in the cumulative b-tagging corresponds to the sum of the [70,60] and [60,0] bins used in the pseudo-continuous b-tagging.

where "bin" is an interval of the MV2c10 value.

The scale factors that correct the efficiency in MC events to the efficiency in the data are defined as functions of p_{T} and the binned MV2c10 value of jets. The scale factors are derived so that the sum of the probability of jets to fall in all the bins of MV2c10 is unity. They are shown in Figure B.4. MC-to-MC scale factors that correct the efficiency for SHERPA 2.2.1 samples to those for POWHEG+PYTHIA8 samples is shown in Figure B.5.

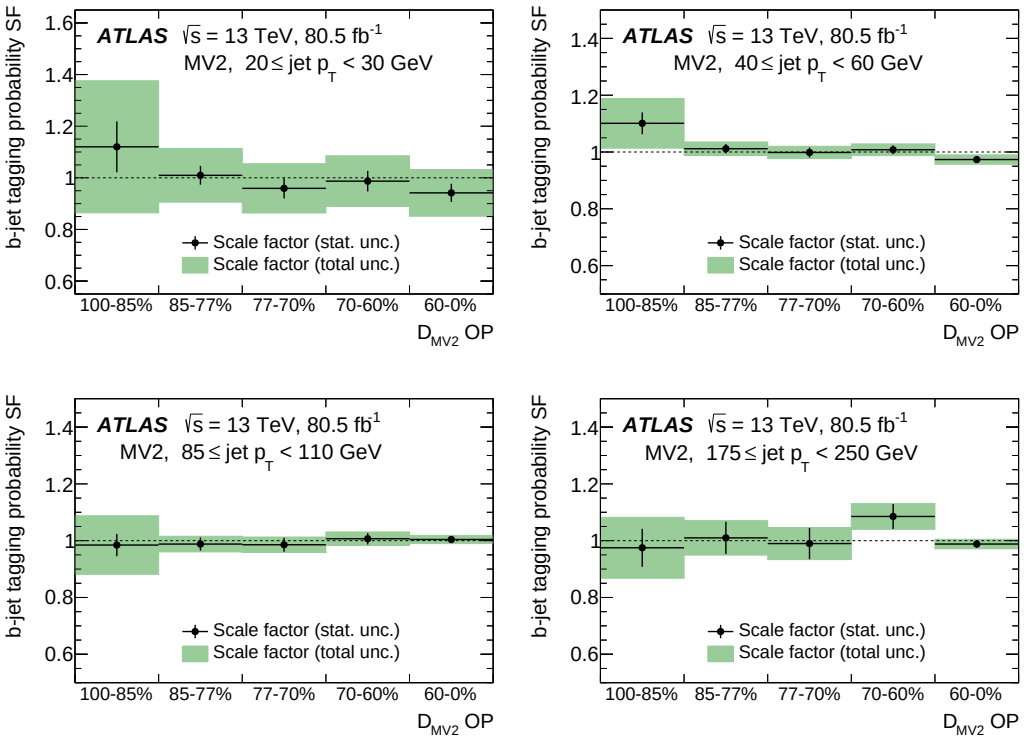

Figure B.4: MC-to-data scale factors of b-tagging probabilities for jets in the different p_{T} regions in different MV2c10 bins. Vertical error bars include the only data statistical uncertainties while the green bands correspond to the sum in quadrature of statistical and systematic uncertainties. The scale factors are derived for the p_{T} ranges: [20,30), [30,40), [40,60), [60,85), [85,110), [110,175), [175,250) and [250,600) GeV, but only the ranges, [20,30), [40,60), [85,110) and [175,250) GeV, are shown as indicated in the plots.

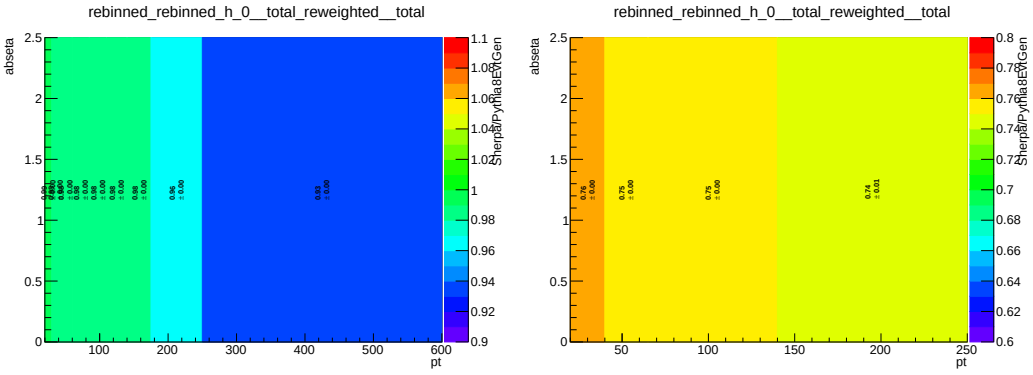

(a) *b*-jet (b) *c*-jet

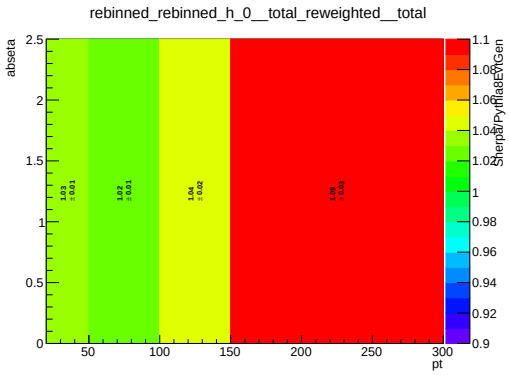

(c) light-jet

Figure B.5: MC-to-MC scale factors for the *b*-tagging between generators, POWHEG+PYTHIA8 and SHERPA 2.2.1.

C Prefit yields

The 0-, 1- and 2-lepton channels, the analysis categories, and the signal and control regions are defined in Chapter 6. The yields in the all the analysis regions before the fit (*prefit yields*) are summarized in this appendix.

The yields in the SRs, low-ΔR-CRs, and high-ΔR-CRs of the 0-lepton channel for the categories with $150 \leq p_{\mathrm{T}}^{V} < 250$ GeV and $p_{\mathrm{T}}^{V} \geq 250$ GeV are shown in Tables C.1 and C.2, respectively.

The yields in the SRs, low-ΔR-CRs, and high-ΔR-CRs of the 1-lepton channel for the categories with $150 \leq p_{\mathrm{T}}^{V} < 250$ GeV and $p_{\mathrm{T}}^{V} \geq 250$ GeV are shown in Tables C.3 and C.4, respectively.

The yields in the SRs, low-ΔR-CRs, and high-ΔR-CRs of the 2-lepton channel for the categories with $75 \leq p_{\mathrm{T}}^{V} < 150$ GeV, $150 \leq p_{\mathrm{T}}^{V} < 250$ GeV, and $p_{\mathrm{T}}^{V} \geq 250$ GeV are shown in Tables C.6, C.6, and C.7, respectively.

The yields in the eμ control regions of the 2-lepton channel for the categories with $75 \leq p_{\mathrm{T}}^{V} < 150$ GeV, $150 \leq p_{\mathrm{T}}^{V} < 250$ GeV, and $p_{\mathrm{T}}^{V} \geq 250$ GeV are shown in Tables C.8, C.9, and C.10, respectively.

Table C.1: The yields of the signals, the backgrounds and the data in the signal regions, the low-ΔR control regions and the high-ΔR control regions of the 0-lepton channel with $150 \leq p_{\mathrm{T}}^{V} < 250$ GeV.

	2-jet, 2-b-tag			3-jet, 2-b-tag		
	Low ΔR CR	SR	High ΔR CR	Low ΔR CR	SR	High ΔR CR
Zl	2.61 ± 0.04	5.14 ± 0.09	6.67 ± 0.11	2.77 ± 0.05	6.99 ± 0.12	10.93 ± 0.19
Zcl	7.74 ± 0.13	19.70 ± 4.50	22.96 ± 0.39	9.06 ± 0.15	29.30 ± 6.80	41.96 ± 0.71
Zhf	831.00 ± 70.00	2240.00 ± 180.00	2520.00 ± 200.00	1119.00 ± 56.00	3120.00 ± 150.00	3730.00 ± 190.00
Wl	2.43 ± 0.04	5.70 ± 1.80	10.16 ± 0.17	3.07 ± 0.05	8.73 ± 0.15	16.54 ± 0.28
Wcl	6.82 ± 0.12	19.30 ± 7.10	27.20 ± 0.46	8.92 ± 0.15	31.00 ± 11.00	51.88 ± 0.88
Whf	440.00 ± 160.00	620.00 ± 220.00	310.00 ± 120.00	790.00 ± 270.00	1310.00 ± 450.00	730.00 ± 260.00
Single-top	38.50 ± 7.90	255.00 ± 46.00	316.00 ± 58.00	102.00 ± 21.00	830.00 ± 160.00	1230.00 ± 250.00
$t\bar{t}$	152.00 ± 22.00	1190.00 ± 170.00	1150.00 ± 160.00	630.00 ± 56.00	5820.00 ± 470.00	8780.00 ± 710.00
diboson	43.00 ± 12.00	351.00 ± 92.00	9.05 ± 0.15	49.00 ± 16.00	360.00 ± 120.00	50.09 ± 0.85
Total bkg.	1520.00 ± 200.00	4710.00 ± 420.00	4370.00 ± 340.00	2710.00 ± 300.00	11530.00 ± 770.00	14640.00 ± 890.00
Signal	2.94 ± 0.38	146.00 ± 19.00	7.13 ± 0.97	4.16 ± 0.38	130.00 ± 14.00	19.90 ± 3.10
Data	1802	5397	5273	3034	11875	15663
Data/Bkg	1.19 ± 0.03	1.15 ± 0.02	1.21 ± 0.02	1.12 ± 0.02	1.03 ± 0.01	1.07 ± 0.01

Table C.2: The yields of the signals, the backgrounds and the data in the signal regions, the low-ΔR control regions and the high-ΔR control regions of the 0-lepton channel with $p_{\mathrm{T}}^{V} \geq 250$ GeV.

	2-jet, 2-b-tag			3-jet, 2-b-tag		
	Low ΔR CR	SR	High ΔR CR	Low ΔR CR	SR	High ΔR CR
Zl	0.13 ± 0.00	1.00 ± 0.02	1.95 ± 0.03	0.28 ± 0.00	1.43 ± 0.02	3.78 ± 0.06
Zcl	0.33 ± 0.01	2.82 ± 0.65	5.43 ± 0.09	0.81 ± 0.01	4.70 ± 1.10	12.27 ± 0.21
Zhf	43.00 ± 4.70	278.00 ± 24.00	455.00 ± 43.00	95.40 ± 6.40	451.00 ± 30.00	845.00 ± 56.00
Wl	0.08 ± 0.00	0.61 ± 0.01	1.50 ± 0.03	0.19 ± 0.00	0.95 ± 0.02	3.08 ± 0.05
Wcl	0.20 ± 0.00	1.82 ± 0.67	4.06 ± 0.07	0.58 ± 0.01	3.30 ± 1.20	9.16 ± 0.16
Whf	18.00 ± 7.30	94.00 ± 37.00	64.00 ± 29.00	54.00 ± 21.00	200.00 ± 77.00	181.00 ± 73.00
Single-top	0.67 ± 0.01	12.90 ± 4.60	40.00 ± 13.00	4.30 ± 1.70	50.00 ± 17.00	187.00 ± 72.00
$t\bar{t}$	1.80 ± 0.33	43.80 ± 8.20	74.00 ± 14.00	12.60 ± 1.80	197.00 ± 23.00	761.00 ± 95.00
diboson	8.10 ± 2.50	83.00 ± 22.00	2.92 ± 0.05	12.50 ± 4.20	76.00 ± 25.00	21.50 ± 6.70
Total bkg.	72.40 ± 9.20	519.00 ± 55.00	648.00 ± 61.00	181.00 ± 23.00	985.00 ± 95.00	2020.00 ± 160.00
Signal	0.47 ± 0.05	40.50 ± 4.50	1.97 ± 0.24	1.34 ± 0.10	33.50 ± 2.70	6.40 ± 1.10
Data	72	578	730	210	1046	2011
Data/Bkg	0.99 ± 0.12	1.11 ± 0.05	1.13 ± 0.04	1.16 ± 0.08	1.06 ± 0.03	1.00 ± 0.02

Table C.3: The yields of the signals, the backgrounds and the data in the signal regions, the low-ΔR control regions and the high-ΔR control regions of the 1-lepton channel with $150 \leq p_{\mathrm{T}}^{V} < 250$ GeV.

	2-jet, 2-b-tag			3-jet, 2-b-tag		
	Low ΔR CR	SR	High ΔR CR	Low ΔR CR	SR	High ΔR CR
Zl	0.01 ± 0.00	0.05 ± 0.00	0.24 ± 0.00	0.02 ± 0.00	0.09 ± 0.00	0.53 ± 0.00
Zcl	0.01 ± 0.00	0.12 ± 0.00	0.43 ± 0.00	0.05 ± 0.00	0.25 ± 0.00	1.19 ± 0.00
Zhf	1.52 ± 0.00	9.45 ± 0.00	21.12 ± 0.00	5.58 ± 0.00	23.54 ± 0.00	53.56 ± 0.01
Wl	0.24 ± 0.00	1.88 ± 0.00	4.87 ± 0.00	0.61 ± 0.00	3.17 ± 0.00	11.50 ± 0.00
Wcl	0.82 ± 0.00	7.58 ± 0.00	20.10 ± 0.00	2.24 ± 0.00	13.23 ± 0.00	49.08 ± 0.00
Whf	69.62 ± 0.01	379.42 ± 0.02	340.51 ± 0.03	197.18 ± 0.02	813.40 ± 0.04	1001.16 ± 0.10
Single-top	3.64 ± 0.00	97.56 ± 0.00	429.84 ± 0.04	29.00 ± 0.00	408.01 ± 0.02	2348.03 ± 0.23
$t\bar{t}$	7.01 ± 0.00	203.64 ± 0.01	1054.93 ± 0.11	73.42 ± 0.01	1164.11 ± 0.06	10882.70 ± 1.10
diboson	7.26 ± 0.00	59.56 ± 0.00	4.02 ± 0.00	16.22 ± 0.00	81.66 ± 0.00	43.07 ± 0.00
multijetEl	0.92 ± 0.00	7.35 ± 0.00	15.37 ± 0.00	1.25 ± 0.00	6.98 ± 0.00	18.50 ± 0.00
multijetMu		12.06 ± 0.00	37.01 ± 0.00	0.18 ± 0.00		1.85 ± 0.00
Total bkg.	91.04 ± 0.01	778.67 ± 0.04	1928.45 ± 0.19	325.75 ± 0.03	2514.44 ± 0.12	14411.20 ± 1.40
Signal	0.38 ± 0.00	51.10 ± 0.01	2.52 ± 0.00	1.69 ± 0.00	43.26 ± 0.00	7.61 ± 0.00
Data	94	727	1686	339	2378	12059
Data/Bkg	1.03 ± 0.11	0.93 ± 0.03	0.87 ± 0.02	1.04 ± 0.06	0.95 ± 0.02	0.84 ± 0.01

Table C.4: The yields of the signals, the backgrounds and the data in the signal regions, the low-ΔR control regions and the high-ΔR control regions of the 1-lepton channel with $p_{\mathrm{T}}^{V} \geq 250$ GeV.

	2-jet, 2-b-tag			3-jet, 2-b-tag		
	Low ΔR CR	SR	High ΔR CR	Low ΔR CR	SR	High ΔR CR
Zl	0.01 ± 0.00	0.05 ± 0.00	0.24 ± 0.00	0.02 ± 0.00	0.09 ± 0.00	0.53 ± 0.00
Zcl	0.01 ± 0.00	0.12 ± 0.00	0.43 ± 0.00	0.05 ± 0.00	0.25 ± 0.00	1.19 ± 0.00
Zhf	1.52 ± 0.00	9.45 ± 0.00	21.12 ± 0.00	5.58 ± 0.00	23.54 ± 0.00	53.56 ± 0.01
Wl	0.24 ± 0.00	1.88 ± 0.00	4.87 ± 0.00	0.61 ± 0.00	3.17 ± 0.00	11.50 ± 0.00
Wcl	0.82 ± 0.00	7.58 ± 0.00	20.10 ± 0.00	2.24 ± 0.00	13.23 ± 0.00	49.08 ± 0.00
Whf	69.62 ± 0.01	379.42 ± 0.02	340.51 ± 0.03	197.18 ± 0.02	813.40 ± 0.04	1001.16 ± 0.10
Single-top	3.64 ± 0.00	97.56 ± 0.00	429.84 ± 0.04	29.00 ± 0.00	408.01 ± 0.02	2348.03 ± 0.23
$t\bar{t}$	7.01 ± 0.00	203.64 ± 0.01	1054.93 ± 0.11	73.42 ± 0.01	1164.11 ± 0.06	10882.70 ± 1.10
diboson	7.26 ± 0.00	59.56 ± 0.00	4.02 ± 0.00	16.22 ± 0.00	81.66 ± 0.00	43.07 ± 0.00
multijetEl	0.92 ± 0.00	7.35 ± 0.00	15.37 ± 0.00	1.25 ± 0.00	6.98 ± 0.00	18.50 ± 0.00
multijetMu		12.06 ± 0.00	37.01 ± 0.00	0.18 ± 0.00		1.85 ± 0.00
Total bkg.	91.04 ± 0.01	778.67 ± 0.04	1928.45 ± 0.19	325.75 ± 0.03	2514.44 ± 0.12	14411.20 ± 1.40
Signal	0.38 ± 0.00	51.10 ± 0.01	2.52 ± 0.00	1.69 ± 0.00	43.26 ± 0.00	7.61 ± 0.00
Data	94	727	1686	339	2378	12059
Data/Bkg	1.03 ± 0.11	0.93 ± 0.03	0.87 ± 0.02	1.04 ± 0.06	0.95 ± 0.02	0.84 ± 0.01

Table C.5: The yields of the signals, the backgrounds and the data in the signal regions, the low-ΔR control regions and the high-ΔR control regions of the 2-lepton channel with $75 \leq p_{\mathrm{T}}^{V} < 150$ GeV.

	2-jet, 2-b-tag			3-jet, 2-b-tag		
	Low ΔR CR	SR	High ΔR CR	Low ΔR CR	SR	High ΔR CR
$Z + ll$	3.04 ± 0.00	5.26 ± 0.00	5.04 ± 0.00	5.92 ± 0.00	17.13 ± 0.00	23.12 ± 0.00
$Z + cl$	11.65 ± 0.00	26.71 ± 0.00	20.66 ± 0.00	23.38 ± 0.00	86.25 ± 0.00	103.00 ± 0.01
Z + hf	1531.81 ± 0.22	4674.88 ± 0.49	3363.30 ± 0.48	3013.16 ± 0.43	9563.86 ± 1.00	8824.66 ± 1.25
$W + ll$	0.00 ± 0.00	0.00 ± 0.00	0.00 ± 0.00	0.00 ± 0.00	0.01 ± 0.00	0.02 ± 0.00
$W + cl$	0.01 ± 0.00	0.02 ± 0.00	0.02 ± 0.00	0.02 ± 0.00	0.09 ± 0.00	0.10 ± 0.00
W + hf	0.18 ± 0.00	1.21 ± 0.00	0.08 ± 0.00	2.64 ± 0.00	5.16 ± 0.00	2.78 ± 0.00
Single top	26.35 ± 0.00	106.84 ± 0.00	86.13 ± 0.01	39.86 ± 0.00	230.35 ± 0.01	216.07 ± 0.02
$t\bar{t}$	734.19 ± 0.10	3149.15 ± 0.35	1619.52 ± 0.23	1306.48 ± 0.18	8281.54 ± 0.90	5852.27 ± 0.83
Diboson	16.23 ± 0.00	276.13 ± 0.01	8.44 ± 0.00	76.42 ± 0.01	441.97 ± 0.01	105.35 ± 0.01
Total bkg.	2323.45 ± 0.29	8240.19 ± 0.64	5103.19 ± 0.63	4467.89 ± 0.55	18626.35 ± 1.42	15127.37 ± 1.85
Signal	0.87 ± 0.00	75.48 ± 0.01	5.17 ± 0.00	5.37 ± 0.00	103.57 ± 0.01	21.37 ± 0.00
Data	2940	9463	5919	5275	20927	17443
Data/Bkg.	1.27 ± 0.00	1.15 ± 0.00	1.16 ± 0.00	1.18 ± 0.00	1.12 ± 0.00	1.15 ± 0.00

Table C.6: The yields of the signals, the backgrounds and the data in the signal regions, the low-ΔR control regions and the high-ΔR control regions of the 2-lepton channel with $150 \leq p_{\mathrm{T}}^{V} < 250$ GeV.

	2-jet, 2-b-tag			3-jet, 2-b-tag		
	Low ΔR CR	SR	High ΔR CR	Low ΔR CR	SR	High ΔR CR
$Z + ll$	0.45 ± 0.00	0.93 ± 0.00	1.71 ± 0.00	1.61 ± 0.00	4.41 ± 0.00	12.30 ± 0.00
$Z + cl$	1.58 ± 0.00	4.16 ± 0.00	6.46 ± 0.00	5.82 ± 0.00	20.15 ± 0.00	50.95 ± 0.01
Z + hf	212.60 ± 0.03	633.39 ± 0.07	926.06 ± 0.13	800.91 ± 0.11	2193.72 ± 0.23	3769.28 ± 0.53
$W + ll$	0.00 ± 0.00	0.00 ± 0.00	0.00 ± 0.00	0.00 ± 0.00	0.00 ± 0.00	0.01 ± 0.00
$W + cl$	0.00 ± 0.00	0.00 ± 0.00	0.01 ± 0.00	0.01 ± 0.00	0.01 ± 0.00	0.04 ± 0.00
W + hf	0.30 ± 0.00	0.30 ± 0.00	0.17 ± 0.00	0.65 ± 0.00	1.70 ± 0.00	1.40 ± 0.00
Single top	1.79 ± 0.00	9.41 ± 0.00	17.61 ± 0.00	5.01 ± 0.00	32.44 ± 0.00	71.74 ± 0.01
$t\bar{t}$	8.87 ± 0.00	55.05 ± 0.01	110.20 ± 0.02	56.80 ± 0.01	378.82 ± 0.04	861.66 ± 0.12
Diboson	3.63 ± 0.00	81.44 ± 0.00	2.58 ± 0.00	29.61 ± 0.00	167.96 ± 0.01	68.34 ± 0.01
Total bkg.	229.23 ± 0.03	784.68 ± 0.07	1064.79 ± 0.14	900.41 ± 0.12	2799.22 ± 0.24	4835.72 ± 0.62
Signal	0.29 ± 0.00	33.01 ± 0.00	2.18 ± 0.00	2.16 ± 0.00	57.25 ± 0.01	18.28 ± 0.00
Data	271	881	1174	1010	3148	5493
Data/Bkg.	1.18 ± 0.00	1.12 ± 0.00	1.10 ± 0.00	1.12 ± 0.00	1.12 ± 0.00	1.14 ± 0.00

Table C.7: The yields of the signals, the backgrounds and the data in the signal regions, the low-ΔR control regions and the high-ΔR control regions of the 2-lepton channel with $p_{\mathrm{T}}^{V} \geq 250$ GeV.

	2-jet, 2-b-tag			3-jet, 2-b-tag		
	Low ΔR CR	SR	High ΔR CR	Low ΔR CR	SR	High ΔR CR
$Z + ll$	0.03 ± 0.00	0.21 ± 0.00	0.56 ± 0.00	0.22 ± 0.00	1.27 ± 0.00	5.97 ± 0.00
$Z + cl$	0.07 ± 0.00	0.66 ± 0.00	1.60 ± 0.00	0.69 ± 0.00	4.69 ± 0.00	21.53 ± 0.00
Z + hf	9.99 ± 0.00	77.63 ± 0.01	164.80 ± 0.02	99.88 ± 0.01	492.46 ± 0.05	1170.56 ± 0.17
$W + ll$	0.00 ± 0.00	0.00 ± 0.00	0.00 ± 0.00	0.00 ± 0.00	0.00 ± 0.00	0.01 ± 0.00
$W + cl$	0.00 ± 0.00	0.00 ± 0.00	0.00 ± 0.00	0.00 ± 0.00	0.00 ± 0.00	0.02 ± 0.00
W + hf	–	0.00 ± 0.00	0.11 ± 0.00	0.05 ± 0.00	0.19 ± 0.00	0.39 ± 0.00
Single top	0.11 ± 0.00	0.95 ± 0.00	3.44 ± 0.00	0.38 ± 0.00	2.03 ± 0.00	14.53 ± 0.00
$t\bar{t}$	0.04 ± 0.00	0.22 ± 0.00	3.00 ± 0.00	2.03 ± 0.00	16.31 ± 0.00	64.91 ± 0.01
Diboson	1.09 ± 0.00	20.26 ± 0.00	0.78 ± 0.00	8.65 ± 0.00	52.73 ± 0.00	40.16 ± 0.00
Total bkg.	11.34 ± 0.00	99.93 ± 0.01	174.29 ± 0.02	111.90 ± 0.02	569.69 ± 0.06	1318.08 ± 0.18
Signal	0.03 ± 0.00	9.92 ± 0.00	0.56 ± 0.00	0.59 ± 0.00	17.35 ± 0.00	7.71 ± 0.00
Data	16	123	168	126	614	1511
Data/Bkg.	1.41 ± 0.00	1.23 ± 0.00	0.96 ± 0.00	1.13 ± 0.00	1.08 ± 0.00	1.15 ± 0.00

Table C.8: The yields of the signals, the backgrounds and the data in the eμ control regions corresponding to the signal regions, the low-ΔR control regions and the high-ΔR control regions of the 2-lepton channel in $75 \leq p_{\mathrm{T}}^{V} < 150$ GeV.

	2-jet, 2-b-tag			3-jet, 2-b-tag		
	Low ΔR	Intermediate ΔR	High ΔR	Low ΔR	Intermediate ΔR	High ΔR
$Z + ll$	0.00 ± 0.00	0.00 ± 0.00	0.00 ± 0.00	0.00 ± 0.00	0.00 ± 0.00	0.00 ± 0.00
$Z + cl$	0.00 ± 0.00	0.00 ± 0.00	0.00 ± 0.00	0.01 ± 0.00	0.02 ± 0.00	0.02 ± 0.00
Z + hf	0.02 ± 0.00	0.88 ± 0.00	0.62 ± 0.00	0.81 ± 0.00	1.43 ± 0.00	1.44 ± 0.00
$W + ll$	0.00 ± 0.00	0.00 ± 0.00	0.00 ± 0.00	0.00 ± 0.00	0.01 ± 0.00	0.01 ± 0.00
$W + cl$	0.01 ± 0.00	0.01 ± 0.00	0.01 ± 0.00	0.01 ± 0.00	0.03 ± 0.00	0.05 ± 0.00
W + hf	0.29 ± 0.00	0.43 ± 0.00	0.42 ± 0.00	1.11 ± 0.00	2.68 ± 0.00	1.57 ± 0.00
Single top	21.05 ± 0.00	114.86 ± 0.01	80.27 ± 0.01	33.78 ± 0.00	243.22 ± 0.02	215.62 ± 0.02
$t\bar{t}$	738.01 ± 0.10	3144.21 ± 0.44	1623.44 ± 0.23	1268.90 ± 0.18	8185.60 ± 1.16	5764.05 ± 0.82
Diboson	0.05 ± 0.00	0.01 ± 0.00	0.01 ± 0.00	0.15 ± 0.00	0.22 ± 0.00	0.07 ± 0.00
Total bkg.	759.42 ± 0.11	3260.40 ± 0.45	1704.77 ± 0.24	1304.79 ± 0.18	8433.21 ± 1.18	5982.84 ± 0.83
Signal	0.00 ± 0.00	0.03 ± 0.00	0.00 ± 0.00	0.00 ± 0.00	0.03 ± 0.00	0.01 ± 0.00
Data	826	3217	1631	1346	8708	6031
Data/Bkg.	1.09 ± 0.00	0.99 ± 0.00	0.96 ± 0.00	1.03 ± 0.00	1.03 ± 0.00	1.01 ± 0.00

Table C.9: The yields of the signals, the backgrounds and the data in the eμ control regions corresponding to the signal regions, the low-ΔR control regions and the high-ΔR control regions of the 2-lepton channel in $150 \leq p_{\mathrm{T}}^{V} < 250$ GeV.

	2-jet, 2-b-tag			3-jet, 2-b-tag		
	Low ΔR	Intermediate ΔR	High ΔR	Low ΔR	Intermediate ΔR	High ΔR
$Z + ll$	–	0.00 ± 0.00	0.00 ± 0.00	0.00 ± 0.00	0.00 ± 0.00	0.00 ± 0.00
$Z + cl$	0.00 ± 0.00	0.00 ± 0.00	0.00 ± 0.00	0.00 ± 0.00	0.00 ± 0.00	0.01 ± 0.00
Z + hf	0.08 ± 0.00	0.22 ± 0.00	0.02 ± 0.00	0.08 ± 0.00	0.43 ± 0.00	0.52 ± 0.00
$W + ll$	–	0.00 ± 0.00	0.00 ± 0.00	0.00 ± 0.00	0.00 ± 0.00	0.01 ± 0.00
$W + cl$	0.00 ± 0.00	0.00 ± 0.00	0.00 ± 0.00	0.00 ± 0.00	0.01 ± 0.00	0.04 ± 0.00
W + hf	0.01 ± 0.00	0.30 ± 0.00	0.02 ± 0.00	0.17 ± 0.00	1.05 ± 0.00	0.72 ± 0.00
Single top	1.75 ± 0.00	11.30 ± 0.00	17.63 ± 0.00	4.57 ± 0.00	32.20 ± 0.00	76.14 ± 0.01
$t\bar{t}$	7.69 ± 0.00	52.58 ± 0.01	116.79 ± 0.02	59.08 ± 0.01	377.11 ± 0.05	868.48 ± 0.12
Diboson	0.00 ± 0.00	0.02 ± 0.00	0.00 ± 0.00	0.04 ± 0.00	0.07 ± 0.00	0.03 ± 0.00
Total bkg.	9.54 ± 0.00	64.42 ± 0.01	134.47 ± 0.02	63.94 ± 0.01	410.88 ± 0.06	945.95 ± 0.13
Signal	0.00 ± 0.00	0.01 ± 0.00	0.00 ± 0.00	0.00 ± 0.00	0.01 ± 0.00	0.00 ± 0.00
Data	8	52	110	53	384	930
Data/Bkg.	0.84 ± 0.00	0.81 ± 0.00	0.82 ± 0.00	0.83 ± 0.00	0.93 ± 0.00	0.98 ± 0.00

Table C.10: The yields of the signals, the backgrounds and the data in the eμ control regions corresponding to the signal regions, the low-ΔR control regions and the high-ΔR control regions of the 2-lepton channel in $p_{\mathrm{T}}^{V} \geq 250$ GeV.

	2-jet, 2-b-tag			3-jet, 2-b-tag		
	Low ΔR	Intermediate ΔR	High ΔR	Low ΔR	Intermediate ΔR	High ΔR
$Z + ll$	0.00 ± 0.00	0.00 ± 0.00	0.00 ± 0.00	0.00 ± 0.00	0.00 ± 0.00	0.00 ± 0.00
$Z + cl$	–	0.00 ± 0.00	0.00 ± 0.00	0.00 ± 0.00	0.00 ± 0.00	0.01 ± 0.00
Z + hf	0.02 ± 0.00	0.00 ± 0.00	0.06 ± 0.00	0.01 ± 0.00	0.06 ± 0.00	0.28 ± 0.00
$W + ll$	0.00 ± 0.00	0.00 ± 0.00	0.00 ± 0.00	0.00 ± 0.00	0.00 ± 0.00	0.00 ± 0.00
$W + cl$	–	0.00 ± 0.00	0.00 ± 0.00	0.00 ± 0.00	0.00 ± 0.00	0.01 ± 0.00
W + hf	–	0.00 ± 0.00	0.01 ± 0.00	0.09 ± 0.00	0.32 ± 0.00	0.42 ± 0.00
Single top	–	0.93 ± 0.00	2.41 ± 0.00	0.29 ± 0.00	2.18 ± 0.00	15.49 ± 0.00
$t\bar{t}$	0.00 ± 0.00	0.12 ± 0.00	2.69 ± 0.00	1.70 ± 0.00	17.05 ± 0.00	62.61 ± 0.01
Diboson	0.00 ± 0.00	0.00 ± 0.00	0.00 ± 0.00	0.00 ± 0.00	0.00 ± 0.00	0.00 ± 0.00
Total bkg.	0.03 ± 0.00	1.05 ± 0.00	5.16 ± 0.00	2.09 ± 0.00	19.62 ± 0.00	78.83 ± 0.01
Signal	0.00 ± 0.00	0.00 ± 0.00	0.00 ± 0.00	0.00 ± 0.00	0.00 ± 0.00	0.00 ± 0.00
Data	0	1	2	0	15	83
Data/Bkg.	–	0.95 ± 0.00	0.39 ± 0.00	–	0.76 ± 0.00	1.05 ± 0.00

D Details of the estimation of the multi-jet background in the 1-lepton channel

Multijet control regions (multijet-CRs) are defined by inverting tight isolation cuts of the SRs separately for the electron and muon sub-channels. As the result, the multijet-CR is enriched in fake leptons. The applied isolation cuts are summarized in Table D.1. The definitions of these cuts are already introduced in Sections 5.2 and 5.3, and summarized in Tables 5.2, 5.3 and 5.5. As shown in the tables, a condition ptcone20<4 GeV is applied to the muon sub-channel since the *FixedCutLoose* criterion is too loose. The 2-b-tag requirement of the SRs is replaced with 1-b-tag to increase the statistics. The m_{T}^{W} [1] distributions in the multijet-CRs for the electron and muon sub-channels are shown in Figure D.1. *Multijet templates* for any variables are obtained by subtracting the electroweak backgrounds, $t\bar{t}$ and W + jets, from the data in the multijet-CRs that correspond to the SRs. The multijet-NFs is obtained by fitting the multijet templates and the electroweak backgrounds in the SRs. For this fit, each SR is separated into two regions one of which is enriched with W + jets to estimate W + jets and $t\bar{t}$ separately.

Table D.1: Isolation criteria of the multijet control region (CR) compared to the signal region. The multijet-CR is defined by inverting the tight isolation cut used in the SR, but the loose isolation cut is kept in order not to make the cut too loose. Leptons that pass the tight isolation cut always pass the loose isolation cut. The definitions of the isolation cuts are summarized in Tables 5.3 and 5.5.

Lepton	Signal Region		Multijet-CR	
	Isolation	Detail	Isolation	Detail
Electron	Tight	FCLoose HighPtCaloOnly	Loose and not tight	FCLoose Not HighPtCaloOnly
Muon	Tight	FixedCutLoose FixedCutHighPtTrackOnly	Loose and not tight	FixedCutLoose Not FixedCutHighPtTrackOnly ptcone20<4 GeV

[1] See Section 6.6 for the definition of m_{T}^{W}.

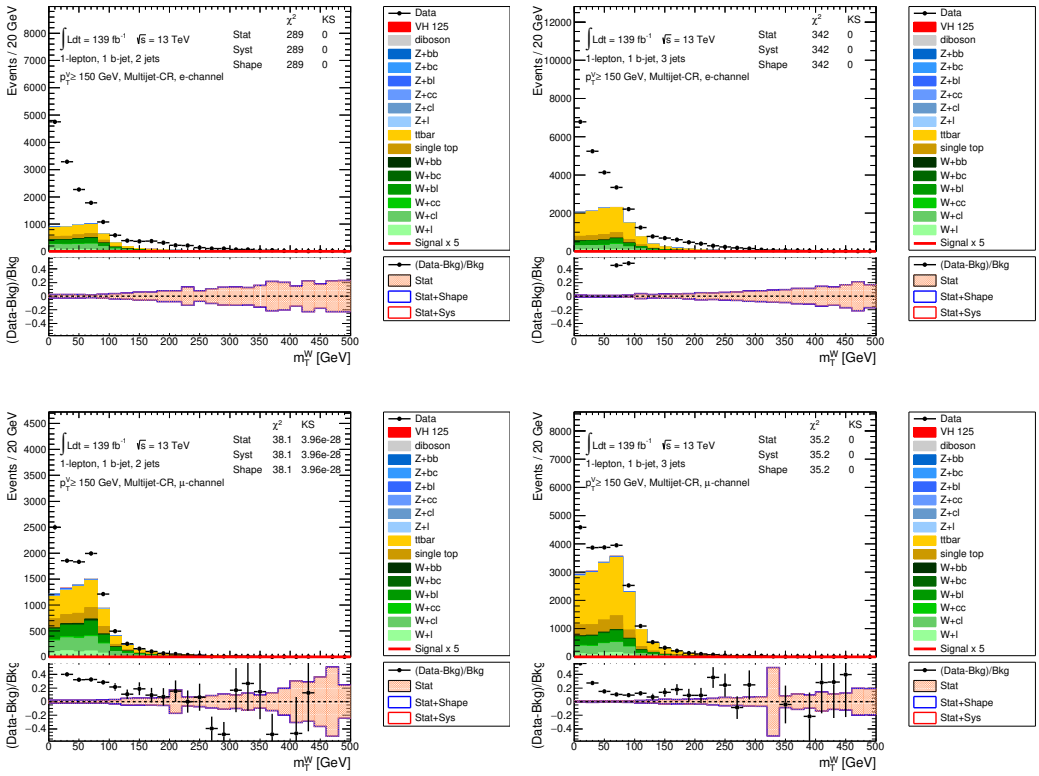

Figure D.1: m_{T}^{W} distributions in the multijet-CRs of the electron (top) and muon (bottom) sub-channels for 2-jet (left) and 3-jet (right). The event selection criteria are the same as those for the SRs with $150 \leq p_{\mathrm{T}}^{V} < 250$ GeV, except the isolation cuts shown in Table D.1 and the 1-b-tag requirement, are applied. The difference between the data (the black points) and the electroweak backgrounds, $t\bar{t}$ and W + jets (the stacked histograms), is considered as the contribution from the multijet.

E Systematic uncertainties on the *b*-tagging efficiency for *c*- and light-jets

Calibration of the *b*-tagging efficiency for *c*-jets

Calibration of the *b*-tagging efficiency for *c*-jets are presented in detail in Ref. [173], which is outlined in this section. Although the analysis employs the pseudo-continuous *b*-tagging, the calibration of the efficiency of the *b*-tagging that keeps 70% of *b*-jets (referred to as *single-cut working point* of 70% efficiency) is presented in this section since description on the calibration for the pseudo-continuous *b*-tagging is not found in references. The calibration is performed using semi-leptonic $t\bar{t}$ events, where one of the W boson decays into a lepton (electron or muon) and a neutrino and the other W boson decays into jets including *c*-jets. At least 2 jets are *b*-tagged to reduce the fraction of *b*-jets in $W \rightarrow jj$ candidates. To avoid a bias on the measurement of the *b*-tagging efficiency, more *b*-tagged jets than two are allowed. *Kinematic Likelihood Fitting* [174] is employed to enhance the fraction of *c*-jets. The efficiency of *c*-jets to be *b*-tagged is extracted by fitting $t\bar{t}$ events with 0 or 1 *b*-tagged jet in data and simulation. The derived mis-tag efficiency, and the scale factors are shown in Figure E.1. As shown in Table E.1, the uncertainties of leptons, jets, $E_{\mathrm{T}}^{\mathrm{miss}}$, and the modelling of $t\bar{t}$ and backgrounds (W + jets, Z + jets, single-top production, $t\bar{t}$ + a weak boson and fake and non-prompt leptons) are propagated. The nominal calibration requires at least two *b*-tagged jets with the *single-cut working point* of 70% efficiency, the analysis is redone with the *single-cut working point* of 60% efficiency, and the difference is taken into account as an additional uncertainty.

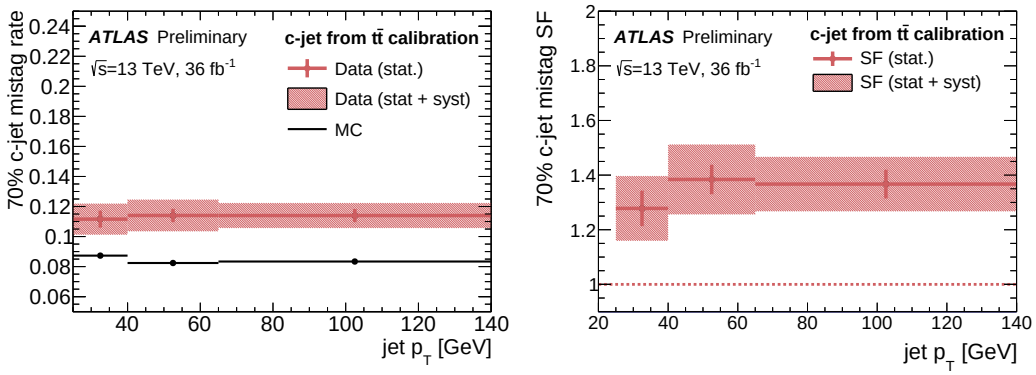

Figure E.1: Left: mis-tagging efficiency for *c*-jets with the *single-cut working point* of 70% efficiency as a function of p_{T} [173]. Right: scale factors of the mis-tagging efficiency for *c*-jets with the *single-cut working point* of 70% efficiency as a function of p_{T}. In both plots, the red bars indicate the statistical uncertainties, and the red area indicates the total uncertainties.

Table E.1: Breakdown of the contributions to the systematic uncertainty on the mis-tagging efficiency scale factors for c-jets with the *single-cut working point* of 70% efficiency [173]. The uncertainties are provided in the individual p_{T} bins.

p_{T} bin	(25 GeV,40 GeV)	(40 GeV,65 GeV)	(65 GeV,140 GeV)
MC statistics	± 1.6	± 1.5	± 1.5
Fit model non-closure	± 3.1	± 3.1	± 3.1
$t\bar{t}$ modelling	± 5.5	± 7.1	± 3.0
$t\bar{t}$+HF	± 2.5	± 1.6	± 0.1
Other backgrounds	± 0.9	± 0.6	± 0.6
Pile up	± 0.6	± 0.2	± 0.3
Jets	± 1.2	± 0.8	± 1.8
Lepton + $E_{\mathrm{T}}^{\mathrm{miss}}$	± 0.4	± 0.3	± 0.8
b-jet tagging SF	± 2.0	± 0.8	± 0.5
light-jet mistag SF	± 2.1	± 2.0	± 3.6
Systematic uncertainty	± 7.8	± 8.4	± 6.3
Statistical uncertainty	± 5.0	± 3.9	± 3.8
Total uncertainty	± 9.3	± 9.2	± 7.3

Calibration of the *b*-tagging efficiency for light-jets

The calibration of the b-tagging efficiency for light-jets is done in two ways: *negative-tagging method* and *adjusted-MC method*. While these are detailed in Ref. [175], only outline is described in this section.

The b-tagging relies on parameters such as signed impact parameters (d_0,z_0) of tracks which show asymmetric distributions around 0 due to the lifetime and the mass of b-hadrons (in other words, these parameters show positive values so that the position of the secondary vertex should be consistent with the direction of a jet). The *negative-tagging* method relies on an assumption that the mis-tagging of light-jets is caused by the finite resolution of the tracking. As such, the variables are expected to show symmetric distributions for light-jets. Thus, inverting these parameters in the b-tagging algorithm almost does not change the efficiency for light-jets. Contrary, the *negative-tagging* method shows the much lower efficiency for b- and c-jets compared to the normal b-tagging algorithm, and they are comparable with light-jets. Based on the assumption of the equal efficiency of the normal b-tagging and the negative-tagging for light-jets, and the assumption of the equal efficiency of the negative-tagging for b-, c- and light-jets, the b-tagging efficiency for light-jets can be estimated both in data and simulation by computing the negative-tag rate for jets including c- and b-jets allowing residual effects. The residual effects can arise because of two reasons: the difference of the impact parameter distributions among the jet flavors, and the real displaced vertices from long-lived particles (K_S, Λ or photon conversion) in light-jets. These residual effects are evaluated with simulation. The evaluated b-tagging efficiency and the scale factors for light-jets are shown in Figure E.2. The systematic uncertainties on the efficiency scale factors are broken down into: uncertainty on the fraction of heavy-flavor jets; uncertainty on the amount of displaced vertices in light-jets; stability against variation of the event selection used in the estimation. These contributions are summarized in Table E.2.

The adjusted-MC method takes a bottom-up approach, and give understanding on the difference between data and simulation, and a cross-check of the negative-tagging method. As hypothesized in the negative-tagging method, the mis-tagging of light-jets is caused by the finite resolution of the tracking. The resolution is worse in data than in simulation, and this results in higher efficiency of the mis-tagging rate in data. The *adjusted-MC* method adjusts the tracking performance in simulation to that of data to improve the agreement of data and simulation in certain variables before evaluating b-tagging probabilities. The

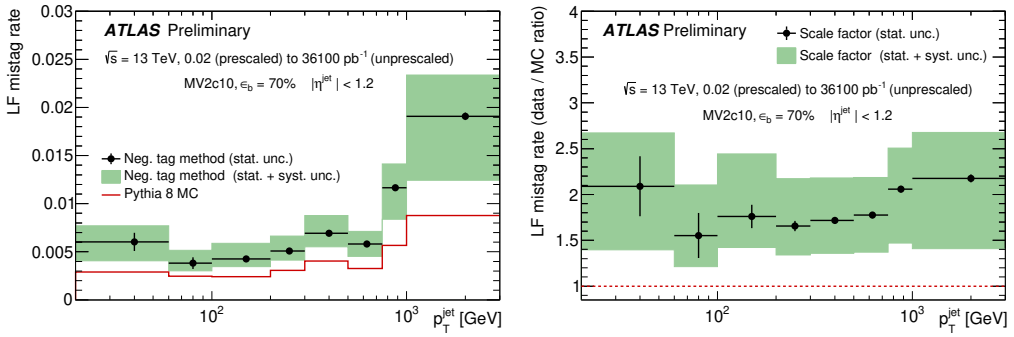

Figure E.2: Left: mis-tagging efficiency for light-jets with the *single-cut working point* of 70% efficiency as a function of p_{T} [175]. Right: scale factors of the mis-tagging efficiency for light-jets with the *single-cut working point* of 70% efficiency as a function of p_{T}. The efficiency and the scale factors derived with the *negative-tagging method* independently in the regions, $|\eta| < 1.2$ and $1.2 < |\eta| < 2.5$. The results for $|\eta| < 1.2$ are shown.

Table E.2: Breakdown of the contributions to the uncertainty on the mis-tagging efficiency for light-jets with the *single-cut working point* of 70% efficiency [175]. The uncertainties are derived in the individual p_{T} bins with the *negative-tagging* method. "cen" and "fwd" represent the central ($|\eta| < 1.2$) and forward ($1.2 < |\eta| < 2.5$) regions. "calibration" represents the uncertainties in the calibration of jets. "HF-related" represents the uncertainties on the fraction of heavy-flavor jets. "IP,fakes" represents the uncertainties on the resolution of the impact parameters and the rate of fake tracks. "vertices" represents the uncertainties on the amount of displaced vertices in due to interactions with material and strange hadrons. "sample" represents the uncertainties in parton shower modelling derived by comparing with alternative samples. "pileup" represents the uncertainties in the profile of the pileup.

$p_{\mathrm{T}}^{\mathrm{jet}}$ [GeV]	20-60		60-100		100-200		200-300		300-500		500-750		750-1000		1000-3000	
$\lvert\eta^{\mathrm{jet}}\rvert$ range	cen	fwd	cen	fwd	cen	fwd	cen	fwd	cen	fwd	cen	fwd	cen	fwd	cen	fwd
mistag (%)	0.6	0.8	0.4	0.9	0.4	0.6	0.5	0.9	0.7	0.9	0.6	0.7	1.2	1.3	1.9	2.2
data/MC	2.1	2.2	1.6	2.8	1.8	1.9	1.7	1.8	1.7	1.7	1.8	2.0	2.1	2.1	2.2	2.4
statistical uncertainties (%, relative)																
data ⊕ MC	±16	±19	±16	±18	±7	±9	±3	±5	±2	±4	±2	±4	±2	±4	±2	±6
jet uncertainties (%, relative)																
calibration	$^{+12}_{-19}$	$^{+8}_{-20}$	$^{+12}_{-2}$	$^{+11}_{-10}$	$^{+9}_{-6}$	$^{+11}_{-5}$	$^{+5}_{-2}$	$^{+4}_{-7}$	$^{+2}_{-3}$	$^{+6}_{-5}$	±2	$^{+4}_{-3}$	±3	$^{+4}_{-3}$	$^{+3}_{-2}$	$^{+3}_{-4}$
HF-related	$^{+11}_{-20}$	$^{+6}_{-17}$	$^{+9}_{-12}$	$^{+7}_{-9}$	$^{+12}_{-15}$	$^{+10}_{-16}$	$^{+12}_{-17}$	$^{+11}_{-17}$	$^{+12}_{-19}$	$^{+11}_{-15}$	$^{+12}_{-20}$	$^{+10}_{-22}$	$^{+11}_{-25}$	$^{+10}_{-31}$	$^{+10}_{-30}$	$^{+9}_{-26}$
tracking uncertainties (%, relative)																
IP, fakes	$^{+17}_{-1}$	$^{+14}_{-1}$	+27	+22	$^{+34}_{-3}$	$^{+29}_{-3}$	$^{+27}_{-4}$	$^{+25}_{-4}$	$^{+22}_{-5}$	$^{+20}_{-4}$	$^{+18}_{-9}$	$^{+15}_{-8}$	$^{+17}_{-12}$	$^{+13}_{-10}$	$^{+19}_{-18}$	$^{+16}_{-15}$
vertices	$^{+2}_{-1}$	+3	$^{+4}_{-1}$	$^{+3}_{-1}$	$^{+6}_{-3}$	$^{+4}_{-2}$	$^{+6}_{-5}$	$^{+5}_{-5}$	$^{+7}_{-5}$	±5	$^{+6}_{-5}$	±5	±5	±5	$^{+5}_{-4}$	±3
other uncertainties (%, relative)																
sample	±5	±5	±5	±5	±5	±5	±5	±5	±5	±5	±5	±5	±5	±5	±5	±5
pileup	$^{+8}_{-7}$	$^{+6}_{-13}$	$^{+0}_{-8}$	$^{+1}_{-5}$	$^{+0}_{-3}$	$^{+1}_{-7}$	+1	$^{+2}_{-1}$	+1	±1	< 1	±1	+1	$+3_{-4}$	$^{+2}_{-1}$	$^{+3}_{-2}$
total	$^{+28}_{-33}$	$^{+26}_{-36}$	$^{+36}_{-22}$	$^{+31}_{-23}$	$^{+39}_{-19}$	$^{+34}_{-21}$	$^{+31}_{-19}$	$^{+29}_{-21}$	$^{+27}_{-21}$	$^{+25}_{-18}$	±23	$^{+20}_{-24}$	$^{+22}_{-29}$	$^{+19}_{-34}$	$^{+23}_{-35}$	$^{+21}_{-32}$

difference between the adjusted b-tagging efficiency for light-jets ($\epsilon_{\mathrm{light}}^{\mathrm{adjusted\ MC}}$) and the nominal b-tagging

efficiency ($\epsilon_{\text{light}}^{\text{nominal MC}}$) provides a scale factor of the b-tagging efficiency for light-jets as

$$\text{SF}_{\text{light}} = \frac{\epsilon_{\text{light}}^{\text{adjusted MC}}}{\epsilon_{\text{light}}^{\text{nominal MC}}}. \tag{E.1}$$

The adjustment in a simulation sample includes smearing of impact parameters d_0 and z_0, an adjustment of the fraction of the tail of the IP distribution, an adjustment of the fake-track reconstruction probability, and an adjustment of the fraction of strange hadrons. The evaluated scale factors of the b-tagging efficiency agree with the result of the negative-tagging method as shown in Figure E.3. Uncertainty is considered for each adjustment above. In addition, uncertainty on the modelling of parton shower is taken into account. The contributions to the uncertainty are summarized in Table E.3.

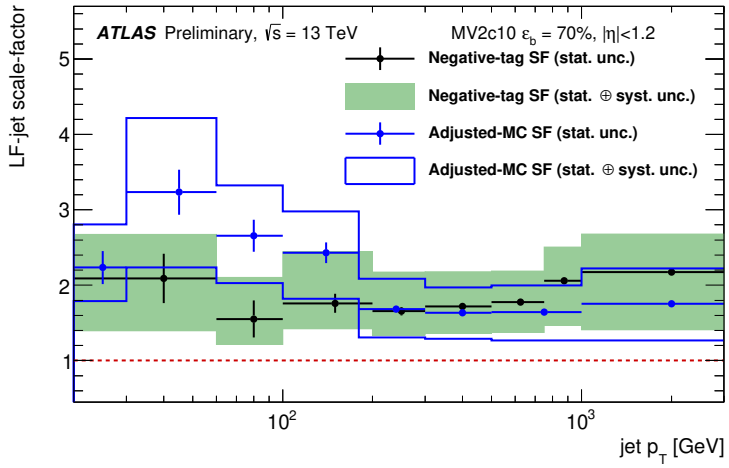

Figure E.3: Comparison of the scale factors of the mis-tagging efficiency for light-jets for the *negative-tagging method* (black points and the green area) and the *adjusted-MC method* (blue) [175]. The scale factors as functions of p_{T} are derived with the *single-cut working point* of 70% efficiency in $|\eta| < 1.2$ and $1.2 < |\eta| < 2.5$, while $|\eta| < 1.2$ is shown. In both methods, the bars indicate the statistical uncertainties and the areas indicates the total uncertainties.

Table E.3: Breakdown of the contributions to the uncertainty of the scale factors of the mis-tagging efficiency for light-jets [175]. The scale factors for the *single-cut working point* of 70% efficiency are derived with the *adjusted-MC method* in the individual p_{T} bins. "cen" represents the central region ($|\eta| < 1.2$), and "fwd" represents the forward region ($1.2 < |\eta| < 2.5$).

$p_{\text{T}}^{\text{jet}}$ [GeV]	20–30		30–60		60–100		100–180		180–300		300–500		500–1000		1000–3000	
$\lvert\eta^{\text{jet}}\rvert$ range	cen	fwd	cen	fwd	cen	fwd	cen	fwd	cen	fwd	cen	fwd	cen	fwd	cen	fwd
SF	2.2	2.1	3.2	2.2	2.7	2.3	2.4	2.0	1.7	1.5	1.6	1.5	1.6	1.6	1.8	1.7
Stat. error	0.2	0.2	0.3	0.1	0.2	0.1	0.1	0.08	0.03	0.03	0.02	0.02	0.02	0.04	0.01	0.03
Syst. error	0.5	0.5	0.9	0.5	0.6	0.4	0.5	0.4	0.4	0.3	0.3	0.3	0.4	0.4	0.5	0.5
Total error	0.5	0.6	1.0	0.5	0.7	0.4	0.5	0.4	0.4	0.3	0.3	0.3	0.4	0.4	0.5	0.5
Parton-shower (%)	2	0.1	16	5	0.3	5	12	2	10	6	10	3	3	8	3	0.7
d_0 smearing unc. (%)	6	17	13	10	17	8	10	8	12	5	9	6	9	5	9	7
z_0 smearing unc. (%)	13	7	0.6	4	4	2	5	2	7	6	5	5	4	4	3	4
Fake-track rate (%)	3	5	5	7	4	9	8	11	9	12	11	15	16	20	24	27
Strange-had. frac. (%)	8	4	9	5	7	7	7	7	6	3	4	3	4	2	2	2
Material interaction (%)	0.4	1	3	5	4	2	7	5	7	6	6	6	6	4	4	2
IP-tail variations (%)	13	18	12	14	11	8	8	8	2	0.5	1	1	0.6	2	3	3
d_0,z_0 correlation (%)	3	4	12	1	6	0.1	3	3	11	6	6	5	6	1	2	3
Total relative err. (%)	23	28	30	22	25	18	23	19	24	18	21	19	21	23	27	28

F On the elimination of the signal uncertainties in the cross-section measurement

To understand the implication of Eqs. 8.7 and 8.8, they are explained combining with Table 8.5 and 8.6 some examples below. For the measurement of WH in the $p_{\mathrm{T}}^{V} \geq 250$ GeV bin, the residual uncertainties are calculated as:

$$\delta^{a}_{\mathrm{res},i} = \frac{(\delta^{a}_{i} - \delta^{a}_{250\times400}) \times \sigma_{250\times400} + (\delta^{a}_{i} - \delta^{a}_{\geq400}) \times \sigma_{\geq400}}{\sigma_{250\times400} + \sigma_{\geq400}} \tag{F.1}$$

The residual effect of the uncertainty associated to the boundary $|y^{\mathrm{Higgs}}| = 2.5$ is:

$$\delta^{y}_{\mathrm{res},i} = 0 \ (\because \delta^{y}_{i} = \Delta^{y}/\sigma_{[0,\infty)} \text{ for } {}^{\forall}i \in \{250\times400, \geq 250\}), \tag{F.2}$$

where Δ is the uncertainty summarized in Table 8.5. Thus, this uncertainty is eliminated from the measurement. On the other hand, the residual effect of the uncertainty on the [250,400] bin and associated to the boundary $p_{\mathrm{T}}^{V} = 400$ GeV is:

$$\delta^{400}_{\mathrm{res},250\times400} = -\Delta^{400} \times \left(1 + \frac{\sigma_{\geq400}}{\sigma_{250\times400}}\right) \times \sigma^{-1}_{\geq250} \tag{F.3}$$

The effect is not fully eliminated for this uncertainty as it creates a variation of the shape in the $p_{\mathrm{T}}^{V} \geq 250$ GeV bin.

For the measurement of WH in the $150 \leq p_{\mathrm{T}}^{V} < 250$ GeV bin, the residual effect of the uncertainty associated to the boundary $p_{\mathrm{T}}^{V} = 250$ GeV are

$$\delta^{a}_{\mathrm{res},150\times250} = \frac{(\delta^{a}_{150\times250} - \delta^{a}_{150\times250}) \times \sigma_{150\times250}}{\sigma_{150\times250}} = 0 \tag{F.4}$$

This simply means that the systematic uncertainty associated to the internal p_{T}^{V} shape in the bin is neglected. If it is considered, further uncertainty is introduced. Actually, an uncertainty related to the number of jets provides finer splits in the p_{T}^{V} regions, and the uncertainty associated to the boundary acts as the leading contribution in the bin.

For the measurement of ZH in the $150 \leq p_{\mathrm{T}}^{V} < 250$ GeV bin, it is important that the overall cross-section of $qq \to ZH$ plus $gg \to ZH$ are measured but uncertainties are separately evaluated for the subprocesses. Thus, the uncertainties that can be eliminated are the merged ones that affect the overall ZH processes, and written as

$$\delta_{\text{merged-bin}} = \frac{\delta^{a}_{QQ,150\times250} \times \sigma_{QQ,150\times250} + \delta^{a}_{GG,150\times250} \times \sigma_{GG,150\times250}}{\sigma_{QQ,150\times250} + \sigma_{GG,150\times250}} \tag{F.5}$$

The general expression for the residual uncertainties becomes

$$\delta^{a}_{\mathrm{res},i} = \frac{(\delta^{a}_{i} - \delta^{a}_{QQ,150\times250}) \times \sigma_{QQ,150\times250} + (\delta^{a}_{i} - \delta^{a}_{GG,150\times250}) \times \sigma_{GG,150\times250}}{\sigma_{QQ,150\times250} + \sigma_{GG,150\times250}}. \tag{F.6}$$

The effects of the uncertainties associated to the boundary $|y^{\text{Higgs}}| = 2.5$ are

$$\delta^{QQ,y}_{\text{res},QQ,150\times250} = \frac{\delta^{QQ,y}_{QQ,150\times250} \times \sigma_{GG,150\times250}}{\sigma_{QQ,150\times250} + \sigma_{GG,150\times250}} \; (\because \delta^{QQ,y}_{GG,150\times250} = 0), \tag{F.7}$$

$$\delta^{GG,y}_{\text{res},QQ,150\times250} = \frac{\delta^{GG,y}_{QQ,150\times250} \times \sigma_{QQ,150\times250}}{\sigma_{QQ,150\times250} + \sigma_{GG,150\times250}} \; (\because \delta^{GG,y}_{QQ,150\times250} = 0). \tag{F.8}$$

Notice that even the overall uncertainties are not eliminated since they affect the fraction of the $qq \to ZH$ and $gg \to ZH$ processes.

G Details of the background modeling uncertainties

G.0.1 Top-pair ($t\bar{t}$) production

The cross-section of the $t\bar{t}$ at $\sqrt{s}$ = 13TeV is calculated at NNLO+NNLL (QCD) accuracy with top++2.0 [109, 176–181]. The cross-section is $\sigma_{t\bar{t}} = 831.76^{+40}_{-46}$ = pb. The uncertainties on PDF and α_S are derived using the PDF4LHC prescription [44] with the MSTW2008 68% CL NNLO [182, 183], CT10 NNLO [184, 185] and NNPDF2.3 5f FFN [77] PDF sets. The PDF uncertainty is ±35.06 pb, and the QCD scale variations are $^{+19.77}_{-29.20}$ pb.

Since the 0- and 1-lepton channels rely on the Monte Carlo simulation, systematic uncertainties need to be taken into account. The 2-lepton channel adopts the data-driven estimation detailed in Sections 7.2.2 and 9.2.2. Thus, no additional uncertainty needs to be considered.

The overall normalization factors for 2-jet and 3-jets regions are determined during the fit process using the control regions.

An acceptance (extrapolation) uncertainty is considered to account for the difference of the normalization factor between the 0- and 1-lepton channels. This uncertainty is evaluated by comparison of parton shower modelling (Powheg+Pythia8 vs Powheg+Herwig7), matrix element calculation (Powheg+Pythia8 vs Madgraph5_aMC@NLO+Pythia8) and radiation uncertainties (different radiation parameters in Powheg+Pythia8). The acceptance uncertainties among the p_{T}^{V} categories are covered by uncertainties on the p_{T}^{V} shape. The acceptance uncertainties among the signal regions (SRs) and the control regions (CRs) are covered by uncertainties evaluated with the BDTr method. The implementation of the uncertainties on the normalization is summarized in Table G.1.

To account for possible mismodeling of flavor compositions and difference of the acceptance among the flavor components (bb, bc, other = bl, cc, cl, ll), uncertainties of the flavor composition should be considered. The uncertainties are evaluated for according to Eqs. 8.3, and summarized in Table G.2.

Table G.1: Uncertainties on the normalization of the $t\bar{t}$ background. The overall normalization uncertainty accounts for variations of the overall cross-section and the acceptance. The rest of the uncertainties cover residual uncertainties on the difference of the normalization factors (acceptance corrections) among the categories.

	Channel	Implementation
Overall	0-/1-lepton	Floating normalization
SR, high-ΔR-CR, low-ΔR-CR acceptance	0-/1-lepton	Covered by BDTr shape uncertainties
p_{T}^{V} region acceptance	0-/1-lepton	Covered by p_{T}^{V} shape uncertainties
Extrapolation from 1-lepton to 0-lepton	0-lepton	8%

Table G.2: Flavor uncertainties associated to variations of the matrix element and the parton shower modelling in the regions. The uncertainties on the relative acceptance corrections for the bc and others (bl, cc, cl, ll) with respect to the bb component are shown.

Channel	Systematic source	2-jet		3-jet	
		bc	other	bc	other
0-lepton	Matrix Element	+8.2%	–	+7.6%	–
		–	−6.36%	–	−2.8%
	Parton Shower	−2.1%	–	−3.2%	–
		–	−13.2%	–	−5.6%
1-lepton	Matrix Element	+1.3%	–	+3.8%	–
		–	+3.3%	–	+5.7%
	Parton Shower	+7.1%	–	+1.5%	–
		–	+0.3%	–	+2.1%

To evaluate the shape uncertainties, the hybrid multidimensional parametrization is adopted. p_{T}^{V} shape uncertainties are derived by comparison to two alternative samples: PowHeg+Herwig7 for the PS/UE modelling and MadGraph5_aMC@NLO+Pythia8 for difference in matrix element. They are derived for the 0- and 1-lepton channels; 2-jet and 3-jet; flavor compositions (bb, bc, others = bl, cc, cl, ll). The difference of the p_{T}^{V} distribution among the Monte Carlo samples are shown in Table G.1. Only the largest difference derived by MadGraph5_aMC@NLO+Pythia8 is taken. After re-weighting the nominal sample by the p_{T}^{V} re-weighting function, training is performed by comparing to the same two alternative samples. They are derived for the 0- and 1-lepton channels; 2-jet and 3-jet; flavor components. Figures G.2 and G.3 show that difference in the $m_{b\bar{b}}$ and $\Delta R_{b\bar{b}}$ distributions between the samples are covered by systematic uncertainties derived with the multidimensional parametrization. As mentioned above, the p_{T}^{V} shape uncertainty covers the acceptance uncertainties among p_{T}^{V} categories, and the shape of the multidimensional parametrization cover the acceptance uncertainties among the SRs and the CRs.

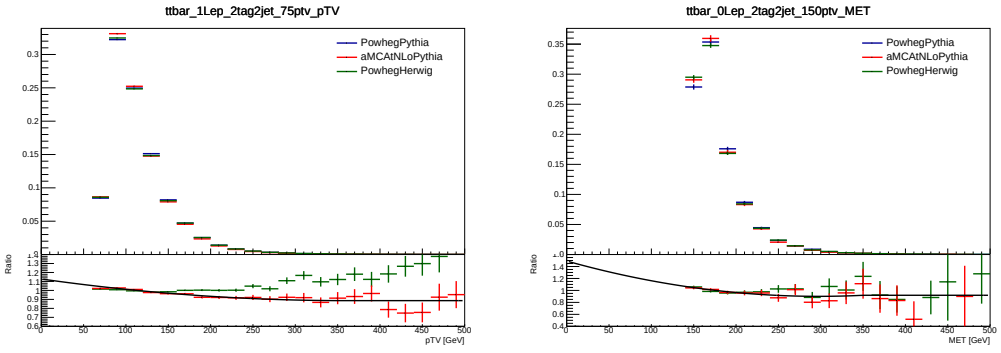

Figure G.1: p_{T}^{V} shape uncertainties in the 1-lepton channel for all flavour categories combined (bb, bc and oth.) and for 1-lepton (left) and 0-lepton (right) in the 2-jet category. The p_{T}^{V} distribution is shown in blue for PowHeg+Pythia8, in red for MadGraph5_aMC@NLO+Pythia8 and in green for PowHeg+Herwig7. The p_{T}^{V} shapes are derived from fits to the ratio between the red and blue histograms and plotted in the black curves in the bottom pane.

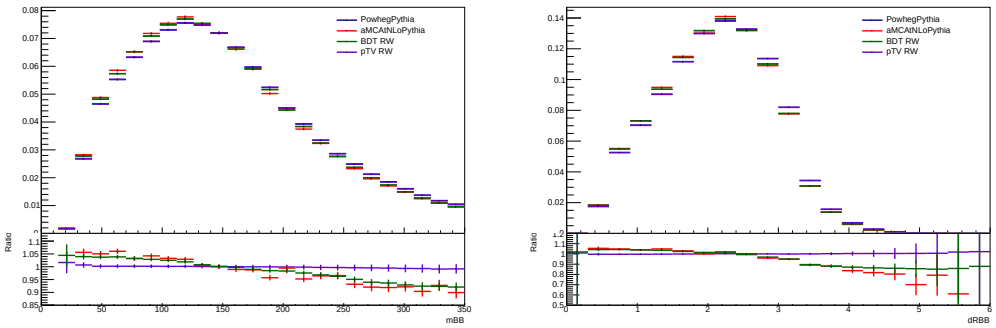

Figure G.2: The $m_{b\bar{b}}$ and $\Delta R_{b\bar{b}}$ distributions of the nominal Powheg+Pythia8 and re-weighted samples are compared to those of the Madgraph5_aMC@NLO+Pythia8 sample in the 1-lepton channel. The p_{T}^{V} distribution is shown in blue for Powheg+Pythia8 and in red for Madgraph5_aMC@NLO+Pythia8. The green graph shows Powheg+Pythia8 re-weighted by the systematic variation with the multidimensional parametrization. The purple graph shows Powheg+Pythia8 re-weighted by the systematic variation for p_{T}^{V} The green graph shows agreement with Madgraph5_aMC@NLO+Pythia8.

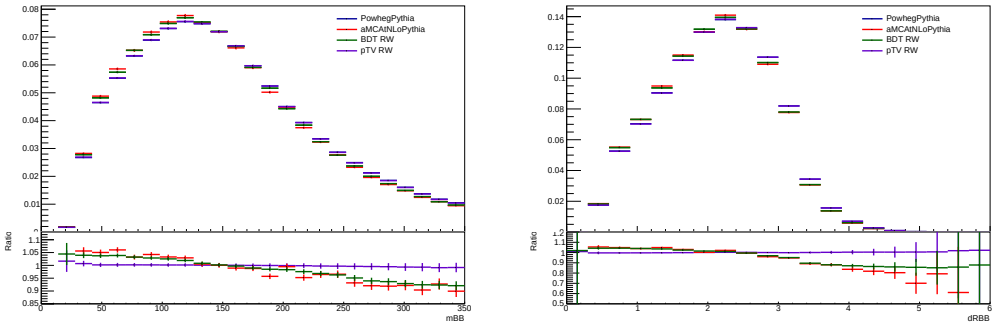

Figure G.3: The $m_{b\bar{b}}$ and $\Delta R_{b\bar{b}}$ distributions of the nominal Powheg+Pythia8 and re-weighted samples are compared to those of the Madgraph5_aMC@NLO+Pythia8 sample in the 0-lepton channel. The p_{T}^{V} distribution is shown in blue for Powheg+Pythia8 and in red for Madgraph5_aMC@NLO+Pythia8. The green graph shows Powheg+Pythia8 re-weighted by the systematic variation with the multidimensional parametrization. The purple graph shows Powheg+Pythia8 re-weighted by the systematic variation for p_{T}^{V} The green graph shows agreement with Madgraph5_aMC@NLO+Pythia8.

G.0.2 W + jets production

To cover uncertainties on the overall cross-section, floating normalization factors are used for W +heavy-flavor (bb, bc, bl, cc) jets in the 2-jet and 3-jet regions separately. The normalization uncertainties are assigned to $W + cl$ and $W + ll$. Since these backgrounds are less than 1%, the uncertainties on the overall normalization are sufficient.

Acceptance (extrapolation) uncertainties are evaluated to account for the difference of the normalization factor between 0- and 1-lepton channels. The uncertainty is derived from comparison of Sherpa and Madgraph5_aMC@NLO+Pythia8. 5% normalization uncertainty is assigned to the 0-lepton channel as shown in Table G.3. The acceptance uncertainty among p_{T}^{V} categories is covered by the p_{T}^{V} shape uncertainties. The acceptance uncertainty for the SRs and the CRs is derived by comparison of Sherpa and Madgraph5_aMC@NLO+Pythia8, scale and PDF variations.

A flavor composition uncertainty is considered to account for the uncertainty on the fraction of the bc, bl, cc components with respect to the bb component. The QCD scale variations, the PDF uncertainties, and the comparison of Sherpa vs Madgraph5_aMC@NLO+Pythia8 are considered. The difference between Sherpa and Madgraph5_aMC@NLO+Pythia8 is taken since it creates the largest variation. The sizes of the uncertainties are summarized in Table G.4.

To evaluate the shape uncertainties, the hybrid multidimensional parametrization is adopted. As explained in Section 8.2.1, the uncertainty on the p_{T}^{V} shape and the other variables are derived. Both the uncertainties are derived by comparison of Sherpa and Madgraph5_aMC@NLO+Pythia8 (both variation for the matrix element and the parton shower modelling are covered). Both uncertainties are evaluated for 2 and 3-jets and the flavor components. The p_{T}^{V} shape uncertainty is shown in the left plot of Figure G.4. This uncertainty is derived in the 1-lepton channel. Since the 0-lepton and 1-lepton channels show consisten shapes, the same shape derived in the 1-lepton channels is applied to both the 0- and 1-lepton channels. The p_{T}^{V} shape uncertainty covers the acceptance uncertainties among the p_{T}^{V} categories. The shape uncertainties from the multidimensional parametrization are derived in the 0- and 1-lepton channels individually and

Table G.3: Normalization uncertainties for the W + jets background. The overall normalization uncertainties account for variations of the overall cross-section and the overall acceptance. The rest of the uncertainties cover residual uncertainties on the difference of the normalization factors (acceptance corrections) among the categories.

Systematic uncertainty	Process	Channel	Implementation					
			low-ΔR-CR, 2-jets	SR, 2-jets	high-ΔR-CR, 2-jets	low-ΔR-CR, 3-jets	SR, 3-jets	high-ΔR-CR, 3-jets
Overall normalization	$W + ll$	0-/1-lepton	32%					
Overall normalization	$W + cl$	0-/1-lepton	37%					
Overall normalization	W + hf	0-/1-lepton	Floating normalization					
SR, high-ΔR-CR, low-ΔR-CR acceptance	W + hf	0-lepton	-7.7%	-	+14.9%	-5.6%	-	+7.0%
SR, high-ΔR-CR, low-ΔR-CR acceptance	W + hf	1-lepton	-11.5%	-	+14.8%	-3.6%	-	+5.1%
Extrapolation from 1-lepton to 0-lepton	W + hf	0-lepton	5%	5%	-	-	-	-
p_{T}^{V} region acceptance	W + hf	0-/1-lepton	Covered by p_{T}^{V} shape uncertainties					

Table G.4: Flavor composition uncertainties for the W + jets background are shown for the 0- and 1-lepton channels. The uncertainties on the bc, cl, cc components with respect to the bb component are shown.

Flavor ratio	Size	
	0-lepton	1-lepton
$W + bc/W + bb$	15%	30%
$W + bl/W + bb$	10%	30%
$W + cc/W + bb$	26%	23%

applied to the same regions where the training is done. The obtained shape uncertainties are shown in Figures G.5 and G.6. These shape uncertainties only cover the shape uncertainties in the SRs.

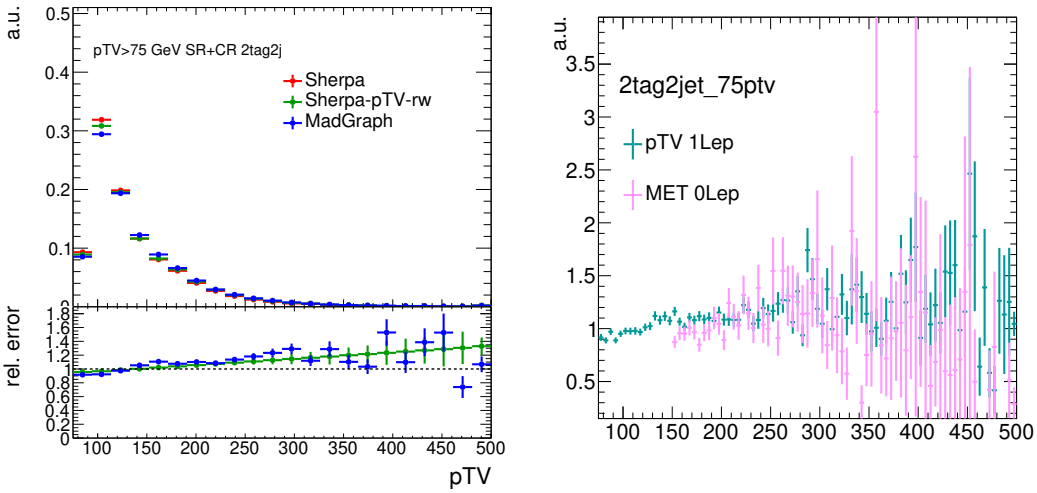

Figure G.4: The p_{T}^{V} distribution of the nominal Sherpa sample and the alternative Madgraph5_aMC@NLO+Pythia8 sample in the 2-jet region of the 1-lepton channel (left). The green histogram shows the Sherpa sample re-weighted by the p_{T}^{V} shape, and it agrees with the alternative prediction. In the right plot, the ratio of the Madgraph5_aMC@NLO+Pythia8 with respect to Sherpa is shown for 0-lepton in $E_{\mathrm{T}}^{\mathrm{miss}}$ and 1-lepton in p_{T}^{V}. The two graphs agree within the uncertainties but the error is much larger for the 0-lepton channel.

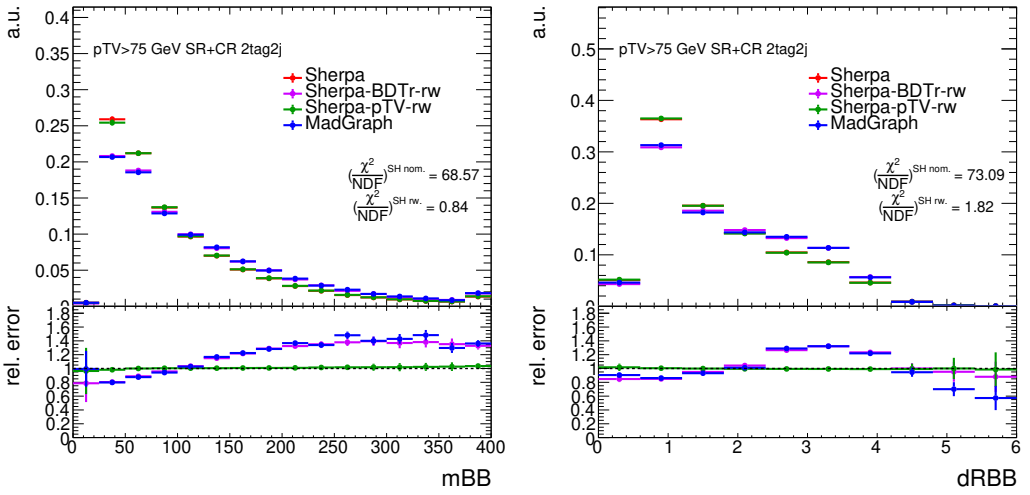

Figure G.5: The $m_{b\bar{b}}$ and $\Delta R_{b\bar{b}}$ distributions of the nominal Powheg+Pythia8 and re-weighted samples are compared to those of the Madgraph5_aMC@NLO+Pythia8 sample in the 1-lepton channel. The sample re-weighted by the p_{T}^{V}-factorized multidimensional parametrization shows agreement with Madgraph5_aMC@NLO+Pythia8.

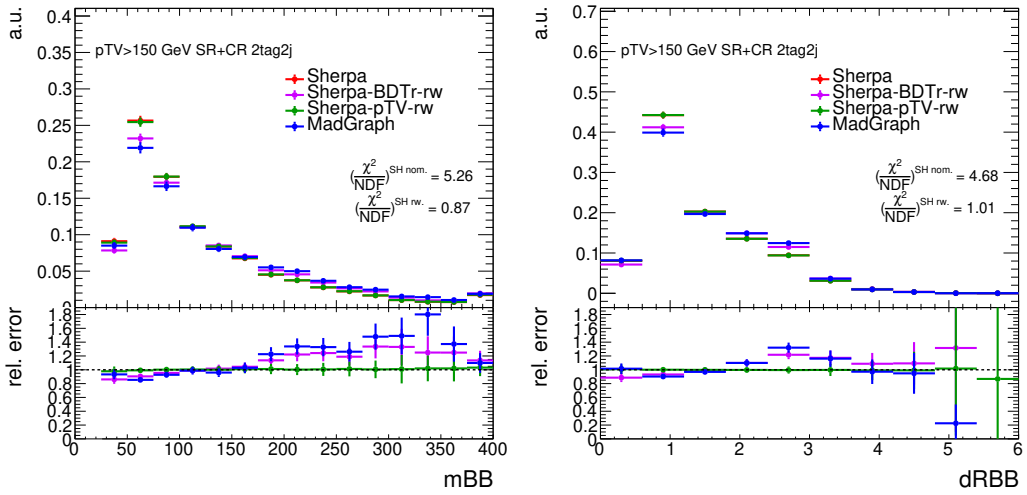

Figure G.6: The $m_{b\bar{b}}$ and $\Delta R_{b\bar{b}}$ distributions of the nominal Powheg+Pythia8 and re-weighted samples are compared to those of the Madgraph5_aMC@NLO+Pythia8 sample in the 0-lepton channel. The sample re-weighted by the p_{T}^{V}-factorized multidimensional parametrization shows agreement with Madgraph5_aMC@NLO+Pythia8.

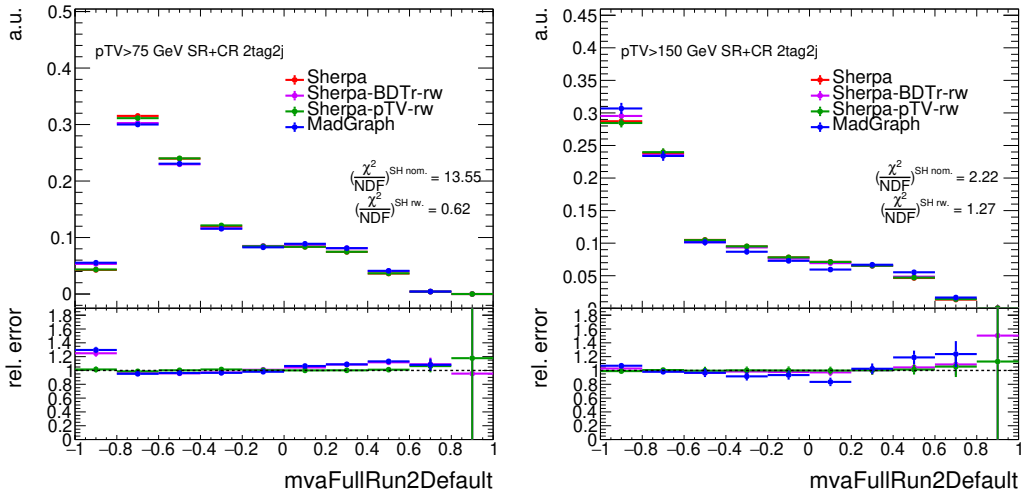

Figure G.7: The BDT distributions of the nominal Powheg+Pythia8 and re-weighted samples are compared to those of the Madgraph5_aMC@NLO+Pythia8 sample in the 1-lepton (left) and 0-lepton (right) channels. The sample re-weighted by the p_{T}^{V}-factorized multidimensional parametrization shows agreement with Madgraph5_aMC@NLO+Pythia8.

G.0.3 Z + jets production

The uncertainties on the overall cross-section are covered by the four floating normalizations in the 2-jet and 3-jet, and $p_{\mathrm{T}}^{V} < 150$ GeV and $p_{\mathrm{T}}^{V} > 150$ GeV regions. Normalization uncertainties are applied to $Z + cl$ and $Z + ll$-jets and they are sufficient due to the small contribution less than 1%.

Acceptance (extrapolation) uncertainties are taken into account to cover the uncertainty on the difference in the normalization factor between the 0- and 2-lepton channels. It is derived by comparing Sherpa and MadGraph5_aMC@NLO+Pythia8, and internal variations in Sherpa. 7% normalization uncertainty is applied in the 0-lepton channel. The acceptance uncertainties across the SRs and the CRs are evaluated with the internal variations within Sherpa and summarized in Table G.5. These MC-based uncertainties are treated independently in $p_{\mathrm{T}}^{V} < 150$ GeV and $p_{\mathrm{T}}^{V} > 150$ GeV in the fit.

Flavor composition uncertainties are considered to account for the uncertainties on the relative normalization of bc, cl, cc with respect to bb. The uncertainties are dominated by comparison of Sherpa and MadGraph5_aMC@NLO+Pythia8. The sizes of the uncertainties are summarized in Table G.6.

To evaluate the shape uncertainties, the one-dimensional parametrization described in Section 8.2.1 is adopted. Since the top backgrounds ($t\bar{t}$ and single-top productions) in the 2-lepton channel is estimated by the data-driven method, the Z + jets process is the single component background of the 2-lepton channel. Thus, data-driven evaluation of shape uncertainties of Z + jets is available using the data in the side-band region of the $m_{b\bar{b}}$ as described below. Difference in the p_{T}^{V} and $m_{b\bar{b}}$ shapes between the data and the nominal Sherpa are evaluated after subtraction of the data templates in eμ control regions (data-driven top background) and the non-Z + jets MC templates (diboson and W + jets) from the data templates in the SRs. This comparison is performed after removing the events within the mass window 80 GeV $< m_{b\bar{b}} <$ 140 GeV to avoid using any information of data sensitive to the signal. The evaluation of the shape uncertainties are performed using events in the SRs and the CRs; 2-jet and 2-jet; $p_{\mathrm{T}}^{V} > 75$ GeV.

Table G.5: Normalization uncertainties for the Z + jets background. The overall uncertainties account for variation of the overall cross-section and the overall acceptance. the rest of the uncertainties cover residual uncertainties on the difference of the normalization factors (acceptance corrections) among the categories.

Systematic uncertainty	Process	Channel	Implementation					
			low-ΔR-CR, 2-jets	SR, 2-jets	high-ΔR-CR, 2-jets	low-ΔR-CR, 3-jets	SR, 3-jets	high-ΔR-CR, 3-jets
Overall normalization	$Z + ll$	0-/2-lepton	18%					
Overall normalization	$Z + cl$	0-/2-lepton	23%					
Overall normalization	Z + hf	0-/2-lepton	Floating normalization					
SR, low-ΔR-CR acceptance	Z + hf	0-lepton	-6.0%	-	-	-6.6%	-	-
SR, low-ΔR-CR acceptance	Z + hf	2-lepton	-9.9%	-	-	-3.8%	-	-
SR, high-ΔR-CR acceptance	Z + hf	0-lepton	-	-	+3.8%	-	-	+3.9%
SR, high-ΔR-CR acceptance	Z + hf	2-lepton	-	-	+2.7%	-	-	+4.1%
Extrapolation from 2-lepton to 0-lepton	Z + hf	0-lepton	7%					
p_{T}^{V} region acceptance	Z + hf	0-/1-lepton	Covered by p_{T}^{V} shape uncertainties					

Table G.6: Flavor composition uncertainties of the Z + jets background are shown for the o- and 2-lepton channels. The uncertainties on the bc, cl, cc components with respect to the bb component are shown.

Flavor ratio	Size		
	0-lepton	2-lepton, 2-jets	2-lepton, $\geq$ 3-jets
$Z + bc/Z \to b\bar{b}$	40%	40%	30%
$Z + bl/Z \to b\bar{b}$	25%	28%	20%
$Z + cc/Z \to b\bar{b}$	15%	16%	13%

Re-weighted functions are derived so that the nominal sample reproduces the distributions of the data. The difference of the nominal MC sample and the data, and the derived weighted functions are shown in Figures G.8 and G.9. Determined functional forms are $-0.197\log_{10}(p_{\mathrm{T}}^{V}/50) + 1.06$ and $0.936 + 0.000481 m_{b\bar{b}}$, where p_{T}^{V} and $m_{b\bar{b}}$ are defined in GeV. The p_{T}^{V} shape variation covers the acceptance uncertainty across the p_{T}^{V} regions. On the other hand, instead of the $m_{b\bar{b}}$ shape variation, the acceptance uncertainties across the SRs and the CRs are covered by the MC driven acceptance uncertainties mentioned above. Thus, the data-driven $m_{b\bar{b}}$ shape uncertainty only acts in the SRs. The uncertainties on the $m_{b\bar{b}}$ and p_{T}^{V} shapes and acceptance uncertainties across the SRs and the CRs are treated independently in $p_{\mathrm{T}}^{V} < 150$ GeV and $p_{\mathrm{T}}^{V} > 150$ GeV in the fit.

G.0.4 Diboson production

The diboson samples are normalized to the cross-sections of the generators (Sherpa 2.2.1), which provides a calculation at NLO (for 0,1 extra partons) and LO (for ≥ 2 extra partons). The uncertainties on the overall cross-sections are derived by variations of the renormalization and factorization scales within Sherpa and comparison of Sherpa and Powheg+Pythia8. These uncertainties are same as in Ref. [186], and the sizes of the uncertainties are 25%, 26% and 20% for WW, WZ and ZZ, respectively. They are summarized in Table G.7.

Unlike the dominant backgrounds where the correction of the overall acceptance is absorbed by the floating normalization.

As described above, it is necessary to take into account uncertainties that changes the overall acceptance (normalization) because the overall cross-sections are constrained to the predictions. Sherpa and Powheg+Pythia8 are compared to evaluate the uncertainties. Powheg+Pythia8 and Powheg+Herwig++ are also compared as the PS/UE uncertainty.

Other acceptance (extrapolation) uncertainties are evaluated to account for differences among the categories (the SRs and the CRs; 2-jet and 3-jet). The uncertainties are derived by scale variations in Sherpa (exploiting Stewart-Tackman method [148]) and comparison of Powheg+Pythia8 and Powheg+Herwig7. The extrapolation uncertainties across the lepton channels are evaluated by comparison of Sherpa and Powheg+Pythia8. The uncertainties have sizes of 11% for the extrapolation of WZ from the 1-lepton to the 0-lepton channel, and 6% for the extrapolation of ZZ from the 2-lepton to the 0-lepton channel. The numbers are summarized in Table G.8.

To evaluate the shape uncertainties, the one-dimensional parametrization is adopted for the $m_{b\bar{b}}$ and p_{T}^{V} shapes. The same systematic sources are considered as the overall acceptance uncertainties.

G.0.5 Single top production

The t, s-channels are normalized to the NLO calculation while the Wt sample is normalized to the NNLO calculation. To evaluate the uncertainties on the overall cross-sections, variations of the renormalization

Table G.7: Uncertainties on the overall cross-sections of the diboson processes, WW, WZ and ZZ.

Systematic uncertainty	WW	WZ	ZZ
Overall normalization	25%	26%	20%

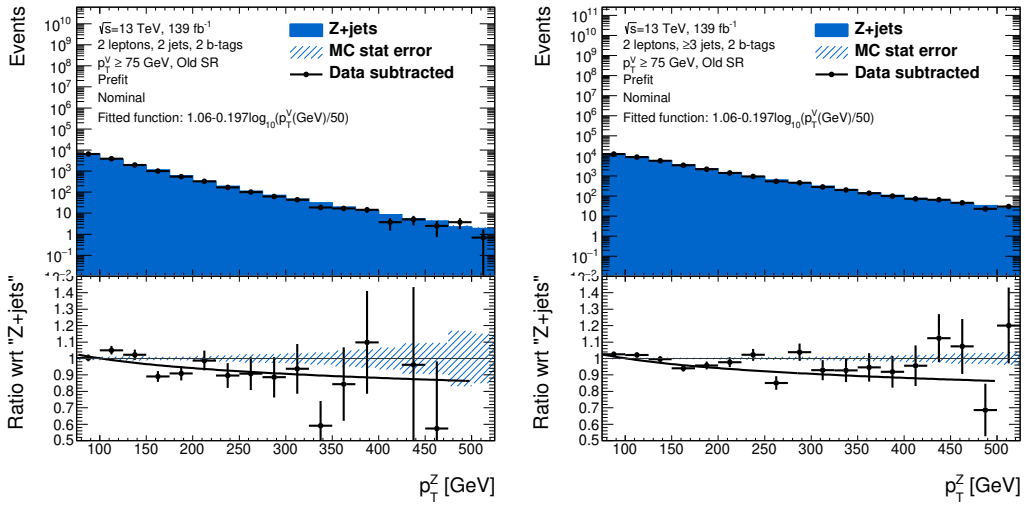

(a) 2-jet

(b) ≥3-jet

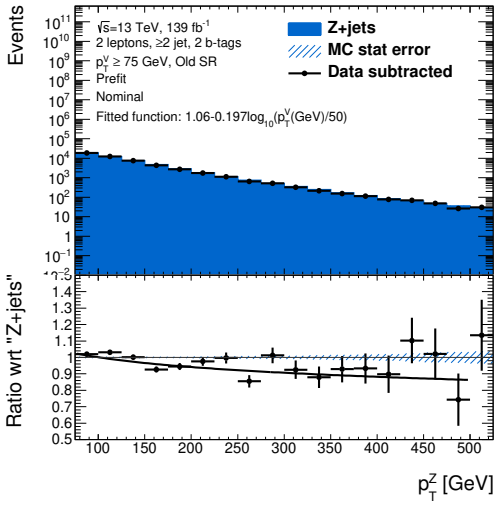

(c) ≥2-jet

Figure G.8: Comparison of the SHERPA sample and the data after the subtraction of the data from the eμ control region and the non-Z + jets MC backgrounds in the p_{T}^{V} distributions. The black curves in the bottom panes represent a function fitted to the ratio in the ≥2-jet region, and defines the p_{T}^{V} shape uncertainty. The analytic expression is $-0.197\log_{10}(p_{\mathrm{T}}^{V}(\text{ GeV})/50) + 1.06$ as also indicated in the plots.

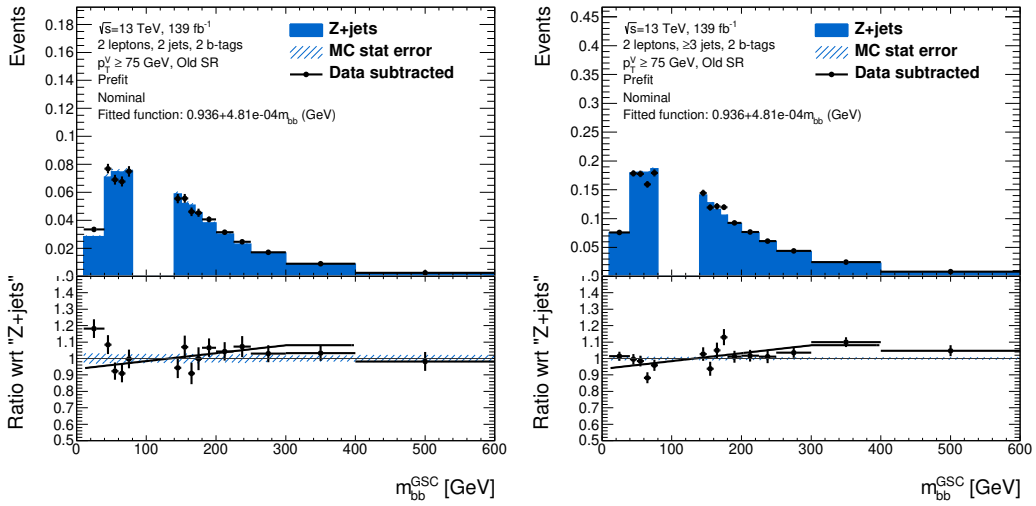

(a) 2-jet

(b) ≥3-jet

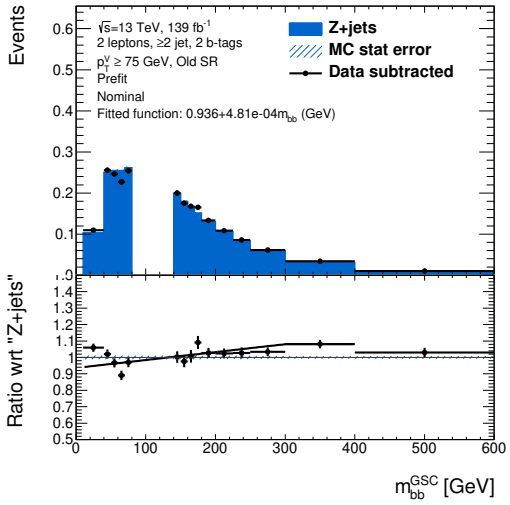

(c) ≥2-jet

Figure G.9: Comparison of the SHERPA sample and the data after the subtraction of the data from the eμ control region and the non-Z + jets MC backgrounds in the $m_{b\bar{b}}$ distributions. The black curves in the bottom panes represent a function fitted to the ratio in the ≥2-jet region, and defines the $m_{b\bar{b}}$ shape uncertainty. The analytic expression is $0.936 + 0.000481 m_{b\bar{b}}$ as also indicated in the plots.

Table G.8: Acceptance uncertainties on the diboson processes. The overall (relative) uncertainties account for the uncertainties on the overall (relative) acceptance corrections. The extrapolation uncertainties account for the relative normalization between the indicated channels. The extrapolation uncertainties consider all the sources of the uncertainties described for the diboson backgrounds except the scale uncertainty on the ZZ production. The Scale uncertainty on the ZZ process is covered by the uncertainty associated to the ≥4-jet veto listed in Table G.8.

Systematic source	Acceptance	$ZZ \to \nu\bar{\nu}b\bar{b}$		$WZ \to \ell\nu b\bar{b}$		$ZZ \to \ell^+\ell^- b\bar{b}$	
		2-jets	3-jets	2-jets	3-jets	2-jets	≥3-jets
UE/PS	Overall acceptance	5.6%	5.6%	3.9%	3.9%	5.8%	5.8%
	Relative acceptance for 2-jets and 3-jets	-	7.3%	-	10.8%	-	3.1%
QCD scale	Acceptance of 2-jet	10.3%	-	12.7%	-	11.9%	-
	Acceptance of 3-jets	-15.7%	+17.4%	-17.7%	+21.2%	-16.4%	+10.1%
	≥ 4-jets veto	-	+18.2%	-	+19.0%	-	-
All sources	Extrapolation from 1-lepton to 0-lepton	11%	11%	-	-	-	-
	Extrapolation from 2-lepton to 0-lepton	6%	6%	-	-	-	-

and factorization scales, α_S and PDF are derived as in Ref. [186]. As summarized in Table G.9, the uncertainties are 4.4%, 4.6% and 6.2% for the t-, s- and Wt-channels, respectively.

Acceptance uncertainties are defined as the sums in quadrature of comparison of the diagram subtraction and diagram removal in Powheg+Pythia6, comparison of Powheg+Pythia6 and Madgraph5_aMC@NLO+Herwig++, comparison of Powheg+Pythia6 and Powheg+Herwig++, and radiation variation in Powheg+Pythia6. The uncertainties explain either the overall acceptance or the relative acceptances. As summarized in Table G.10, these uncertainties are evaluated separately in the 2- and 3-jet regions, and for the flavor combination (bb or others).

To evaluate the shape uncertainties, the one-dimensional parametrization is adopted for $m_{b\bar{b}}$ and p_{T}^{V}. The uncertainties are defined as the largest variations among: comparison of diagram subtraction and diagram removal in Powheg+Pythia6, comparison of Powheg+Pythia6 and Madgraph5_aMC@NLO+Herwig++, comparison of Powheg+Pythia6 and Powheg+Herwig++, and radiation variation in Powheg+Pythia6. The chosen sources for the Wt- and t-channel are summarized in Table G.12.

Table G.9: Uncertainties on the overall cross-sections for the single-top production in the Wt-, t- and s-channels.

Wt-channel	t-channel	s-channel
6.2%	4.4%	4.6%

Table G.10: Acceptance uncertainties for the single top Wt-channel. The uncertainties cover both the overall acceptance correction and the relative acceptance corrections.

Systematic uncertainties	$Wt \to b\bar{b}$		$Wt \to$ oth.	
	2-jets	3-jets	2-jets	3-jets
Diagram subtraction vs diagram removal	-49.1%	-44.4 %	+0.4%	-2.2%
Powheg+Pythia6 (RadLo)	-4.2%	-4.6 %	+6.0%	+0.3%
Powheg+Pythia6 (RadHi)	+9.8%	+1.6 %	-5.2%	+1.1%
Powheg+Herwig++	-10.9%	-16.3 %	-20.1%	-17.0%
Madgraph5_aMC@NLO+Herwig++	-19.3%	+17.6 %	+10.7%	+12.4%
Total	54.9%	50.7%	24.1%	21.2%

Table G.11: Acceptance uncertainties for the single top t-channel. The uncertainties cover both the overall acceptance correction and the relative acceptance corrections.

Systematic uncertainty	2-jets	3-jets
PowHeg+Pythia6 (RadLo)	+0.7 %	+2.1 %
PowHeg+Pythia6 (RadHi)	+0.5 %	-3.8 %
PowHeg+Herwig7 (PH7)	-10.6 %	-19.2 %
Madgraph5_aMC@NLO+Herwig++ (aMC)	+13.1 %	+3.2 %
Total	16.8%	19.9%

Table G.12: Summary of the shape uncertainties on the indicated variables for the single top productions in Wt- and t-channels.

Process	Variable	Source
Wt channel, $Wt \to b\bar{b}$	p_{T}^{V}	PowHeg+Pythia6 with diagram subtraction
	$m_{b\bar{b}}$	PowHeg+Pythia6 with diagram subtraction
	m_{top}	PowHeg+Pythia6 with diagram subtraction
Wt channel, $Wt \to$ oth.	p_{T}^{V}	PowHeg+Pythia6 with diagram subtraction
	$m_{b\bar{b}}$	PowHeg+Herwig++
	m_{top}	PowHeg+Pythia6 with diagram subtraction
t-channel	p_{T}^{V}	PowHeg+Herwig++
	$m_{b\bar{b}}$	PowHeg+Pythia6 |radHi-radLo|

H Fundamentals of likelihood ratio tests

The mathematical foundation of the compatibility test is so-called likelihood-ratio test. This test is approximated to the chi-squared test when a considered sample is large.

The probability density function (PDF) is given as $f(x;\alpha,\theta)$, where x is a variable that can be a vectorial quantity, and $\alpha = \{\alpha_i\}_{i=1,\cdots,k}$ and $\theta = \{\theta_i\}_{i=1,\cdots,\ell}$ are sets of quantities that parametrize the PDF. When data points $\{x\} = \{x_i\}_{i=1,\cdots,n}$ are observed, the likelihood is defined as

$$\mathcal{L}(\{x\}|\alpha,\theta) = \prod_{i=1}^{n} f(x_i|\alpha,\theta). \tag{H.1}$$

The null hypothesis is represented by the constraint such as $\alpha = \alpha_0$, and an alternative hypothesis is represented by removing the constraint.

A test statistic is defined as[1]:

$$q_\alpha = -\ln \frac{\mathcal{L}(\{x\}|\alpha,\hat{\hat{\theta}}_\alpha)}{\mathcal{L}(\{x\}|\hat{\alpha},\hat{\theta})}, \tag{H.2}$$

where $\hat{\alpha}$ and $\hat{\theta}$ are the values that minimize the likelihood $\mathcal{L}(\{x\}|\alpha,\theta)$ without the constraints on α, while $\hat{\hat{\theta}}_\alpha$ are the values that minimize the likelihood under constraints on α. An important feature of the test statistic is that $2q_\alpha$ distributes like the χ^2 distribution with k degree of freedom, where k is the degree of freedom of the α parameters, when toy datasets are taken from an ensemble [156, 187].

The χ^2-distribution with a variable x and k degree of freedom has a probability density as

$$f(x;k) = \frac{x^{k/2-1}e^{-x/2}}{2^{k/2}\Gamma(k/2)}. \tag{H.3}$$

The probability of x to be greater than x_0 is given by

$$\int_{x_0}^{\infty} \frac{x^{k/2-1}e^{-x/2}}{2^{k/2}\Gamma(k/2)}dx = \frac{1}{\Gamma(k/2)}\int_{x_0/2}^{\infty} t^{k/2-1}e^{-t}dt = \frac{\Gamma(k/2,x_0/2)}{\Gamma(k/2)} \tag{H.4}$$

Now, the compatibility of the observation to a null hypothesis (represented by α_0) is defined as the probability that a larger fluctuation of the test statistic q_α is observed, and the probability is computed by substituting $x_0 = 2q_\alpha$ as

$$\text{Compatibility} = \frac{\Gamma(k/2,q_{\alpha_0})}{\Gamma(k/2)}, \tag{H.5}$$

where k represents the difference in the degree of freedom of the null hypothesis and an alternative hypothesis. This can be computed in the ROOT framework as

$$\text{Compatibility} = \text{TMath::Prob}(k, 2q_{\alpha_0}). \tag{H.6}$$

[1] The test statistic is often defined as $-2\ln\frac{\mathcal{L}(\{x\}|\alpha,\hat{\hat{\theta}}_\alpha)}{\mathcal{L}(\{x\}|\hat{\alpha},\hat{\theta})}$, but the consistent notation with Chapter 9 is used in this appendix.

In the special case that α has only 1 degree of freedom, the probability of a variable x to be greater than x_0 is given by

$$\frac{\Gamma(1/2, x_0/2)}{\Gamma(1/2)} = \frac{1}{\sqrt{\pi}} \int_{x_0}^{\infty} \frac{x^{1/2-1} e^{-x/2}}{2^{1/2}} dx = 2/\sqrt{\pi} \int_{\sqrt{x_0/2}}^{\infty} e^{-t^2} dt = \text{erfc}(\sqrt{x_0/2}). \tag{H.7}$$

The compatibility of the observation to a null hypothesis (represented by α_0) is computed as

$$\text{Compatibility} = \text{erfc}(\sqrt{q_{\alpha_0}}), \tag{H.8}$$

where erfc is the error function. This can be computed in the ROOT framework as

$$\text{Compatibility} = \text{TMath::Erfc}(\sqrt{q_{\alpha_0}}). \tag{H.9}$$

If α distributes like a normal distribution around the null hypothesis α_0, $q_{\alpha_0} > x_0$ is realized when $|\alpha - \alpha_0| >$ Confidence Interval. If the probability of the maximum likelihood estimate α to be greater than $\bar{\alpha}$ that gives $q_{\bar{\alpha}} = x_0$ is desired, one should compute $\text{erfc}(\sqrt{q_{\alpha_0}})/2$. This has a particular importance when one discusses the significance of an excess.

I Unblinded results detailes

I.1 The VH analysis with the multivariate analysis

Unblinded distributions

The unblinded distributions of the BDT_{VH} in the $75 \leq p_{\mathrm{T}}^{V} < 150$ GeV categories of the 2-lepton channel and ($\geq$)3 jets categories are shown in Figure I.1 and I.2.

Compatibility tests

The dependence of μ on p_{T}^{V} and the number of jets is studied in each lepton channel. Note that the 0-, 1-, 2-lepton, the number of jets, and p_{T}^{V} indicate just the number of the selected leptons and jets.

The test is based on the fact that the ratio of the log-likelihoods of a null-hypothesis and an alternative hypothesis obeys the chi-square distribution of the additional degree of freedom of the alternative hypothesis as discussed in Appendix H. The results of the test are shown in Table I.1.

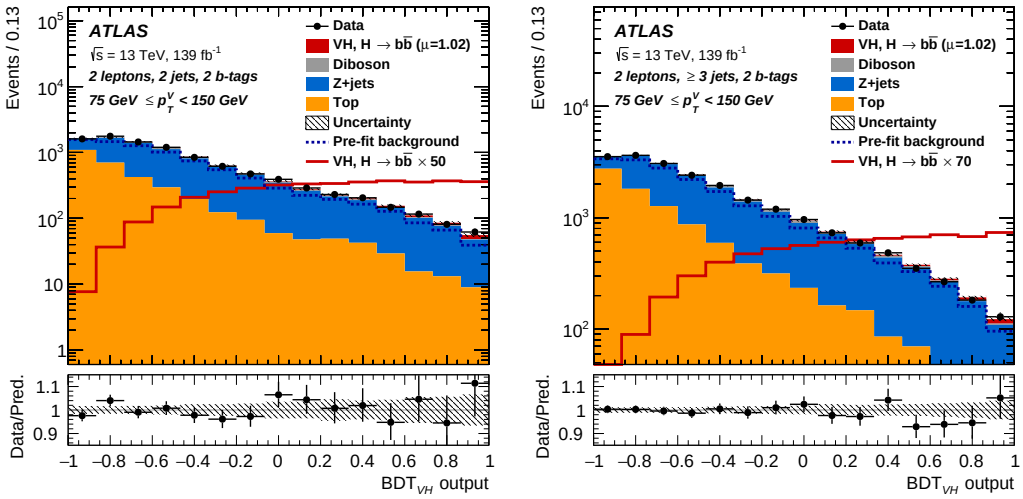

Figure I.1: Distributions of the BDT_{VH} scores in the categories with 2, $\geq$ 3 jets and $75 \leq p_{\mathrm{T}}^{V} < 150$ GeV of the 2-lepton channel. The stacked histograms show the prediction after the fitting. The red unstacked and unfilled histograms show the VH signals with the scale factors indicated in the legend. The lower panels show the ratio of the data and the prediction of the signals and the backgrounds. The hatched bands in the lower and upper panels show the total uncertainty that includes both the statistical and systematic uncertainties.

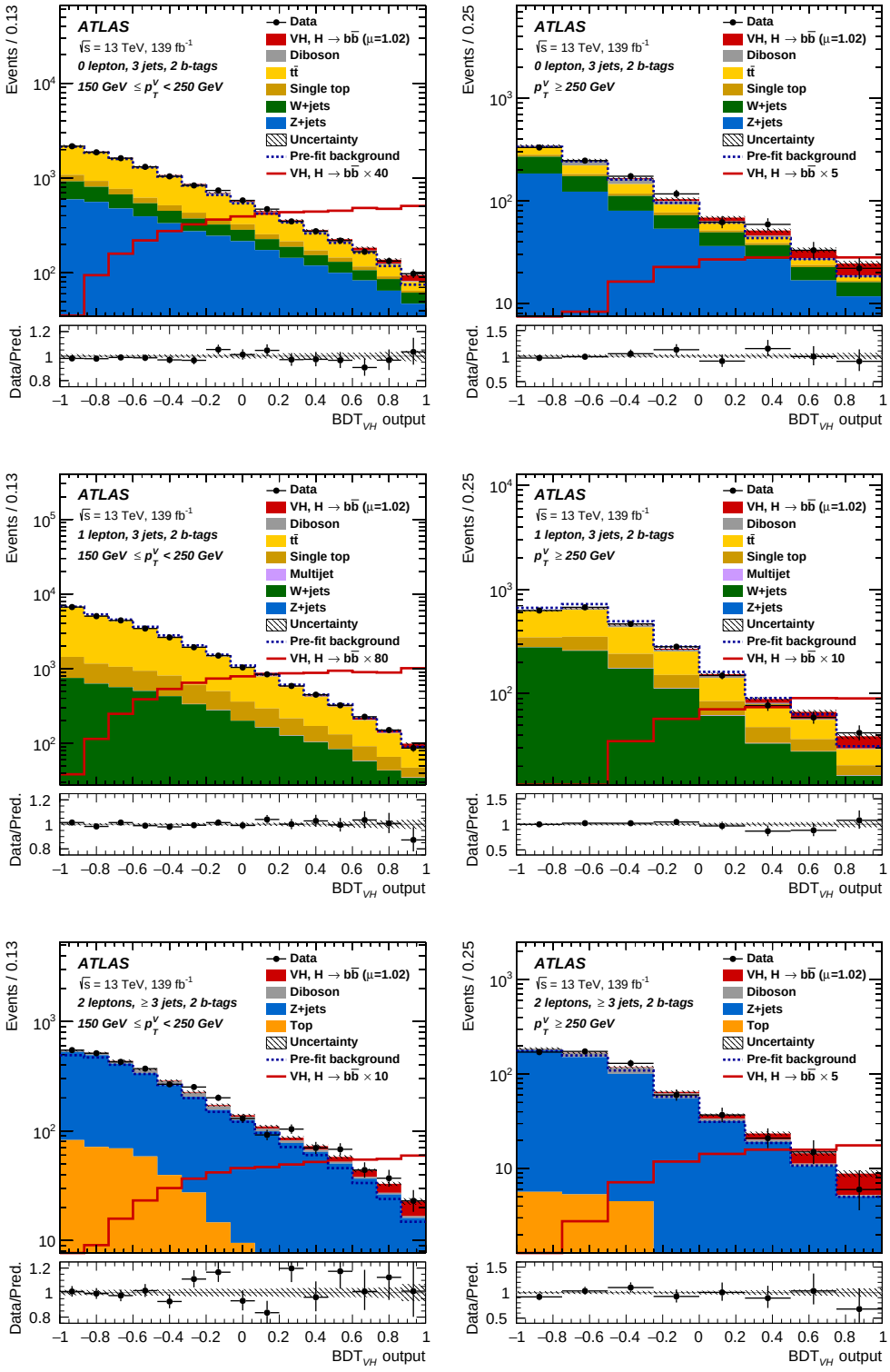

Figure I.2: The distributions of the BDT_{VH} scores in the categories with 3 or $\geq$ 3 jets and $150 \leq p_{\mathrm{T}}^{V} < 250$ GeV, $p_{\mathrm{T}}^{V} \geq 250$ GeV of the 0-,1- and 2-lepton channels. The stacked histograms show the prediction after the fitting. The red unstacked and unfilled histograms show the VH signals with the scale factors indicated in the legend. The lower panels show the ratio of the data and the prediction of the signals and the backgrounds. The hatched bands in the lower and upper panels show the total uncertainty that includes both the statistical and systematic uncertainties.

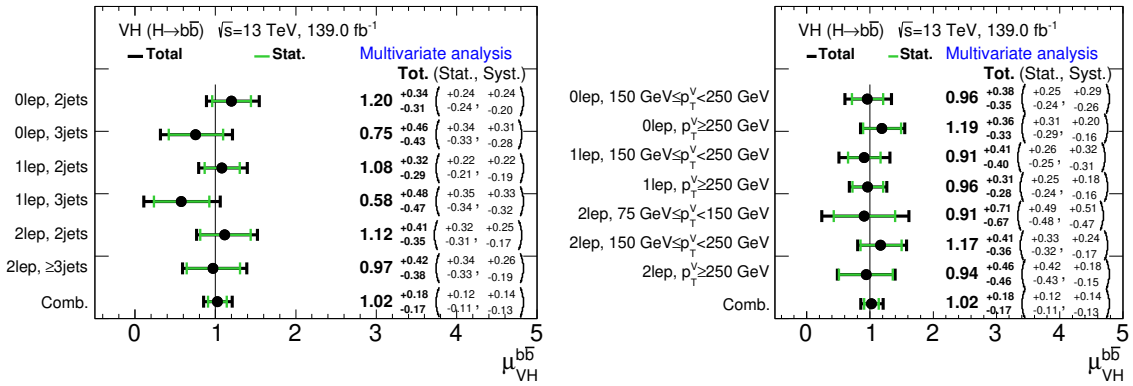

Figure I.3: Observed signal strengths μ_{VH}^{bb} of the VH processes in the categories with the number of jets and p_{T}^{V}. The μ_{VH}^{bb} values for the categories are obtained from the simultaneous fits with the individual signal strengths for these regions. The combined μ_{VH}^{bb} is obtained from the fit with the single signal strength for both of the signals.

Table I.1: Summary of the compatibility of the VH fits using BDT_{VH} when the indicated null hypotheses and the alternative hypotheses are given.

Null hypothesis	Alternative hypothesis	Compatiblility
Combined fit	Fit separated into WH&ZH	71%
Combined fit	Fit separated with the numbers of leptons and jets	90%
Combined fit	Fit separated with the numbers of leptons and p_{T}^{V}	99%
SM prediction	Fit separated into WH&ZH	93%
SM prediction	Fit separated with the numbers of leptons and jets	95%
SM prediction	Fit separated with the numbers of leptons and p_{T}^{V}	99%
SM prediction	Combined fit	89%

I.2 The VH analysis with the dijet mass distribution

Unblinded distributions

Compatibility tests

The dependence of μ on p_{T}^{V} and the number of jets is studied in each lepton channel. The signal strengths in the separated analysis regions are shown in Figure I.6. They show consistent results within their uncertainties. Note that 0-, 1-, 2-lepton, the number of jets and p_{T}^{V} indicate the number of the selected leptons and jets; the transverse momentum of the vector boson, and they are not quantities unfolded to any categories based on truth information. The compatibility test is performed to estimate the quantitative consistency among the categories, and the consistency of the measurement with the Standard Model prediction. The results of the compatibility tests are shown in Table I.2.

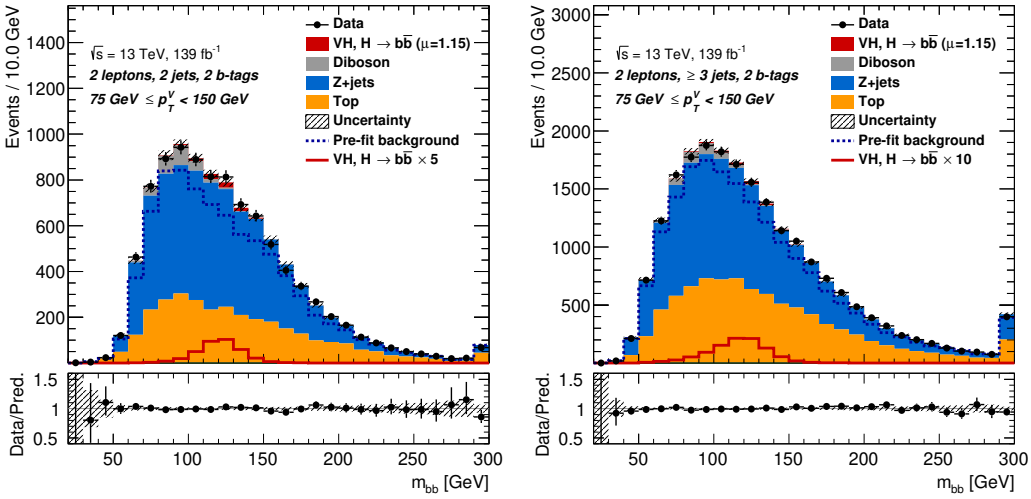

Figure I.4: The distributions of the $m_{b\bar{b}}$ in the categories with 2, $\geq$ 3 jets and 75 $\leq p_{\mathrm{T}}^{V} <$ 150 GeV of the 2-lepton channel. The stacked histograms show the prediction after the fitting. The red unstacked and unfilled histograms show the VH signals with the scale factors indicated in the legend. The lower panels show the ratio of the data and the prediction of the signals and the backgrounds. The hatched bands in the lower and upper panels show the total uncertainty that includes both the statistical and systematic uncertainties.

Table I.2: Summary of the compatibility of the VH fits using the $m_{b\bar{b}}$ distribution when the indicated null hypotheses and the alternative hypotheses are given.

Null hypothesis	Alternative hypothesis	Compatiblility
Combined fit	Fit separated with the number of leptons	78%
Combined fit	Fit separated with the numbers of leptons and jets	73%
Combined fit	Fit separated with the numbers of leptons and p_{T}^{V}	99%
SM prediction	Fit separated with the number of leptons	87%
SM prediction	Fit separated with the numbers of leptons and jets	80%
SM prediction	Fit separated with the numbers of leptons and p_{T}^{V}	99%
SM prediction	Combined fit	47%

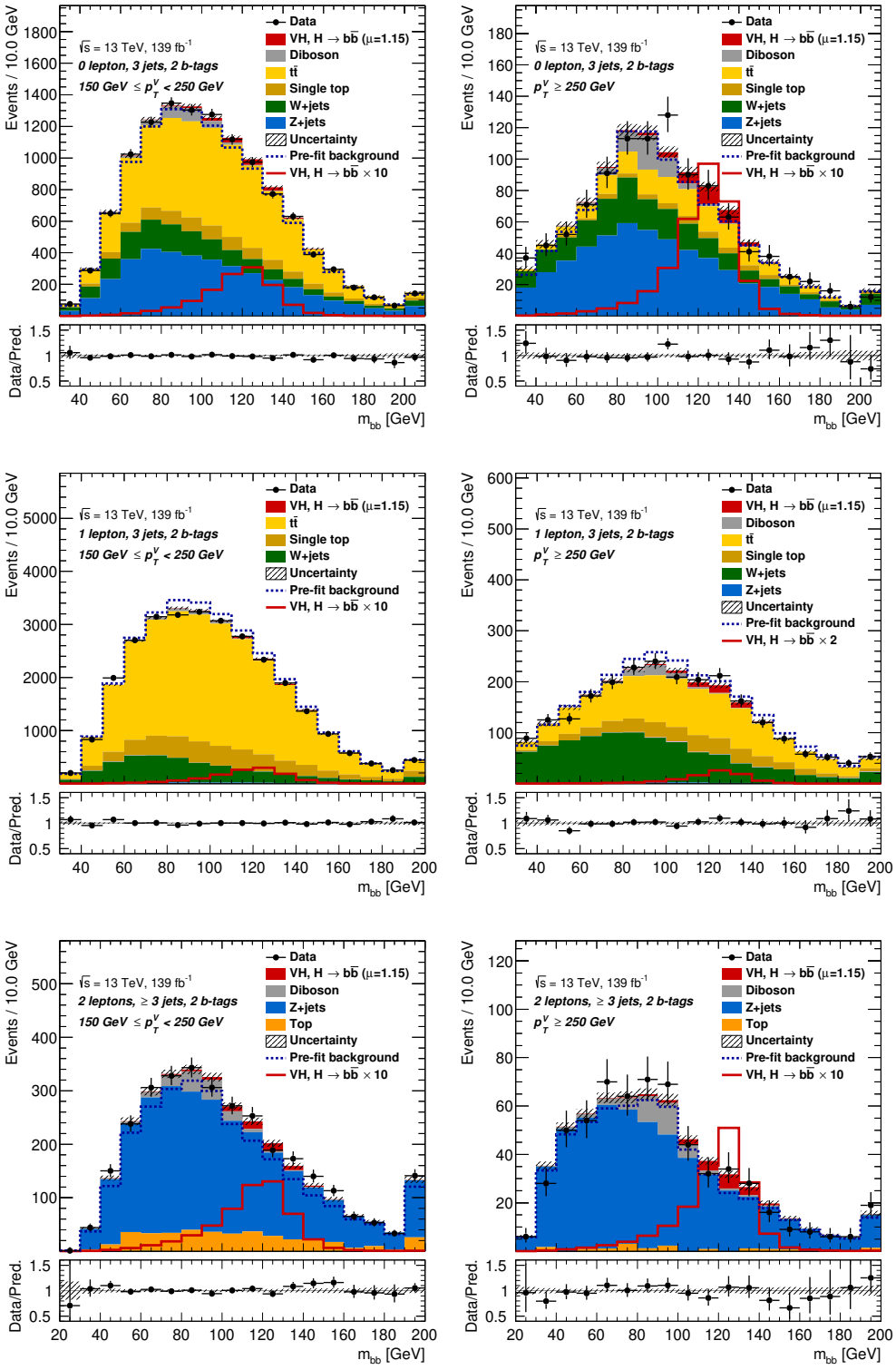

Figure I.5: The distributions of the $m_{b\bar{b}}$ in the categories with 3 or $\geq$ 3 jets and $150 \leq p_{\mathrm{T}}^{V} < 250$ GeV, $p_{\mathrm{T}}^{V} \geq 250$ GeV of the 0-,1- and 2-lepton channels. The stacked histograms show the prediction after the fitting. The red unstacked and unfilled histograms show the VH signals with the scale factors indicated in the legend. The lower panels show the ratio of the data and the prediction of the signals and the backgrounds. The hatched bands in the lower and upper panels show the total uncertainty that includes both the statistical and systematic uncertainties.

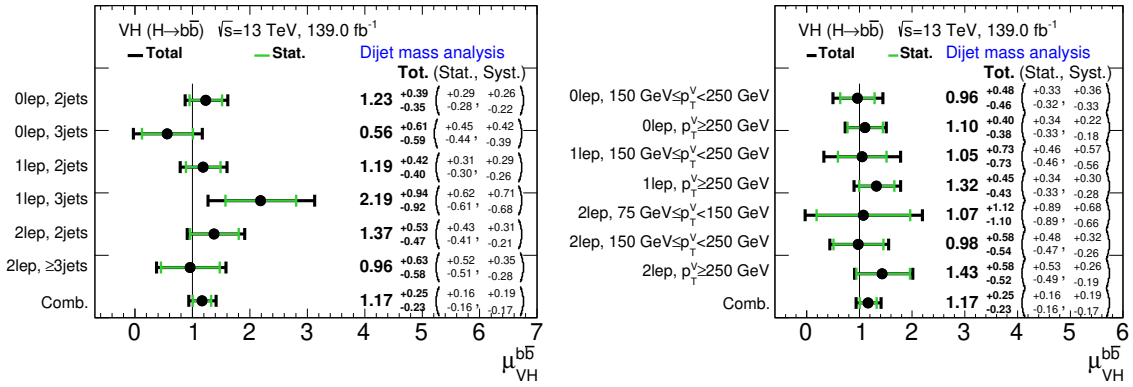

Figure I.6: Observed signal strengths μ_{VH}^{bb} of the VH processes in the categories with number of jets and p_{T}^{V} in the dijet mass analysis. The μ_{VH}^{bb} values for the categories are obtained from the simultaneous fit with the individual signal strengths for the categories. The combined μ_{VH}^{bb} is obtained from the fit with the single signal strength for the signals in all the categories.

Comparison to the multivariate analysis

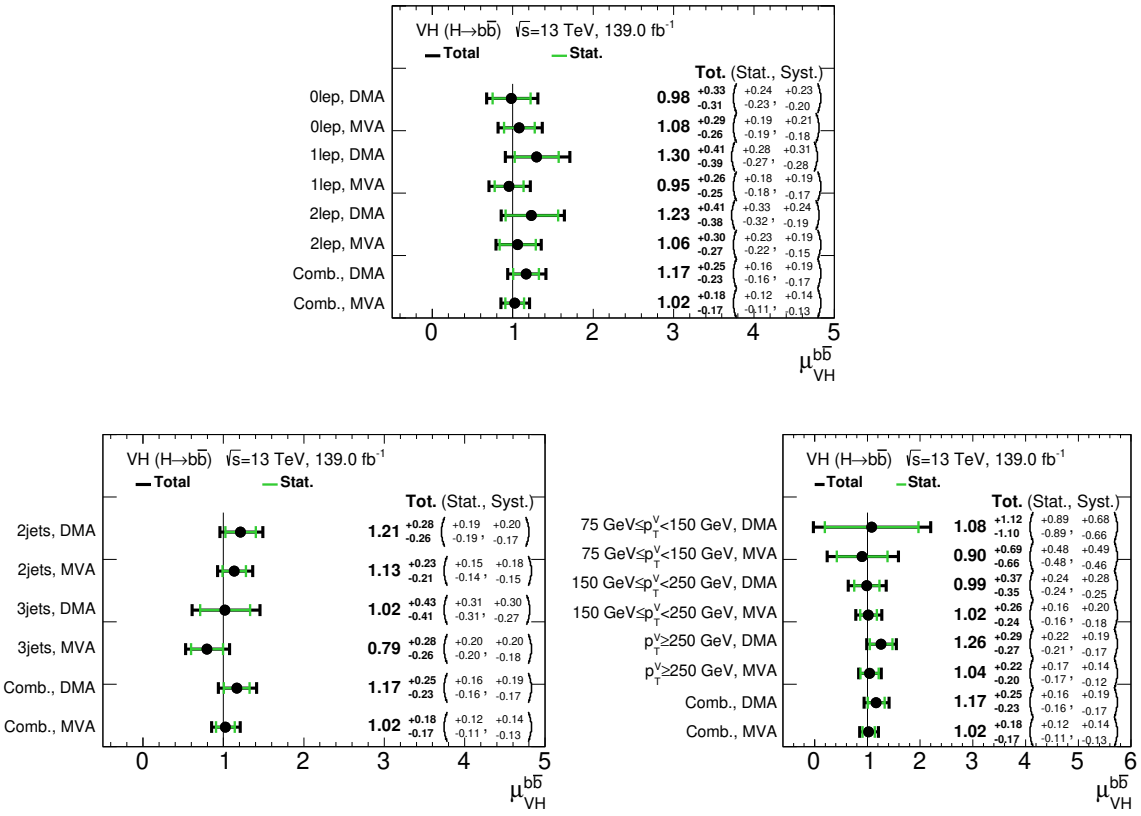

Figure I.7: Comparison of the measured signal strengths from the MVA-based analysis (MVA) and the dijet mass analyses (DMA). The individual μ_{VH}^{bb} values are obtained from the simultaneous fits with the individual signal strengths for the indicated categories. The combined μ_{VH}^{bb} is obtained from the fit with the single signal strength for the signals in all the categories.

I.3 The VZ analysis

Unblinded distributions

The unblinded distributions of the BDT_{VZ} in the $75 \leq p_{\mathrm{T}}^{V} < 150$ GeV categories of the 2-lepton channel and (≥)3 jets categories are shown in Figure I.8 and I.9.

Statistical significance

The measurements exclude the background-only hypothesis by considering the hypothesis of the VZ signal with observed (expected) significance of 10.3 (10.5) standard deviation. The significance with various signal hypotheses are shown in Table I.3.

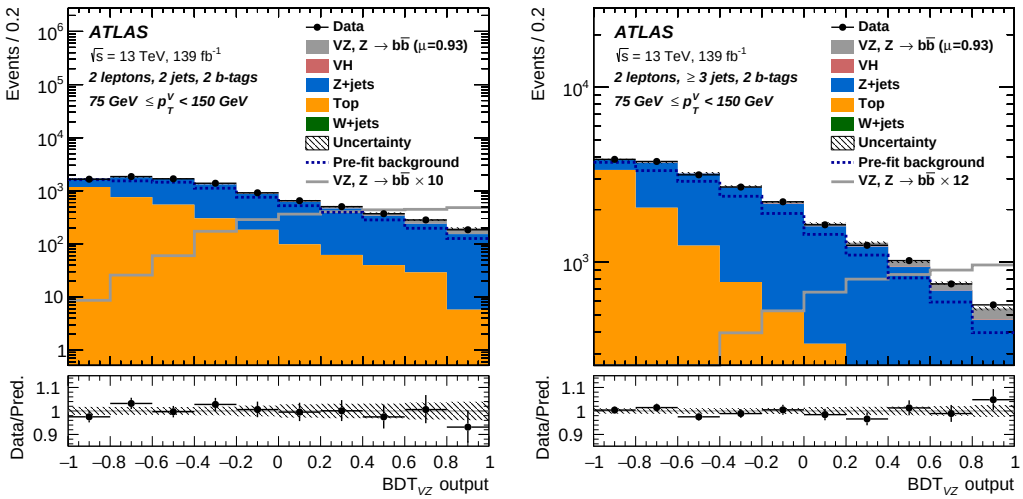

Figure I.8: The distributions of the BDT_{VZ} scores in the categories with 2, ≥ 3 jets and $75 \leq p_{\mathrm{T}}^{V} < 150$ GeV of the 2-lepton channel. The stacked histograms show the prediction after the fitting. The gray unstacked and unfilled histograms show the diboson signals with the scale factors indicated in the legend. The lower panels show the ratio of the data and the prediction of the signals and the backgrounds. The hatched bands in the lower and upper panels show the total uncertainty that includes both the statistical and systematic uncertainties.

Table I.3: Summary of the significance of the excess by the diboson signal hypotheses from the background-only hypothesis.

Signal hypothesis	Expected significance	Observed significance
VZ	10.5	10.3
WZ	3.9	2.7
ZZ	9.3	9.4

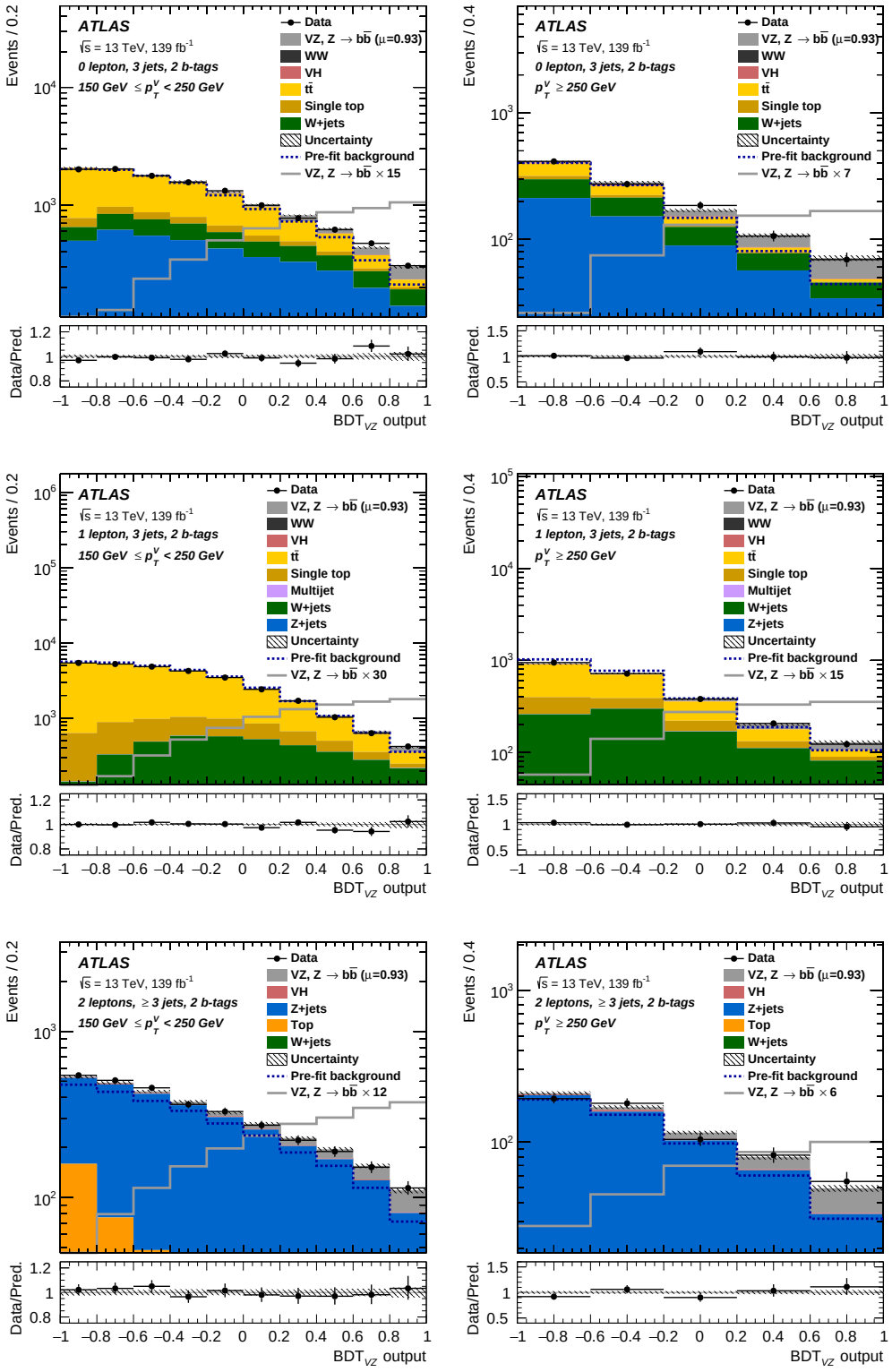

Figure I.9: The distributions of the BDT$_{VZ}$ scores in the categories with 3 or ≥ 3 jets and 150 ≤ p_{T}^{V} < 250 GeV, p_{T}^{V} ≥ 250 GeV of the 0-,1- and 2-lepton channels. The stacked histograms show the prediction after the fitting. The gray unstacked and unfilled histograms show the diboson signals with the scale factors indicated in the legend. The lower panels show the ratio of the data and the prediction of the signals and the backgrounds. The hatched bands in the lower and upper panels show the total uncertainty that includes both the statistical and systematic uncertainties.

Compatibility tests

The dependence of μ on the p_{T}^{V} and the number of jets in each lepton channel are shown in Figure I.10. All the measurements are consistent within their uncertainties. A compatibility test is performed to estimate the quantitative consistency among categories. The results show fair compatibility of the indicated hypotheses as shown in Table I.4. Note that 0-, 1-, 2-lepton, the number of jets and p_{T}^{V} indicate just the number of the selected leptons and jets; the reconstructed transverse momentum of the vector boson, and they are not quantities unfolded to any truth categories.

I.4 Cross-section measurement

The cross-section times the branching ratio is measured in Section 10.3. The measurements are performed in the bins with $150 \leq p_{\mathrm{T}}^{V} < 250$ GeV and $p_{\mathrm{T}}^{V} \geq 250$ GeV for WH and $75 \leq p_{\mathrm{T}}^{V} < 150$ GeV, $150 \leq p_{\mathrm{T}}^{V} < 250$ GeV and $p_{\mathrm{T}}^{V} \geq 250$ GeV for ZH.

The correlations between the measured cross-sections in the bins are derived as explained in Section 9.1.3 and shown in Figure I.11. The correlations are $O(1\%)$ because each analysis category allows for

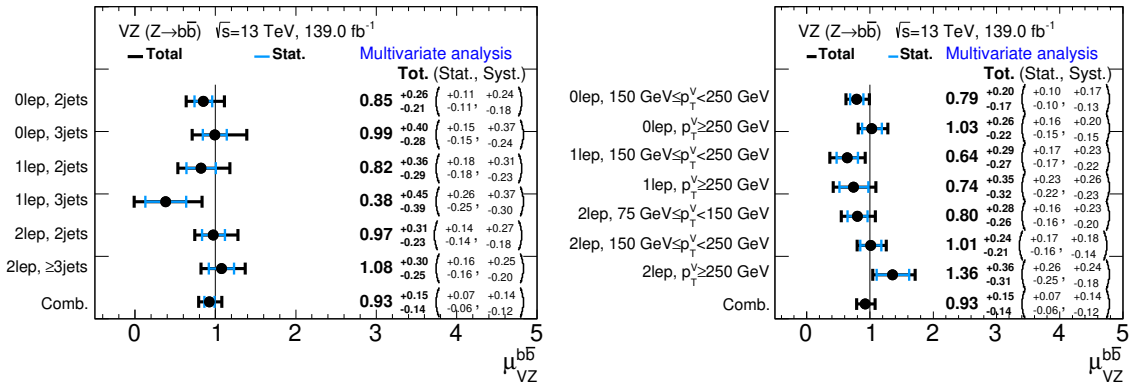

Figure I.10: Observed signal strengths μ_{VZ}^{bb} of the diboson processes in the categories with number of jets and p_{T}^{V}. The μ_{VZ}^{bb} values for the sub-categories are obtained from the simultaneous fit with the individual signal strengths for these signals. The combined μ_{VZ}^{bb} value are obtained from the fit with the single signal strengths for all the categories.

Table I.4: Summary of the compatibility of the VZ fits when the indicated null hypotheses and the alternative hypotheses are given.

Null hypothesis	Alternative hypothesis	Compatiblility
Combined fit (1 POI for VZ)	Fit separated into WZ&ZZ	27%
Combined fit (1 POI for VZ)	Fit separated with the numbers of leptons and jets	69%
Combined fit (1 POI for VZ)	Fit separated with the numbers of leptons and p_{T}^{V}	59%
SM prediction	Fit separated into WZ&ZZ	48%
SM prediction	Fit separated with the numbers of leptons and jets	77%
SM prediction	Fit separated with the numbers of leptons and p_{T}^{V}	67%
SM prediction	Combined fit (1 POI for VZ)	62%

independent measurement.

The breakdown of the contributions to the relative uncertainties on the signal cross-sections in the measured bins are shown in Tables I.5 and I.6. The data statistical uncertainty is the leading uncertainty in $p_{\mathrm{T}}^{V} \geq 150$ GeV for ZH and in $p_{\mathrm{T}}^{V} \geq 250$ GeV for WH, while the systematic uncertainty have the similar or larger size than the statistical one in the other bins. The leading sources of the systematic uncertainties are common with the measurement of the signal strength in Section 10.1: detector related uncertainties, the calibration of jets, $E_{\mathrm{T}}^{\mathrm{miss}}$ and b-tag; and theoretical uncertainties of the signal and background processes. One difference can be seen in the $75 \leq p_{\mathrm{T}}^{V} < 150$ GeV bin for ZH. The uncertainties on $E_{\mathrm{T}}^{\mathrm{miss}}$ has relatively high contribution compare to the other regions. This is because the $E_{\mathrm{T}}^{\mathrm{miss}}$ acts as a strong variable in the BDTs of the 2-lepton channel to reject the $t\bar{t}$ backgrond decaying leptonicly whereas the signal does not have the $E_{\mathrm{T}}^{\mathrm{miss}}$. The large overall uncertainty in this bin is due to the low S/N ratio.

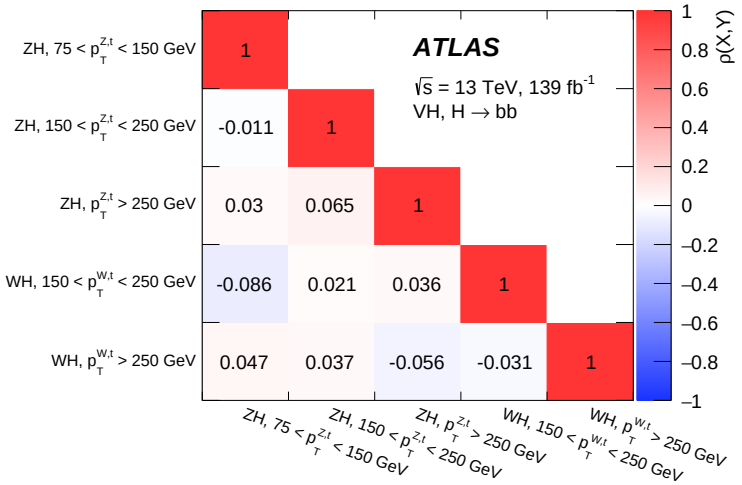

Figure I.11: Correlations of the Measured cross sections of the VH production (σ) times the branching ratio of the $V \rightarrow$ leptons and $H \rightarrow b\bar{b}$ decays (B). The $\sigma \times B$ values are unfolded to the indicated bins.

Table I.5: Breakdown of the contribution to the uncertainties on the cross-sections of ZH in the indicated phase-spaces. These are the relative uncertainties that are normalized by dividing by the SM $\sigma \times B$ predictions.

Source of uncertainty		Uncertainty in $\sigma \times B$ w.r.t. the SM prediction		
		$75 < p_{\mathrm{T}}^{Z,\,\mathrm{truth}} < 150$ GeV	$150 < p_{\mathrm{T}}^{Z,\,\mathrm{truth}} < 250$ GeV	$p_{\mathrm{T}}^{Z,\,\mathrm{truth}} > 250$ GeV
Total		0.710	0.330	0.330
Statistical		0.501	0.262	0.291
Systematic		0.503	0.200	0.156
Statistical uncertainties				
Data statistical		0.421	0.243	0.284
$t\bar{t}$ $e\mu$ control region		0.221	0.039	0.023
Floating normalisations		0.181	0.095	0.047
Experimental uncertainties				
Jets		0.266	0.082	0.040
$E_{\mathrm{T}}^{\mathrm{miss}}$		0.235	0.027	0.016
Leptons		0.027	0.007	0.007
b-tagging	b-jets	0.176	0.082	0.041
	c-jets	0.028	0.020	0.006
	light-jets	0.006	0.013	0.015
Pile-up		0.012	0.016	0.017
Luminosity		0.012	0.016	0.017
Theoretical and modelling uncertainties				
Signal		0.110	0.096	0.091
Z + jets		0.271	0.089	0.071
W + jets		0.020	0.019	0.008
$t\bar{t}$		0.108	0.036	0.025
Single top quark		0.044	0.015	0.015
Diboson		0.073	0.044	0.029
Multi-jet		0.009	0.008	0.005
MC statistical		0.168	0.057	0.055

Table I.6: Breakdown of the contribution to the uncertainties on the cross-sections of WH in the indicated phase-spaces. These are the relative uncertainties that are normalized by dividing by the SM $\sigma \times B$ predictions.

Source of uncertainty		Uncertainty in $\sigma \times B$ w.r.t. the SM prediction	
		150 GeV $< p_{\mathrm{T}}^{W,\,\mathrm{truth}} <$ 250 GeV	$p_{\mathrm{T}}^{W,\,\mathrm{truth}} >$ 250 GeV
Total		0.502	0.311
Statistical		0.320	0.263
Systematic		0.386	0.166
Statistical uncertainties			
Data statistical		0.298	0.252
$t\bar{t}$ $e\mu$ control region		0.032	0.007
Floating normalisations		0.157	0.050
Experimental uncertainties			
Jets		0.145	0.054
$E_{\mathrm{T}}^{\mathrm{miss}}$		0.171	0.009
Leptons		0.019	0.018
b-tagging	b-jets	0.049	0.023
	c-jets	0.109	0.060
	light-jets	0.004	0.005
Pile-up		0.017	0.015
Luminosity		0.017	0.015
Theoretical and modelling uncertainties			
Signal		0.035	0.050
Z + jets		0.038	0.011
W + jets		0.159	0.072
$t\bar{t}$		0.152	0.037
Single top quark		0.135	0.032
Diboson		0.040	0.034
Multi-jet		0.015	0.019
MC statistical		0.112	0.068

J Ranking of nuisance parameters in the measurements

J.1 Evaluation of ranking

It is useful to make a ranking of systematics that have big impacts on parameters of interest. A *postfit error* of a nuisance parameter is defined as the interval of the parameter, where the test statistic q_μ gives larger values by 1/2 than the minimum. A *prefit error* is defined as the 1 σ of the predefined constraint term in Eq.9.3. The signal strength μ is computed when the nuisance parameter is set to the upper/lower bound of the postfit error. The size of the variation of μ is called *postfit impact* of the nuisance parameter on μ. This is also explained in Figure J.1. The same procedure can be performed with the prefit errors, and the variation of μ defines the *prefit impact* of the nuisance parameters on μ. By repeating this computation for all the nuisance parameters, a ranking of important nuisance parameters become available.

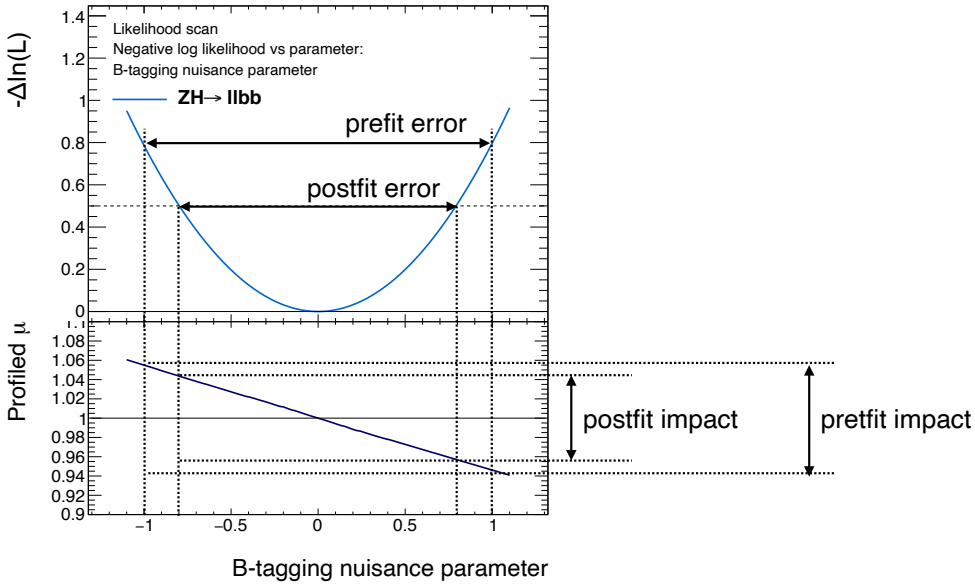

Figure J.1: A negative log likelihood ($-\Delta \ln(L)$) as a function of a b-tag nuisance parameter (θ) in the top panel. The negative log likelihood is minimized with respect to the other parameters than θ at each given value of θ. The signal strength μ is also fitted in the minimization, thus it deviates from unity at a large value of θ as shown in the bottom panel. The parameter θ is defined so that the size of the prefit error is unity, while the postfit error is defined as the interval that the NLL gives larger value by 1/2 than the minimum. The postfit (prefit) impact on μ is defined as the deviation of μ at the postfit (prefit) bounds of the nuisance parameters.

J.2 Ranking in the signal strength measurement

Ranking plots are shown in Figures J.2 and J.3 for the WH and ZH signals derived in the signal strength measurement presented in Section 10.1. The contribution is consistent to the description on the systematic uncertainties in that section. For WH, the modelling uncertainties of the W + jets and $t\bar{t}$ backgrounds and the uncertainties on the b-tagging efficiency for c-jets have contribution. For ZH, the modelling uncertainties of the Z + jets and $gg \rightarrow ZH$ have large contribution. Uncertainties on the calibration of the b-tagging and jet energy scale contribute to both channels.

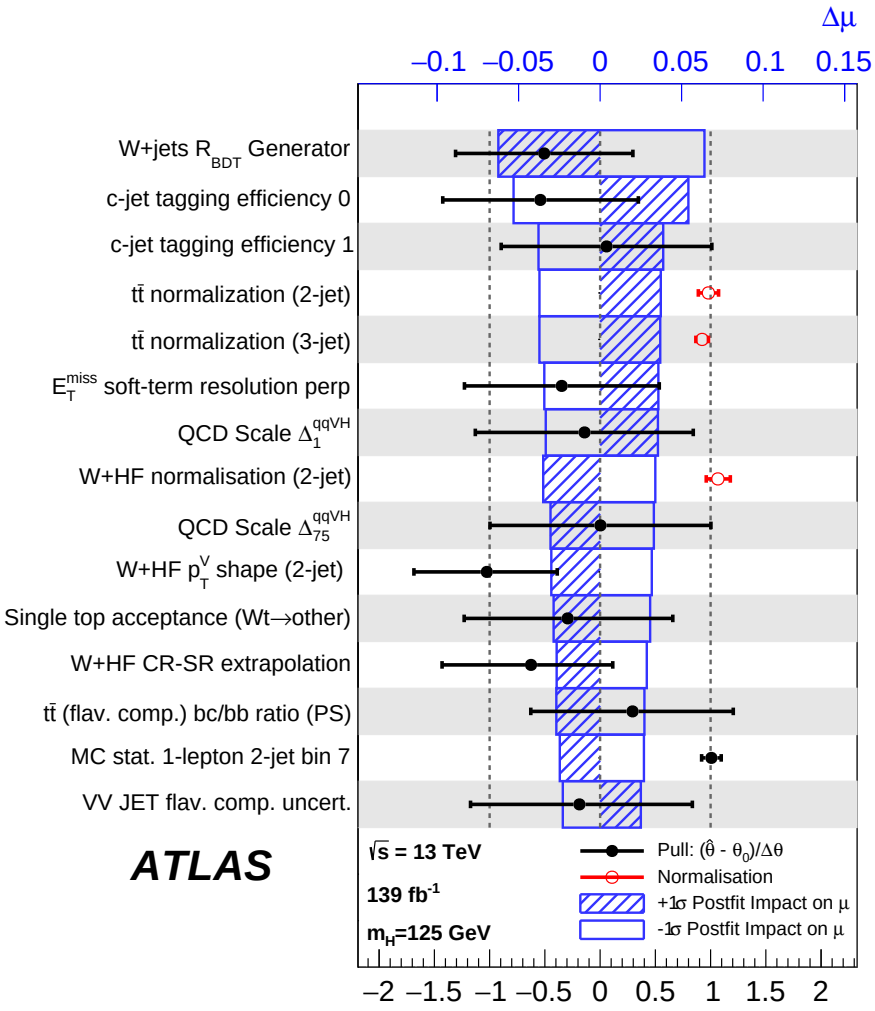

Figure J.2: Ranking of nuisance parameters in the signal strength measurement of WH. The simultaneous fit to the 0-, 1- and 2-lepton channels are performed with signal strengths μ assigned to the WH and ZH signals. The black points and bars represent the fitted values of the nuisance parameters and their postfit errors. The red points represent the fitted values of floating normalization factors introduced in Section 9.2.1. The blue boxes show the postfit impact on μ. The nuisance parameters are sorted in the postfit impact.

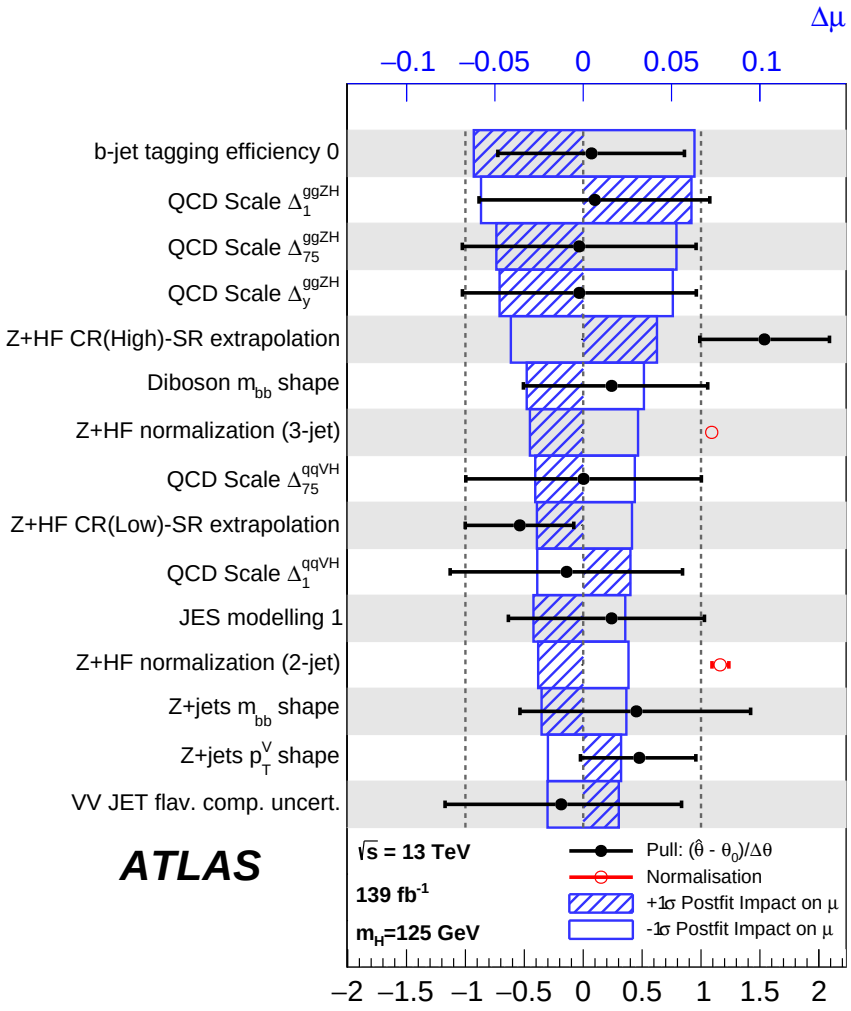

Figure J.3: Ranking of nuisance parameters in the signal strength measurement of ZH. The simultaneous fit to the 0-, 1- and 2-lepton channels are performed with signal strengths μ assigned to the WH and ZH signals. The black points and bars represent the fitted values of the nuisance parameters and their postfit errors. The red points represent the fitted values of floating normalization factors introduced in Section 9.2.1. The blue boxes show the postfit impact on μ. The nuisance parameters are sorted in the postfit impact.

K EFT parametrization

Dimension-6 operators in the Warsaw basis

The fields in the SM are summarized in K.1 to introduce the notation in this appendix. The isospin, color, and the generation indices are denoted by j, α, and p, respectively. The indices L and R denote the chirality.

The dimension-6 operators defined in the Warsaw basis are summarized in Tables K.2 and K.3. The field strength tensors $G^a_{\mu\nu}$, $W^i_{\mu\nu}$, and $B_{\mu\nu}$ correspond the gauge fields associated to the $SU(3)_C$, $SU(2)_L$, and $U(1)_Y$ gauge groups, and defined as follows:

$$G^a_{\mu\nu} = \partial_\mu G^a_\nu - \partial_\nu G^a_\mu - g_s f^{abc} G^b_\mu G^c_\nu, \tag{K.1}$$

$$W^i_{\mu\nu} = \partial_\mu W^i_\nu - \partial_\nu W^i_\mu - g\epsilon^{ijk} W^j_\mu W^k_\nu, \tag{K.2}$$

$$B_{\mu\nu} = \partial_\mu B_\nu - \partial_\nu B_\mu, \tag{K.3}$$

where f^{abc} and ϵ^{ijk} are the structure constants of $SU(3)_C$ and $SU(2)_L$, respectively. The dual tensors corresponding to these tensors are defined by $X_{\mu\nu} = \frac{1}{2}\epsilon_{\mu\nu\rho\sigma}X^{\rho\sigma}$ ($\epsilon_{0123} = +1$), where $X_{\mu\nu}$ stands for $G^a_{\mu\nu}$, $W^i_{\mu\nu}$, and $B_{\mu\nu}$. Similarly, the dual scalar field is defined as $\widetilde{\varphi}^j = \epsilon_{jk}(\varphi^k)^*$, where the asterisk denotes the complex conjugate and $\epsilon_{12} = +1$.

The covariant derivative is defined as:

$$(D_\mu q)^{\alpha j} = \left[\delta_{\alpha\beta}\delta_{jk}\left(\partial_\mu + ig' Y_q B_\mu\right) + ig\delta_{\alpha\beta}S^I_{jk}W^I_\mu + g_s\delta_{jk}T^A_{\alpha\beta}G^A_\mu\right] q^{\beta k}, \tag{K.4}$$

where T^A and S^I are the generators of $SU(3)_C$ and $SU(2)_L$, respectively. The Hermitian derivative is defined as follows:

$$\varphi^\dagger i\overleftrightarrow{D}_\mu \varphi = i\varphi^\dagger\left(D_\mu - \overleftarrow{D}_\mu\right)\varphi = i\varphi^\dagger\left(D_\mu\varphi\right) - i\left(D_\mu\varphi\right)^\dagger\varphi, \tag{K.5}$$

$$\varphi^\dagger i\overleftrightarrow{D}^i_\mu \varphi = i\varphi^\dagger\left(\tau^i D_\mu - \overleftarrow{D}_\mu\tau^i\right)\varphi = i(\tau^i\varphi)^\dagger(D_\mu\varphi) - i(D_\mu\varphi)^\dagger(\tau^i\varphi). \tag{K.6}$$

Table K.1: The mater fields in the Standard Model.

	Fermion					Scalars
Field	l^j_{Lp}	e_{Rp}	$q^{\alpha j}_{Lp}$	u^α_{Rp}	d^α_{Rp}	ϕ^j
Hyper charge Y	$-\frac{1}{2}$	-1	$\frac{1}{6}$	$\frac{2}{3}$	$-\frac{1}{3}$	$\frac{1}{2}$

Table K.2: Dimension-6 operators defined in the Warsaw formulation other than the four-fermion ones. The table is taken from Ref. [26].

X^3		φ^6 and $\varphi^4 D^2$		$\varphi^2\varphi^3$	
Q_G	$f^{abc}G_\mu^{a\nu}G_\nu^{b\rho}G_\rho^{c\mu}$	Q_φ	$(\varphi^\dagger\varphi)^3$	$Q_{e\varphi}$	$(\varphi^\dagger\varphi)(\bar{l}_p e_r \varphi)$
$Q_{\tilde{G}}$	$f^{abc}\tilde{G}_\mu^{a\nu}G_\nu^{b\rho}G_\rho^{c\mu}$	$Q_{\varphi\Box}$	$(\varphi^\dagger\varphi)\Box(\varphi^\dagger\varphi)$	$Q_{u\varphi}$	$(\varphi^\dagger\varphi)(\bar{q}_p u_r \tilde{\varphi})$
Q_W	$\epsilon^{ijk}W_\mu^{i\nu}W_\nu^{j\rho}W_\rho^{k\mu}$	$Q_{\varphi D}$	$(\varphi^\dagger D^\mu\varphi)^*(\varphi^\dagger D_\mu\varphi)$	$Q_{d\varphi}$	$(\varphi^\dagger\varphi)(\bar{q}_p d_r \varphi)$
$Q_{\tilde{W}}$	$\epsilon^{ijk}\tilde{W}_\mu^{i\nu}W_\nu^{j\rho}W_\rho^{k\mu}$				
$X^2\varphi^2$		$\psi^2 X\varphi$		$\psi^2\varphi^2 D$	
$Q_{\varphi G}$	$\varphi^\dagger\varphi G_{\mu\nu}^a G^{a\mu\nu}$	Q_{eW}	$(\bar{l}_p\sigma^{\mu\nu}e_r)\tau^i\varphi W_{\mu\nu}^i$	$Q_{\varphi l}^{(1)}$	$(\varphi^\dagger i\overleftrightarrow{D}_\mu\varphi)(\bar{l}_p\gamma^\mu l_r)$
$Q_{\varphi\tilde{G}}$	$\varphi^\dagger\varphi\tilde{G}_{\mu\nu}^a G^{a\mu\nu}$	Q_{eB}	$(\bar{l}_p\sigma^{\mu\nu}e_r)\varphi B_{\mu\nu}$	$Q_{\varphi l}^{(3)}$	$(\varphi^\dagger i\overleftrightarrow{D}_\mu^i\varphi)(\bar{l}_p\tau^i\gamma^\mu l_r)$
$Q_{\varphi W}$	$\varphi^\dagger\varphi W_{\mu\nu}^i W^{i\mu\nu}$	Q_{uG}	$(\bar{l}_p\sigma^{\mu\nu}T^a e_r)\tilde{\varphi}G_{\mu\nu}^a$	$Q_{\varphi e}$	$(\varphi^\dagger i\overleftrightarrow{D}_\mu\varphi)(\bar{e}_p\gamma^\mu e_r)$
$Q_{\varphi\tilde{W}}$	$\varphi^\dagger\varphi\tilde{W}_{\mu\nu}^i W^{i\mu\nu}$	Q_{uW}	$(\bar{q}_p\sigma^{\mu\nu}u_r)\tau^i\tilde{\varphi}W_{\mu\nu}^i$	$Q_{\varphi q}^{(1)}$	$(\varphi^\dagger i\overleftrightarrow{D}_\mu\varphi)(\bar{q}_p\gamma^\mu q_r)$
$Q_{\varphi B}$	$\varphi^\dagger\varphi B_{\mu\nu}B^{\mu\nu}$	Q_{uB}	$(\bar{q}_p\sigma^{\mu\nu}u_r)\tilde{\varphi}B_{\mu\nu}$	$Q_{\varphi q}^{(3)}$	$(\varphi^\dagger i\overleftrightarrow{D}_\mu^i\varphi)(\bar{q}_p\tau^i\gamma^\mu q_r)$
$Q_{\varphi\tilde{B}}$	$\varphi^\dagger\varphi\tilde{B}_{\mu\nu}B^{\mu\nu}$	Q_{dG}	$(\bar{q}_p\sigma^{\mu\nu}T^a d_r)\varphi G_{\mu\nu}^a$	$Q_{\varphi u}$	$(\varphi^\dagger i\overleftrightarrow{D}_\mu\varphi)(\bar{u}_p\gamma^\mu u_r)$
$Q_{\varphi WB}$	$\varphi^\dagger\tau^i\varphi W_{\mu\nu}^i B^{\mu\nu}$	Q_{dW}	$(\bar{q}_p\sigma^{\mu\nu}d_r)\tau^i\varphi W_{\mu\nu}^i$	$Q_{\varphi d}$	$(\varphi^\dagger i\overleftrightarrow{D}_\mu\varphi)(\bar{d}_p\gamma^\mu d_r)$
$Q_{\varphi\tilde{W}B}$	$\varphi^\dagger\tau^i\varphi\tilde{W}_{\mu\nu}^i B^{\mu\nu}$	Q_{dB}	$(\bar{q}_p\sigma^{\mu\nu}d_r)\varphi B_{\mu\nu}$	$Q_{\varphi ud}$	$(\varphi^\dagger i\overleftrightarrow{D}_\mu\varphi)(\bar{u}_p\gamma^\mu d_r)$

Table K.3: Four-fermion operators with dimension-6 defined in the Warsaw formulation. The table is taken from Ref. [26].

$(\bar{L}L)(\bar{L}L)$		$(\bar{R}R)(\bar{R}R)$		$(\bar{L}L)(\bar{R}R)$	
Q_{ll}	$(\bar{l}_p\gamma_\mu l_r)(\bar{l}_s\gamma^\mu l_t)$	Q_{ee}	$(\bar{e}_p\gamma_\mu e_r)(\bar{e}_s\gamma^\mu e_t)$	Q_{le}	$(\bar{l}_p\gamma_\mu l_r)(\bar{e}_s\gamma^\mu e_t)$
$Q_{qq}^{(1)}$	$(\bar{q}_p\gamma_\mu q_r)(\bar{q}_s\gamma^\mu q_t)$	Q_{uu}	$(\bar{u}_p\gamma_\mu u_r)(\bar{u}_s\gamma^\mu u_t)$	Q_{lu}	$(\bar{l}_p\gamma_\mu l_r)(\bar{u}_s\gamma^\mu u_t)$
$Q_{qq}^{(3)}$	$(\bar{q}_p\gamma_\mu\tau^i q_r)(\bar{q}_s\gamma^\mu\tau^i q_t)$	Q_{dd}	$(\bar{d}_p\gamma_\mu d_r)(\bar{d}_s\gamma^\mu d_t)$	Q_{ld}	$(\bar{l}_p\gamma_\mu l_r)(\bar{d}_s\gamma^\mu d_t)$
$Q_{lq}^{(1)}$	$(\bar{l}_p\gamma_\mu l_r)(\bar{l}_s\gamma^\mu l_t)$	Q_{eu}	$(\bar{e}_p\gamma_\mu e_r)(\bar{u}_s\gamma^\mu u_t)$	Q_{qe}	$(\bar{q}_p\gamma_\mu q_r)(\bar{e}_s\gamma^\mu e_t)$
$Q_{lq}^{(3)}$	$(\bar{l}_p\gamma_\mu\tau^i l_r)(\bar{l}_s\gamma^\mu\tau^i l_t)$	Q_{ed}	$(\bar{e}_p\gamma_\mu e_r)(\bar{d}_s\gamma^\mu d_t)$	$Q_{qu}^{(1)}$	$(\bar{q}_p\gamma_\mu q_r)(\bar{u}_s\gamma^\mu u_t)$
		$Q_{ud}^{(1)}$	$(\bar{u}_p\gamma_\mu u_r)(\bar{d}_s\gamma^\mu d_t)$	$Q_{qu}^{(8)}$	$(\bar{q}_p\gamma_\mu T^a q_r)(\bar{u}_s\gamma^\mu T^a u_t)$
		$Q_{ud}^{(8)}$	$(\bar{u}_p\gamma_\mu T^a u_r)(\bar{d}_s\gamma^\mu T^a d_t)$	$Q_{qd}^{(1)}$	$(\bar{q}_p\gamma_\mu q_r)(\bar{d}_s\gamma^\mu d_t)$
				$Q_{qd}^{(8)}$	$(\bar{q}_p\gamma_\mu T^a q_r)(\bar{d}_s\gamma^\mu T^a d_t)$
$(\bar{L}R)(\bar{R}L)$ and $(\bar{L}R)(\bar{L}R)$		B-violating			
Q_{ledq}	$(\bar{l}_p^j e_r)(\bar{d}_s q_t^j)$	Q_{duq}	$\epsilon^{\alpha\beta\gamma}\epsilon_{jk}[(d_p^\alpha)^T C u_r^\beta][(q_s^{\gamma j})^T C l_t^k]$		
$Q_{quqd}^{(1)}$	$(\bar{q}_p^j u_r)\epsilon_{jk}(\bar{q}_s^k q_t)$	Q_{qqu}	$\epsilon^{\alpha\beta\gamma}\epsilon_{jk}[(q_p^{\alpha j})^T C q_r^{\beta k}][(u_s^\gamma)^T C e_t]$		
$Q_{quqd}^{(8)}$	$(\bar{q}_p^j T^a u_r)\epsilon_{jk}(\bar{q}_s^k T^a q_t)$	Q_{qqq}	$\epsilon^{\alpha\beta\gamma}\epsilon_{jn}\epsilon_{km}[(q_p^{\alpha j})^T C q_r^{\beta k}][(q_s^{\gamma m})^T C l_t^n]$		
$Q_{lequ}^{(1)}$	$(\bar{l}_p^j e_r)\epsilon_{jk}(\bar{q}_s^k u_t)$	Q_{duu}	$\epsilon^{\alpha\beta\gamma}[(d_p^\alpha)^T C u_r^\beta][(u_s^\gamma)^T C e_t]$		
$Q_{lequ}^{(3)}$	$(\bar{l}_p^j\sigma_{\mu\nu}e_r)\epsilon_{jk}(\bar{q}_s^k\sigma^{\mu\nu}u_t)$				

Parametrization of the production cross-sections and the Higgs decay widths

The production cross-sections is parametrized as a function of all the relevant Wilson coefficients in Table 11.1. The parametrization is shown in Tables K.4-K.8 for WH in $150 \leq p_{\mathrm{T}}^{V} < 250$ GeV and $p_{\mathrm{T}}^{V} \geq 250$ GeV and for $qq \to ZH$ in $75 \leq p_{\mathrm{T}}^{V} < 150$ GeV, $150 \leq p_{\mathrm{T}}^{V} < 250$ GeV, and $p_{\mathrm{T}}^{V} \geq 250$ GeV.

In order to predict the event yield, it is necessary to parametrize the partial width of the $H \to b\bar{b}$ decay and the total width of the Higgs boson. The results are shown in Table K.9.

Table K.4: Parametrization of the production cross-section of WH in $150 \leq p_{\mathrm{T}}^{V} < 250$ GeV as a function of considered Wilson coefficients.

$q\bar{q} \to H\ell\nu$, $(150 \leq p_T^V \leq 250)$ GeV
$\sigma/\sigma_{\mathrm{SM}} = 1 + 0.122\, c_{H\Box} + 3.83\, c_{Hq}^{(3)} + 1.04\, c_{HW} - 0.24\, c_{Hl}^{(3)} + 0.182\, c_{ll}^{(1)} - 0.0302\, c_{HDD} + 0.231\, c_{H\Box}\, c_{Hq}^{(3)} + 0.0611\, c_{H\Box}\, c_{HW} - 0.0146\, c_{H\Box}\, c_{Hl}^{(3)} + 0.0111\, c_{H\Box}\, c_{ll}^{(1)} - 0.00186\, c_{H\Box}\, c_{HDD} + 2.14\, c_{Hq}^{(3)}\, c_{HW} - 0.464\, c_{Hq}^{(3)}\, c_{Hl}^{(3)} + 0.349\, c_{Hq}^{(3)}\, c_{ll}^{(1)} - 0.0523\, c_{Hq}^{(3)}\, c_{HDD} - 0.119\, c_{Hl}^{(3)}\, c_{HW} + 0.092\, c_{ll}^{(1)}\, c_{HW} - 0.0196\, c_{HDD}\, c_{HW} - 0.0219\, c_{Hl}^{(3)}\, c_{ll}^{(1)} + 0.00367\, c_{Hl}^{(3)}\, c_{HDD} - 0.00274\, c_{ll}^{(1)}\, c_{HDD} + 0.00369\, (c_{H\Box})^2 + 4.28\, \left(c_{Hq}^{(3)}\right)^2 + 0.671\, (c_{HW})^2 + 0.0151\, \left(c_{Hl}^{(3)}\right)^2 + 0.00828\, \left(c_{ll}^{(1)}\right)^2$

Table K.5: Parametrization of the production cross-section of WH in $p_{\mathrm{T}}^{V} \geq 250$ GeV as a function of considered Wilson cboefficients.

$q\bar{q} \to H\ell\nu$, $(p_T^V \geq 250)$ GeV
$\sigma/\sigma_{\mathrm{SM}} = 1 + 0.12\, c_{H\Box} + 10.8\, c_{Hq}^{(3)} + 1.1\, c_{HW} - 0.235\, c_{Hl}^{(3)} + 0.181\, c_{ll}^{(1)} - 0.0299\, c_{HDD} + 0.735\, c_{H\Box}\, c_{Hq}^{(3)} + 0.0758\, c_{H\Box}\, c_{HW} - 0.0141\, c_{H\Box}\, c_{Hl}^{(3)} + 0.0108\, c_{H\Box}\, c_{ll}^{(1)} - 0.0018\, c_{H\Box}\, c_{HDD} + 6.35\, c_{Hq}^{(3)}\, c_{HW} - 1.21\, c_{Hq}^{(3)}\, c_{Hl}^{(3)} + 1.01\, c_{Hq}^{(3)}\, c_{ll}^{(1)} - 0.194\, c_{Hq}^{(3)}\, c_{HDD} - 0.111\, c_{Hl}^{(3)}\, c_{HW} + 0.096\, c_{ll}^{(1)}\, c_{HW} - 0.00378\, c_{HDD}\, c_{HW} - 0.0212\, c_{Hl}^{(3)}\, c_{ll}^{(1)} + 0.0037\, c_{Hl}^{(3)}\, c_{HDD} - 0.00274\, c_{ll}^{(1)}\, c_{HDD} + 0.00359\, (c_{H\Box})^2 + 53.1\, \left(c_{Hq}^{(3)}\right)^2 + 1.89\, (c_{HW})^2 + 0.0154\, \left(c_{Hl}^{(3)}\right)^2 + 0.00816\, \left(c_{ll}^{(1)}\right)^2$

Table K.6: Parametrization of the production cross-section of $qq \to ZH$ in $75 \leq p_{\mathrm{T}}^{V} < 150$ GeV as a function of considered Wilson cboefficients.

$q\bar{q} \to H\ell\ell/\nu\nu$, $(75 \leq p_T^V \leq 150)$ GeV
$\sigma/\sigma_{\mathrm{SM}} = 1 + 0.122\, c_{H\Box} + 1.8\, c_{Hq}^{(3)} + 0.767\, c_{HW} - 0.237\, c_{Hl}^{(3)} + 0.181\, c_{ll}^{(1)} + 0.0113\, c_{HDD} + 0.0907\, c_{HB} + 0.335\, c_{HWB} - 0.0516\, c_{Hl}^{(1)} - 0.0303\, c_{Hq}^{(1)} + 0.412\, c_{Hu} - 0.164\, c_{Hd} - 0.0296\, c_{He} + 0.106\, c_{H\Box}\, c_{Hq}^{(3)} + 0.0468\, c_{H\Box}\, c_{HW} - 0.0145\, c_{H\Box}\, c_{Hl}^{(3)} + 0.0111\, c_{H\Box}\, c_{ll}^{(1)} + 0.00513\, c_{H\Box}\, c_{HB} + 0.0206\, c_{H\Box}\, c_{HWB} - 0.00314\, c_{Hl}^{(1)}\, c_{H\Box} - 0.0107\, c_{H\Box}\, c_{Hq}^{(1)} + 0.02\, c_{H\Box}\, c_{Hu} - 0.01\, c_{H\Box}\, c_{Hd} - 0.00181\, c_{H\Box}\, c_{He} + 0.847\, c_{Hq}^{(3)}\, c_{HW} - 0.217\, c_{Hq}^{(3)}\, c_{Hl}^{(3)} + 0.167\, c_{Hq}^{(3)}\, c_{ll}^{(1)} + 0.0354\, c_{Hq}^{(3)}\, c_{HDD} + 0.307\, c_{Hq}^{(3)}\, c_{HWB} - 0.0442\, c_{Hl}^{(1)}\, c_{Hq}^{(3)} - 0.254\, c_{Hq}^{(3)}\, c_{Hq}^{(1)} - 0.00161\, c_{Hq}^{(3)}\, c_{Hu} - 0.0108\, c_{Hq}^{(3)}\, c_{Hd} - 0.0302\, c_{Hq}^{(3)}\, c_{He} - 0.0889\, c_{Hl}^{(3)}\, c_{HW} + 0.0699\, c_{ll}^{(1)}\, c_{HW} + 0.0149\, c_{HDD}\, c_{HW} + 0.00527\, c_{HB}\, c_{HW} + 0.161\, c_{HWB}\, c_{HW} - 0.0205\, c_{Hl}^{(1)}\, c_{HW} - 0.0981\, c_{Hq}^{(1)}\, c_{HW} + 0.00265\, c_{Hu}\, c_{HW} - 0.0139\, c_{Hd}\, c_{HW} - 0.011\, c_{He}\, c_{HW} - 0.0217\, c_{Hl}^{(3)}\, c_{ll}^{(1)} + 0.00137\, c_{Hl}^{(3)}\, c_{HDD} - 0.0107\, c_{Hl}^{(3)}\, c_{HB} - 0.0367\, c_{Hl}^{(3)}\, c_{HWB} + 0.00795\, c_{Hl}^{(1)}\, c_{Hl}^{(3)} - 0.00309\, c_{Hl}^{(3)}\, c_{Hq}^{(1)} - 0.0511\, c_{Hl}^{(3)}\, c_{Hu} + 0.0149\, c_{Hl}^{(3)}\, c_{Hd} + 0.00534\, c_{Hl}^{(3)}\, c_{He} + 0.00111\, c_{ll}^{(1)}\, c_{HDD} + 0.00809\, c_{HB}\, c_{ll}^{(1)} + 0.0308\, c_{HWB}\, c_{ll}^{(1)} - 0.0047\, c_{Hl}^{(1)}\, c_{ll}^{(1)} - 0.00454\, c_{Hq}^{(1)}\, c_{ll}^{(1)} + 0.0371\, c_{ll}^{(1)}\, c_{Hu} - 0.02\, c_{Hd}\, c_{ll}^{(1)} - 0.0027\, c_{ll}^{(1)}\, c_{He} - 0.00968\, c_{HB}\, c_{HDD} + 0.00468\, c_{HWB}\, c_{HDD} + 0.003\, c_{Hl}^{(1)}\, c_{HDD} - 0.0286\, c_{Hq}^{(1)}\, c_{HDD} - 0.0491\, c_{HDD}\, c_{Hu} + 0.0147\, c_{Hd}\, c_{HDD} + 0.00308\, c_{HDD}\, c_{He} + 0.0359\, c_{HB}\, c_{HWB} - 0.00265\, c_{Hl}^{(1)}\, c_{HB} + 0.062\, c_{HB}\, c_{Hq}^{(1)} + 0.175\, c_{HB}\, c_{Hu} - 0.0721\, c_{HB}\, c_{Hd} - 0.00158\, c_{HB}\, c_{He} - 0.00591\, c_{Hl}^{(1)}\, c_{HWB} + 0.0103\, c_{HWB}\, c_{Hq}^{(1)} + 0.116\, c_{HWB}\, c_{Hu} - 0.0484\, c_{HWB}\, c_{Hd} - 0.00207\, c_{HWB}\, c_{He} - 0.00478\, c_{Hl}^{(1)}\, c_{Hq}^{(1)} - 0.012\, c_{Hl}^{(1)}\, c_{Hu} - 0.00176\, c_{Hq}^{(1)}\, c_{Hu} - 0.0172\, c_{Hq}^{(1)}\, c_{Hd} - 0.00151\, c_{Hq}^{(1)}\, c_{He} - 0.00477\, c_{Hd}\, c_{Hu} - 0.00709\, c_{Hu}\, c_{He} + 0.00251\, c_{Hd}\, c_{He} + 0.0037\, (c_{H\Box})^2 + 1.04\, \left(c_{Hq}^{(3)}\right)^2 + 0.243\, (c_{HW})^2 + 0.0154\, \left(c_{Hl}^{(3)}\right)^2 + 0.00827\, \left(c_{ll}^{(1)}\right)^2 + 0.00421\, (c_{HDD})^2 + 0.0265\, (c_{HB})^2 + 0.0459\, (c_{HWB})^2 + 0.00511\, \left(c_{Hl}^{(1)}\right)^2 + 1.05\, \left(c_{Hq}^{(1)}\right)^2 + 0.584\, (c_{Hu})^2 + 0.46\, (c_{Hd})^2 + 0.00219\, (c_{He})^2$

Table K.7: Parametrization of the production cross-section of $qq \to ZH$ in $150 \leq p_{\mathrm{T}}^{V} < 250$ GeV as a function of considered Wilson cboefficients.

$q\bar{q} \to H\ell\ell/\nu\nu$, $(150 \leq p_T^V \leq 250)$ GeV
$\sigma/\sigma_{\mathrm{SM}} = 1 + 0.122\, c_{H\Box} + 3.55\, c_{Hq}^{(3)} + 0.867\, c_{HW} - 0.237\, c_{Hl}^{(3)} + 0.183\, c_{ll}^{(1)} + 0.0126\, c_{HDD} + 0.103\, c_{HB} + 0.378\, c_{HWB} - 0.0462\, c_{Hl}^{(1)} - 0.228\, c_{Hq}^{(1)} + 0.852\, c_{Hu} - 0.308\, c_{Hd} - 0.0328\, c_{He} + 0.198\, c_{H\Box}\, c_{Hq}^{(3)} + 0.0547\, c_{H\Box}\, c_{HW} - 0.0145\, c_{H\Box}\, c_{Hl}^{(3)} + 0.0111\, c_{H\Box}\, c_{ll}^{(1)} + 0.00603\, c_{H\Box}\, c_{HB} + 0.0221\, c_{H\Box}\, c_{HWB} - 0.0028\, c_{Hl}^{(1)}\, c_{H\Box} + 0.00154\, c_{H\Box}\, c_{Hq}^{(1)} + 0.0401\, c_{H\Box}\, c_{Hu} - 0.00704\, c_{H\Box}\, c_{Hd} - 0.00196\, c_{H\Box}\, c_{He} + 1.92\, c_{Hq}^{(3)}\, c_{HW} - 0.401\, c_{Hq}^{(3)}\, c_{Hl}^{(3)} + 0.327\, c_{Hq}^{(3)}\, c_{ll}^{(1)} + 0.0944\, c_{Hq}^{(3)}\, c_{HDD} - 0.0217\, c_{Hq}^{(3)}\, c_{HB} + 0.601\, c_{Hq}^{(3)}\, c_{HWB} - 0.0785\, c_{Hl}^{(1)}\, c_{Hq}^{(3)} - 1.33\, c_{Hq}^{(3)}\, c_{Hq}^{(1)} - 0.00117\, c_{Hq}^{(3)}\, c_{Hu} - 0.0297\, c_{Hq}^{(3)}\, c_{Hd} - 0.0426\, c_{Hq}^{(3)}\, c_{He} - 0.101\, c_{Hl}^{(3)}\, c_{HW} + 0.0804\, c_{ll}^{(1)}\, c_{HW} + 0.0203\, c_{HDD}\, c_{HW} - 0.00329\, c_{HB}\, c_{HW} + 0.284\, c_{HWB}\, c_{HW} - 0.0202\, c_{Hl}^{(1)}\, c_{HW} - 0.293\, c_{Hq}^{(1)}\, c_{HW} - 0.0115\, c_{Hu}\, c_{HW} + 0.0103\, c_{Hd}\, c_{HW} - 0.0144\, c_{He}\, c_{HW} - 0.0218\, c_{Hl}^{(3)}\, c_{ll}^{(1)} + 0.00152\, c_{Hl}^{(3)}\, c_{HDD} - 0.0117\, c_{Hl}^{(3)}\, c_{HB} - 0.0416\, c_{Hl}^{(3)}\, c_{HWB} + 0.00753\, c_{Hl}^{(1)}\, c_{Hl}^{(3)} + 0.0411\, c_{Hl}^{(3)}\, c_{Hq}^{(1)} - 0.0978\, c_{Hl}^{(3)}\, c_{Hu} + 0.046\, c_{Hl}^{(3)}\, c_{Hd} + 0.00592\, c_{Hl}^{(3)}\, c_{He} + 0.00115\, c_{ll}^{(1)}\, c_{HDD} + 0.00932\, c_{HB}\, c_{ll}^{(1)} + 0.0332\, c_{HWB}\, c_{ll}^{(1)} - 0.00422\, c_{Hl}^{(1)}\, c_{ll}^{(1)} + 0.00231\, c_{Hq}^{(1)}\, c_{ll}^{(1)} + 0.0565\, c_{ll}^{(1)}\, c_{Hu} - 0.0221\, c_{Hd}\, c_{ll}^{(1)} - 0.003\, c_{ll}^{(1)}\, c_{He} - 0.0122\, c_{HB}\, c_{HDD} + 0.0033\, c_{HWB}\, c_{HDD} + 0.00333\, c_{Hl}^{(1)}\, c_{HDD} - 0.0352\, c_{Hq}^{(1)}\, c_{HDD} - 0.106\, c_{HDD}\, c_{Hu} + 0.0436\, c_{Hd}\, c_{HDD} + 0.0033\, c_{HDD}\, c_{He} + 0.0785\, c_{HB}\, c_{HWB} - 0.00303\, c_{Hl}^{(1)}\, c_{HB} + 0.198\, c_{HB}\, c_{Hq}^{(1)} + 0.391\, c_{HB}\, c_{Hu} - 0.143\, c_{HB}\, c_{Hd} - 0.00215\, c_{HB}\, c_{He} - 0.00674\, c_{Hl}^{(1)}\, c_{HWB} + 0.0425\, c_{HWB}\, c_{Hq}^{(1)} + 0.289\, c_{HWB}\, c_{Hu} - 0.108\, c_{HWB}\, c_{Hd} - 0.00436\, c_{HWB}\, c_{He} + 0.00893\, c_{Hl}^{(1)}\, c_{Hq}^{(1)} - 0.0289\, c_{Hl}^{(1)}\, c_{Hu} + 0.0187\, c_{Hl}^{(1)}\, c_{Hd} - 0.00902\, c_{Hq}^{(1)}\, c_{Hu} + 0.0425\, c_{Hq}^{(1)}\, c_{Hd} + 0.00692\, c_{Hq}^{(1)}\, c_{He} + 0.00393\, c_{Hd}\, c_{Hu} - 0.029\, c_{Hu}\, c_{He} + 0.0023\, c_{Hd}\, c_{He} + 0.00372\, (c_{H\Box})^2 + 4.14\, \left(c_{Hq}^{(3)}\right)^2 + 0.498\, (c_{HW})^2 + 0.0158\, \left(c_{Hl}^{(3)}\right)^2 + 0.00834\, \left(c_{ll}^{(1)}\right)^2 + 0.00452\, (c_{HDD})^2 + 0.0573\, (c_{HB})^2 + 0.0886\, (c_{HWB})^2 + 0.00558\, \left(c_{Hl}^{(1)}\right)^2 + 4.12\, \left(c_{Hq}^{(1)}\right)^2 + 2.41\, (c_{Hu})^2 + 1.73\, (c_{Hd})^2 + 0.00257\, (c_{He})^2$

Table K.8: Parametrization of the production cross-section of $qq \to ZH$ in $p_{\mathrm{T}}^{V} \geq 250\,\mathrm{GeV}$ as a function of considered Wilson cboefficients.

$q\bar{q} \to H\ell\ell/\nu\nu$, $(p_T^V \geq 250)\,\mathrm{GeV}$
$\sigma/\sigma_{\mathrm{SM}} = 1 + 0.119\,c_{H\Box} + 9.19\,c_{Hq}^{(3)} + 0.884\,c_{HW} - 0.234\,c_{Hl}^{(3)} + 0.177\,c_{ll}^{(1)} + 0.0134\,c_{HDD} + 0.13\,c_{HB} + 0.404\,c_{HWB} - 0.0441\,c_{Hl}^{(1)} - 1.14\,c_{Hq}^{(1)} + 2.39\,c_{Hu} - 0.756\,c_{Hd} - 0.0332\,c_{He} + 0.698\,c_{H\Box}\,c_{Hq}^{(3)} + 0.0564\,c_{H\Box}\,c_{HW} - 0.0142\,c_{H\Box}\,c_{Hl}^{(3)} + 0.0111\,c_{H\Box}\,c_{ll}^{(1)} + 0.00466\,c_{H\Box}\,c_{HB} + 0.0247\,c_{H\Box}\,c_{HWB} - 0.00264\,c_{Hl}^{(1)}\,c_{H\Box} - 0.18\,c_{H\Box}\,c_{Hq}^{(1)} + 0.201\,c_{H\Box}\,c_{Hu} - 0.0333\,c_{H\Box}\,c_{Hd} - 0.002\,c_{H\Box}\,c_{He} + 5.75\,c_{Hq}^{(3)}\,c_{HW} - 1.09\,c_{Hq}^{(3)}\,c_{Hl}^{(3)} + 0.864\,c_{Hq}^{(3)}\,c_{ll}^{(1)} + 0.234\,c_{Hq}^{(3)}\,c_{HDD} + 0.12\,c_{Hq}^{(3)}\,c_{HB} + 2.03\,c_{Hq}^{(3)}\,c_{HWB} - 0.125\,c_{Hl}^{(1)}\,c_{Hq}^{(3)} - 22.6\,c_{Hq}^{(3)}\,c_{Hq}^{(1)} + 0.0749\,c_{Hq}^{(3)}\,c_{Hu} + 0.311\,c_{Hq}^{(3)}\,c_{Hd} - 0.0996\,c_{Hq}^{(3)}\,c_{He} - 0.105\,c_{Hl}^{(3)}\,c_{HW} + 0.0787\,c_{ll}^{(1)}\,c_{HW} + 0.0268\,c_{HDD}\,c_{HW} - 0.0506\,c_{HB}\,c_{HW} + 0.692\,c_{HWB}\,c_{HW} - 0.0291\,c_{Hl}^{(1)}\,c_{HW} - 1.37\,c_{Hq}^{(1)}\,c_{HW} + 0.168\,c_{Hu}\,c_{HW} + 0.0849\,c_{Hd}\,c_{HW} - 0.0246\,c_{He}\,c_{HW} - 0.0212\,c_{Hl}^{(3)}\,c_{ll}^{(1)} + 0.00123\,c_{Hl}^{(3)}\,c_{HDD} - 0.0141\,c_{Hl}^{(3)}\,c_{HB} - 0.0435\,c_{Hl}^{(3)}\,c_{HWB} + 0.00728\,c_{Hl}^{(1)}\,c_{Hl}^{(3)} + 0.0104\,c_{Hl}^{(3)}\,c_{Hq}^{(1)} - 0.211\,c_{Hl}^{(3)}\,c_{Hu} + 0.141\,c_{Hl}^{(3)}\,c_{Hd} + 0.00616\,c_{Hl}^{(3)}\,c_{He} + 0.00115\,c_{ll}^{(1)}\,c_{HDD} + 0.0108\,c_{HB}\,c_{ll}^{(1)} + 0.0358\,c_{HWB}\,c_{ll}^{(1)} - 0.00384\,c_{Hl}^{(1)}\,c_{ll}^{(1)} - 0.283\,c_{Hq}^{(1)}\,c_{ll}^{(1)} + 0.289\,c_{ll}^{(1)}\,c_{Hu} - 0.00649\,c_{Hd}\,c_{ll}^{(1)} - 0.00294\,c_{ll}^{(1)}\,c_{He} - 0.0149\,c_{HB}\,c_{HDD} + 0.00325\,c_{Hl}^{(1)}\,c_{HDD} - 0.16\,c_{Hq}^{(1)}\,c_{HDD} - 0.261\,c_{HDD}\,c_{Hu} + 0.109\,c_{Hd}\,c_{HDD} + 0.00346\,c_{HDD}\,c_{He} + 0.235\,c_{HB}\,c_{HWB} - 0.00368\,c_{Hl}^{(1)}\,c_{HB} + 0.648\,c_{HB}\,c_{Hq}^{(1)} + 1.47\,c_{HB}\,c_{Hu} - 0.372\,c_{HB}\,c_{Hd} - 0.00358\,c_{HB}\,c_{He} - 0.0103\,c_{Hl}^{(1)}\,c_{HWB} - 0.0795\,c_{HWB}\,c_{Hq}^{(1)} + 1.05\,c_{HWB}\,c_{Hu} - 0.229\,c_{HWB}\,c_{Hd} - 0.00571\,c_{HWB}\,c_{He} - 0.0275\,c_{Hl}^{(1)}\,c_{Hq}^{(1)} + 0.00373\,c_{Hl}^{(1)}\,c_{Hu} + 0.04\,c_{Hl}^{(1)}\,c_{Hd} - 0.214\,c_{Hq}^{(1)}\,c_{Hu} - 0.0578\,c_{Hq}^{(1)}\,c_{Hd} - 0.00469\,c_{Hq}^{(1)}\,c_{He} - 0.0273\,c_{Hd}\,c_{Hu} + 0.0654\,c_{Hu}\,c_{He} + 0.0591\,c_{Hd}\,c_{He} + 0.00367\,(c_{H\Box})^2 + 41.5\left(c_{Hq}^{(3)}\right)^2 + 1.37\,(c_{HW})^2 + 0.0163\left(c_{Hl}^{(3)}\right)^2 + 0.00806\left(c_{ll}^{(1)}\right)^2 + 0.00465\,(c_{HDD})^2 + 0.167\,(c_{HB})^2 + 0.231\,(c_{HWB})^2 + 0.00637\left(c_{Hl}^{(1)}\right)^2 + 41.7\left(c_{Hq}^{(1)}\right)^2 + 26.4\,(c_{Hu})^2 + 15.2\,(c_{Hd})^2 + 0.00299\,(c_{He})^2$

Table K.9: Parametrization of the total decay width of the Higgs boson and the partial decay width of $H \to b\bar{b}$.

decay channel	parametrisation
$H \to b\bar{b}$	$\Gamma^{H\to b\bar{b}}/\Gamma_{\mathrm{SM}}^{H\to b\bar{b}} = 1 + 0.121\,c_{H\Box} - 0.0303\,c_{HDD} - 0.121\,c_{Hl}^{(3)} + 0.0606\,c_{ll}^{(1)} - 0.121\,\lvert c_{dH}\rvert - 0.00184\,c_{H\Box}\,c_{HDD} - 0.00735\,c_{H\Box}\,c_{Hl}^{(3)} + 0.00368\,c_{H\Box}\,c_{ll}^{(1)} - 0.00735\,c_{H\Box}\,\lvert c_{dH}\rvert + 0.00184\,c_{Hl}^{(3)}\,c_{HDD} + 0.00184\,c_{HDD}\,\lvert c_{dH}\rvert - 0.00367\,c_{Hl}^{(3)}\,c_{ll}^{(1)} + 0.00735\,c_{Hl}^{(3)}\,\lvert c_{dH}\rvert - 0.00367\,c_{ll}^{(1)}\,\lvert c_{dH}\rvert + 0.00367\,(c_{H\Box})^2 + 0.00367\left(c_{Hl}^{(3)}\right)^2 + 0.00367\,(\lvert c_{dH}\rvert)^2$
$H \to \mathrm{all}$	$\Gamma^{\mathrm{total}}/\Gamma_{\mathrm{SM}}^{\mathrm{total}} = 1 - 0.146\,c_{Hl}^{(3)} - 0.0284\,c_{HDD} + 0.0136\,c_{Hq}^{(3)} + 0.0513\,c_{HWB} - 0.0495\,c_{HW} - 0.0628\,c_{HB} + 0.0764\,c_{ll}^{(1)} + 1.37\,c_{HG} - 0.00804\,\lvert c_{uH}\rvert - 0.0852\,\lvert c_{dH}\rvert - 0.00518\,\lvert c_{eH}\rvert + 0.117\,c_{H\Box} + 0.00189\,c_{Hl}^{(3)}\,c_{HW} - 0.00733\,c_{Hl}^{(3)}\,c_{ll}^{(1)} - 0.00517\,c_{H\Box}\,\lvert c_{dH}\rvert + 0.00519\,c_{Hl}^{(3)}\,\lvert c_{dH}\rvert - 0.00172\,c_{H\Box}\,c_{HDD} - 0.027\,c_{HG}\,c_{HW} - 0.0283\,c_{HB}\,c_{HG} + 0.00125\,c_{Hq}^{(3)}\,c_{ll}^{(1)} - 0.00108\,c_{ll}^{(1)}\,c_{HDD} + 0.423\,c_{HB}\,c_{HW} - 0.00258\,c_{ll}^{(1)}\,\lvert c_{dH}\rvert - 0.038\,c_{HDD}\,c_{HG} - 0.0278\,\lvert c_{uH}\rvert\,c_{HG} - 0.00109\,c_{ll}^{(1)}\,c_{HW} - 0.0214\,c_{HG}\,\lvert c_{dH}\rvert - 0.0426\,c_{Hq}^{(3)}\,c_{HG} - 0.0612\,c_{Hl}^{(3)}\,c_{HG} + 0.0021\,c_{Hl}^{(3)}\,c_{HDD} - 0.0285\,c_{H\Box}\,c_{HG} - 0.0212\,c_{HWB}\,c_{HG} - 0.00241\,c_{Hq}^{(3)}\,c_{Hl}^{(3)} - 0.0258\,\lvert c_{eH}\rvert\,c_{HG} - 0.00888\,c_{H\Box}\,c_{Hl}^{(3)} - 0.366\,c_{HWB}\,c_{HW} - 0.0267\,c_{ll}^{(1)}\,c_{HG} + 0.00129\,c_{HDD}\,\lvert c_{dH}\rvert + 0.00463\,c_{H\Box}\,c_{ll}^{(1)} - 0.93\,c_{HB}\,c_{HWB} + 0.00198\left(c_{ll}^{(1)}\right)^2 + 0.00693\left(c_{Hl}^{(3)}\right)^2 + 0.295\,(c_{HWB})^2 + 0.998\,(c_{HB})^2 + 0.00258\,(\lvert c_{dH}\rvert)^2 + 13.5\,(c_{HG})^2 + 0.00354\,(c_{H\Box})^2 + 0.136\,(c_{HW})^2$

L EFT results details

1-dimensional limits on the Wilson coefficients

The likelihood is scanned along a Wilson coefficient with all other coefficients set to 0. Examples of the scan are shown in Figure 11.4. Limits on the Wilson coefficients are set based on the scanned values of the likelihood. A value of a Wilson coefficient is excluded with the confidence level of 68% and 95% if the value of the negative log likelihood is greater by 0.5 and 1.96 than its minimum. These "thresholds" are based on the 68% and 95% quantiles of the *imcomplete gamma function of 1 degree of freedom* since this is a fit with one fitting parameter. (See Appendix H.) A summary of allowed regions for the Wilson coefficients are shown in Figure L.1. The allowed intervals are also summarized in Tables L.1 and L.2.

2-dimensional limits on the Wilson coefficients

2-dimensional limits are derived by scanning the likelihood in the 2-dimensional plane of Wilson coefficients with other coefficients set to 0. Values of Wilson coefficients are excluded with the confidence level of

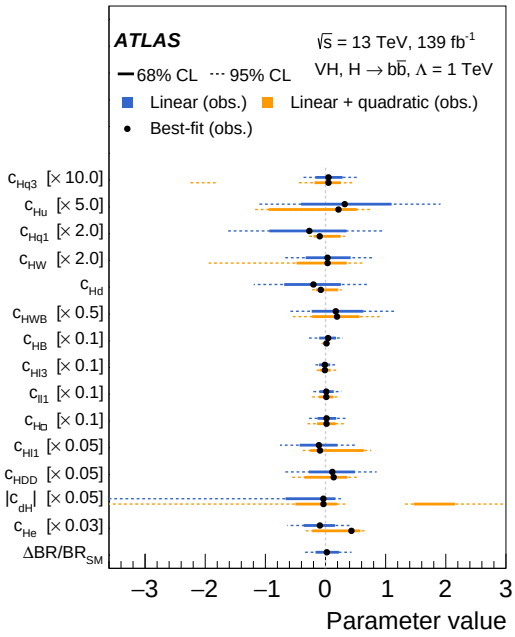

Figure L.1: Summary of the allowed intervals for the relevant Wilson coefficients. The black points show the best fit points. The solid and dashed bars show the intervals of the 68% and 95% confidence level. The orange and blue bars represent the results for the linear and linear+quadratic parametrization, respectively. The values of the Wilson coefficients are scaled as indicated on the y-axis. It is assumed that the scale Λ is 1 TeV .

Table L.1: Derived allowed intervals of 68% confidence level for the Wilson coefficients. Results are shown for the linear and the linear+quadratic parametrizations. It is assumed that the scale Λ is 1 TeV .

Wilson	linear		linear + quadratic	
coefficient	expected (68% CL)	observed (68% CL)	expected (68% CL)	observed (68% CL)
c_{HWB}	[-0.75, 0.86]	[-0.46, 1.3]	[-0.66, 0.89]	[-0.44, 1.1]
c_{HW}	[-0.19, 0.2]	[-0.17, 0.21]	[-0.27, 0.17]	[-0.24, 0.18]
c_{Hu}	[-0.14, 0.15]	[-0.081, 0.22]	[-0.17, 0.08]	[-0.19, 0.1]
$c_{Hq}^{(3)}$	[-0.022, 0.024]	[-0.017, 0.029]	[-0.025, 0.022]	[-0.018, 0.026]
$c_{Hq}^{(1)}$	[-0.32, 0.29]	[-0.47, 0.18]	[-0.08, 0.11]	[-0.1, 0.13]
$c_{ll}^{(1)}$	[-1.2, 1.3]	[-1, 1.4]	[-1.2, 1.2]	[-1, 1.3]
$c_{Hl}^{(3)}$	[-0.99, 0.91]	[-1.1, 0.78]	[-0.93, 0.97]	[-1, 0.83]
$c_{Hl}^{(1)}$	[-6.2, 5.9]	[-8.6, 3.9]	[-4, 11]	[-5.1, 13]
c_{HDD}	[-8.4, 8.2]	[-5.5, 9.8]	[-7.4, 5.7]	[-7, 7.3]
c_{Hd}	[-0.47, 0.44]	[-0.69, 0.26]	[-0.13, 0.18]	[-0.16, 0.21]
$c_{H\Box}$	[-1.6, 1.7]	[-1.3, 1.8]	[-1.6, 1.6]	[-1.4, 1.7]
c_{HB}	[-1.5, 1.4]	[-1.1, 1.8]	[-0.44, 0.58]	[-0.38, 0.56]
c_{He}	[-8.6, 8.3]	[-12, 5.2]	[-5.8, 17]	[-7.3, 19]
$\lvert c_{dH}\rvert$	[-11, 3.7]	[-13, 3.3]	[-8.8, 4.2] $\cup$ [29, 42]	[-10, 3.8] $\cup$ [29, 43]
$\Delta BR/BR_{SM}$	[-0.19, 0.21]	[-0.17, 0.22]	—	—

Table L.2: Derived allowed intervals of 95% confidence level for the Wilson coefficients. Results are shown for the linear and the linear+quadratic parametrizations. It is assumed that the scale Λ is 1 TeV .

Wilson	linear		linear + quadratic	
coefficient	expected (95% CL)	observed (95% CL)	expected (95% CL)	observed (95% CL)
c_{HWB}	[-1.4, 1.8]	[-1.2, 2.3]	[-1.2, 1.8]	[-1.1, 1.9]
c_{HW}	[-0.37, 0.4]	[-0.34, 0.41]	[-0.9, 0.3]	[-0.97, 0.31]
c_{Hu}	[-0.27, 0.3]	[-0.22, 0.38]	[-0.22, 0.13]	[-0.24, 0.15]
$c_{Hq}^{(3)}$	[-0.043, 0.05]	[-0.037, 0.053]	[-0.22, -0.18] $\cup$ [-0.059, 0.042]	[-0.23, -0.18] $\cup$ [-0.047, 0.044]
$c_{Hq}^{(1)}$	[-0.65, 0.56]	[-0.81, 0.47]	[-0.12, 0.15]	[-0.14, 0.16]
$c_{ll}^{(1)}$	[-2.2, 2.6]	[-2, 2.7]	[-2.5, 2.4]	[-2.2, 2.5]
$c_{Hl}^{(3)}$	[-2, 1.7]	[-2.1, 1.6]	[-1.8, 2]	[-1.9, 1.8]
$c_{Hl}^{(1)}$	[-12, 12]	[-15, 9.7]	[-6.7, 14]	[-7.6, 15]
c_{HDD}	[-17, 16]	[-13, 17]	[-11, 9.2]	[-12, 10]
c_{Hd}	[-0.95, 0.84]	[-1.2, 0.69]	[-0.2, 0.25]	[-0.22, 0.27]
$c_{H\Box}$	[-3, 3.4]	[-2.7, 3.5]	[-3.3, 3.1]	[-3, 3.2]
c_{HB}	[-3.3, 2.6]	[-2.7, 2.9]	[-0.72, 0.9]	[-0.67, 0.85]
c_{He}	[-17, 16]	[-21, 13]	[-9.6, 21]	[-11, 23]
$\lvert c_{dH}\rvert$	[-2700, 5.4]	[-∞, 5.2]	[-241, 7] $\cup$ [26, 266]	[-∞, 6.6] $\cup$ [26, ∞]
$\Delta BR/BR_{SM}$	[-0.37, 0.42]	[-0.34, 0.43]	—	—

68% and 95% if the negative log likelihood, $-\ln L$, is greater by 1.15 and 3.00 than the minimum. The "thresholds" correspond to the 68% and 95% quantiles of the *imcomplete gamma function of two degrees of freedom* since this is a fit with two fitting parameters as explained in Appendix H. Examples for the 2-dimensional scan is shown in Figure L.2.

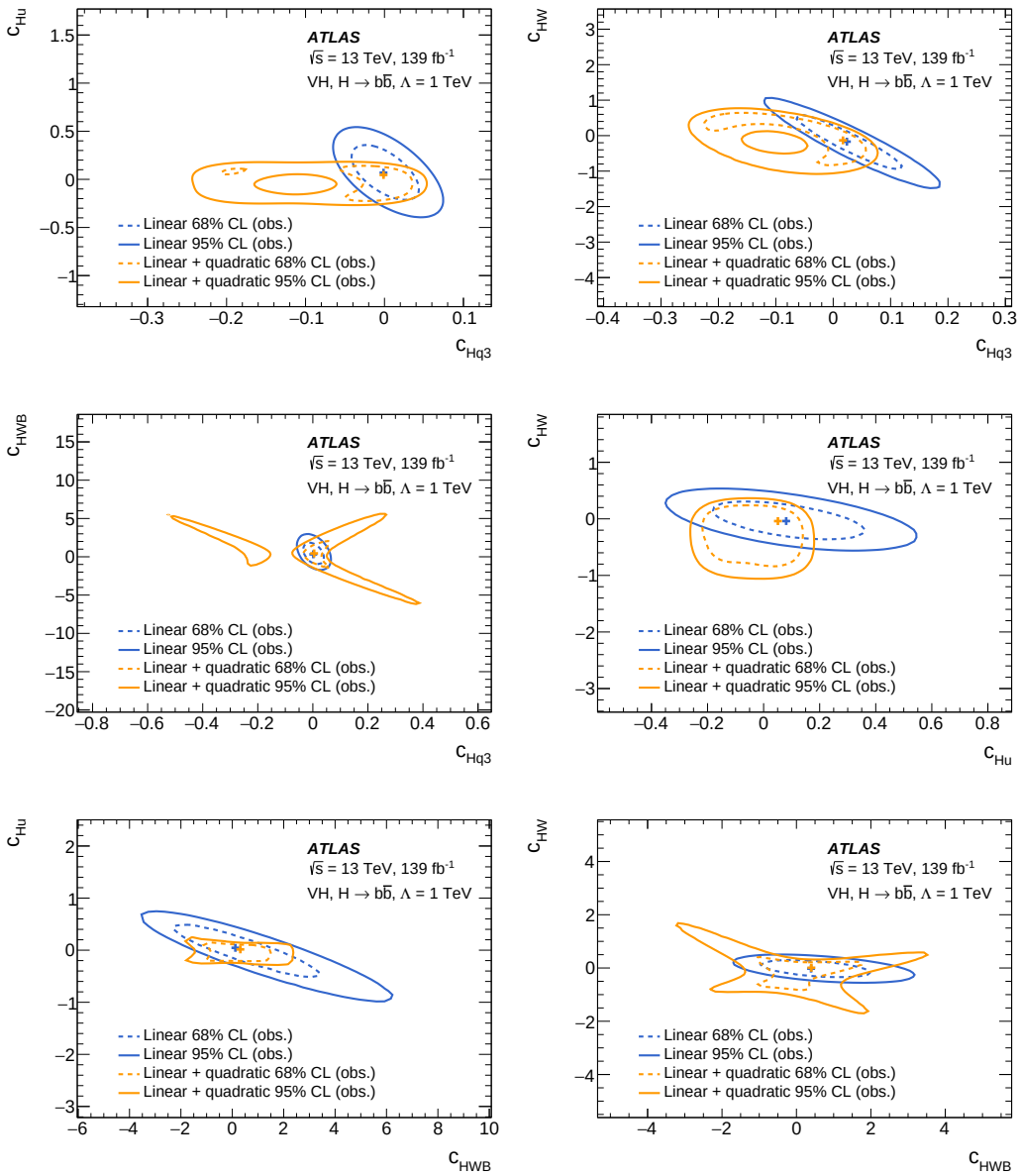

Figure L.2: Example of the contours of the scanned negative log likelihoods derived from the observed data. The dashed and solid curves show the contours of the 68% and 95% confidence level. The blue and orange curves represent the linear and linear+quadratic parametrization, respectively. It is assumed that the scale Λ is 1 TeV .

Bibliography

[1] F. Englert and R. Brout. "Broken Symmetry and the Mass of Gauge Vector Mesons." In: *Phys. Rev. Lett.* 13 (1964), p. 321. DOI: 10.1103/PhysRevLett.13.321.

[2] P. W. Higgs. "Broken symmetries, massless particles and gauge fields." In: *Phys. Lett.* 12 (1964), p. 132. DOI: 10.1016/0031-9163(64)91136-9.

[3] P. W. Higgs. "Broken Symmetries and the Masses of Gauge Bosons." In: *Phys. Rev. Lett.* 13 (1964), p. 508. DOI: 10.1103/PhysRevLett.13.508.

[4] G. S. Guralnik, C. R. Hagen, and T. W. B. Kibble. "Global conservation laws and massless particles." In: *Phys. Rev. Lett.* 13 (1964), p. 585. DOI: 10.1103/PhysRevLett.13.585.

[5] P. W. Higgs. "Spontaneous symmetry breakdown without massless bosons." In: *Phys. Rev.* 145 (1966), p. 1156. DOI: 10.1103/PhysRev.145.1156.

[6] T. W. B. Kibble. "Symmetry breaking in non-Abelian gauge theories." In: *Phys. Rev.* 155 (1967), p. 1554. DOI: 10.1103/PhysRev.155.1554.

[7] ATLAS Collaboration. "Observation of a new particle in the search for the Standard Model Higgs boson with the ATLAS detector at the LHC." In: *Phys. Lett. B* 716 (2012), p. 1. DOI: 10.1016/j.physletb.2012.08.020. arXiv: 1207.7214 [hep-ex].

[8] CMS Collaboration. "Observation of a new boson at a mass of 125 GeV with the CMS experiment at the LHC." In: *Phys. Lett. B* 716 (2012), p. 30. DOI: 10.1016/j.physletb.2012.08.021. arXiv: 1207.7235 [hep-ex].

[9] G. Aad et al. "The ATLAS Experiment at the CERN Large Hadron Collider." In: *JINST* 3 (2008), S08003. DOI: 10.1088/1748-0221/3/08/S08003.

[10] CMS Collaboration. "The CMS experiment at the CERN LHC." In: *JINST* 3 (2008), S08004. DOI: 10.1088/1748-0221/3/08/S08004.

[11] CMS Collaboration. "Observation of the Higgs boson decay to a pair of tau leptons." In: (2017). arXiv: 1708.00373 [hep-ex].

[12] ATLAS Collaboration. "Evidence for the Higgs-boson Yukawa coupling to tau leptons with the ATLAS detector." In: *JHEP* 04 (2015), p. 117. DOI: 10.1007/JHEP04(2015)117. arXiv: 1501.04943 [hep-ex].

[13] ATLAS and CMS Collaborations. "Measurements of the Higgs boson production and decay rates and constraints on its couplings from a combined ATLAS and CMS analysis of the LHC *pp* collision data at $\sqrt{s}$ = 7 and 8 TeV." In: *JHEP* 08 (2016), p. 045. DOI: 10.1007/JHEP08(2016)045. arXiv: 1606.02266 [hep-ex].

[14] ATLAS Collaboration. "Observation of Higgs boson production in association with a top quark pair at the LHC with the ATLAS detector." In: *Phys. Lett. B* 784 (2018), p. 173. DOI: 10.1016/j.physletb.2018.07.035. arXiv: 1806.00425 [hep-ex].

[15] CMS Collaboration. "Observation of $t\bar{t}H$ Production." In: *Phys. Rev. Lett.* 120 (2018), p. 231801. DOI: 10.1103/PhysRevLett.120.231801. arXiv: 1804.02610 [hep-ex].

[16] ATLAS Collaboration. "Observation of $H \to b\bar{b}$ decays and VH production with the ATLAS detector." In: *Phys. Lett. B* 786 (2018), p. 59. DOI: 10.1016/j.physletb.2018.09.013. arXiv: 1808.08238 [hep-ex].

[17] CMS Collaboration. "Observation of Higgs Boson Decay to Bottom Quarks." In: *Phys. Rev. Lett.* 121 (2018), p. 121801. DOI: 10.1103/PhysRevLett.121.121801. arXiv: 1808.08242 [hep-ex].

[18] LHC Higgs Cross Section Working Group et al. "Handbook of LHC Higgs Cross Sections: 2. Differential Distributions." In: *CERN-2012-002* (CERN, Geneva, 2012). arXiv: 1201.3084 [hep-ph].

[19] G. Branco et al. "Theory and phenomenology of two-Higgs-doublet models." In: *Phys. Rept.* 516 (2012), p. 1. DOI: 10.1016/j.physrep.2012.02.002. arXiv: 1106.0034 [hep-ph].

[20] K. Fuyuto, W.-S. Hou, and E. Senaha. "Electroweak baryogenesis driven by extra top Yukawa couplings." In: *Phys. Lett. B* 776 (2018), pp. 402–406. DOI: 10.1016/j.physletb.2017.11.073. arXiv: 1705.05034 [hep-ph].

[21] T. Modak and E. Senaha. "Electroweak baryogenesis via bottom transport." In: *Phys. Rev. D* 99.11 (2019), p. 115022. DOI: 10.1103/PhysRevD.99.115022. arXiv: 1811.08088 [hep-ph].

[22] G. Aad et al. "Study of the spin and parity of the Higgs boson in diboson decays with the ATLAS detector." In: *Eur. Phys. J.* C75.10 (2015). [Erratum: Eur. Phys. J.C76,no.3,152(2016)], p. 476. DOI: 10.1140/epjc/s10052-015-3685-1, 10.1140/epjc/s10052-016-3934-y. arXiv: 1506.05669 [hep-ex].

[23] D. Pappadopulo et al. "Heavy Vector Triplets: Bridging Theory and Data." In: *JHEP* 09 (2014), p. 060. DOI: 10.1007/JHEP09(2014)060. arXiv: 1402.4431 [hep-ph].

[24] R. Contino et al. "On the effect of resonances in composite Higgs phenomenology." In: *JHEP* 10 (2011), p. 081. DOI: 10.1007/JHEP10(2011)081. arXiv: 1109.1570 [hep-ph].

[25] R. Contino et al. "Effective Lagrangian for a light Higgs-like scalar." In: *JHEP* 07 (2013), p. 035. DOI: 10.1007/JHEP07(2013)035. arXiv: 1303.3876 [hep-ph].

[26] B. Grzadkowski et al. "Dimension-Six Terms in the Standard Model Lagrangian." In: *JHEP* 10 (2010), p. 085. DOI: 10.1007/JHEP10(2010)085. arXiv: 1008.4884 [hep-ph].

[27] P. Artoisenet et al. "A framework for Higgs characterisation." In: *JHEP* 11 (2013), p. 043. DOI: 10.1007/JHEP11(2013)043. arXiv: 1306.6464 [hep-ph].

[28] F. Maltoni, K. Mawatari, and M. Zaro. "Higgs characterisation via vector-boson fusion and associated production: NLO and parton-shower effects." In: *Eur. Phys. J. C* 74.1 (2014), p. 2710. DOI: 10.1140/epjc/s10052-013-2710-5. arXiv: 1311.1829 [hep-ph].

[29] ATLAS Collaboration. *A combination of measurements of Higgs boson production and decay using up to* $139\,fb^{-1}$ *of proton–proton collision data at* $\sqrt{s} = 13\,TeV$ *collected with the ATLAS experiment*. ATLAS-CONF-2020-027. 2020. URL: https://cds.cern.ch/record/2725733.

[30] M. E. Peskin and D. V. Schroeder. *An Introduction to quantum field theory*. Reading, USA: Addison-Wesley, 1995. ISBN: 978-0-201-50397-5.

[31] F. Halzen and A. D. Martin. *QUARKS & LEPTONS: An Introductory Course in Modern Particle Physics*. Jan. 1984. ISBN: 978-0-471-88741-6.

[32] LHC Higgs Cross Section Working Group et al. "Handbook of LHC Higgs Cross Sections: 1. Inclusive Observables." In: *CERN-2011-002* (CERN, Geneva, 2011). DOI: 10.5170/CERN-2011-002. arXiv: 1101.0593 [hep-ph].

[33] LHC Higgs Cross Section Working Group. "Handbook of LHC Higgs Cross Sections: 4. Deciphering the Nature of the Higgs Sector." In: *CERN-2017-002-M* (2016). DOI: 10.2172/1345634. arXiv: 1610.07922 [hep-ph].

[34] W. Beenakker et al. "NLO QCD corrections to $t\bar{t}H$ production in hadron collisions." In: *Nucl. Phys. B* 653 (2003), p. 151. DOI: 10.1016/S0550-3213(03)00044-0. arXiv: hep-ph/0211352.

[35] S. Dawson et al. "Next-to-leading order QCD corrections to $pp \to t\bar{t}h$ at the CERN Large Hadron Collider." In: *Phys. Rev. D* 67 (2003), p. 071503. DOI: 10.1103/PhysRevD.67.071503. arXiv: hep-ph/0211438.

[36] S. Dawson et al. "Associated Higgs production with top quarks at the large hadron collider: NLO QCD corrections." In: *Phys. Rev. D* 68 (2003), p. 034022. DOI: 10.1103/PhysRevD.68.034022. arXiv: hep-ph/0305087.

[37] Y. Zhang et al. "QCD NLO and EW NLO corrections to $t\bar{t}H$ production with top quark decays at hadron collider." In: *Phys. Lett. B* 738 (2014), p. 1. DOI: 10.1016/j.physletb.2014.09.022. arXiv: 1407.1110 [hep-ph].

[38] S. Frixione et al. "Weak corrections to Higgs hadroproduction in association with a top-quark pair." In: *JHEP* 09 (2014), p. 065. DOI: 10.1007/JHEP09(2014)065. arXiv: 1407.0823 [hep-ph].

[39] S. Glashow, D. V. Nanopoulos, and A. Yildiz. "Associated production of Higgs bosons and Z particles." In: *Phys. Rev. D* 18 (1978), p. 1724. DOI: 10.1103/PhysRevD.18.1724.

[40] G. Aad et al. "Combined Measurement of the Higgs Boson Mass in pp Collisions at $\sqrt{s} = 7$ and 8 TeV with the ATLAS and CMS Experiments." In: *Phys. Rev. Lett.* 114 (2015), p. 191803. DOI: 10.1103/PhysRevLett.114.191803. arXiv: 1503.07589 [hep-ex].

[41] LHC Higgs Cross Section Working Group. *SM Higgs production cross sections at 13 TeV*. https://twiki.cern.ch/twiki/bin/view/LHCPhysics/CERNYellowReportPageAt13TeV.

[42] L. H.C.S. W. Group. "LHC Higgs Cross Section Working Group." In: (2016). https://twiki.cern.ch/twiki/bin/view/L URL: https://twiki.cern.ch/twiki/bin/view/LHCPhysics/LHCHXSWG (visited on 03/18/2016).

[43] C. Anastasiou et al. "High precision determination of the gluon fusion Higgs boson cross-section at the LHC." In: *JHEP* 05 (2016), p. 058. DOI: 10.1007/JHEP05(2016)058. arXiv: 1602.00695 [hep-ph].

[44] M. Botje et al. "The PDF4LHC Working Group Interim Recommendations." In: (2011). arXiv: 1101.0538 [hep-ph].

[45] B. Mellado Garcia et al. *CERN Report 4: Part I Standard Model Predictions*. Tech. rep. LHCHXSWG-DRAFT-INT-2016-008. Geneva: CERN, 2016. URL: https://cds.cern.ch/record/2150771.

[46] A. Sakharov. "Violation of CP Invariance, C asymmetry, and baryon asymmetry of the universe." In: *Sov. Phys. Usp.* 34.5 (1991), pp. 392–393. DOI: 10.1070/PU1991v034n05ABEH002497.

[47] P. Huet and E. Sather. "Electroweak baryogenesis and standard model CP violation." In: *Phys. Rev. D* 51 (1995), pp. 379–394. DOI: 10.1103/PhysRevD.51.379. arXiv: hep-ph/9404302.

[48] Y. A. Gol'fand and E. P. Likhtman. "Extension of the Algebra of Poincare Group Generators and Violation of p Invariance." In: *JETP Lett.* 13 (1971). [Pisma Zh.Eksp.Teor.Fiz.13:452-455,1971], pp. 323–326.

[49] J. Wess and B. Zumino. "Supergauge Transformations in Four-Dimensions." In: *Nucl. Phys. B* 70 (1974), pp. 39–50. DOI: 10.1016/0550-3213(74)90355-1.

[50] A. Salam and J. A. Strathdee. "Supersymmetry and Nonabelian Gauges." In: *Phys. Lett. B* 51 (1974), pp. 353–355. DOI: 10.1016/0370-2693(74)90226-3.

[51] I. Brivio, Y. Jiang, and M. Trott. "The SMEFTsim package, theory and tools." In: *JHEP* 12 (2017), p. 070. DOI: 10.1007/JHEP12(2017)070. arXiv: 1709.06492 [hep-ph].

[52] G. Aad et al. "Search for diboson resonances in hadronic final states in 139 fb^{-1} of pp collisions at $\sqrt{s}$ = 13 TeV with the ATLAS detector." In: *JHEP* 09 (2019). [Erratum: JHEP 06, 042 (2020)], p. 091. DOI: 10.1007/JHEP09(2019)091. arXiv: 1906.08589 [hep-ex].

[53] G. Aad et al. "Search for heavy diboson resonances in semileptonic final states in pp collisions at $\sqrt{s}$ = 13 TeV with the ATLAS detector." In: *Eur. Phys. J. C* 80.12 (2020), p. 1165. DOI: 10.1140/epjc/s10052-020-08554-y. arXiv: 2004.14636 [hep-ex].

[54] K. Agashe, R. Contino, and A. Pomarol. "The Minimal composite Higgs model." In: *Nucl. Phys. B* 719 (2005), pp. 165–187. DOI: 10.1016/j.nuclphysb.2005.04.035. arXiv: hep-ph/0412089.

[55] V. D. Barger, W.-Y. Keung, and E. Ma. "A Gauge Model With Light W and Z Bosons." In: *Phys. Rev. D* 22 (1980), p. 727. DOI: 10.1103/PhysRevD.22.727.

[56] V. Andreev et al. "Improved limit on the electric dipole moment of the electron." In: *Nature* 562.7727 (2018), pp. 355–360. DOI: 10.1038/s41586-018-0599-8.

[57] K. Fuyuto, W.-S. Hou, and E. Senaha. "Cancellation mechanism for the electron electric dipole moment connected with the baryon asymmetry of the Universe." In: *Phys. Rev. D* 101 (1 2020), p. 011901. DOI: 10.1103/PhysRevD.101.011901. URL: https://link.aps.org/doi/10.1103/PhysRevD.101.011901.

[58] J. de Blas et al. "Higgs Boson Studies at Future Particle Colliders." In: *JHEP* 01 (2020), p. 139. DOI: 10.1007/JHEP01(2020)139. arXiv: 1905.03764 [hep-ph].

[59] "LHC Design Report Vol.1: The LHC Main Ring." In: (June 2004). Ed. by O. S. Bruning et al. DOI: 10.5170/CERN-2004-003-V-1. URL: https://cds.cern.ch/record/782076.

[60] "LHC Design Report. 3. The LHC injector chain." In: (Dec. 2004). Ed. by M. Benedikt et al. DOI: 10.5170/CERN-2004-003-V-3.

[61] E. Mobs. "The CERN accelerator complex - 2019, Complexe des accélérateurs du CERN - 2019." In: (2019). URL: https://cds.cern.ch/record/2684277/.

[62] J. Alves A.Augusto et al. "The LHCb Detector at the LHC." In: *JINST* 3 (2008), S08005. DOI: 10.1088/1748-0221/3/08/S08005.

[63] K. Aamodt et al. "The ALICE experiment at the CERN LHC." In: *JINST* 3 (2008), S08002. DOI: 10.1088/1748-0221/3/08/S08002.

[64] ATLAS Collaboration. "Performance of the ATLAS Transition Radiation Tracker in Run 1 of the LHC: tracker properties." In: *JINST* 12 (2017), P05002. DOI: 10.1088/1748-0221/12/05/P05002. arXiv: 1702.06473 [hep-ex].

[65] ATLAS Collaboration. "Topological cell clustering in the ATLAS calorimeters and its performance in LHC Run 1." In: *Eur. Phys. J. C* 77 (2017), p. 490. DOI: 10.1140/epjc/s10052-017-5004-5. arXiv: 1603.02934 [hep-ex].

[66] ATLAS Collaboration. *Standard Model Summary Plots Spring 2020*. ATL-PHYS-PUB-2020-010. 2020. URL: http://cdsweb.cern.ch/record/2718937.

[67] ATLAS Collaboration. "Performance of the ATLAS trigger system in 2015." In: *Eur. Phys. J. C* 77 (2017), p. 317. DOI: 10.1140/epjc/s10052-017-4852-3. arXiv: 1611.09661 [hep-ex].

[68] ATLAS Collaboration. "Trigger menu in 2018." In: (2019). URL: https://cds.cern.ch/record/2693402.

[69] ATLAS Collaboration. "2015 start-up trigger menu and initial performance assessment of the ATLAS trigger using Run-2 data." In: (2016). URL: http://cdsweb.cern.ch/record/2136007.

[70] ATLAS Collaboration. "Trigger menu in 2016." In: (2017). URL: http://cdsweb.cern.ch/record/2242069.

[71] ATLAS Collaboration. "Trigger Menu in 2017." In: (2018). URL: http://cdsweb.cern.ch/record/2625986.

[72] ATLAS collaboration. *LuminosityPublicResultsRun2*. 2020. URL: https://twiki.cern.ch/twiki/bin/view/AtlasPublic/LuminosityPublicResultsRun2.

[73] ATLAS Collaboration. "The ATLAS Simulation Infrastructure." In: *Eur. Phys. J. C* 70 (2010), p. 823. DOI: 10.1140/epjc/s10052-010-1429-9. arXiv: 1005.4568 [physics.ins-det].

[74] S. Agostinelli et al. "GEANT4: a simulation toolkit." In: *Nucl. Instrum. Meth. A* 506 (2003), pp. 250–303. DOI: 10.1016/S0168-9002(03)01368-8.

[75] T. Sjöstrand, S. Mrenna, and P. Z. Skands. "A brief introduction to PYTHIA 8.1." In: *Comput. Phys. Commun.* 178 (2008), pp. 852–867. DOI: 10.1016/j.cpc.2008.01.036. arXiv: 0710.3820 [hep-ph].

[76] ATLAS Collaboration. *The Pythia 8 A3 tune description of ATLAS minimum bias and inelastic measurements incorporating the Donnachie–Landshoff diffractive model*. ATL-PHYS-PUB-2016-017. 2016. URL: https://cds.cern.ch/record/2206965.

[77] R. D. Ball et al. "Parton distributions with LHC data." In: *Nucl. Phys.* B867 (2013), pp. 244–289. DOI: 10.1016/j.nuclphysb.2012.10.003. arXiv: 1207.1303 [hep-ph].

[78] E. Bothmann et al. "Event Generation with Sherpa 2.2." In: *SciPost Phys.* 7.3 (2019), p. 034. DOI: 10.21468/SciPostPhys.7.3.034. arXiv: 1905.09127 [hep-ph].

[79] D. Lange. "The EvtGen particle decay simulation package." In: *Nucl. Instrum. Meth. A* 462 (2001), pp. 152–155. DOI: 10.1016/S0168-9002(01)00089-4.

[80] S. Alioli et al. "A general framework for implementing NLO calculations in shower Monte Carlo programs: the POWHEG BOX." In: *JHEP* 06 (2010), p. 043. DOI: 10.1007/JHEP06(2010)043. arXiv: 1002.2581 [hep-ph].

[81] G. Cullen et al. "Automated one-loop calculations with GOSAM." In: *Eur. Phys. J. C* 72 (2012), p. 1889. DOI: 10.1140/epjc/s10052-012-1889-1. arXiv: 1111.2034 [hep-ph].

[82] K. Hamilton, P. Nason, and G. Zanderighi. "MINLO: multi-scale improved NLO." In: *JHEP* 10 (2012), p. 155. DOI: 10.1007/JHEP10(2012)155. arXiv: 1206.3572 [hep-ph].

[83] G. Luisoni et al. "$HW^{\pm}/HZ$ + 0 and 1 jet at NLO with the POWHEG BOX interfaced to GoSam and their merging within MiNLO." In: *JHEP* 10 (2013), p. 083. DOI: 10.1007/JHEP10(2013)083. arXiv: 1306.2542 [hep-ph].

[84] R. D. Ball et al. "Parton distributions for the LHC Run II." In: *JHEP* 04 (2015), p. 040. DOI: 10.1007/JHEP04(2015)040. arXiv: 1410.8849 [hep-ph].

[85] ATLAS Collaboration. "Measurement of the Z/γ^* boson transverse momentum distribution in pp collisions at $\sqrt{s}$ = 7 TeV with the ATLAS detector." In: *JHEP* 09 (2014), p. 145. DOI: 10.1007/JHEP09(2014)145. arXiv: 1406.3660 [hep-ex].

[86] M. Ciccolini, S. Dittmaier, and M. Kramer. "Electroweak radiative corrections to associated WH and ZH production at hadron colliders." In: *Phys.Rev.* D68 (2003), p. 073003. DOI: 10.1103/PhysRevD.68.073003. arXiv: hep-ph/0306234 [hep-ph].

[87] O. Brein, A. Djouadi, and R. Harlander. "NNLO QCD corrections to the Higgs-strahlung processes at hadron colliders." In: *Phys.Lett.* B579 (2004), pp. 149–156. DOI: 10.1016/j.physletb.2003.10.112. arXiv: hep-ph/0307206 [hep-ph].

[88] G. Ferrera, M. Grazzini, and F. Tramontano. "Associated WH production at hadron colliders: a fully exclusive QCD calculation at NNLO." In: *Phys.Rev.Lett.* 107 (2011), p. 152003. DOI: 10.1103/PhysRevLett.107.152003. arXiv: 1107.1164 [hep-ph].

[89] O. Brein et al. "Top-Quark Mediated Effects in Hadronic Higgs-Strahlung." In: *Eur. Phys. J.* C72 (2012), p. 1868. DOI: 10.1140/epjc/s10052-012-1868-6. arXiv: 1111.0761 [hep-ph].

[90] G. Ferrera, M. Grazzini, and F. Tramontano. "Higher-order QCD effects for associated WH production and decay at the LHC." In: *JHEP* 04 (2014), p. 039. DOI: 10.1007/JHEP04(2014)039. arXiv: 1312.1669 [hep-ph].

[91] G. Ferrera, M. Grazzini, and F. Tramontano. "Associated ZH production at hadron colliders: the fully differential NNLO QCD calculation." In: *Phys. Lett. B* 740 (2015), p. 51. DOI: 10.1016/j.physletb.2014.11.040. arXiv: 1407.4747 [hep-ph].

[92] J. M. Campbell, R. K. Ellis, and C. Williams. "Associated production of a Higgs boson at NNLO." In: *JHEP* 06 (2016), p. 179. DOI: 10.1007/JHEP06(2016)179. arXiv: 1601.00658 [hep-ph].

[93] A. Denner et al. "Electroweak corrections to Higgs-strahlung off W/Z bosons at the Tevatron and the LHC with Hawk." In: *JHEP* 03 (2012), p. 075. DOI: 10.1007/JHEP03(2012)075. arXiv: 1112.5142 [hep-ph].

[94] L. Altenkamp et al. "Gluon-induced Higgs-strahlung at next-to-leading order QCD." In: *JHEP* 02 (2013), p. 078. DOI: 10.1007/JHEP02(2013)078. arXiv: 1211.5015 [hep-ph].

[95] B. Hespel, F. Maltoni, and E. Vryonidou. "Higgs and Z boson associated production via gluon fusion in the SM and the 2HDM." In: *JHEP* 06 (2015), p. 065. DOI: 10.1007/JHEP06(2015)065. arXiv: 1503.01656 [hep-ph].

[96] R. V. Harlander et al. "Soft gluon resummation for gluon-induced Higgs Strahlung." In: *JHEP* 11 (2014), p. 082. DOI: 10.1007/JHEP11(2014)082. arXiv: 1410.0217 [hep-ph].

[97] R. V. Harlander, S. Liebler, and T. Zirke. "Higgs Strahlung at the Large Hadron Collider in the 2-Higgs-doublet model." In: *JHEP* 02 (2014), p. 023. DOI: 10.1007/JHEP02(2014)023. arXiv: 1307.8122 [hep-ph].

[98] O. Brein, R. V. Harlander, and T. J. E. Zirke. "vh@nnlo - Higgs Strahlung at hadron colliders." In: *Comput. Phys. Commun.* 184 (2013), pp. 998–1003. DOI: 10.1016/j.cpc.2012.11.002. arXiv: 1210.5347 [hep-ph].

[99] A. Denner et al. "HAWK 2.0: A Monte Carlo program for Higgs production in vector-boson fusion and Higgs strahlung at hadron colliders." In: *Comput. Phys. Commun.* 195 (2015), pp. 161–171. DOI: 10.1016/j.cpc.2015.04.021. arXiv: 1412.5390 [hep-ph].

[100] F. Cascioli, P. Maierhöfer, and S. Pozzorini. "Scattering Amplitudes with Open Loops." In: *Phys. Rev. Lett.* 108 (2012), p. 111601. DOI: 10.1103/PhysRevLett.108.111601. arXiv: 1111.5206 [hep-ph].

[101] T. Gleisberg and S. Höche. "Comix, a new matrix element generator." In: *JHEP* 12 (2008), p. 039. DOI: 10.1088/1126-6708/2008/12/039. arXiv: 0808.3674 [hep-ph].

[102] S. Schumann and F. Krauss. "A parton shower algorithm based on Catani-Seymour dipole factorisation." In: *JHEP* 03 (2008), p. 038. DOI: 10.1088/1126-6708/2008/03/038. arXiv: 0709.1027 [hep-ph].

[103] S. Höche et al. "QCD matrix elements + parton showers. The NLO case." In: *JHEP* 04 (2013), p. 027. DOI: 10.1007/JHEP04(2013)027. arXiv: 1207.5030 [hep-ph].

[104] S. Catani et al. "Vector Boson Production at Hadron Colliders: A Fully Exclusive QCD Calculation at Next-to-Next-to-Leading Order." In: *Phys. Rev. Lett.* 103 (2009), p. 082001. DOI: 10.1103/PhysRevLett.103.082001. arXiv: 0903.2120 [hep-ph].

[105] J Butterworth et al. *Single Boson and Diboson Production Cross Sections in pp Collisions at sqrts=7 TeV*. Tech. rep. ATL-COM-PHYS-2010-695. Geneva: CERN, 2010. URL: https://cds.cern.ch/record/1287902.

[106] S. Frixione, P. Nason, and G. Ridolfi. "A positive-weight next-to-leading-order Monte Carlo for heavy flavour hadron production." In: *JHEP* 09 (2007), p. 126. DOI: 10.1088/1126-6708/2007/09/126. arXiv: 0707.3088 [hep-ph].

[107] *ATLAS Run 1 Pythia8 tunes*. Tech. rep. ATL-PHYS-PUB-2014-021. Geneva: CERN, 2014. URL: https://cds.cern.ch/record/1966419.

[108] *Studies on top-quark Monte Carlo Modelling for Top 2016*. Tech. rep. ATL-PHYS-PUB-2016-020. Geneva: CERN, 2016. URL: https://cds.cern.ch/record/2216168.

[109] M. Czakon and A. Mitov. "Top++: A program for the calculation of the top-pair cross-section at hadron colliders." In: *Comput. Phys. Commun.* 185 (2014), p. 2930. DOI: 10.1016/j.cpc.2014.06.021. arXiv: 1112.5675 [hep-ph].

[110] E. Re. "Single-top Wt-channel production matched with parton showers using the POWHEG method." In: *Eur. Phys. J. C* 71 (2011), p. 1547. DOI: 10.1140/epjc/s10052-011-1547-z. arXiv: 1009.2450 [hep-ph].

[111] S. Alioli et al. "NLO single-top production matched with shower in POWHEG: s- and t-channel contributions." In: *JHEP* 09 (2009). [Erratum: JHEP 02 (2010) 011], p. 111. DOI: 10.1088/1126-6708/2009/09/111. arXiv: 0907.4076 [hep-ph].

[112] N. Kidonakis. "Two-loop soft anomalous dimensions for single top quark associated production with a W^- or H^-." In: *Phys. Rev. D* 82 (2010), p. 054018. DOI: 10.1103/PhysRevD.82.054018. arXiv: 1005.4451 [hep-ph].

[113] N. Kidonakis. "Next-to-next-to-leading resummation for s-channel single top quark production." In: *Phys. Rev. D* 81 (2010), p. 054028. DOI: 10.1103/PhysRevD.81.054028. arXiv: 1001.5034 [hep-ph].

[114] N. Kidonakis. "Next-to-next-to-leading-order collinear and soft gluon corrections for t-channel single top quark production." In: *Phys. Rev. D* 83 (2011), p. 091503. DOI: 10.1103/PhysRevD.83.091503. arXiv: 1103.2792 [hep-ph].

[115] ATLAS Collaboration. "Performance of the ATLAS track reconstruction algorithms in dense environments in LHC Run 2." In: *Eur. Phys. J. C* 77 (2017), p. 673. DOI: 10.1140/epjc/s10052-017-5225-7. arXiv: 1704.07983 [hep-ex].

[116] R. Fruehwirth. "Application of Kalman Filtering to Track Fitting in the DELPHI Detector." In: (Mar. 1987).

[117] ATLAS Collaboration. "Reconstruction of primary vertices at the ATLAS experiment in Run 1 proton–proton collisions at the LHC." In: *Eur. Phys. J. C* 77 (2017), p. 332. DOI: 10.1140/epjc/s10052-017-4887-5. arXiv: 1611.10235 [hep-ex].

[118] ATLAS Collaboration. "A neural network clustering algorithm for the ATLAS silicon pixel detector." In: *JINST* 9 (2014), P09009. DOI: 10.1088/1748-0221/9/09/P09009. arXiv: 1406.7690 [hep-ex].

[119] W. Lampl et al. *Calorimeter Clustering Algorithms: Description and Performance*. ATL-LARG-PUB-2008-002. 2008. URL: https://cds.cern.ch/record/1099735.

[120] ATLAS Collaboration. "Electron and photon performance measurements with the ATLAS detector using the 2015-2017 LHC proton–proton collision data." In: *JINST* 14.12 (2019), P12006. DOI: 10.1088/1748-0221/14/12/P12006. arXiv: 1908.00005 [hep-ex].

[121] "Electron reconstruction and identification in the ATLAS experiment using the 2015 and 2016 LHC proton-proton collision data at $\sqrt{s}$ = 13 TeV." In: *Eur. Phys. J.* C79.8 (2019), p. 639. DOI: 10.1140/epjc/s10052-019-7140-6. arXiv: 1902.04655 [physics.ins-det].

[122] R. Frühwirth. "Application of Kalman filtering to track and vertex fitting." In: *Nuclear Instruments and Methods in Physics Research Section A: Accelerators, Spectrometers, Detectors and Associated Equipment* 262.2 (1987), pp. 444 –450. ISSN: 0168-9002. DOI: https://doi.org/10.1016/0168-9002(87)90887-4. URL: http://www.sciencedirect.com/science/article/pii/0168900287908874.

[123] D. W. Scott. *Multivariate Density Estimation, Theory, Practice, and Visualization*. Wiley-Interscience, 1992. DOI: 10.1002/9780470316849.

[124] A. Hoecker et al. *TMVA - Toolkit for Multivariate Data Analysis*. 2007. arXiv: 0703039 [physics.data-an].

[125] ATLAS Collaboration. "Muon reconstruction performance of the ATLAS detector in proton–proton collision data at $\sqrt{s}$ = 13 TeV." In: *Eur. Phys. J. C* 76 (2016), p. 292. DOI: 10.1140/epjc/s10052-016-4120-y. arXiv: 1603.05598 [hep-ex].

[126] M. Cacciari, G. P. Salam, and G. Soyez. "The anti-k_t jet clustering algorithm." In: *JHEP* 04 (2008), p. 063. DOI: 10.1088/1126-6708/2008/04/063. arXiv: 0802.1189 [hep-ph].

[127] M. Cacciari, G. P. Salam, and G. Soyez. "FastJet User Manual." In: *Eur. Phys. J. C* 72 (2012), p. 1896. DOI: 10.1140/epjc/s10052-012-1896-2. arXiv: 1111.6097 [hep-ph].

[128] ATLAS Collaboration. *Tagging and suppression of pileup jets with the ATLAS detector*. Tech. rep. ATLAS-CONF-2014-018. Geneva: CERN, 2014. URL: https://cds.cern.ch/record/1700870.

[129] ATLAS Collaboration. "Performance of pile-up mitigation techniques for jets in pp collisions at $\sqrt{s}$ = 8 TeV using the ATLAS detector." In: *Eur. Phys. J. C* 76.11 (2016), p. 581. DOI: 10.1140/epjc/s10052-016-4395-z. arXiv: 1510.03823 [hep-ex].

[130] ATLAS Collaboration. "Jet energy measurement with the ATLAS detector in proton–proton collisions at $\sqrt{s}$ = 7 TeV." In: *Eur. Phys. J. C* 73 (2013), p. 2304. DOI: 10.1140/epjc/s10052-013-2304-2. arXiv: 1112.6426 [hep-ex].

[131] ATLAS Collaboration. "Jet energy scale measurements and their systematic uncertainties in proton–proton collisions at $\sqrt{s}$ = 13 TeV with the ATLAS detector." In: *Phys. Rev. D* 96 (2017), p. 072002. DOI: 10.1103/PhysRevD.96.072002. arXiv: 1703.09665 [hep-ex].

[132] M. Cacciari, G. P. Salam, and G. Soyez. "The Catchment Area of Jets." In: *JHEP* 04 (2008). DOI: 10.1088/1126-6708/2008/04/005. eprint: 0802.1188. URL: https://iopscience.iop.org/article/10.1088/1126-6708/2008/04/005.

[133] *Selection of jets produced in 13TeV proton-proton collisions with the ATLAS detector*. Tech. rep. ATLAS-CONF-2015-029. Geneva: CERN, 2015. URL: https://cds.cern.ch/record/2037702.

[134] J. Gonski. *Jet Cleaning in 2016 and the Event Level Cleaning Tool*. Tech. rep. ATL-COM-PHYS-2017-982. Geneva: CERN, 2017. URL: https://cds.cern.ch/record/2272136.

[135] ATLAS Collaboration. E_T^{miss} *performance in the ATLAS detector using 2015–2016 LHC pp collisions*. ATLAS-CONF-2018-023. 2018. URL: https://cds.cern.ch/record/2625233.

[136] ATLAS Collaboration. "ATLAS b-jet identification performance and efficiency measurement with $t\bar{t}$ events in pp collisions at $\sqrt{s}$ = 13 TeV." In: (2019). arXiv: 1907.05120 [hep-ex].

[137] S. Badger et al. "Les Houches 2015: Physics at TeV Colliders Standard Model Working Group Report." In: (2016). arXiv: 1605.04692 [hep-ph]. URL: https://lss.fnal.gov/archive/2016/conf/fermilab-conf-16-175-ppd-t.pdf.

[138] N. Berger et al. "Simplified Template Cross Sections - Stage 1.1." In: (2019). arXiv: 1906.02754 [hep-ph].

[139] D. Gonçalves and J. Nakamura. "Role of the Z polarization in the $H \to b\bar{b}$ measurement." In: *Phys. Rev. D* 98 (9 2018), p. 093005. DOI: 10.1103/PhysRevD.98.093005. URL: https://link.aps.org/doi/10.1103/PhysRevD.98.093005.

[140] ATLAS Collaboration. "Electron reconstruction and identification in the ATLAS experiment using the 2015 and 2016 LHC proton–proton collision data at $\sqrt{s}$ = 13 TeV." In: *Eur. Phys. J. C* 79 (2019), p. 639. DOI: 10.1140/epjc/s10052-019-7140-6. arXiv: 1902.04655 [hep-ex].

[141] ATLAS Collaboration. "Jet energy resolution in proton–proton collisions at $\sqrt{s}$ = 7 TeV recorded in 2010 with the ATLAS detector." In: *Eur. Phys. J. C* 73 (2013), p. 2306. DOI: 10.1140/epjc/s10052-013-2306-0. arXiv: 1210.6210 [hep-ex].

[142] ATLAS Collaboration. "Performance of missing transverse momentum reconstruction with the ATLAS detector using proton–proton collisions at $\sqrt{s}$ = 13 TeV." In: *Eur. Phys. J. C* 78 (2018), p. 903. DOI: 10.1140/epjc/s10052-018-6288-9. arXiv: 1802.08168 [hep-ex].

[143] ATLAS Collaboration. "Luminosity determination in pp collisions at $\sqrt{s}$ = 8 TeV using the ATLAS detector at the LHC." In: *Eur. Phys. J. C* 76 (2016), p. 653. DOI: 10.1140/epjc/s10052-016-4466-1. arXiv: 1608.03953 [hep-ex].

[144] G. Avoni et al. "The new LUCID-2 detector for luminosity measurement and monitoring in ATLAS." In: *JINST* 13.07 (2018), P07017. DOI: 10.1088/1748-0221/13/07/P07017.

[145] ATLAS Collaboration. "Measurement of the Inelastic Proton–Proton Cross Section at $\sqrt{s} = 13$ TeV with the ATLAS Detector at the LHC." In: *Phys. Rev. Lett.* 117 (2016), p. 182002. DOI: 10.1103/PhysRevLett.117.182002. arXiv: 1606.02625 [hep-ex].

[146] ATLAS Collaboration. *Evaluation of theoretical uncertainties for simplified template cross section measurements of V-associated production of the Higgs boson*. ATL-PHYS-PUB-2018-035. 2018. URL: https://cds.cern.ch/record/2649241.

[147] A. Denner et al. "Electroweak corrections to Higgs-strahlung off W/Z bosons at the Tevatron and LHC with HAWK." In: *JHEP* 03 (2012), p. 075. DOI: 10.1007/JHEP03(2012)075. arXiv: 1211.5142 [hep-ph].

[148] I. W. Stewart and F. J. Tackmann. "Theory uncertainties for Higgs mass and other searches using jet bins." In: *Phys. Rev. D* 85 (3 2012), p. 034011. DOI: 10.1103/PhysRevD.85.034011. URL: http://link.aps.org/doi/10.1103/PhysRevD.85.034011.

[149] J. Butterworth et al. "PDF4LHC recommendations for LHC Run II." In: *J. Phys.* G43 (2016), p. 023001. DOI: 10.1088/0954-3899/43/2/023001. arXiv: 1510.03865 [hep-ph].

[150] L. A. Harland-Lang et al. "Parton distributions in the LHC era: MMHT 2014 PDFs." In: *Eur. Phys. J.* C75.5 (2015), p. 204. DOI: 10.1140/epjc/s10052-015-3397-6. arXiv: 1412.3989 [hep-ph].

[151] S. Dulat et al. "New parton distribution functions from a global analysis of quantum chromodynamics." In: *Phys. Rev.* D93.3 (2016), p. 033006. DOI: 10.1103/PhysRevD.93.033006. arXiv: 1506.07443 [hep-ph].

[152] J. Gao and P. Nadolsky. "A meta-analysis of parton distribution functions." In: *JHEP* 07 (2014), p. 035. DOI: 10.1007/JHEP07(2014)035. arXiv: 1401.0013 [hep-ph].

[153] S. Carrazza et al. "An Unbiased Hessian Representation for Monte Carlo PDFs." In: *Eur. Phys. J.* C75.8 (2015), p. 369. DOI: 10.1140/epjc/s10052-015-3590-7. arXiv: 1505.06736 [hep-ph].

[154] G. Watt and R. S. Thorne. "Study of Monte Carlo approach to experimental uncertainty propagation with MSTW 2008 PDFs." In: *JHEP* 08 (2012), p. 052. DOI: 10.1007/JHEP08(2012)052. arXiv: 1205.4024 [hep-ph].

[155] R. J. Barlow and C. Beeston. "Fitting using finite Monte Carlo samples." In: *Comput. Phys. Commun.* 77 (1993), pp. 219–228. DOI: 10.1016/0010-4655(93)90005-W.

[156] G. Cowan et al. "Asymptotic formulae for likelihood-based tests of new physics." In: *Eur. Phys. J. C* 71 (2011). [Erratum: Eur. Phys. J. C 73 (2013) 2501], p. 1554. DOI: 10.1140/epjc/s10052-011-1554-0. arXiv: 1007.1727 [physics.data-an].

[157] L. Lehman. "Extending the Standard Model Effective Field Theory with the Complete Set of Dimension-7 Operators." In: *Phys. Rev. D* 90.12 (2014), p. 125023. DOI: 10.1103/PhysRevD.90.125023. arXiv: 1410.4193 [hep-ph].

[158] F. F. Deppisch et al. "Falsifying High-Scale Baryogenesis with Neutrinoless Double Beta Decay and Lepton Flavor Violation." In: *Phys. Rev. D* 92.3 (2015), p. 036005. DOI: 10.1103/PhysRevD.92.036005. arXiv: 1503.04825 [hep-ph].

[159] J. Alwall et al. "The automated computation of tree-level and next-to-leading order differential cross sections, and their matching to parton shower simulations." In: *JHEP* 07 (2014), p. 79. DOI: 10.1007/JHEP07(2014)079. arXiv: 1405.0301 [hep-ph].

[160] M. Bahr et al. "Herwig++ physics and manual." In: *Eur. Phys. J. C* 58 (2008), pp. 639–707. DOI: 10.1140/epjc/s10052-008-0798-9. arXiv: 0803.0883 [hep-ph].

[161] ATLAS Collaboration. "Test of CP invariance in vector-boson fusion production of the Higgs boson in the $H \to \tau\tau$ channel in proton–proton collisions at $\sqrt{s} = 13$ TeV with the ATLAS detector." In: *Phys. Lett. B* 805 (2020), p. 135426. DOI: 10.1016/j.physletb.2020.135426. arXiv: 2002.05315 [hep-ex].

[162] ATLAS Collaboration. *Luminosity determination in pp collisions at $\sqrt{s} = 13$ TeV using the ATLAS detector at the LHC*. ATLAS-CONF-2019-021. 2019. URL: https://cds.cern.ch/record/2677054.

[163] ATLAS Collaboration. *Measurement of the properties of Higgs boson production at $\sqrt{s} = 13$ TeV in the $H \to \gamma\gamma$ channel using 139 fb^{-1} of pp collision data with the ATLAS experiment*. ATLAS-CONF-2020-026. 2020. URL: https://atlas.web.cern.ch/Atlas/GROUPS/PHYSICS/CONFNOTES/ATLAS-CONF-2020-026.

[164] ATLAS Collaboration. "Higgs boson production cross-section measurements and their EFT interpretation in the 4ℓ decay channel at $\sqrt{s} = 13$ TeV with the ATLAS detector." In: *Submitted to: EPJC* (Apr. 2020). arXiv: 2004.03447 [hep-ex].

[165] ATLAS Collaboration. "Evidence for the associated production of the Higgs boson and a top quark pair with the ATLAS detector." In: *Phys. Rev. D* 97 (2018), p. 072003. DOI: 10.1103/PhysRevD.97.072003. arXiv: 1712.08891 [hep-ex].

[166] ATLAS Collaboration. "Measurements of gluon-gluon fusion and vector-boson fusion Higgs boson production cross-sections in the $H \to WW^* \to e\nu\mu\nu$ decay channel in pp collisions at $\sqrt{s} = 13$ TeV with the ATLAS detector." In: *Phys. Lett. B* 789 (2019), p. 508. DOI: 10.1016/j.physletb.2018.11.064. arXiv: 1808.09054 [hep-ex].

[167] ATLAS Collaboration. "Cross-section measurements of the Higgs boson decaying into a pair of τ-leptons in proton–proton collisions at $\sqrt{s} = 13$ TeV with the ATLAS detector." In: *Phys. Rev. D* 99 (2019), p. 072001. DOI: 10.1103/PhysRevD.99.072001. arXiv: 1811.08856 [hep-ex].

[168] ATLAS Collaboration. "Search for Higgs bosons produced via vector-boson fusion and decaying into bottom quark pairs in $\sqrt{s} = 13$ TeV pp collisions with the ATLAS detector." In: *Phys. Rev. D* 98 (2018), p. 052003. DOI: 10.1103/PhysRevD.98.052003. arXiv: 1807.08639 [hep-ex].

[169] ATLAS Collaboration. "Measurements of WH and ZH production in the $H \to bb$ decay channel in pp collisions at 13 TeV with the ATLAS detector." In: *Submitted to EPJC* (July 2020). DOI: 10.3204/PUBDB-2020-02666. arXiv: 2007.02873 [hep-ex].

[170] ATLAS Collaboration. "Search for the standard model Higgs boson produced in association with top quarks and decaying into a $b\bar{b}$ pair in pp collisions at $\sqrt{s} = 13$ TeV with the ATLAS detector." In: *Phys. Rev. D* 97 (2018), p. 072016. DOI: 10.1103/PhysRevD.97.072016. arXiv: 1712.08895 [hep-ex].

[171] ATLAS Collaboration. "Search for the dimuon decay of the Standard Model Higgs Boson with the ATLAS Detector." In: *Submitted to Phys. Lett. B* (July 2020). arXiv: 2007.07830 [hep-ex].

[172] ATLAS Collaboration. *Search for invisible Higgs boson decays with vector boson fusion signatures with the ATLAS detector using an integrated luminosity of* $139\,fb^{-1}$. ATLAS-CONF-2020-008. 2020. URL: https://atlas.web.cern.ch/Atlas/GROUPS/PHYSICS/CONFNOTES/ATLAS-CONF-2020-008.

[173] ATLAS Collaboration. *Measurement of b-tagging efficiency of c-jets in $t\bar{t}$ events using a likelihood approach with the ATLAS detector*. ATLAS-CONF-2018-001. 2018. URL: https://cds.cern.ch/record/2306649.

[174] J. Johannes et al. "A likelihood-based reconstruction algorithm for top-quark pairs and the KLFitter framework." In: *Nucl. Instr. Meth. A 748 (2014) 18-25* 748 (2014), pp. 18–25. DOI: 10.1016/j.nima.2014.02.029. arXiv: 0018.32003arXiv:1312.5595 [hep-ex]. URL: https://www.sciencedirect.com/science/article/pii/S0168900214001855?via%3Dihub.

[175] ATLAS Collaboration. *Calibration of light-flavour b-jet mistagging rates using ATLAS proton–proton collision data at* $\sqrt{s} = 13$ *TeV*. ATLAS-CONF-2018-006. 2018. URL: https://cds.cern.ch/record/2314418.

[176] M. Beneke et al. "Hadronic top-quark pair production with {NNLL} threshold resummation." In: *Nuclear Physics B* 855.3 (2012), pp. 695 –741. ISSN: 0550-3213. DOI: http://dx.doi.org/10.1016/j.nuclphysb.2011.10.021. URL: http://www.sciencedirect.com/science/article/pii/S0550321311005803.

[177] M. Cacciari et al. "Top-pair production at hadron colliders with next-to-next-to-leading logarithmic soft-gluon resummation." In: *Physics Letters B* 710.4–5 (2012), pp. 612 –622. ISSN: 0370-2693. DOI: http://dx.doi.org/10.1016/j.physletb.2012.03.013. URL: http://www.sciencedirect.com/science/article/pii/S0370269312002766.

[178] P. Bärnreuther, M. Czakon, and A. Mitov. "Percent-Level-Precision Physics at the Tevatron: Next-to-Next-to-Leading Order QCD Corrections to $q\bar{q} \to t\bar{t}+X$." In: *Phys. Rev. Lett.* 109 (13 2012), p. 132001. DOI: 10.1103/PhysRevLett.109.132001. URL: http://link.aps.org/doi/10.1103/PhysRevLett.109.132001.

[179] M. Czakon and A. Mitov. "NNLO corrections to top-pair production at hadron colliders: the all-fermionic scattering channels." English. In: *Journal of High Energy Physics* 2012.12, 54 (2012). DOI: 10.1007/JHEP12(2012)054. URL: http://dx.doi.org/10.1007/JHEP12%282012%29054.

[180] M. Czakon and A. Mitov. "NNLO corrections to top pair production at hadron colliders: the quark-gluon reaction." English. In: *Journal of High Energy Physics* 2013.1, 80 (2013). DOI: 10.1007/JHEP01(2013)080. URL: http://dx.doi.org/10.1007/JHEP01%282013%29080.

[181] M. Czakon, P. Fiedler, and A. Mitov. "Total Top-Quark Pair-Production Cross Section at Hadron Colliders Through $O(\alpha_S^4)$." In: *Phys. Rev. Lett.* 110 (25 2013), p. 252004. DOI: 10.1103/PhysRevLett.110.252004. URL: http://link.aps.org/doi/10.1103/PhysRevLett.110.252004.

[182] A. Martin et al. "Parton distributions for the LHC." English. In: *The European Physical Journal C* 63.2 (2009), pp. 189–285. ISSN: 1434-6044. DOI: 10.1140/epjc/s10052-009-1072-5. URL: http://dx.doi.org/10.1140/epjc/s10052-009-1072-5.

[183] A. Martin et al. "Uncertainties on α_S in global PDF analyses and implications for predicted hadronic cross sections." English. In: *The European Physical Journal C* 64.4 (2009), pp. 653–680. ISSN: 1434-6044. DOI: 10.1140/epjc/s10052-009-1164-2. URL: http://dx.doi.org/10.1140/epjc/s10052-009-1164-2.

[184] H.-L. Lai et al. “New parton distributions for collider physics.” In: *Phys. Rev. D* 82 (7 2010), p. 074024. DOI: 10.1103/PhysRevD.82.074024. URL: http://link.aps.org/doi/10.1103/PhysRevD.82.074024.

[185] J. Gao et al. “CT10 next-to-next-to-leading order global analysis of QCD.” In: *Phys. Rev. D* 89 (3 2014), p. 033009. DOI: 10.1103/PhysRevD.89.033009. URL: http://link.aps.org/doi/10.1103/PhysRevD.89.033009.

[186] M. Aaboud et al. “Observation of $H \to b\bar{b}$ decays and VH production with the ATLAS detector.” In: *Phys. Lett.* B786 (2018), pp. 59–86. DOI: 10.1016/j.physletb.2018.09.013. arXiv: 1808.08238 [hep-ex].

[187] S. S. Wilks. “The Large-Sample Distribution of the Likelihood Ratio for Testing Composite Hypotheses.” In: *Ann. Math. Statist.* 9.1 (1938), pp. 60–62. DOI: 10.1214/aoms/1177732360. eprint: 0018.32003. URL: https://projecteuclid.org/euclid.aoms/1177732360.